ABSTRACT

Title of dissertation: MOLECULAR EVOLUTION AND BIOPHYSICAL CHARACTERIZATION OF PLANT GLUTAMATE RECEPTOR-LIKE ION CHANNELS

Alexander Arthur Simon
Doctor of Philosophy, 2020

Dissertation directed by: Professor José A. Feijó
Department of Cell Biology and Molecular Genetics

Plant and animal cells live in different ionic milieus and evolved different electrical membrane properties. As membrane transport in plants and animals has diversified through the population of ion channels to tailor signaling strategies, the glutamate receptor superfamily has emerged to conserve a prominent role in Ca^{2+} and electrical signaling. Ionotropic glutamate receptors (iGluRs) in the mammalian central nervous system are ligand-gated cation channels. Their specificity for glutamate as a ligand required to promote ion channel opening is critical to fast excitatory synaptic transmission and is indispensable for higher cognitive function.

Plant glutamate receptor-like channels (GLRs) are also involved in Ca^{2+} and electrical signaling for a breadth of biotic and abiotic stress responses, sexual reproduction, and cell-cell communication events as determined by genetic analysis. However, the

biophysical underpinnings to GLR's role in cell signaling have only begun to emerge. We addressed the evolutionary conservations of function within the glutamate receptor superfamily and their specialization for plant membrane transport by means of genetics and an electrophysiological characterization of GLR1 encoded by the moss *Physcomitrium patens (Pp*GLR1) using whole-cell patch clamp and Ca^{2+} imaging.

We present a role of *Pp*GLR1 in moss development as a homomeric ion channel involved in light signal transduction that suggests a conservation of function with GLRs found in angiosperms at the physiological level. At the molecular level, we identify the extracellular ligand binding domain of plant GLRs retains structural homology to iGluRs—without the glutamate specificity— while CORNICHON homolog proteins (CNIHs) also have a conserved role in glutamate receptor gating. We further establish distinctive properties of GLRs in ion channel gating and ion selectivity derive from the transmembrane channel pore. The pore works as a direct gate and co-opts the ion selectivity necessary for a membrane depolarization in plant cells by yielding a strong anion permeability with weak mono-cation and Ca^{2+} permeability. By targeted-mutagenesis, the *Pp*GLR1 selectivity filter was swapped out for the mammalian GluA2 (Q-form) selectivity filter converting a predominantly anion-selective channel poorly responsive to ligands into a primarily cationic channel significantly potentiated by the ligand ACC (1-aminocyclopropane-1-carboxylic acid). These results map the molecular evolution of glutamate receptors shaping the ion channel properties conserving plant GLR's role in Ca^{2+} and electrical signaling.

MOLECULAR EVOLUTION AND BIOPHYSICAL CHARACTERIZATION OF PLANT GLUTAMATE RECEPTOR-LIKE ION CHANNELS

by:

Alexander Arthur Simon

Thesis submitted to the Faculty of the Graduate School of the
University of Maryland, College Park in partial fulfillment
of the requirements for the degree
of Doctor of Philosophy
2020

Advisory Committee:
Professor José A. Feijó
Professor Caren Chang
Professor Quentin Gaudry
Professor Angus S. Murphy
Professor Sergi I. Sukharev

Dedication

To

Shae Rose Simon

That the process of scientific discovery may enlighten a conscientious view of the world.

And that my findings shared here may look measly compared to yours.

Acknowledgements

To my lab mates and co-authors who conferred invaluable wisdom and made my project possible, listed in alphabetical order of last name:

Juan Barbosa-Caro
Jörg D. Becker
Caren Chang
Sandra Correia
Daniel S. C. Damineli
Dongdong Li
José A. Feijó
Shanti Pal Gangwar
Marriah N. Green
Marcela Hernández-Coronado
Yun-Ting Kao
Michael A. Lizzio
Erwan Michard
Wangshu Mou
Francisco Neves
Custódio Oliveira Nunes
Carlos Ortiz-Ramírez
Samantha Riesberg
Maria Teresa Portes
Alexander I. Sobolevsky
Bárbara Tavares
Yuhua Wang
Michael M. Wudick

And
To Big Joe, thank you for making the thesis writing the most comfortable experience.

Table of contents

List of tables

List of figures

List of abbreviations

Selected abbreviations commonly used

GLR – glutamate receptor-like gene

iGluR – ionotropic glutamate receptor

CNIH – CORNICHON homolog protein

Pp – Physcomitrium patens

At – Arabidopsis thaliana

Vm – membrane potential

I – current

I-V – current-voltage

Vrev – reversal potential

LBD – ligand binding domain

TMD – transmembrane domain

ATD – amino terminal domain

CTD – carboxyl Terminal Domain

YC3.6 – Yellow CaMeleon 3.6

ACC- 1-aminocyclopropane-1-carboxylic acid

Identification of amino acids adopted the 3-letter nomenclature (i.e. Glu – Glutamate)

WT- Wild-Type

$[Ca^{2+}]$cyt – cytosolic calcium concentration

AP – action potential

VP – variation potential

SP – system potential

Motivation

Glutamate receptors are an evolutionarily conserved superfamily of ion channels crucial for cell signaling and cell-cell communication. Glutamate receptors from the moss *Physcomitrium patens* are uniquely situated to offer perspective not only on plant physiology— aiding efforts to improve general ecosystem health and agronomy— but also on human physiology because of homology to ionotropic glutamate receptors (iGluRs).

Many human diseases resulting from improper ion channel function, known as channelopathies, have been traced back to iGluRs. Malfunctioning iGluRs are common culprits of neurodegenerative diseases like amyotrophic lateral sclerosis (ALS), Alzheimer's disease, schizophrenia, and Parkinson's disease(1–6). In peripheral tissues, iGluRs are also associated with diseases. There is mounting evidence suggesting iGluR expression in a vast array of cancer tissues is responsible for cell proliferation(7). Additionally, iGluRs are promising therapeutic targets for addressing diabetes, osteoporosis, and heart arrhythmias(8, 9). The cause of iGluR-associated diseases is often rooted in an aberrant Ca^{2+} permeability of the channel.

Amidst intensive efforts studying iGluRs to identify the distinct molecular basis underlying channelopathies, many undetermined molecular mechanisms still govern iGluR function. Such absent molecular determinants include factors influencing Ca^{2+} permeation(10). A biophysical investigation of plant glutamate receptors can serve as a powerful hypothesis generator and illuminate fresh perspectives to appreciate the determinants of iGluR (mal)function by identifying evolutionarily conserved mechanisms

key to signaling functions, or otherwise give physiological context to the evolutionary divergence in animals. The recent emergence of moss as a model for designer pharmaceuticals underscores the translational research impact moss glutamate receptor analysis, in particular, can have on humans(11).

As an early land plant, mosses' evolutionary implications extend into angiosperms where expansion and redundancy of gene families, like GLRs, hamper scientific discovery. Identification of similar conservations of function can guide future studies on seed plant development that can significantly impact carbon capture and crop yield, and do so by studying a plant vitally important to the preservation of terrestrial ecosystems.

Mosses were among the first classifications of plants to transition from aquatic to land environments, suggesting significant adaptations to perceive and cope with environmental stress. When one considers moss as (1) an important bio-indicator of ecosystem health; (2) a new source of sustainable fuel cells; and (3) a force for curtailing greenhouse gas emissions —it is evident that knowledge of the cell signaling strategies employed by mosses unlocks their ecological benefit to present insights for tackling ecological threats(12).

Declaration of scientific collaborations

Portions of this dissertation have been published in the following manuscripts and are indicated within the main text accordingly:

Michard E, Simon AA, Tavares B, Wudick MM, Feijó JA. (2017). Signaling with ions: the keystone for apical cell growth and morphogenesis in pollen tubes. **Plant Physiology**. 173: 91-111

Ortiz-Ramirez C, Michard E, Simon AA, Daniel S.C. Damineli, Hernandez-Coronado M, Becker JD, Feijó JA. (2017). GLUTAMATE RECEPTOR-LIKE channels are essential for chemotaxis and reproduction in mosses. **Nature**, 549:91-95.

Mou W, Kao Y*, Michard E*, Simon AA*, Li D, Wudick MM, Lizzio MA, Feijó JA, Chang C. (2020). "Ethylene-independent signaling by ACC in ovular pollen tube attraction in *Arabidopsis*". **Nature Communications**, 11:4082.
**contributed equal work*

Gangwar SP , Green MN , Michard E, Simon AA, Feijó JA, Sobolevsky AI. (2020). The Structure of the Arabidopsis Glutamate Receptor, GLR 3.2, Ligand-Binding Domain. **Structure,** 28:1-9.

Michard, E. and Simon AA. (2020) Melatonin's antioxidant properties protect plants under salt stress. **Plant, Cell & Environment,** 43:2587–2590.

Unless explicitly stated, the data presented was completed by myself under the supervision of my doctoral advisor, Professor José A. Feijó, as well as Dr. Erwan Michard. I have generated data, designed experiments, or critically discussed results in all figures.

Figure 44: Barbosa-Caro, J (University of Maryland, Department of Cell Biology and Molecular Genetics), performed the ion selectivity experiments on *At*GLR3.4.

Figure 45: Barbosa-Caro, J (University of Maryland, Department of Cell Biology and Molecular Genetics), contributed to generating data measuring Asn potentiated *At*GLR3.4 currents.

Figure 48: Gangwar SP, Green MN, and Sobolevsky AI (Department of Biochemistry and Molecular Biophysics, Columbia University), performed the *At*GLR3.2 protein purification and structure determination.

Figure 49: Michard, E (University of Maryland, Department of Cell Biology and Molecular Genetics), performed the YC3.6 based Ca^{2+} imaging of *At*GLR3.2 in transfected COS-7 cells.

Chapter 1: Introduction

1.0 Membrane transport and ion channels

Membrane transport is the process of transporting ions and solutes across the cell membrane. Ion channels are key elements of membrane transport as integral membrane proteins that mediate ionic fluxes down electrochemical gradients bypassing an energetic barrier imposed by the lipid cell membrane. An aqueous pore spanning the membrane allows ions to flow through at rates of 10^6 ions per second, faster than can be accomplished by other passive transport mechanisms through carrier proteins or active transport mechanisms working against electrochemical gradients using pumps, or co-transporters(13, 14). An ion channel's main features that optimize its biological role are its ion selectivity and channel gating. Ion selectivity is the preference for specific ionic species to permeate through a channel and illustrates the concept that the channel determines what ions are permeant. The channel excludes the flow of an undesirable ion type while permitting a desirable one to pass. Ion channels exist along a spectrum from being highly selective, strongly favoring one ionic species, to being non-selective where multiple diffusing ions experience little difficulty to permeate. The other key feature, channel gating, is the mechanism of opening and closing the ion channel. Gating defines under what conditions the selected ions may permeate. Various stimuli such as the membrane voltage or ligand binding commonly initiate ion channel gating.

Membrane transport —and the sum of ion fluxes across the membrane— contributes to accomplishing a myriad of cellular processes, principally, cell signaling.

The transport of ions which carry an electrical charge modulates the membrane potential as an electrical signal. Ca^{2+} transport additionally triggers signal transduction pathways based on Ca^{2+}'s second messenger functions. Collectively, electrical and Ca^{2+} signaling prompt a systemic response for transcriptional regulation, altering gene expression, metabolism, and hormone biosynthesis(15–18). As electrical and Ca^{2+} signaling reflect the membrane transport network, an understanding of these cell signaling strategies among eukaryotes brings the broader context of membrane transport into view. After referencing animal models, I will briefly review electrical and Ca^{2+} signaling in plants.

1.1 Overview of electrical signaling and Ca^{2+} signaling

The membrane potential (*Vm*) is the difference in electrical voltage between the interior and exterior of a biological cell. A change in *Vm* —constituted by an ionic flux across the membrane— confers an electrical signal. Essential to the ion flux's energetic origins, the resting *Vm* is an important parameter as it establishes the starting point for membrane transport. The *Vm* reflects standing gradients in electrical charge and chemical (solute) concentrations — the two electrochemical gradients driving passive ion transport— making ionic flux directly dependent on *Vm*. Reciprocally, ion fluxes also shape the *Vm*.

Along a continuous plasma membrane, the *Vm* can be excited (or depolarized) and self-propagate by activating voltage-dependent ion channels. Deciphering this excitable system underpinning nerve action potentials earned Alan Hodgkin and Andrew Huxley a share of the 1963 Nobel Prize(19–24) (with John Eccles who evaluated

chemical transmission at the synapse). Their work galvanized the study of ion channels advancing all aspects of mammalian physiology. Well-defined in animals, electrical signaling frequently directs behavioral responses(25) and is the core phenomena behind action potentials that control muscle movements, a rhythmic heartbeat, and how nerve impulses travel throughout the brain in which the frequency of firing codes information. The work of Hodgkin and Huxley on excitable systems also paved the way to discoveries illustrating that neighboring cells influence each other's membrane potential, making an electrical propagation a reliable mechanism for long-distance or cell-cell communication. At cellular junctions, where two cells are physically separated, electrical signaling continues to display a consistent pattern across cell types. A membrane depolarization evokes a neurotransmitter's release into the extracellular space that opens ligand-gated cation channels propagating the membrane depolarization onto the next cell. For example, at the neuromuscular junction, a depolarization evokes the release of acetylcholine activating acetylcholine receptors. At the presynaptic neuron, a depolarization evokes the release of glutamate activating ionotropic glutamate receptors. The gate-keeper for any signal transduction to proceed is the translation of the electrical signal (i.e. the membrane depolarization) into a chemical message. Ca^{2+} influx almost always fulfills this process, most notably performed by depolarization activated Ca^{2+} channels(26–28). Single action potentials can stimulate cytosolic Ca^{2+} ($cyt Ca^{2+}$) increases, tightly intertwining the relationship between electrical and Ca^{2+} signaling (29).

Ca^{2+} signaling then serves as a local message. Poor diffusion rates of Ca^{2+} in highly buffered cytosolic environments confines Ca^{2+} signaling to an immediate spatial

range(30). Ca^{2+}'s long lasting impacts on cell biology come courtesy of vast Ca^{2+} based signaling cascades for transcriptional regulation(31). The fundamental features that make Ca^{2+} a robust second messenger are conserved among eukaryotes. More urgently, many of the long standing questions asked to appreciate Ca^{2+} signaling are based on the regulation of the proteins necessary for Ca^{2+} transport.

1.2 Electrical signaling in plants

Action potentials were first discovered in plants in 1873(32) and later recorded by microelectrodes in 1930(33), two decades before Nastuk and Hodgkin(34) recorded action potentials from animal cells by impaling frog muscle fibers in 1950. With this early success, electrical properties of plants were even used as models to study neuronal impulses (35). Although electrical signaling in plants has been widely recognized, it remains poorly resolved as its physiological purpose and biophysical prerequisites have posed a challenge to understand.

A variety of plant cell types qualify as excitable cells by demonstrating changes in *Vm* in response to environmental stimuli such as light(36–40), temperature(41–43), pathogens (44), salinity or amino acids(45), and mechano-sensation(46) by touch, wounding, and herbivory(47). All such stimuli activate ion channels or other transporters(48). Recent efforts to define electrical signaling in plants have so far carved out a dizzying variety of electrical signals tuned by various stimuli(49). They are generally classified into three categories of; action potentials, variation potentials, and system potentials.

An action potential (AP) is an all-or-nothing depolarization of quantal amplitude and duration that self-propagates along the membrane, effectively connecting multiple cells (13). APs in plants are known to occur from exposure to cold, touch or direct electrical stimulation(50). While fitting the criteria of an AP, the kinetics of APs in plants are pronounceably slower than in animals and also vary between species (Figure 1). For comparison, cardiac cells display action potentials of 200ms. In the nervous system, an AP occurs over momentary time scales of 1-2ms propagating at rates from 1-100m/s (51). The algal genus *Chara* exhibits APs occurring over time scales of 2-3s with a propagation rate of 20mm/s, three orders of magnitude slower than in nerves. Similarly, cold shock and touch-induced APs are well-documented in *Mimosa pudica* to propagate at rates of 20-30mm/s. APs in *Arabidopsis* were shown to last longer than ten seconds with a propagation velocity of 1mm/s (52). In *Physcomitrium patens*, *Vm* changes expected to be APs lasted over minutes when elicited by either shining far-red light or abrupt light to dark transitions(39, 53). Compared to APs, variation potentials and system potentials vary in biophysical properties, including magnitude, polarization, and kinetics; but each demonstrates multicellular propagations covering long distances (Figure 2). Just as applying various stimuli activates ion channels, an electrical propagation further insinuates a process of ion channel activation and inactivation.

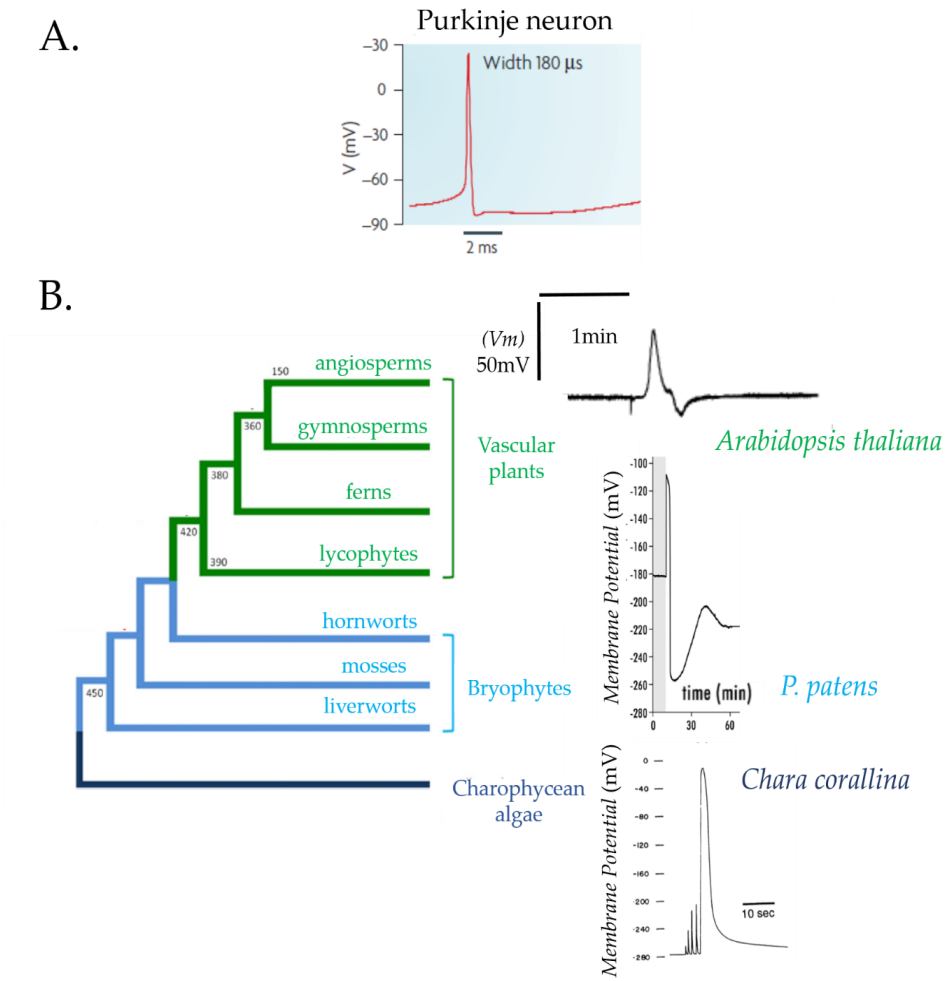

Figure 1: Action potentials along the plasma membrane over an evolutionary span. A.) The classical action potential recorded in neurons is fast and depolarizes the plasma membrane to positive potentials. B.) The succession of land plants coincides with variable action potential waveforms reflected in the after-hyperpolarization phase and kinetics. The maximal membrane potential does not exceed 0mV. The representative action potential shown from a neuron and *Chara* were elicited by current injection. The representative action potential from *P.patens* was elicited by exposure to light stimuli. The representative signal in *Arabidopsis* was elicited by direct voltage stimulation of 9V. Numerical annotations within cladogram indicate evolutionary divergence in millions of years. Adapted from Favre and Agosti, 2007 (54); Koselski *et al.*, 2008 (39); Shimmen *et al.*, *1994* (55) ; Ruszala *et al.*, 2011 (56); Bean, 2007 (51).

Variation potentials (VPs), also known as slow-wave potentials (SWPs), are different than APs and unique to plants (Figure 2). VPs are graded electrical

depolarizations induced by physical damage to the tissue that travels through distant undamaged cells. They are distinct from APs in their irregular waveform (Figure 2). Based on data from *M. pudica* where VP propagation rates are four times slower than APs at 5-6mm/s, all VPs are generally hypothesized to propagate slower as well (52). On the contrary, *Arabidopsis* VPs have recently been described to propagate at 9.2cm/min when elicited by herbivory-induced wounding, matching the AP stimulated by direct voltage(50, 57).

A third type of propagating electrical signal is the system potential (SP) (Figure 2). A graded hyperpolarization of the membrane characterizes a system potential differentiating it from APs or VPs. The conditions for SP elicitation are also specific, known to occur after tissue wounding and upon the two stimulations of glutamate or Ca^{2+}. The first stimulation excites an AP, and the second produces the SP (Figure 2)(58, 59).

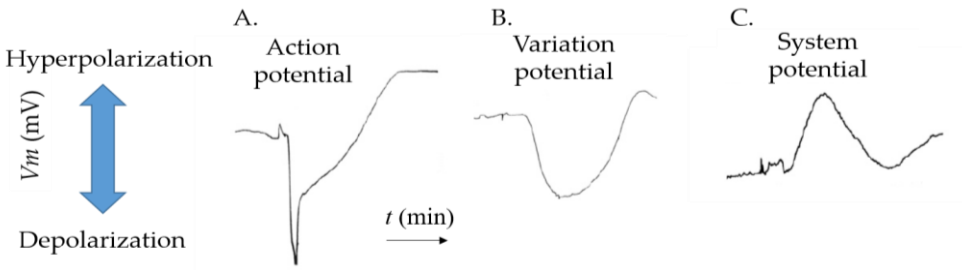

Figure 2: The variety of electrical signals recorded in angiosperms. Downward defections of membrane potentials correspond to a depolarization of the membrane. Extracellular recordings of electrical signals performed by Zimmermann *et al.,* 2016 (59).

Lastly, non-propagating potentials may be electrical signals. Membrane potential dynamics significantly impact single cells like guard cells and pollen tubes, where propagation is not possible. In guard cells, membrane transport dictates an oscillatory *Vm* and drives stomatal function for adjusting osmotic relations and regulating gas

exchange(60–63). The correlations that can be observed indicate an opening of the stomata aperture is associated with the plasma membrane's hyperpolarization. Therefore, a closing of the stomata aperture correlates with the plasma membrane's depolarization(64). The pollen tube receives special attention as an example where ion signaling plays a key role in morphogenesis. The growing pollen tube has complete dependence on distinct gradients of H^+, Cl^-, and Ca^{2+} formed by a system of ion fluxes choreographed by a network of ion channels, transporters, and pumps. Due to the standing gradients, a membrane potential gradient is hypothesized to exist with a depolarized apical zone as a marker for growth polarity(65).

However, despite the description of various electrical signals in plants there still is a general dearth of information about the membrane potential, including the molecular properties that make it a useful signal. The second messenger functions of H^+, and especially Ca^{2+}, which are consequential of the ion transport are more visible and better appreciated. As a case study, a more thorough examination of ion signaling as it relates to the second messenger functions in the pollen tube can be found in Appendix B.

1.3 Ca^{2+} signaling in plants

Ca^{2+} is a universal intracellular second messenger(66). Ca^{2+} signaling in plants plays a prominent role in reproduction, cell growth, and in response to environmental stress— to name a few general examples we can draw from *P.patens* and *Arabidopsis* covering the lineage of land plants. Like in animals, freely swimming sperm from the

moss *P. patens* demonstrate a dependence on [Ca^{2+}]cyt (67–69). In *Arabidopsis*, non-motile sperm are delivered to the female ovule by the tip-growing pollen tube that display an apical Ca^{2+} gradient which oscillates in particular patterns correlated with cell growth regimes(70–72). Other tip-growing plant cells, such as root hairs, show a similar apical gradient(73). Moreover, an apical gradient of Ca^{2+} featuring oscillatory patterns is a phenomenon also shared by tip-growing protonema cells of *P. patens*(74). Environmental stresses from salinity(75, 76), light(77), herbivory and wound(47, 78, 79), symbionts and pathogens(80, 81), temperature and touch(82), oxidative stress(83), and osmoticum evoke Ca^{2+} signals (84). Ca^{2+} elevations have been reported in a single cell compartmentalized to the cytosol, chloroplast, nucleus, or occupying entire tissues(85). Elicited signals are also unique to specific stimuli(86, 87) are generated in a concentration dependent manner(88), and vary by cell type(89).

The Ca^{2+} signaling function foremost depends on its transport across the plasma membrane and endomembranes by ion channels and pumps generating Ca^{2+} gradients. Ca^{2+} transport is able to create the conditions for an efficient second messenger due to steep electrochemical driving forces generated in large part from low free [Ca^{2+}]cyt and abundant Ca^{2+} stores in other cellular compartments like the apoplast and vacuole. Small influxes of Ca^{2+} into the cytosol give rise to transient changes in the cytosolic concentration. Following the generation of a cytosolic Ca^{2+} signal by Ca^{2+} influx, the Ca^{2+} buffering machinery—primarily Ca^{2+} transporters and pumps creating Ca^{2+} efflux—enable distinct signatures to develop over time and space by the use of stores in the apoplast and organelles that allocate [Ca^{2+}] (90–95). Of all the stores, the apoplast with

free concentrations up to 1mM has been proposed to the primary source of Ca^{2+} required for the signaling because inhibiting plasma membrane Ca^{2+} channels or chelating free apoplastic Ca^{2+} largely abolishes all of the ensuing Ca^{2+} signature(91). Thus, a Ca^{2+} signal's generation is critical, and bequeaths Ca^{2+} permeable channels on the plasma membrane a central function. The identity of the Ca^{2+} permeable ion channels on the plasma membrane will be discussed in greater detail below (Section 1.5).

A plethora of Ca^{2+} sensing proteins that decode the Ca^{2+} signature cements the specificity of a given Ca^{2+} signal. Universal decoders include calmodulin (CaM), calmodulin-like (CML), calcineurin B-like (CBL) proteins, CBL-interacting protein kinases (CIPK), and the Ca^{2+}-dependent protein kinases (CDPK)(64). Many membrane proteins contain EF-hands or other Ca^{2+}-binding domains, namely RBOHs an important family of NADPH oxidases involved in ROS signaling(96). Other transporters are also subjected to post-translational modifications through Ca^{2+} binding sites or Ca^{2+}-dependent phosphorylation (e.g. the anion channel family SLAH(97, 98)) deepening the sophistication of Ca^{2+} signaling.

In light of the powerful signaling capabilities bestowed by rapid and large elevations of Ca^{2+}, these same attributes of Ca^{2+} signaling also present risks. The cell must balance the influx required for signaling, but maintain $[Ca^{2+}]$cyt within a homeostatic range. Ca^{2+} homeostasis anchors elevated $[Ca^{2+}]$cyt to sub-micromolar levels from a basal concentration typically less than 500nM. Excessive Ca^{2+} presents lethal side effects of ion toxicity and interferes with precipitation of phosphate compounds such as Adenosine Triphosphate (ATP)(28, 95). An unchecked Ca^{2+} concentration leads to

apoptosis in all cells and is intimately tied to many human pathologies like heart disease, diabetes, and various neurological disorders. In light of Ca^{2+} signaling's universality, transcriptomic and computational studies have shown the genetic machinery in plants involved in Ca^{2+} signaling has been modified(99, 100). The evolutionary pressure to maintain a low [Ca^{2+}]cyt has encouraged the diversity of membrane proteins transporting Ca^{2+}, whether it is across the plasma membrane or endomembrane. Plant cells have seemingly expanded the capacity for Ca^{2+} efflux out of the cytosol and into stores safeguarding the potency of Ca^{2+} signaling(99, 100). The primary Ca^{2+} efflux proteins include: the auto-inhibited Ca^{2+}-ATPase (ACA)(87, 101, 102) , endoplasmic reticulum Ca^{2+}-ATPase (ECA)(103), Ca^{2+}/H^{+} exchanges (CAX)(104, 105), and the mitochondrial Ca^{2+} uniporter complex (MCUC)(106).

1.4 Coupling electrical and Ca^{2+} signaling

Electrical and Ca^{2+} signaling are two major cell signals that are intimately linked. The role of the two associated signals underlies the fundamental thinking about cell-cell communication. In animal neurons, AP propagation is unequivocally an electrical phenomenon characterized by a fast depolarization that is regenerated from place to place by voltage-gated channels. In contrast, Ca^{2+} influx generates the local cell signal. However, a theoretical model of electrical signaling in plants is far less resolved than in animals. Such a model would need to include the plant cell plasma membrane's biophysical properties, the molecular identity of proteins involved in ion transport, their electrophysiological characteristics, and their sequential organization. An overlooked yet

fundamental challenge to building such a model is reconciling the demands of Ca^{2+} transport. The movement of the charged second messenger is inherently predicted to transiently produce subcellular Ca^{2+} elevations (the generation of a Ca^{2+} signal) and change the *Vm* (an electrical signal) simultaneously; Ca^{2+} signaling does not exist without electrical signaling. To be clear, Ca^{2+} signaling is inarguably critical for plant cell signaling, but its relationship to *Vm* should be considered(107).

It is worth addressing an ongoing debate discussing if an electrical mechanism for cell-cell communication of plant cells is conserved. Mobility of oligosaccharides(108) , abscisic acid(109) , reactive oxygen species(110), and Ca^{2+} itself have all been proposed to underlie a signal propagation. Early on, Bose's ingenuity (1907)(111) isolated electrical activity as the core phenomenon underlining a signal propagation since the activity once stimulated was insensitive to temperature. If signal propagation was due to chemical mobility, thermodynamic principles would predict slower propagation at lower thermal energy (i.e. such phenomena should have a thermal Q_{10} close to one). As other possible explanations became evident —such as temperature sensitive membrane proteins—genetic experimentation re-enforced the likelihood of electrical propagation. From wounded tomato plants, Wildon *et al.,* (1992)(112) detailed transmission speeds incompatible with chemical mobility and indicated an electrical propagation with genetic evidence for the first time by knocking out *pin* genes. These data begin to assert an electrical component into signal propagation. Now, the implementation of genetically encoded Ca^{2+} probes into plants has further aroused new questioning into the precise mechanism and some authors propose a Ca^{2+} induced Ca^{2+} release mechanism(79, 110).

Ca^{2+} propagations, frequently called "waves", appear to exist in plants outside the realm of what was previously acknowledged. The work of Lionel Jaffe pioneered the study of intracellular Ca^{2+} waves that come about by Ca^{2+} induced Ca^{2+}-release by grouping them according to their speed as the chief metric: ultraslow, slow, fast and ultrafast waves (113). Ultrafast waves travel at top speeds of 6µm/s. Reported in *Arabidopsis*—by the genetically encoded Ca^{2+} indicator YC-nano-65— salt stress-induced Ca^{2+} waves propagated up to 400µm/s (75). In a separate study, aequorin-based GFP sensor measurements described systemic Ca^{2+} propagations from 50µm/s to 300µm/s (76). Faster still, Ca^{2+} waves illustrated by the group of Ted Farmer with genetically encoded Ca^{2+} reporter GCaMP3 quantified propagation rates at a blistering 9.2cm/min (1500µm/s) in response to herbivory(57). The conclusions of this work by Nguyen *et al.*, were able to maintain that the membrane depolarization preceded the maximal $[Ca^{2+}]$cyt, aligning with an electrical propagation model conserved among animals. They further supported this conclusion through genetic knockouts of the plasma membrane H^+ pump AHA1(114) validating prior H^+ pump pharmacology describing fusicoccin as a variation potential (VP) inhibitor(115). Impressively, mutant *Arabidopsis pdko3* plants defective in plasmodesmata integrity have lost the herbivory-induced long-distance electrical propagation(116). The mutants revealed no voltage-gated K^+ channel activity and a complete loss of the plasma membrane depolarization from the root to shoot. In this study, wild-type and mutant plasmodesmata showed equal cytosolic accumulations of reactive oxygen species (NO, H_20_2) and Ca^{2+}. Losing only the *Vm* signal was sufficient to decrease the expression of the JAZ gene, a known herbivory

induced transcriptional upregulation. Bricchi *et al.*, therefore showed the membrane potential is affected by plasmodesmata disruption and disentangled the *Vm* effect from Ca^{2+} suggestive than an electrical signal can be independent of a Ca^{2+} signal (2013). Another mutant plant expressing a PLDP5 over-expression gene— which impairs plasmodesmata conductance— was later shown to limit the transmission of cytosolic Ca^{2+}, emphasizing the suggestion the plasmodesmata may play an intricate role in coupling of electrical and Ca^{2+} signaling via the connection of adjacent cells(117).

More aligned with Jaffe's characterization are Ca^{2+} waves induced by osmotic stress. Using the genetically encoded YC3.6, Ca^{2+} waves in *Arabidopsis* plantlets traveled at 58.5+18.9 μm/s. With the same protocol, osmotic-induced systemic Ca^{2+} waves in the moss *P. patens* traveled at 4.5+3.8μm/s (84), falling in the fast to ultra-fast range matching the rate found within a single cell when monitoring fluorescence from the cell-permeable dye fura-dextran(118). Because systemic propagations and those within a single cell report the same speed, it suggests, at least in *P.patens*, anatomical differences may not figure. However, perhaps the biophysical properties of membrane transport between *P.patens* and *Arabidopsis* account for the differences in the propagation rate. Additionally, the variety of propagating electrical potentials found in all plants alludes to a variety of ion transporters regulated by voltage. This dissertation now turns its attention to focus on the evolution of the membrane transport system to integrate the electrical signaling with Ca^{2+} signaling.

1.5 Evolution of membrane transport

The specialization of electrical and Ca^{2+} signaling in plants compared to animals is delineated by the evolution of the membrane transporters involved and their biophysical properties(119). The transport of H^+, Ca^{2+}, anions, and K^+ form the basis of the unique electrical properties of plant cells.

Anion channels command membrane depolarizations in plant cells.

Hodgkin and Huxley demonstrated that voltage-dependent ion transport—particularly of Na^+— is the keystone for animal cell electrical signaling. As ion channels allow the passive ion movement, the ion concentration gradients across the membrane are part and parcel with the electrical membrane potential (*Vm*) to determine the transport direction. Accordingly, the ionic basis of animal APs depends on an inwardly facing NaCl gradient. The influx of Na^+, through Na^+-selective channels, is electrochemically conducive to depolarizing the plasma membrane(19). Fast voltage-dependent Na^+ channels are even conserved in unicellular protists, the aquatic chlorophytic algae *Chlamydomynas*, and diatoms in addition to their expression in animals. However, the genetic material for fast voltage-dependent Na^+ channels is absent from the more terrestrial charophytic algae, mosses, and developed land plants like *Arabidopsis* (120, 121). This loss of fast voltage-dependent signaling from the ion-selective 4-domain voltage-sensitive ion channels suggests adaptive signaling mechanisms for plant life.

To fit the physiological demands and surrounding milieu, the ionic basis of plant electrical signals has seemingly adapted. The major difference is that, under non-stress conditions, a low concentration of extracellular NaCl is present around plant cells. A

marginal Na^+ gradient exists, compounding the absence of Na^+ channels and leaving a vacancy for what ions and transporters command the *Vm* (the membrane transport events occurring under salt stress can be found in Appendix C.). Atop the hierarchy of the transport network are the P-type ATPases(122). In plants and fungi, this will be the H^+-ATPase that establishes what is known as the proton motive force used to set the electrochemical parameters driving solutes through channels and energizing co-transporters. It is a motor hyperpolarizing the membrane by pushing protons out of the cytosol and into the apoplast. This activity generates a H^+ concentration gradient and an electrical charge difference stabilizing a resting membrane potential that is hyperpolarized compared to animal cell models, with values from -150mV to -200mV (123, 124). As a result of the proton motive forces, particularly the negative resting membrane potential, anion channels are apt to mediate the dominant depolarizing current in plant cells through an efflux of the negatively charged ions. K^+ can also act as a depolarizing ion, yet the equilibrium potential for anions is significantly more positive than for K^+ permitting anions to depolarize the membrane to a greater extent. Ca^{2+} is another ion capable of driving a depolarization, but a robust buffer system lessens the capacity for a sustained depolarization.

The experimentally determined model of plant APs isolates each ion's activity (Figure 3). A $[Ca^{2+}]$cyt increase initiates the depolarization, depending to some degree on crossing the plasma membrane but mostly as a result of release from internal stores(125). An anion efflux then drives the predominant depolarizing phase while the proton pump (H^+-ATPase) shuts down. K^+ efflux, like in animals, plays the major role in membrane

repolarization. As previously mentioned, K^+ influx does induce a depolarization, but because the *Vm* depolarizes beyond the K^+ equilibrium potential its flux direction is thereby reversed. The described ionic basis has been most comprehensively derived from giant characean cells of *Chara* and *Nitella* (126). However, it is now becoming clear that the trends are consistent with other species along the evolutionary span from freshwater algae to terrestrial angiosperms. The ionic basis fits the charophytes(127, 128) including *Chara* (125, 129), *Nitellopsis obtuse* (130), the liverwort *Conocephalum conicum L.*(131), the moss *Physcomitrium patens(* formerly known as *Physcomitrella patens)* (39, 132), and the flowering plant *Arabidopsis thaliana*(133, 134). Importantly, the role of anions as the primary depolarizing ion in plants is consistent across cell types in roots and the single-cell models of guard cells and pollen tubes(62)-(135).

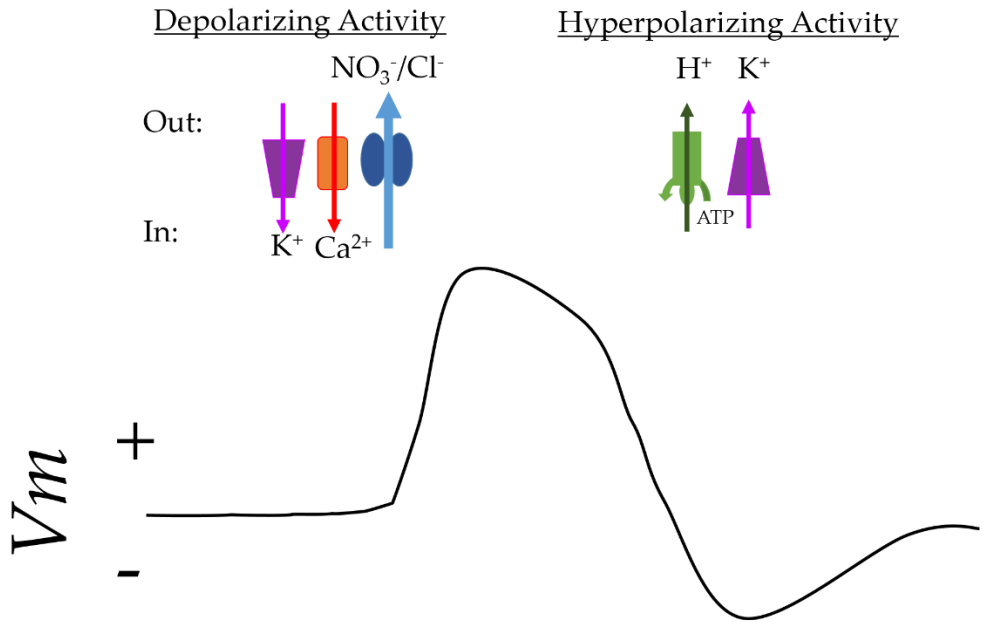

Figure 3: Ion activities in plant cells. This picture demonstrates the ionic basis of electrical membrane potential in plant cells. Directionality of major ionic fluxes from a typical plant cell (top) associated with its effect on the membrane potential (*Vm*) is modeled below as a cartoon (bottom). The largest magnitude of depolarization is carried by an anionic efflux. Influxes of K^+ and Ca^{2+} also depolarize the membrane. The electrogenic H^+-ATPase is a hyperpolarizing motor that pushes protons out of the cytosol into the apoplast. Outward K^+ fluxes play a role in repolarizing the membrane potential.

Evolution of anion channels

A lot is unknown about the function and molecular nature of plant anion channels. Rigorous electrophysiological investigations of anion currents from protoplasts have revealed categorically distinct types(136–138). Among those with some known molecular identity include depolarization-activated anion channels designated by a 1.) slow action (S-type), encoded by the slowly activating anion channel (SLAC) family and their homologs (SLAH), and a 2.) rapid action (R-type) channels sometimes referred to as quickly activating anion channels (or QUAC-like) and known to be encoded by genes for aluminum activated malate transporters (ALMTs)(139, 140). Both the SLAC and QUAC families emerged with land plant evolution and are absent in animals(141). The anion-selective mechanosensitive channels— now known to be encoded by the MSL family homologous to bacterial small conductance mechanosensitive channels (MscS)— constitute the third class of anion channels with no animal equivalent. Many more anion channel types have been proposed with roles extending beyond voltage control for nutrition, metabolism, and regulating turgor pressure (142, 143). Other classifications of described anion channels include inward-rectifying anion channels (IRAC), an outward-rectifying anion channel (ORAC), hyperpolarized-activated anion channels (HAAC), and light-activated anion channels (Reviewed by Roberts 2006(138); Tavares *et al.*,

2011(137)). Additional orthologues exhibiting SLAC and QUAC-like characteristics may also still be outstanding. However, molecular identity of the channels or transporters mediating many of the described anion currents described from protoplasts have yet to be discovered.

Some of the best characterized anion channels found in animals share homology to anion channels in plants. Arguably one of the most important animal anion channels is the cystic fibrosis transmembrane regulator (CFTR) Cl^- channel belonging to the ATP-binding cassette (ABC) family. With over one hundred ABC transporters encoded by the plant genome, most are uncharacterized. Provocatively, CFTR pharmacology regulates *Arabidopsis* anion currents(144). Found throughout the plant and animal kingdoms are the class of CLC transporters. In animals, they can be Cl^- channels or Cl^-/H^+ exchangers(145–147). *Arabidopsis* CLC-a localized to tonoplast and endomembranes was convincingly demonstrated to be a selective NO_3^-/H^+ exchanger(148). It is unknown if any plant CLCs encode ion channels. The cys-loop ligand-gated ion channel superfamily comprises the largest set of anion channels in mammals that include GABA receptors and Glycine receptors (GlyR)(149). $GABA_A$ receptors, the larger subset of Cl^- channels, mediate the primary inhibitory current on adult neurons. Under special conditions—such as in immature neurons— $GABA_A$ receptors can, in fact, mediate an excitatory Cl^- efflux. The excitatory action of $GABA_A$ receptors is due to a reversed Cl^- gradient mimicking the excitable basis of plant cells, rather than stemming from an alternative molecular mechanism for mammalian cell excitability(150). No putative plant $GABA_A$ receptors homologous have been discovered, but AMLTs (QUAC-type anion

channels), however, do share a functional 12-amino acid GABA-binding motif, and are regulated by GABA pharmacology(151, 152).

The diversification of plant anion channels involved in membrane depolarization supports the most parsimonious explanation that they played a fulfilling role in the adaptation of membrane transport strategies required for plant cell signaling. Those anion channels with voltage-dependent properties— particularly the fast inactivating R-type— are reminiscent of neuronal Na^+ channels and have led to general speculation that plants evolved to utilize anion channels for exciting electrical propagations. However, this has never been proven. A formidable challenge to address that hypothesis remains to identify the various anion channels hypothesized in protoplasts. Looking again at the ionic basis of APs and VPs, only the molecular identity of channels localized to the plasma membrane directly associated with the depolarization phase has been from the glutamate receptor family and the K^+ -selective channel, AKT1(133, 153, 154), neither of which are thought to allow an anion permeation.

Evolution of Ca^{2+} channels

The relatively few Ca^{2+} permeable ion channels in plants that also have poor Ca^{2+} selectivity demarcates the genetic and biophysical basis of Ca^{2+} transport in plant cells compared to animals(99). In animal cells, a plethora of channel families mediate Ca^{2+} transport such as NMDA-type ionotropic glutamate receptors (iGluRs), cyclic nucleotide gated channels (CNGs), transient receptor potential channels (TRPs), P2X receptors, the Ca_v family that codes for voltage-dependent Ca^{2+} channels (VDCCs), and two-pore

channels (TPCs). Plus some highly Ca^{2+} selective channel families with $P_{Ca^{2+}}/P_{Na^{+}}$ > 1000 like Ca^{2+} release - Ca^{2+} activated channels (CRACs), inositol 1,4,5-trisphosphate receptors (IP_3Rs), and ryanodine receptors (RyRs) have prominent roles in Ca^{2+} induced-Ca^{2+} release. The understanding of Ca^{2+} transport in plants is only in its infancy. Just five families including glutamate receptor-like channels (GLRs)(72, 155), cyclic nucleotide gated channels (CNGCs)(156, 157), hyperosmolality-gated Ca^{2+}-permeable channels (OSCAs)(158, 159), two-pore channels (TPCs)(160) and mechanosensitive channels(161, 162) have been proposed to mediate Ca^{2+} influx where none are known to be selective for Ca^{2+} as they also permeate monovalent cations including K^{+}. A potential shortcoming in assessing what transporters may be involved in a given Ca^{2+} flux is the electrophysiological characterization of currents from unidentified ion channels endogenously expressing in plant protoplasts. These include voltage-dependent channels that are either hyperpolarization-activated Ca^{2+} channels(163–166) or depolarization-activated Ca^{2+} channels(167–171).

Table 1 summarizes the differences in anion channels between plants and mammals as well as the view that plants lost some of the prominent cation/Ca^{2+} channels of mammals. Strikingly, both mammalian and plant cells express a family of glutamate receptors (referred to as iGluRs in mammals and GLRs in plants) that form functional ion channels. Both iGluRs and GLRs are heavily associated with cell signaling and cell-cell communication events stemming from properties that generate a depolarization of the plasma membrane and elevate $[Ca^{2+}]$cyt. iGluRs are among the most well-characterized ion channels for synaptic connectivity. Even so, the biophysical properties of plant GLRs

governing their ion channel gating and ion selectivity remain unresolved, leaving the molecular mechanism underpinning their participation in membrane transport unknown. This observation yields intriguing questions of how the molecular basis of membrane transport and cell signaling has evolved between organisms with a central nervous system, including mammals, and organisms such as plants who lack a nervous system and face varying physiological demands.

Table 1: Evolution of anion and Ca^{2+} channel populations between an alga, an early land plant, a flowering plant, and from mammals (based on rodent and human models). The quantity of genes for selected ion channels were identified by a literature search, with references provided in brackets. All annotations of *Chara* were published by Nishiyama *et al.,* 2018 (120). If reference is unlisted, gene annotations were obtained from Edel and Kudla, 2015(100) or Edel *et al.,* 2017 (99). The lone *Pp*TMEM16 was identified by accession number: Pp3c7_22640V3.1 based on protein BLAST of *At*TMEM16.

	Chara	*P.patens*	*Arabidopsis*	Mammals
Anion Channels				
(S-type) SLAC/SLAH	0/0	2/2 ([(172)],[(173)])	1/4 [(172)]	0 [(141)]
(R-type) ALMT/QUAC-like	1	5 [(172)]	13 [(172)]	0 [(141)]
MscS (MSL)	2	16 [(174)]	10 [(175)]	0 ([(176)], [(177)])
Bestrophins	3	1 ?	2 ([(141)], [(178)])	4 [(179)]
TMEM16/Anoctamin	1	1	1 [(152)]	10 [(180)]
CLC	4	3 [(181)]	7 [(182)]	9 [(183)]
$GABA_A$ Receptors	0	0	0	19 [(150)]
GlyR	0	0	0	5 [(184)]
Ca^{2+}/Cation Channels				
Glutamate Receptors	0	2	20	18
TPC	1	9	1	2
CNGC	7	8	20	6
MCA	0	?	2	?
Piezo	1	1 [(174)]	1	2
OSCA	5	15	15	3 (TMEM63) [(185)]
Orai	2	1	0	3 [(186)]
Catsper	3	0	0	4 [(187)]
TRP	0	0	0	27
VDCC (Ca_v)	0	0	0	10
P2X	0	0	0	7 [(188)]
4D-Na_v	0	0	0	10 [(189)]
IP_3	0	0	0	3
RyR	0	0	0	3 [(190)]

1.6: Ionotropic glutamate receptors

iGluRs in neuronal physiology

Ionotropic Glutamate Receptors (iGluRs) are ligand-gated cation channels that electro-chemically connect two neurons. Well defined biophysical properties and substrate specificity foster high fidelity synaptic connectivity crucial for learning and memory. Glutamate is the principal neurotransmitter in the central nervous system that mediates neurotransmission upon binding to its ion channel forming receptor protein.

The eighteen mammalian iGluR members are classified into four groups based on ligand specificity; N- methyl-D-aspartate (NMDA) receptors (NMDARs) (six members; GluN1, GluN2A-D, GluN3A-B), alpha-amino-3-hydroxy-5-methyl-4-isoxazolepropionic acid (AMPA) receptors (AMPARs)(four members; GluA1-4), kainate receptors (KARs) (five members; GluK1-5), and δ receptors (two members; GluD1-2). Each group plays distinctive roles in neurotransmission. NMDARs are cationic and Ca^{2+} permeable channels(191, 192). Post-transcriptionally edited R-form channels derive the majority of AMPAR and KAR characteristics that in their homomeric form are impermeable to Ca^{2+} and weakly permeable to anions ($P_{Cl/Cs}$ AMPAR is 0.14 and KAR is 0.74)(193). Only the Q-form AMPARs and KARs are permeable to Ca^{2+}. δ receptors are the least characterized of the four subgroups, but appear to resemble the AMPARs and KARs as non-selective cations channels whose Ca^{2+} permeability is dependent on the Q-form(194–196).

Under physiological conditions, an incoming electrical signal at the pre-synapse, manifested by a depolarization of the plasma membrane, activates Ca_Vs to induce Ca^{2+}-

dependent exocytosis releasing glutamate into the synaptic cleft(197–199). Glutamate binding to the non-NMDARs at the post-synaptic membrane initiates a rapid depolarization carried by an influx of Na^+ ions and propagates the electrical signal when the voltage threshold is reached to the adjacent neuron relaying the message. A Ca^{2+} influx at the post-synaptic neuron follows when glutamate plus glycine or D-Ser binds to NMDARs generating an elevation of $[Ca^{2+}]$cyt initiating second messenger functions for transcriptional regulation (Figure 4).

δ receptors have long been considered non-ligand gated channels whose molecular participation in synaptic function was observed, but mechanistically uncertain. In recent years, δ receptors' functionality as ionotropic receptors has been granted through an endogenous ligand-gating action evoked by D-Ser(200–202). For simplicity, an input of δ receptors on synaptic connectivity has been omitted from Figure 4 until a physiological clarification is obtained.

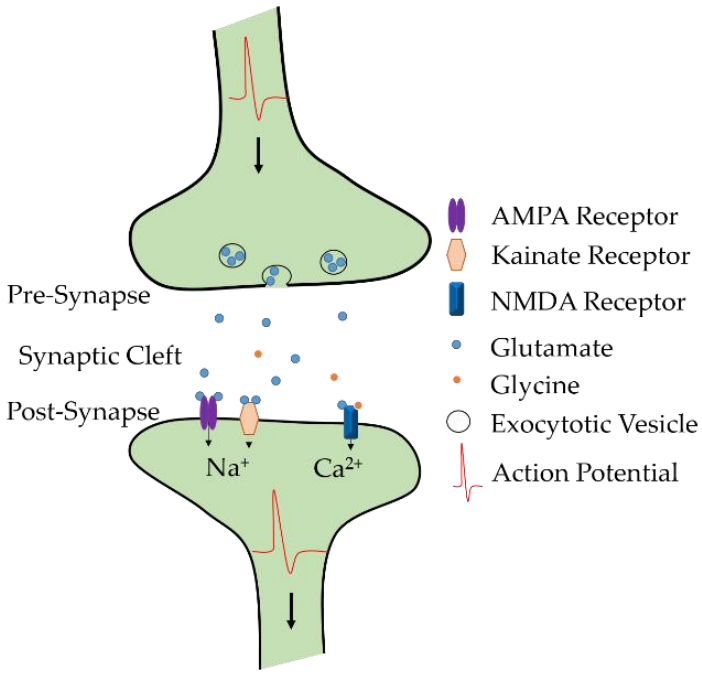

Figure 4: Glutamatergic signaling. High fidelity synaptic transmission is moderated by Glu and iGluRs at the post-synaptic membrane.

iGluR structure determination

Neuronal iGluRs, first cloned by Hollmann *et al.*, (1989) have experienced rigorous structure determination studies incorporating electrophysiology, x-ray crystallography, and cryo-electron microscopy (cryo-EM) (203). The collective effort has revealed various structural conformations detailing the channel structure, permeation pathway, and gating scheme.

Architecture of iGluRs

iGluRs are tetramers with a modular layout comprised of four structural layers; a ligand binding domain (LBD), an amino terminal domain (ATD) , a transmembrane

domain (TMD), and a C-terminal domain (CTD). Four isoforms build a “dimer of dimers” creating four extracellular ligand binding sites acting as the receptors with a central transmembrane pore (Figure 5). Intermediate between the receptor and the pore is a third functional domain in the TMD known as the “gate” (204, 205).

The LBD and ATD are both extracellular domains in a two-fold symmetry. The LBD is encoded by the S1 and S2 segments of each gene and is translated into the clamshell-like “receptor” with two globular lobes, an upper lobe (D1) and a lower lobe (D2). The mouth of the lobes accommodates ligand binding. The ATD layer sits on top of the LBD. It is also organized as a pair of dimers but displays a subunit crossing over to twist and alternate the dimer pairing entangling the protein. The ATD is thought to be an essential domain in NMDARs for receptor assembly(206, 207), membrane trafficking, and as a site for allosteric modulation, notably by Zn^{2+} (208, 209). Interestingly, for some KARs, albeit under overexpression conditions, the ATD may be nonessential as mutants with the ATD cleaved off remain functional(210).

The TMD layer is made up of three transmembrane spanning domains (M1, M3, M4) and one re-entry loop (M2). It is attached directly below the LBD by polypeptide linkers (S1-M1, M3-S2, S2-M4). Achieving a four-fold symmetry, four M3 subunits converge as a teepee acting as the “gate” for the central “pore” made by the M2 subunits. As part of the TMD and comprising the permeation pathway, the “gate” (M3) and the “pore” (M2) are considered to be the effector domains of ligand binding. These are the gates that need to open through the gating scheme (detailed below) to allow selective ion permeation. M1 and M4 flank the permeation pathway and communicate LBD movement

influencing channel opening and the degree of desensitization. Part of their function is attributed to their connection to the polypeptide linkers and the M4 flip/flop cassette(211).

Finally, the C-terminal domain has not been verified by structure determination studies. However, it is known to influence channel localization and regulation(212). Among the NMDAR family, the C-terminal domain bears a prominent CaM complex the dictates a Ca^{2+} dependent inactivation(213).

iGluR gating scheme

The iGluR gating scheme consists of a continuum of transient conformational arrangements marked by several key states. Ligand binding to the LBD initiates the iGluR gating scheme to open the channel. Important for channel gating is the interplay between the modular layers as ligand binding induces a conformational rearrangement of the entire protein. Ultimately, LBD mobility translates into a structural rearrangement of the pore reflected by an ionic conductance.

The conformational states adopted by iGluRs— specifically referring to AMPARs unless otherwise stated— include a "resting" or closed state, a pre-active state, an open state, and a desensitized state. A closed configuration reflects a non-conducting ion channel where the receptor is free of glutamate and the clamshell-like LBD is fully open. Glutamate binding to the LBD initiates the gating cycle transitioning into the pre-active state where glutamate binding partially closes the clamshell, but still leaves the transmembrane domain unaffected and pore occluded. With sufficient energy—

dependent on the specific ligand and concentration— the clamshell closes a complete 26˚ bringing D1 and D2 closer together. More critically, individual D2 upper lobes move out and away from a central axis (205, 214, 215). This separation exerts a strain to pull the linkers connecting the LBD to the TMD and splay open a helical bundle formed by the transmembrane "gate". The pore itself then also needs to widen in the open state for current to flow.

iGluR heteromerization

Heteromerization with different channel isoforms or auxiliary proteins adds to the channel structure, forming a more diverse or larger complex. AMPARs and KARs are known to exist as homo-tetramers and diheteromers. NMDARs are obligate hetero-tetramers, unknown to function as homomers, and are even capable of forming diheteromers and triheteromers(216, 217). The dimerization itself is not inconsequential— besides forming the central ion channel pore— inter-subunit contacts bonding the dimers together affect the ligand-gating kinetics, especially in the desensitization process(218). Despite being tetrameric receptor proteins, iGluR subunits are gated independently, lending heteromerization the ability to tune the gating response in a stoichiometric dependent manner (219).

The most well studied auxiliary proteins are the TARPs (transmembrane AMPAR regulatory proteins)— specifically γ2 known as stargazin(220)— and the CORNICHON homologs (CNIH)(221). TARPs and CNIH are both positive regulators of AMPARs working to maintain an open conductive channel (Figure 5C, 5D). They enhance glutamate sensitivity, slow desensitization rates, enhance a steady-state current following

an attenuated desensitization process, and relieve polyamine block by promoting polyamine permeation(222)(223)(224). Mutagenesis of TARPS illustrated that these transmembrane proteins buttress against that iGluR TMD and affect gating by interacting with the extracellular LBD-TMD linkers(225). The conserved role of TARPS in *C.elegans* speaks for their obligatory nature in synaptic function(226). The cryo-EM structure of GluA2 in complex with CNIH3 showed extracellular C- and N- terminal domains, similarly indicating an interaction with the extracellular channel domains(227). Negative regulators like germline specific gene 1 (GsG1L) maintain a closed configuration of the channel(228, 229).

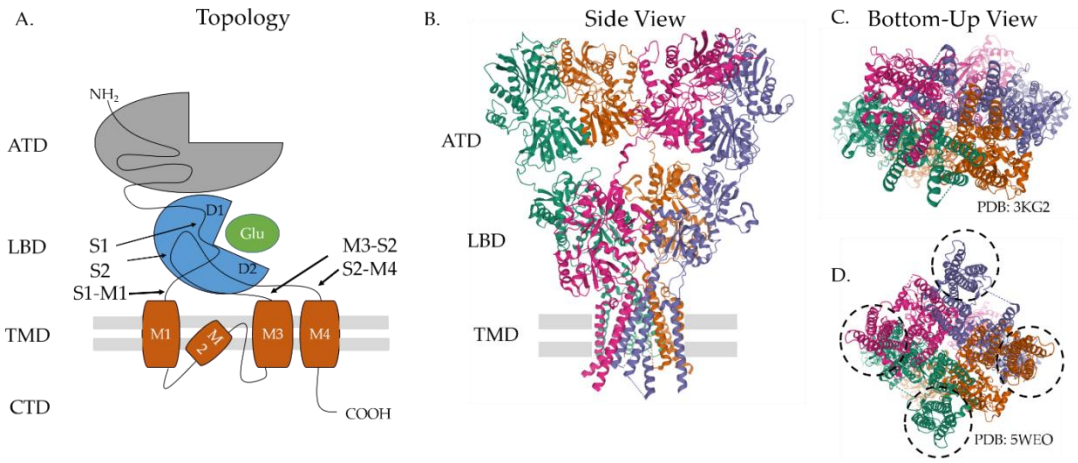

Figure 5: iGluR Structure. A.) Topology cartoon of a single subunit outlining channel domains. B.) Cryo-EM structure of homomeric GluA2 (PDB: 3KG2) illustrating the modular design of a tetramer, individual subunits color coded by purple, magenta, green and orange. Each subunit consists of four transmembrane alpha-helices, a receptor and an amino terminal domain. C.) top panel; bottom-up view of GluA2 depicting a central pore formed by four subunits in a closed configuration representing a non-conducting channel, (PDB Accession code: 3KG2). Bottom panel; bottom-up view of GluA2 depicting an open central pore in complex with the auxiliary protein stargazin that contribute an additional four transmembrane helices on the periphery of the iGluR TMD denoted by dashed circles (PDB Accession code: 5WEO).

Overview: molecular determinants of glutamate receptor ion selectivity

The iGluR pore, the space where ions pass through the channel, is formed by the re-entry loop M2. M2 consists of the selectivity filter harboring the key residues determining ion selectivity in each iGluR subfamily. The bacterial glutamate receptor, GluR0, is a potassium selective ion channel expressing the conserved K^+ selectivity "TTVGYGD" motif found in other voltage-gated K^+ channels(230). A glutamate receptor from the freshwater bdelloid rotifer *Adineta vaga*, *Av*GluR1, is likewise a K^+ channel encoded by the similar "TxVGYGx" motif(231). The selectivity filter of iGluRs found in mammals lost the motif conferring K^+ selectivity in favor of a non-selective cation permeability conducive to divalent (Ca^{2+}, Ba^{2+}, Mg^{2+}) and monovalent cations (Na^+, K^+, Cs^+). The iGluR selectivity filter spans from a "Q/R/N" site to a narrow constriction point and ending with a negatively charged entry point from the cytoplasmic side. Non-NMDARs (AMPARs and KARs) and NMDARs have distinct ion selectivity and ion permeation properties that can be explained in part by differences in the selectivity filter (Figure 6).

Molecular determinants of ion selectivity in AMPARs and KARs

The Q/R/N site at the tip of the pore is an essential residue that regulates the varying ion selectivity. Genes for AMPARs and KARs exonically encode for a Gln (Q) to be transcribed and translated. However, in postnatal mRNA, an editing event converts the Gln (Q-Form) to an Arg (R-Form) in AMPARs and KARs. This editing event switches AMPARs and KARs from Ca^{2+} permeable cation channels to Ca^{2+} impermeable

channels with the slight anionic permeability. A Cl^- permeability is argued to come from electrostatic forces on the extracellular side of the pore(232). The Q/R/N site also renders the channel insensitive to polyamine block and yields a smaller unitary conductance(211). Farther into the ion permeation pathway, the narrow constriction exerts either electrostatic or steric hindrances to limit the maximum rate of ion permeation. At the pore entry facing the cytosol, a highly conserved negatively charged Asp has been speculated to play a role in cation vs. anion selectivity(229). Remarkably, Asp to Asn mutations in GluA3 channels that neutralized the charge did not alter divalent permeability or appreciably shift the reversal potential compared to wild-type channels. The mutation did, however, produce substantially greater outwardly rectifying currents(233).

Molecular determinants of ion selectivity in NMDARs

NMDARs display a notable Ca^{2+} permeability that makes their cell signaling function unique to that of Ca^{2+}-impermeable AMPARs. What accounts for selectivity differences between AMPARs and NMDARs? In NMDARs, an encoded Asn (N) at the Q/R/N site likewise plays a determining role in Ca^{2+} permeability such that targeted mutagenesis to a Gln (Q) lowers Ca^{2+} permeability(234). Although the amino acid encoded differs, the aligned position nonetheless plays a determining role in the Ca^{2+} permeability. At the cytosolic entry point— aligned to the conserved Asp in AMPARs— a negatively charged Glu was indeed shown to be responsible for divalent permeability(235).

The effect of heteromerization on NMDRs electrophysiological properties supports the role of pore lining residues to determine ion selectivity. GluN3 subunits lack the conserved negatively charged residue within the pore, and hetero-tetrameric channels with GluN3 show strongly attenuated Ca^{2+} permeability. Relative $P_{Ca/Na}$ for GluN1-GluN2A heteromeric channels could be calculated between 2.8 and 4.5, whereas the $P_{Ca/Na}$ of GluN1+GluN3A heterotetrameric combinations was calculated to 0.6(211). In another example experiment, triheteromic NMDARs consisting of GluN1-GluN2A-GluN3A yielded an estimated of P_{Ca} /P_{mono}= 0.6 compared to 3.4 in diheteromeric GluN1-GluN2A(236).

The higher Ca^{2+} permeability makes for a more complicated permeation pathway involving more cation binding sites in or around the selectivity filter. Referring to GluN1, tryptophan residues in the pore contribute to the narrow constriction and confers a divalent cation selectivity over mono-valent cations(237, 238). A unique DRPEER motif in GluN1 peripheral to the pore and gate—outside the selectivity filter— also serves as Ca^{2+} binding locations aiding Ca^{2+} permeability. This motif imposes a strongly negative electrostatic potential attracting cations and was specifically shown to attenuate fractional Ca^{2+} currents when the charges were neutralized(239, 240). Also outside the pore, a G815 residue in the M4 domain permits high Ca^{2+} permeability and participates in channel deactivation by exerting a conformational change on the pore. The mutation of GluN1(G815A)/N2A narrows the pore to 1.2 Å compared to 1.8 Å (241).

The pore is also the site of a pronounced voltage-dependent block from intracellular, as well as extracellular, Mg^{2+}. Inward currents are inhibited until the Mg^{2+}

binding is ejected by depolarization. The Mg^{2+} interacts at two sites; the Q/R/N site and the subsequent downstream residue (N+1) that form the narrow constriction point(242). The same residues essential for Ca^{2+} selectivity also present a barrier for other divalent ions suggesting these sites is actively involved in the ion permeation process.

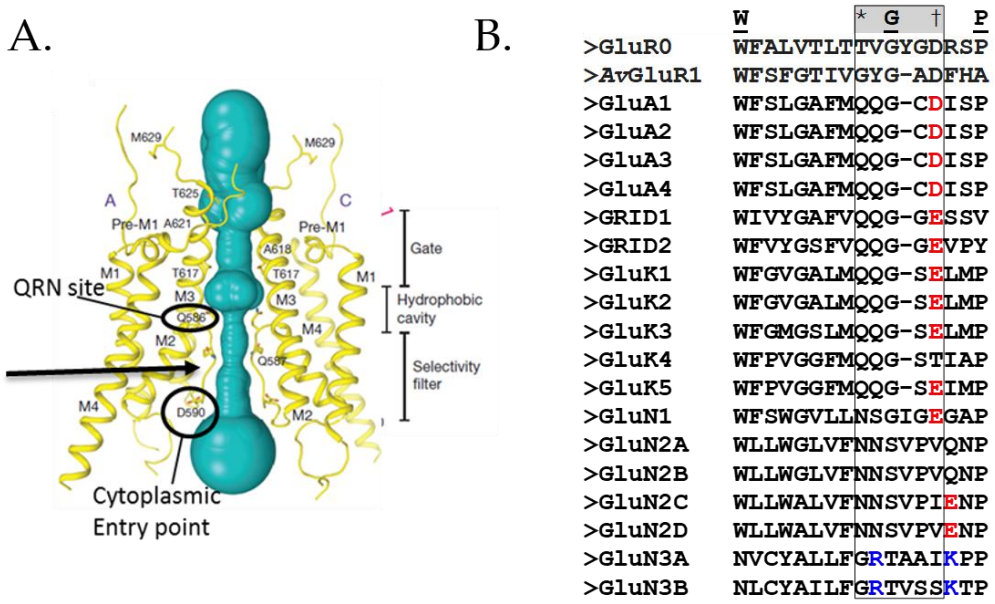

Figure 6: iGluR pore representation. A.) Molecular resolution of an AMPAR (GluA2) TMD with an open pore configuration depicting key selectivity filter residues and the gate forming the upper conduction pathway. Bubbled area (cyan) is representative of volume available for the ion conduction pathway. Arrow indicates the narrow constriction. Adapted from Twomey *et al.*, 2017(229). B.) Sequence alignment of iGluR pore region flanked by the WGP motif with bacterial GluR0 and *Av*GluR1. Boxed in residues contain the selectivity filer. Asterisk (*) denotes the Q/R/N site. Dagger (†) denotes the cytoplasmic entry point. Alignment generated by ClustalOmega.

1.7: Glutamate Receptor-Like Channel Introduction; GLR physiology

The discovery of glutamate receptor homologs in plants was an eye opening finding considering the absence of a central nervous system. It is now clear the glutamate receptor superfamily is an evolutionarily conserved family of ion channels, only absent in archeabacteria and fungi(231, 243–247). Specifically, plant GLRs are conserved

throughout the succession of land plants from algae to angiosperms coinciding with a substantial expansion in the number of GLR coding sequences. There are two genes in the moss of *Physcomitrium patens (P.patens),* while the model flowering plant of *Arabidopsis thaliana* (*At*) has twenty genes divided into three clades(248). *Pp*GLRs phylogenetically cluster near the *Arabidopsis* clade three intermediate to the most ancestral glutamate receptor (Figure 7) (249, 250). Documented in *Arabidopsis,* GLRs are expressed throughout the whole plant (being in the roots, leaves, and the stem and petiole tissue) and exhibit subcellular localization to the plasma membrane, the vacuolar system, endoplasmic reticulum, and plastids (41, 57, 71, 251–253). Only a few Clade 2 *At*GLRs (*At*GLR2.2/2.3/2.4/2.6) have shown a preferential expression exclusive to the roots(254). The remainder of this chapter will continue to discover the current understanding of GLRs in *Arabidopsis*. Chapter 2 will then discuss the role of GLRs in *P.patens* in greater detail.

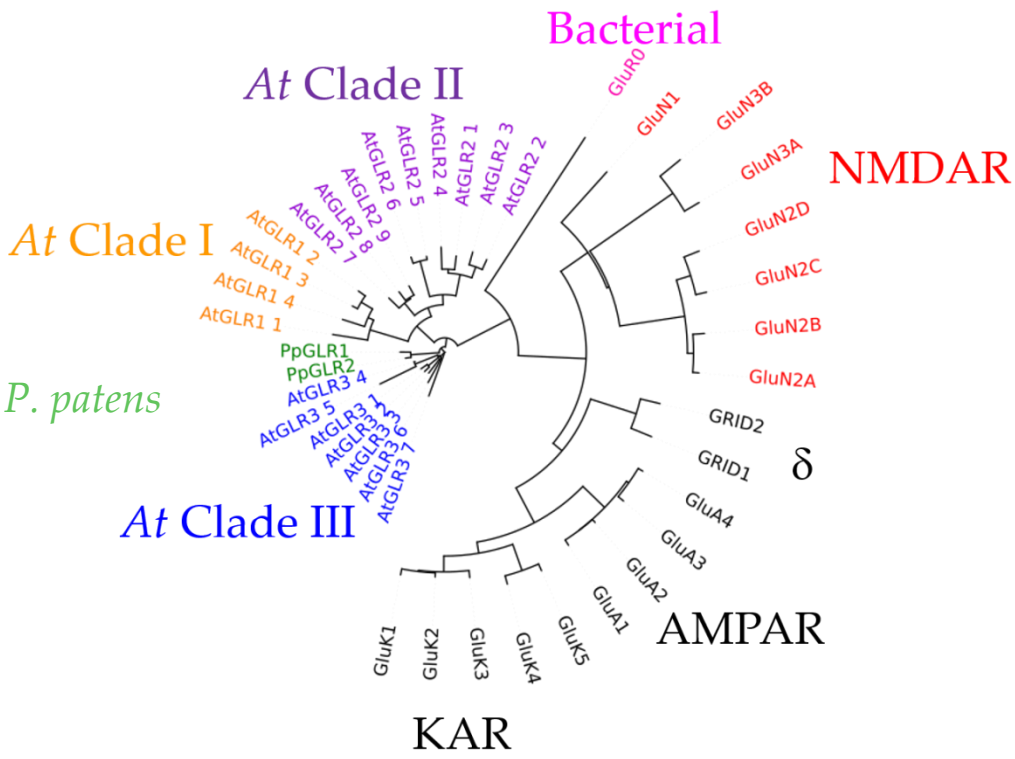

Figure 7: Evolutionary relationship of glutamate receptors. Phylogenetic tree depicting the eighteen mammalian iGluRs (NMDARs, AMPARs, KARs, δRs) twenty *Arabidopsis* GLRs (*At*), two *P. patens* GLRs (*Pp*), and one bacterial GluR0. Phylogenetic distances were calculated with ClustalOmega.

The abundance of coding sequences and ubiquitous expression bears participation in diverse physiological processes, including; light signal transduction and photosynthesis(155, 253), nitrogen sensing and metabolism (255–257), water loss for drought tolerance(18, 258) , Abscisic acid biosynthesis (18, 259), self-incompatibility(260), root morphogenesis(252), seed germination(261), and root development (262). Early pharmacological approaches hinted at a major contribution of GLRs might be mediated by Ca^{2+} fluxes and through depolarizing the plasma membrane(263, 264).

To date, the most fruitful research to uncover the roles of glutamate receptors in plants has been done by genetic analysis looking for differences in Ca^{2+} and electrical signaling. GLR mediated Ca^{2+} signaling in *Arabidopsis* has been incorporated explicitly in pollen tube growth (71, 72), defense against herbivory, wounding and pathogens(57, 79, 81, 117), as well as regulation of stomatal aperture (265, 266) among others like immune responses(81, 267). In response to herbivory or abiotic stress(17, 41, 268), a depolarization of the membrane potential was associated with an elevation of $[Ca^{2+}]$cyt .Reminiscent of iGluR-dependent neuronal transmission, GLR-dependent electrical signals are systemic responses traveling long-distances. GLRs involvement was oriented on the propagation through the undamaged tissue, and less so at the damage site(269).

Consistent with a predicted ligand-gating mode, amino acid application has been shown to be a general stimulator to increase $[Ca^{2+}]$cyt and membrane depolarizations(270–272). The outstanding parameter regarding amino acid induced signaling is the variety of amino acids capable of stimulating a response, at least a dozen proteinogenic amino acids are GLR agonists: Glu, Gly, D-Ser, L-Ser, Asn, Thr, Ala, Cys, Met, Trp, Phe, Leu, Tyr. The physiological reason for this mostly non-specific response is yet to be understood. Current hypothesizes postulate a role for an amino acid sensor monitoring metabolic status or picking up on environmental chemical cues.

1.8: Ion channel properties of Glutamate Receptor-Like Channels

Crystallization of isolated LBDs from *At*GLR 3.2 and 3.3 has verified the evolutionary relationship between GLRs and iGluRs, revealing structural homology by

adopting a bi-lobed clamshell shape (273),(274) (Figure 27A). As full-length proteins, plant GLRs are predicted to share the modular design of iGluRs and dimerize into tetrameric ion channels (Figure 8). With limited the structural data, challenges to understand plant glutamate receptors arise as they are poorly conserved from mammalian iGluRs, sharing between 5% and 19% identity(275). The pore region, for example, is so divergent from iGluRs it is impossible to predict ion selectivity(276) (Figure 9). Genetic analysis of GLRs credibly finds their role in a plethora of physiological functions, yet has been unable to describe an underpinning molecular mechanism. Before turning our attention to the ion channel properties of *Pp*GLR1, the foundational data on *At*GLRs will first be introduced.

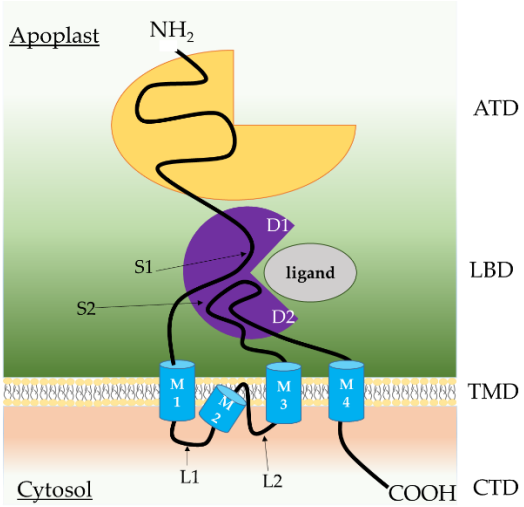

Figure 8: Predicted GLR structure. Topology of plant GLRs matches modular design of iGluRs.

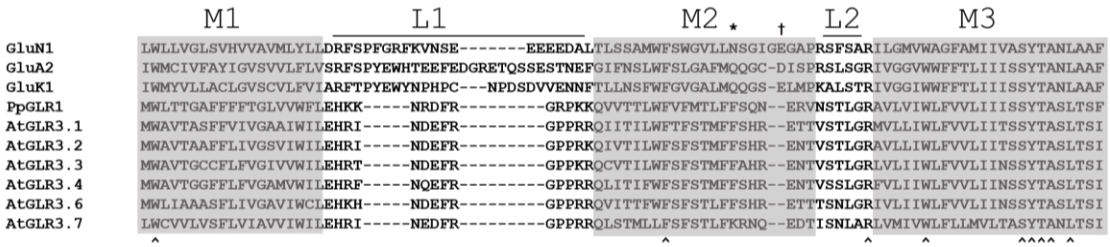

Figure 9: Sequence alignment of the continuous GLR transmembrane portion comprising the channel pore (M2) and gate (M3) (between S1 and S2) to representative iGluRs. Above the sequences; the asterisk (*) denotes the aligned Q/R/N site, and the dagger (†) denotes the aligned cytoplasmic entry point. Below the sequences; a caret (^) denotes a fully conserved amino acids residue.

Ion channel properties of *At*GLRs

The standard for obtaining a functional ion channel characterization is the ability to incorporate a heterologous expression system. This has proven to be a challenge for investigating GLRs (41, 71). When expressed in *Xenopus laevis* oocytes, at least fifteen of the twenty *At*GLRs have been considered pore dead ion channels. The proposed pore dead channels included: *At*GLR 1.2/1.3, 2.2/2.4/2.5/2.7/2.8/2.9, and all of clade 3 being 3.1/3.2/3.3/3.4/3.5/3.6/3.7. When the pore domain of these *At*GLRs was independently transplanted into the kainite type receptor (KAR), GluR6, only isoforms of *At*GLR1.1 and 1.4 mediated Glu-gated currents. Sequences from the other GLRs could not yield a current despite Western blot analysis showing protein expression. The natural interpretation being that most GLRs are not functional ionotropic receptors(277). At the beginning of the Ph.D. thesis presented herein, only two GLRs out of twenty had been successfully expressed as full-length proteins in a heterologous system; *At*GLR1.4 was characterized in *Xenopus* oocytes(272) and *At*GLR3.4 in HEK293 cells(278). These separate investigations found differences regarding ion selectivity and suggested a high

degree of diversity in terms of ligand gating properties. *At*GLR1.4 was suggested to be a nonselective cation channel gated by large hydrophobic amino acids, primarily methionine. *At*GLR3.4 was suggested to be a highly selective Ca^{2+} channel, most responsive to asparagine. Currents from these channels were never recapitulated in a second system to ameliorate the differences or broaden the experimental interpretation. A report from rice (*Oryza sativa, Os*) found Glu triggers Ca^{2+} influx, first in roots, and then in HEK293 cells expressing *Os*GLR2.1. Unlike *At*GLRs, *Os*GLR2.1 showed faster Ca^{2+} signals lasting less than one minute after applying Glu(279).

The difficulty in heterologous expression is possibly due to cell toxicity, post-translational modifications, failed protein folding, or from the absence of critical channel subunits(41, 71). As previously noted, a prominent role for auxiliary subunits and subunit heteromerization to alter iGluR properties provided grounds to test if *At*GLRs may also require a more elaborate complex to be operational.

Qualitative demonstration of *At*GLR assemble with CNIH and heterodimerize

Only one family of auxiliary proteins, the CORNICHON homolog proteins (CNIH), have been identified in plants. When co-expressing *At*CNIH with *At*GLRs, it was discovered *At*CNIH1 and *At*CNIH4 synergistically exert a necessary functional regulation of *At*GLR3.2 as well as *At*GLR3.3 to produce a functional ion channel(71). To evaluate the general need of the *At*CNIH proteins for *At*GLR activity, clade 3 *At*GLRs with or without *At*CNIHs in COS-7 cells and monitored GLR activity with the whole-cell patch clamp experiments(71) (Erwan Michard, unpublished). *At*GLR3.2, *At*GLR3.3,

*At*GLR3.4, *At*GLR3.6, and *At*GLR3.7 were observed to not conduct any current when expressed by themselves, even after the addition of 1mM Glu — compatible with the findings of Tapken *et al.*, 2008(277). *At*GLR3.1 was the exception showing the behavior of a *bona fide* ligand-activated channel as a homomer. He, therefore, co-expressed the clade 3 *At*GLRs with *At*CNIH1+*At*CNIH4 and examined a cell's ability to conduct a background current and their sensitivity to Glu. All GLRs tested now induced background currents when co-expressed with *At*CNIH1+*At*CNIH4. The sensitivity to Glu was dependent on the GLR expressed, with a respective ligand-sensitivity as follows: (marginal or no activation) *At*GLR3.6=*At*GLR3.3 < *At*GLR3.2 < *At*GLR3.4 < *At*GLR3.1 (strong current activation by the ligand).

The necessity of heteromerization with other GLR subunits constitutes another limitation in characterizing GLR functionality. Two-hybrid experiments performed in yeast previously suggested the ability of GLRs to form heteromers (280). FRET analysis in HEK293 cells showed an interaction of *At*GLR3.2 with *At*GLR3.4 and suggested *At*GLR3.3 may form heteromers with unidentified channels(252). As a proof of principle that GLRs can form heteromers, three GLRs that did not form active channels when expressed alone in COS-7 cells, namely *At*GLR3.3, *At*GLR3.6, and *At*GLR3.7, were co-expressed in pairs for patch clamp analysis (Erwan Michard, unpublished). Ionic currents were recorded in three heterodimer combinations and were potentiated by Glu (1 mM). The ability of heteromerization to produce functional ion channels serves as important control for the combinatorial pairing of *At*GLRs and *At*CNIHs, especially considering that the stoichiometric relationship of iGluR subunit dimerization and TARP co-assembly

differentially modulates gating properties(219, 281). Since many GLRs require *At*CNIHs for functional expression, Michard surveyed possible GLR heteromers using *At*CNIH4 as a current activator. The co-expression study showed that heteromerization modulates current amplitudes and sensitivity to Glu. This appeared particularly evident from data analysis related to heteromers involving *At*GLR3.7 and *At*GLR3.2. While *At*GLR3.7 gave no current when expressed with *At*CNIH4 alone, its co-expression enhanced the whole-cell currents with all other GLRs tested. The *At*GLR3.7 subunit also enhanced the Glu-activation of the current when co-expressed with other subunits. Co-expression of *At*GLR3.2 with other subunits also demonstrated a pattern of a dominant channel. The co-expression of *At*GLR3.2 tended to decrease current amplitudes (*At*GLR3.2+*At*GLR3.4 currents were smaller than *At*GLR3.4 currents). And in contrast to *At*GLR3.7, the presence of *At*GLR3.2 subunit decreased Glu sensitivity of the currents.

The systematic analysis of clade 3 GLRs revealed that obligatory heteromerization attributes three levels of functional diversity. First and secondly, *At*GLRs require the presence of either of two CNIH proteins or another GLR subunit. Thirdly, the heterodimer combination impacts the ion channel gating illustrated by the various proportions of background current compared to ligand-activated current. That is to say, some heterodimers are leaky channels while other channels open and close promptly by exposure to an amino acid ligand. Still uncertain in the end are the naturally occurring heteromeric combinations.

1.9: GLRs in *Physcomitrium patens*

The pivotal evolutionary leap for establishing all terrestrial ecosystems — plant and animal alike — was when plants first colonized the land nearly 500 million years ago. Among the early colonizers were members of the bryophytes like mosses, liverworts, and hornworts(282). Plants then diversified along the succession of land plants adapting in physiology and the accompanying anatomy; for example, land plants established true roots and a developed vasculature system. Perhaps the most significant adaption was a genomic reconstruction where the diploid sporophyte emerged as the prominent generation in land plants. The physical and molecular diversification that occurred is now thought to be accomplished by the expansion of pre-existing gene families rather than the emergence of new gene families(283, 284). New regulatory gene networks (and their translated protein networks) promoted the adaptive traits. Hence, the existence of ancestral genes may have evolutionarily conserved characteristics. Such evolutionary conserved genes have already been identified between *P.patens* and *Arabidopsis* in tip-growing cells as well as the sporophyte suggesting the genetic basis governing, for example, a tip-growing behavior, is the same (284). The family of GLRs follows suit in that from only two genes encoded by the genome of *P.patens* the *Arabidopsis* genome expanded to encode for twenty genes. GLRs in both *P.patens* and *Arabidopsis* are thought to be involved in the same physiological roles as they are active in tip growing cells and also have roles in sexual reproduction of both species, but the molecular manifestation of the expanded genome remains an open question. Significantly, there is an emerging acknowledgment that *At*GLRs participate in many

protein-protein interactions as shown by their obligatory heteromerization. We aim to investigate in what capacity *At*GLRs diversified from *Pp*GLRs and what evolutionary conservations may exist.

The present thesis adopted an approach to study an evolutionarily ancestral GLR from the moss *Physcomitrium patens* as a model to address the functional properties of GLRs. Genetic studies performed in *Physcomitrium patens* previously suggested a conserved function in Ca^{2+}-dependent signal transduction. *Pp*GLRs were demonstrated to participate in Ca^{2+} signaling during male gamete mobility and targeting toward the female egg(67). Additionally, single *glr1* and *glr2* gene knockouts presented additive loss-of-function phenotypes in sporophyte maturation as well as spore quantity and size. Of two genes encoded, *Pp*GLR1 is expressed in all developmental stages and is the only one expressed in the haploid gametophyte that comprises the dominant vegetative tissue of the plant life cycle, and contributing the bulk of the biomass in mosses (Figure 10A). *Pp*GLR2 is expressed only in the reproductive tissues of the diploid sporophyte(67, 285)(Figure 10C,D).

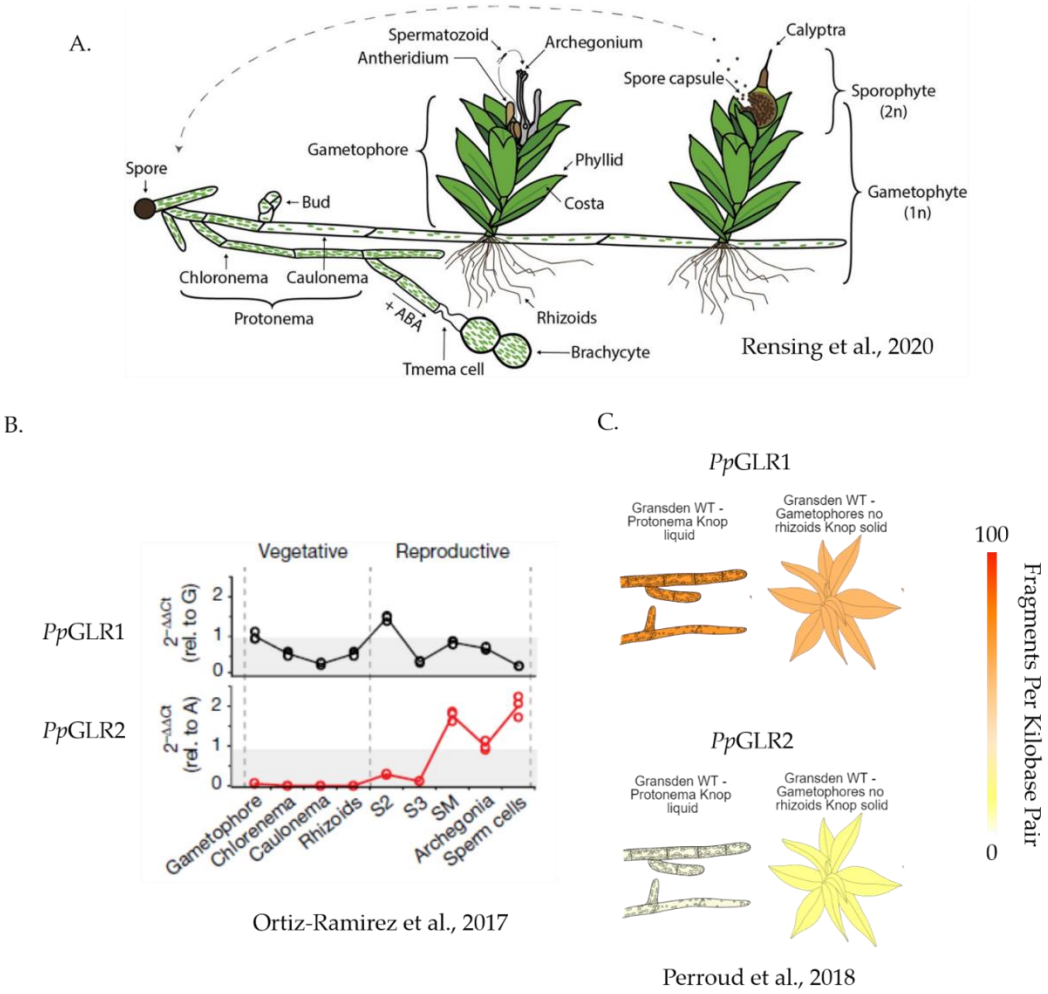

Figure 10: Expression of GLRs in moss. A.) Life cycle of *P.patens*. Haploid spores germinate into protonema that are classified into two cell types: chloronema and caulonema. Choloronema develop from spores first and are identified by transverse cell walls and an abundance of chloroplasts with roles in photosynthesis. Caulonema differentiate from chloronema. Caulonema show oblique cell walls and have faster growth rates and thought to be necessary for territorial and nutrient procurement. They later branch to develop buds forming the leafy gametophores(286, 287). Reproductive tissues belonging to the sporophyte develop from the gametophore. B.) *Pp*GLR1 expression patterns. Adapted from Rensing *et al.*, 2020(288), Ortiz-Ramirez *et al.*, 2017(67), and Perroud *et al.*, 2018(285).

Core Objective

The present thesis addresses the molecular evolution of membrane transport in plants. The core objective of the data shown is to characterize the biophysical properties of GLR1 from *Physcomitrium patens* focusing on the ion selectivity as well as the ion channel gating. Paired with targeted mutagenesis, I aim to illustrate structure-function data for *Pp*GLR1 mapping the molecular basis for GLR operation. The overall goal is to advance the evolutionary relationships within the glutamate receptor superfamily by identifying the conservations and diversifications of function that allow for membrane transport.

Chapter 2: Results

Part 1: Genetic analysis of *Pp*GLR1

We targeted the genetic basis of a GLR activity based on the expression patterns of *Pp*GLRs where we expect only a single gene to be expressed in the gametophore. Although phenotypes in the reproductive tissues were previously reported, no phenotypes have been found in the vegetative tissues.

Phenotypic characterization of *Pp*GLR1

Here we described that *Ppglr1* and *Ppglr1/2* have an etiolation-related senescence phenotype characterized by a loss of chlorophyll upon dark exposure (Figure 11). The fact that these mutants were generated by homologous recombination, and they were generated from independent lines (67), strongly suggest the phenotype is dependent on the mutation of *PpGLR1*. When tissues were re-exposed to light (16 hours light/ 8 hours dark), the chlorophyll content recovered showing the plants remained viable and chlorophyll synthesis could be reactivated (Figure 11B). *Ppglr1* plants deficient in chlorophyll provides the first genetic evidence of GLR involvement in light-signal transduction. Supporting a role in senescence, gene expression analysis of *Arabidopsis* plants indicated GLRs were upregulated in senescent leaves(289).

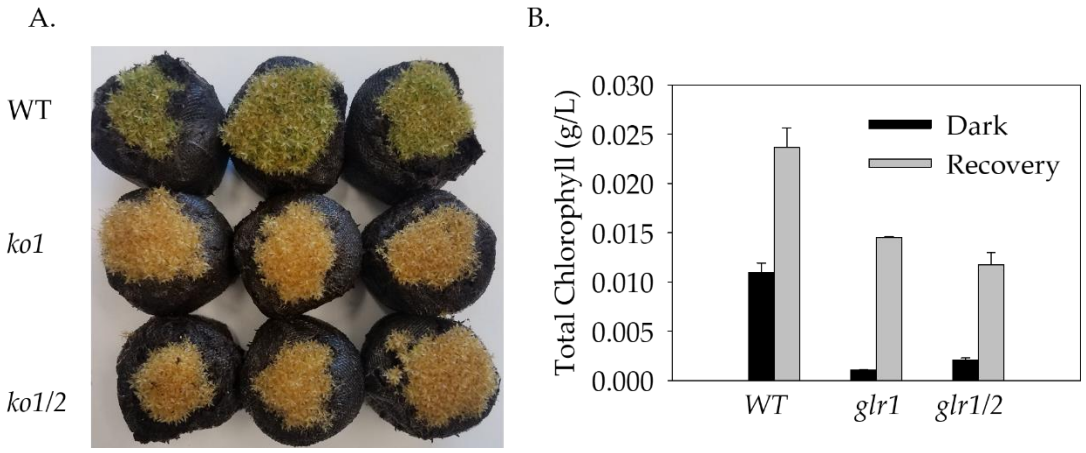

Figure 11: *Ppglr1* and *Ppglr1/2* gene knockout plants demonstrate senescence phenotype under dark growth conditions. A.) Representative photograph of each genotype, Wild-type (WT), *glr*1, and *glr1/2*, planted on three independent Jiffies Peat-Pellets. B.) Chlorophyll measurements corresponding to plants shown in (A) after a 4 week exposure to darkness (Dark) and when returned to light cycles of 16hour light and 8hour dark per day for another 4 weeks (Recovery). Dark: WT, n=13; *glr1* n=11; *glr1/2*, n=13. Recovery: WT, n=7; *glr1* n=3; *glr1/2*, n=7.

Similar studies on *P.patens* that exposed protonema colonies to dark conditions found the senescence was related to a macroautophagy pathway (macroautophagy will simply be termed autophagy from herein). Both senescence-associated genes and autophagy related (ATG) genes were upregulated in plants living in the dark. ATG5 was identified as being necessary(290). Among other physiological changes included variations in amino acid concentrations including Arg, Ala, Val, Lys, Leu, Tyr, His, and Glu (290).The most compelling factor motivating the further inquiry into GLR's participation in autophagy is that it also plays an integral part in *P.patens* development through gamete differentiation— drawing a striking parallel to the behaviorally defective sperm from *glr1/2* that are impotent(67, 291). In moss sperm, *atg5* leads to infertility through a reduction in cytoplasmic volume and abnormal flagellar formation. To detect

autophagy in the dark induced senescent *glr1* and *glr1/2* lines, chloronema cells (identified by the appearance of a transverse cell wall), were challenged with pharmacology commonly used to identify the occurrence of autophagy; E-64d, a cysteine protease inhibitor, and concanamycin A (ConA) a vacuolar H^+-ATPase inhibitor(292). Incubation of the autophagy inhibitor E-64d (100μM) with chloronema under dark conditions produced an accumulation of autophagic bodies— visible as protein aggregates— evident in *glr1*, but not WT, only under dark conditions suggesting that *Pp*GLR1's role in bulk degradation is dependent on light cues (Figure 12). Protonema placed in the dark for only 24 hours with E-64d did not yield the same dramatic effect as chloroplasts were still clearly present (Figure 13) Incubation of ConA (100nM) with dark treated plants also resulted in the appearance of protein aggregates in chloronema (Figure 14).

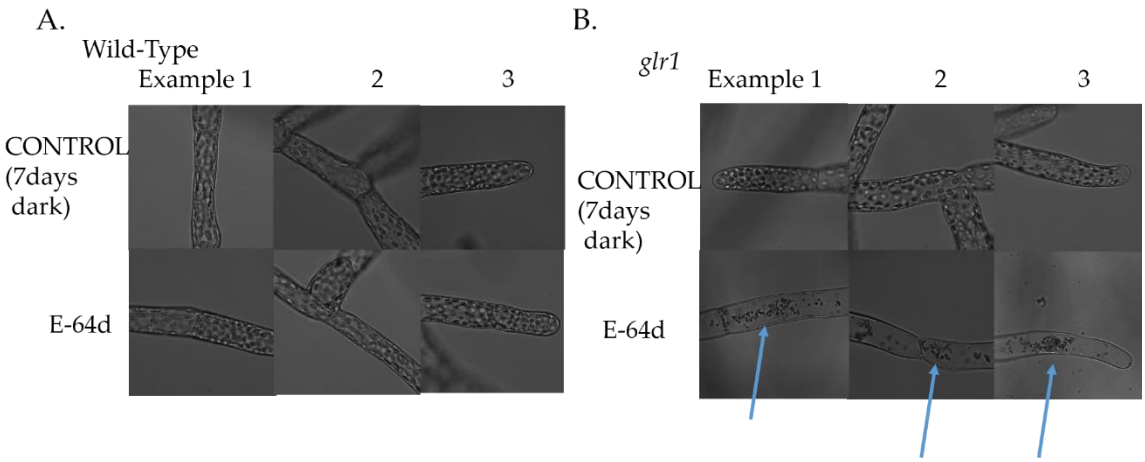

Figure 12: Detection of autophagy in dark grown *glr1* plants by application of E-64d. A.) Example photographs of wild-type (WT) *P.patens* chloronema after week long dark storage (CONTROL. Top row) or after week long dark storage and 24 hour treatment with 100μM E-64d (E-64d. Bottom row). B.) Example photographs of *glr1 P.patens* chloronema after week long dark storage (CONTROL. Top row) or after week long dark storage and 24 hour treatment with 100μM E-64d (E-64d. Bottom row). Arrows point to stabilized autophagic bodies.

Example: 1 2 3

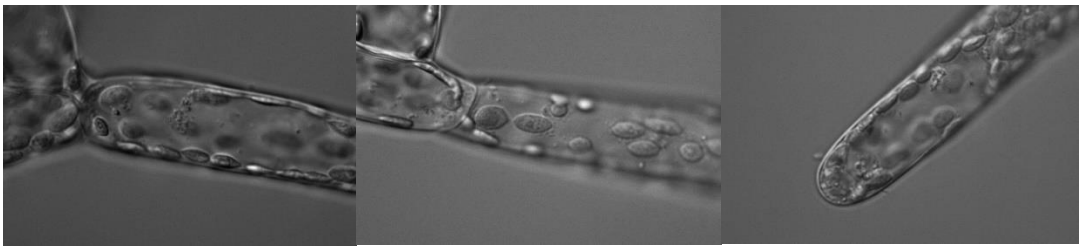

Figure 13: *glr1* plants treated with E-64d under 24 hour dark exposure retain chloroplasts. Example photographs of light grown *glr1* choloronema treated with 100μM E-64d for 24 hours.

Figure 14: Detection of autophagy in dark grown *glr1* plants by application of 100nM concanamycin A. Example photographs of WT (left column) and *glr1* (right column) *P.patens* chloronema after week long dark storage (CONTROL; Top row) or after week long dark storage and 24 hour treatment with 100nM concanamycin A (ConA; Bottom row). Arrows point to stabilized autophagic bodies.

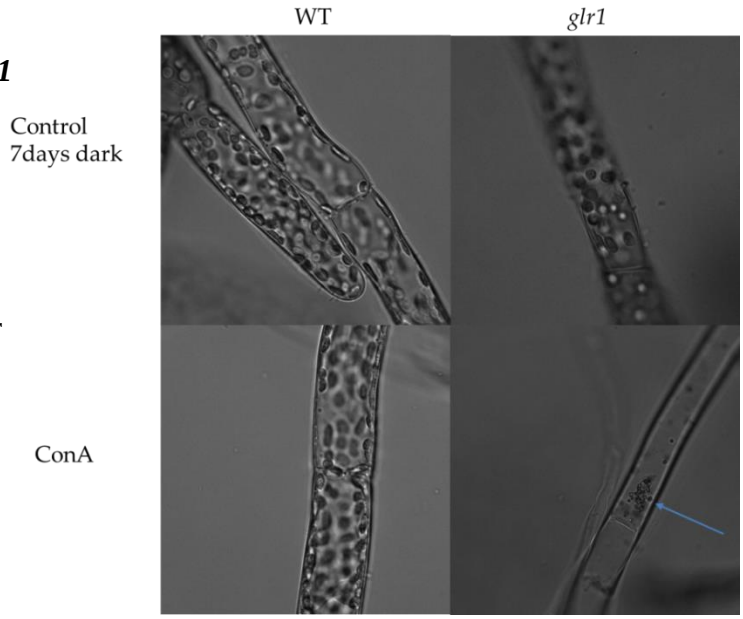

Part 2: Basic characterization of *Pp*GLR1 in heterologous system of COS-7 cells

Author's Note:

The bulk of the experimental evidence presented in this thesis relies on electrophysiology experiments and concepts. A sufficient primer for understanding the core concepts implied in the design of the experiments and in the interpretation of the results is offered in Appendix A.

Copyright Notice:

Figure 15, 16, and 17 were incorporated into the publication by Ortiz-Ramirez *et al.*, 2017.

Ortiz-Ramirez C, Michard E, Simon AA, Daniel S.C. Damineli, Hernandez-Coronado M, Becker JD, Feijó JA. (2017) . GLUTAMATE RECEPTOR-LIKE channels are essential for chemotaxis and reproduction in mosses. ***Nature***, 549:91-95

Patch clamp solutions:
A detailed list of the internal and external solutions used for patch clamp experiments in this chapter 2 part 2 can be found in Table 5 (pg. 142-143). The major charge carriers are indicated within each main figure.

Since a single *Ppglr1* gene knockout has a complete phenotype— of equal magnitude to the double *Ppglr 1/2* gene knockout— it provides genetic evidence that *Pp*GLR1 works as a functional homomer. The value of identifying a homomeric GLR is that *At*GLRs represent a difficult family of channels to address with twenty genes that show a genetic redundancy and compensation in addition to the functional diversification achieved by undergoing heteromerization(293). Studying the minimal complex as the

model constitutes an experimental approach to identify the conserved features among plant GLRs and provides a reference to more precisely investigate structure-function relations and how they are altered by targeted mutagenesis or the addition of CNIH proteins. Expression of a single gene, *Pp*GLR1, removes the possibility of heteromerization between the two *Pp*GLR isoforms and creates two opportunities to optimize functional expression systems that favorably express the single GLR. First, we show *Pp*GLR1 is a functional ion channel when expressed in the heterologous system of COS-7 cells(67) without the need for CNIH proteins. Second, protonema in the early developmental stage are able to be cultured and are usable for patch clamp on protoplasts.

An electrophysiological characterization of *Pp*GLR1 was conducted by optimizing a heterologous expression system of COS-7 cells for transient transfections. A basic characterization of *Pp*GLR1 addressing the properties of ion permeability and ligand-gating by glutamate (Glu) produced three unexpected findings: 1.) *Pp*GLR1 is not a strictly ligand-gated ion channel like mammalian iGluRs, but is characterized by a constitutive activity yielding a background conductance in the absence of exogenous ligands; 2.) GLR-mediated currents are modulated by Glu in a manner dependent on the extracellular ion conditions; and 3.) *Pp*GLR1 is permeable to anions. Furthermore, the genetic data indicating the homomerization of *Pp*GLR1 was validated.

Ion permeability and glutamate gating properties of *Pp*GLR1

Considering the substantiated data that GLRs, including *Pp*GLR1, are involved in Ca^{2+} signaling, GLRs are expected to be Ca^{2+} permeable ion channels. To test for a Ca^{2+}

permeability, *Pp*GLR1 expressing COS-7 cells were challenged in whole-cell patch clamp recordings to various extracellular [Ca^{2+}]. In this experiment, an inward current amplitude corresponding to the relative extracellular concentration was observed such that higher [Ca^{2+}] yielded larger current amplitudes (Figure 15A,B). Control cells transfected with an empty mammalian expression vector *pCI*, lacking the cDNA for *Pp*GLR1, showed minimal current when facing high [Ca^{2+}] (Figure 15C,D). To further appreciate the cationic permeability, the ability to conduct Na^{+} ions while exposed to a constant [Ca^{2+}] was also analyzed. Perfusion of 130mM Na^{+} to the extracellular solution— already containing 10mM Ca^{2+} and 10mM Cl^{-}— resulted in an inward current that approximately doubled at negative voltages (Figure 16). *I-V* curves from both cation permeability experiments point toward a voltage-independent conductance where instantaneous current equaled the current after 1.5sec of voltage stimulation.

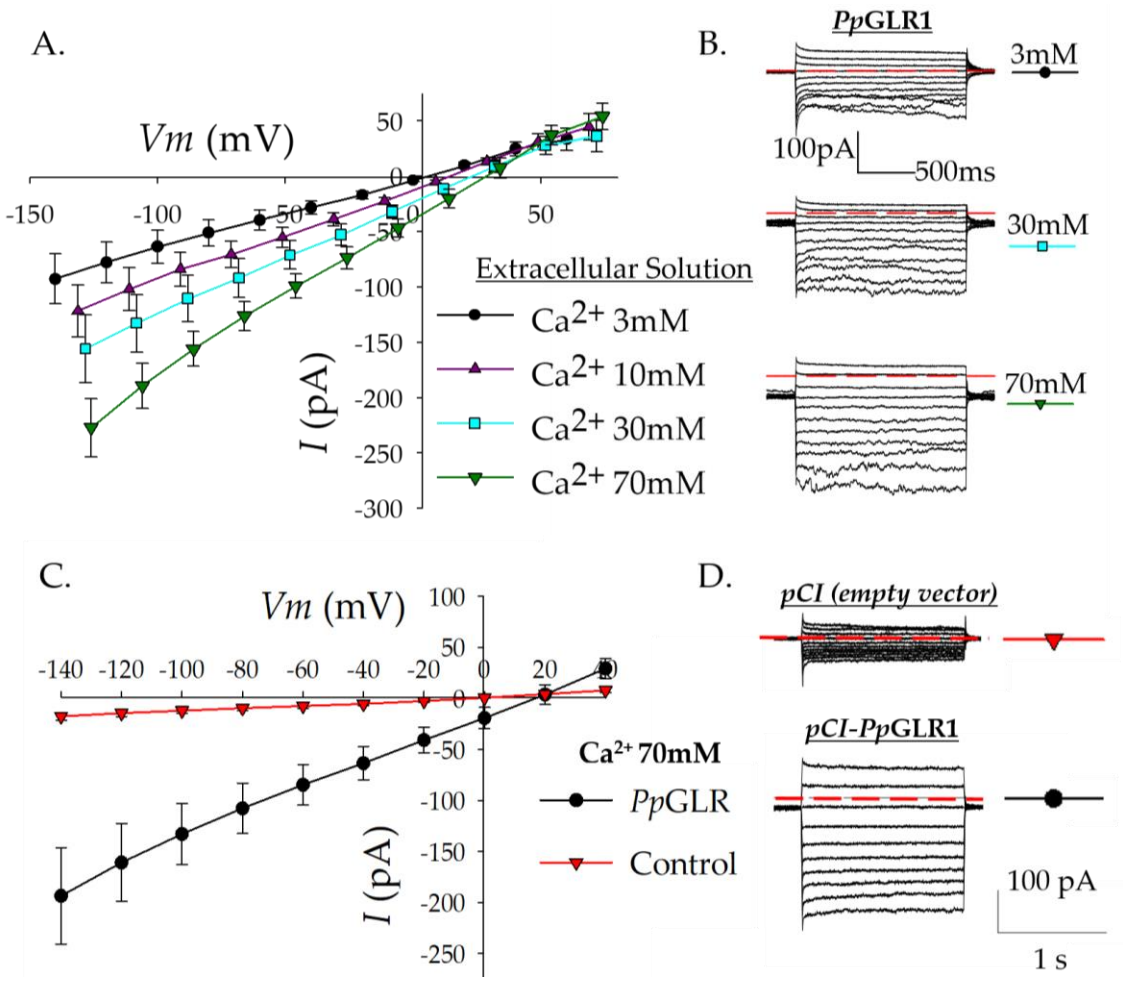

Figure 15: *Pp*GLR1 is permeable to Ca^{2+}. A.) *I-V* curve from whole-cell patch clamp experiments on *Pp*GLR1 expressing COS-7 cells. A perfusion of various [Ca^{2+}] of 3mM, 10mM, 30mM, and 70mM correlates to the current amplitude, (n=5, Ca^{2+} 3,10,30mM ; n=4 Ca^{2+} 70mM). Solution set, S1, was used. Extracellular Ca^{2+} was paired with the counter-ion gluconate upon exchanging solutions to keep extracellular Cl^- constant at 6mM. B.) Representative current traces corresponding to *I-V* in shown in panel A. C.) *I-V* curve illustrating whole-cell current amplitudes in *Pp*GLR1 transfected cells (n=3) are greater than *pCI* (empty vector) transfected cells (n=3) in extracellular solution set 2 (Ca^{2+} 70mM, Gluc 134, and Cl^- 6mM). D.) Representative traces from the *I-V* curve shown in panel C. All error bars represent SE. Major charge carriers are indicated in the panel insets. COS-7 cells were clamped to a holding potential of 0mV. Test pulses were run for 1.5sec from -140mV to +60mV in +20mV steps

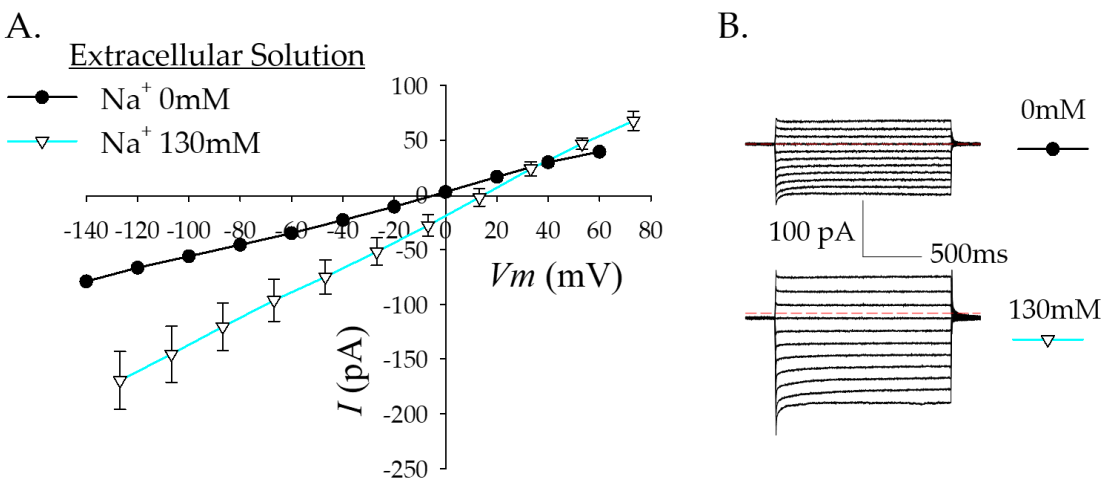

Figure 16: *Pp*GLR1 is permeable to Na^+. A.) *I-V* curve obtained from whole-cell patch clamp experiments on *Pp*GLR1 expressing COS-7 cells. A perfusion of increasing [Na^+] potentiates current amplitude against a fixed gradient of Ca^{2+} (10mM outside; 100nM inside) and Cl^- (10mM outside; 6mM inside), (n=3). Na^+ was paired with the counter-ion gluconate upon exchanging solutions to keep extracellular concentrations of Ca^{2+} and Cl^- constant. Error bars represent SE. B.) Representative current traces corresponding to the *I-V* curve shown in panel A. Solution set 3 was used. Major charge carriers are indicated in the panel inset. COS-7 cells were clamped to a holding potential of 0mV. Test pulses were run for 1.5sec from -140mV to +60mV in +20mV steps

In support of the *Pp*GLR1 Ca^{2+} permeability established by whole-cell patch clamp, complimentary Ca^{2+} imaging studies in COS-7 cells using Yellow CaMeleon 3.6 (YC3.6) illustrated *Pp*GLR1 has a role in cell signaling as its expression promotes elevations of [Ca^{2+}]cyt (Figure 17A,B). When *Pp*GLR1 transfected cells were incubated in a buffered Ca^{2+} -free media, exposure to Ca^{2+} resulted in changes in [Ca^{2+}]cyt. Incubation of cells in the Ca^{2+}- free media supplemented with Gd^{3+} prevented the rise in [Ca^{2+}]cyt, suggesting Ca^{2+} transport across the plasma membrane was responsible for the increased cytCa^{2+} (Figure 17A,B). Moreover, cell culture media (DMEM) already contains small amounts of Ca^{2+} needed for cell nutrition (1.8mM in the form of $CaCl_2$), hence the resting [Ca^{2+}]cyt levels between *Pp*GLR1 and empty-vector transfected cells

could be analyzed. Cells expressing *Pp*GLR1 revealed elevated steady-state $[Ca^{2+}]$cyt over empty-vector transfected cells highlighting a physiological value of *Pp*GLR1 Ca^{2+} transport for Ca^{2+} homeostasis (Figure 17B,C).

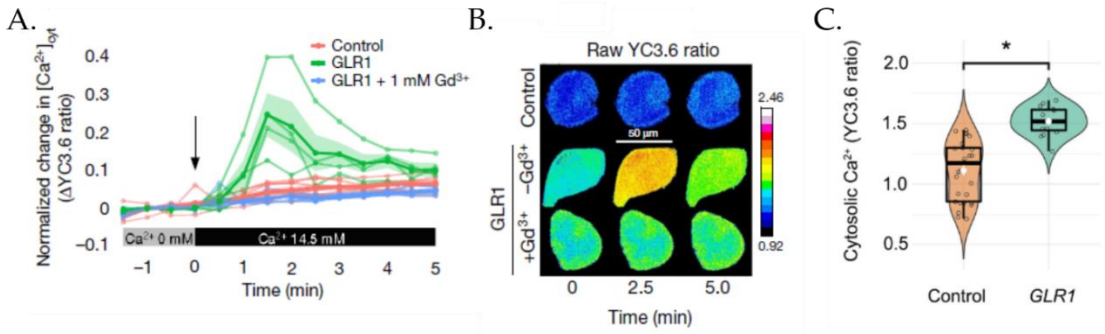

Figure 17: *Pp*GLR1 elevates $[Ca^{2+}]$cyt monitored with Yellow CaMeleon 3.6. A.) Time course of the change in $[Ca^{2+}]$cyt before and after the addition of Ca^{2+} (14.5mM) in the bath (indicated by the arrow). The *y* axis shows the change in YC3.6 ratio. A normalization was completed by averaging the values of YC3.6 ratio (cpVenus/CFP ratio) before the Ca^{2+} increase and subtracting the average from all time points. Cells expressing *Pp*GLR1 (n = 4), control cells (n = 7), and cells expressing *Pp*GLR1 exposed to Gd^{3+} (1 mM; n = 7) are shown. The bold lines display the mean response for each treatment, the shaded area denotes the SE, and thin lines denote individual replicates. EGTA (1 mM) was added to the medium to create Ca^{2+} free buffer. B.) Representative images of YC3.6 ratio for control cells (pCI empty vector + pEF1-YC3.6) (top, representative of 7 images), and cells expressing *Pp*GLR1 (pCI-*Pp*GLR1 + pEF1-YC3.6) without Gd^{3+} (middle, representative of 4 images) or with Gd^{3+} (1 mM; bottom, representative of 7 images) at time 0, 2.5 and 5.0 min after the addition of Ca^{2+} (14.5 mM) (color scale depicts raw YC3.6 ratio). C.) Violin plot for YC3.6 ratios obtained from control and *Pp*GLR1 expressing cells prior to the addition of Ca^{2+} showing a steady-state difference in basal $[Ca^{2+}]$cyt, n = 29 (control), n = 15 (*Pp*GLR1). There was a statistically significant difference between the two samples performed by Welch's t-test for unequal variances, * $P = 3 \times 10^{-8}$.

The prevailing hypothesis is that GLRs are amino acid gated ion channels. Yet, heterologous expression of *Pp*GLR1 foremost produces a background ion conductance. Both Ca^{2+} (Figure 15) and Na^{+} currents (Figure 16) did not require activation by Glu. The membrane voltage was sufficient stimulus to produce the cationic current characterizing a constitutively active ion channel. Similarly, Ca^{2+} imaging experiments indicated

perfusion of Ca^{2+} alone was enough for a cytosolic Ca^{2+} response. To challenge if the principle neurotransmitter, Glu, potentiates ionic currents in *Pp*GLR1 expressing COS-7 cells, Glu (100μM, 1mM, 5mM) was exogenously applied in Ca^{2+} - dominant ionic solutions (solution S4).

In a dose-dependent manner, Glu indeed potentiated inward currents predominantly carried by Ca^{2+} (Figure 18A). Potentiated currents could be subsequently inhibited by the cation channel pore blocker Gd^{3+} (500μM) (Figure 18B). A Ca^{2+} permeability and Glu induced potentiation aligns with a mechanism compatible with the direct generation of Ca^{2+} signals(67). However, application of exogenous Glu differentially altered *Pp*GLR1 current in multi-ion bathing conditions. Adding an anion, either Cl^- or NO_3^-, to the Ca^{2+} dominant bathing solution (S4) resulted in an antagonistic effect of Glu with a rundown of the current amplitude (Figure 18C,D). In these experiments adding anions to the extracellular solution also produced a left-ward shift in the reversal potential (*Vrev*) prior to Glu application, suggesting an increased anion permeability across the whole-cell membrane. No background current could be recorded when Ca^{2+} 30mM was in solution with Na^+ (data not shown). Recognizing ligand activation in iGluRs results in a conformational change in the pore domain and that the pore blocker Gd^{3+} also inhibits *Pp*GLR1 currents in the presence of Glu, I could hypothesize that anions are similarly occupying binding sites within the pore.

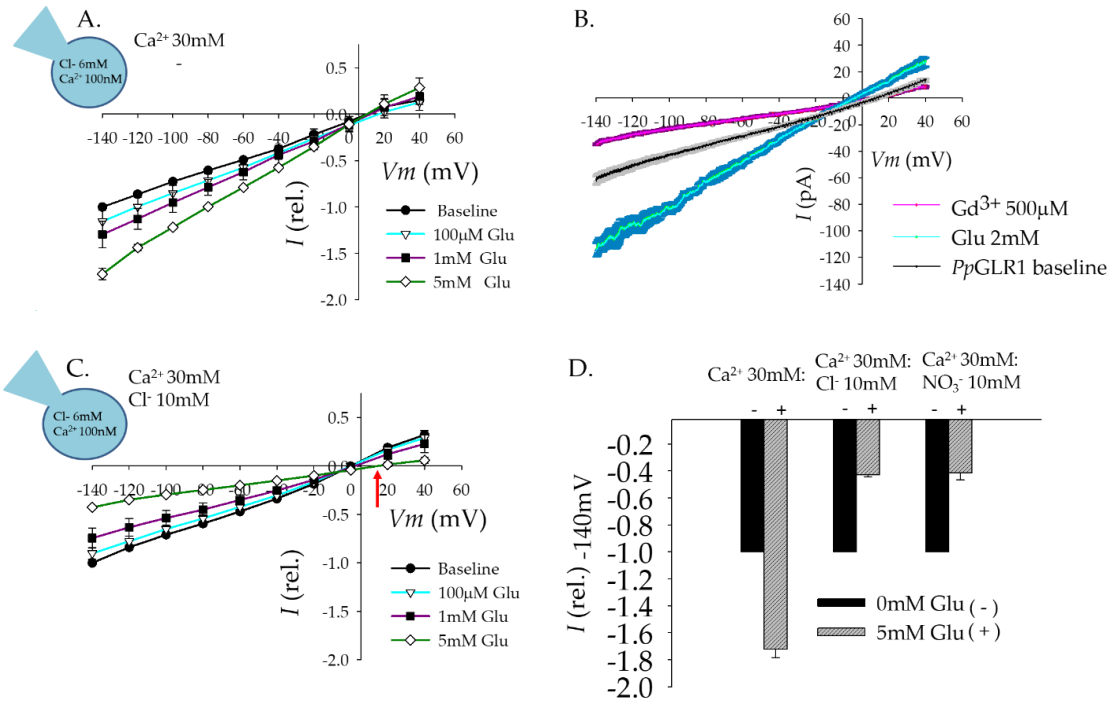

Figure 18: Glu conditionally modulates *Pp*GLR1 channel properties. A.) *I-V* curve of whole-cell patch clamp experiments on COS-7 cells expressing *Pp*GLR1 indicate Glu (100µM, 1mM, 5mM) potentiates an inward current when Ca^{2+} was the sole extracellular bathing ion (n=3). B.) Ca^{2+} current potentiated by Glu (2mM) was sensitive to channel block by Gd^{3+} (500µM), (n=4). Current recordings were performed in the same ionic conditions as A, but obtained by fast voltage ramps from -140mV to +60mV over 2seconds after a brief conditioning pulse at -140mV for 500ms. Error bars or shaded area represents SE. C.) When Cl^- was added to the extracellular solution with Ca^{2+}, Glu induces a rundown of the current — decreasing the current amplitude. Red arrow indicates the reversal potential in Ca^{2+} only solutions of panel (A). Note the leftward shift in the reversal potential away from positive voltages toward 0mV. D.) Bar graphs summarize the differential effect of Glu based on extracellular solutions with only Ca^{2+} (n=3) or when Ca^{2+} was supplemented with an anion, Cl^- (n=3) or NO_3^- (n=3). 0mM Glu conditions correspond to the baseline *I-V* curve of panel A and C. Error bars represent SE. Data was generated with solution set S4, S5, and S6. Major charge carriers are indicated in the panel insets. In panel A and C, COS-7 cells were clamped to a holding potential of 0mV. Test pulses were run for 1.5sec from -140mV to +60mV in +20mV steps.

To investigate the relevance of a possible anion permeability, channel properties in native moss plants were analyzed by whole-cell patch clamp experiments in protonema protoplasts. Ortiz-Ramirez *et al.*, previously reported the double gene knockout *Ppglr1*/*Ppglr2* abolishes all ionic current in solutions of Na^+, Ca^{2+}, and high concentrations of Cl^- (67). Specifically interested in a Cl^- permeability— of an otherwise presumed cation channel— the ionic solutions were stripped to isolate Cl^-. In bi-ionic $BaCl_2$ solutions (Solution S7), Cl^- is the only component to comprise the outward currents observed at positive voltages. In those conditions, wild-type (WT) protoplasts displayed significantly larger background currents than *Ppglr1* and *Ppglr1/2* gene knockout (KO) mutants, revealing that *Pp*GLR1 expression alone controlled the dominant current carried across the plasma membrane(Figure 19.).

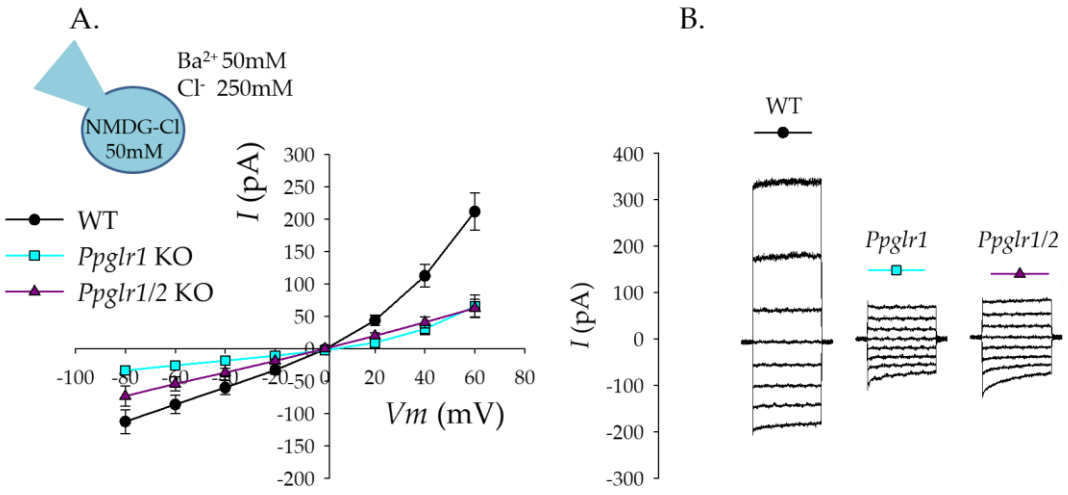

Figure 19: *Pp*GLR1 commands an anion current in moss protonema protoplasts. A.) *I-V* curve and B.) representative current traces from WT, single KO *glr1*, and double KO *glr1/2* in bi-ionic $BaCl_2$ solutions. WT (n=30), *Ppglr1* (n=12) and *Ppglr1/2* (n=4). Error bars represent SE. Data was generated with solution set S7. Major charge carriers are

indicated in the panel A inset. Protoplasts were exposed to voltages from -80mV to +60mV for 1.5sec.

Cl^- is not the most relevant anion in terms of membrane transport and ionic homeostasis in plants. NO_3^- and malate play prominent roles in controlling the membrane voltage, nutrition, and cell osmolarity. Extracellular anion substitution experiments on COS-7 cells expressing *Pp*GLR1 show that outward current amplitude was strongest with NO_3^- coinciding with a leftward shift in the *Vrev*, revealing an ion selectivity among anions in the sequence of $NO_3^- > Cl^- >$ malate. Substitution by the impermeable ion gluconate decreased the current to the level of control cells transfected with the empty vector indicating *Pp*GLR1 mediated the currents. Because of a role as a ligand, a Glu permeability could not be verified but may permeate like other anions. When applying Glu in the single ion Ca^{2+} dominant solutions (Figure 20), an outward current at positive membrane voltages was also potentiated, which could be carried by Glu or Mg^{2+}. Gd^{3+} inhibition of this current suggests it is not a leak artifact.

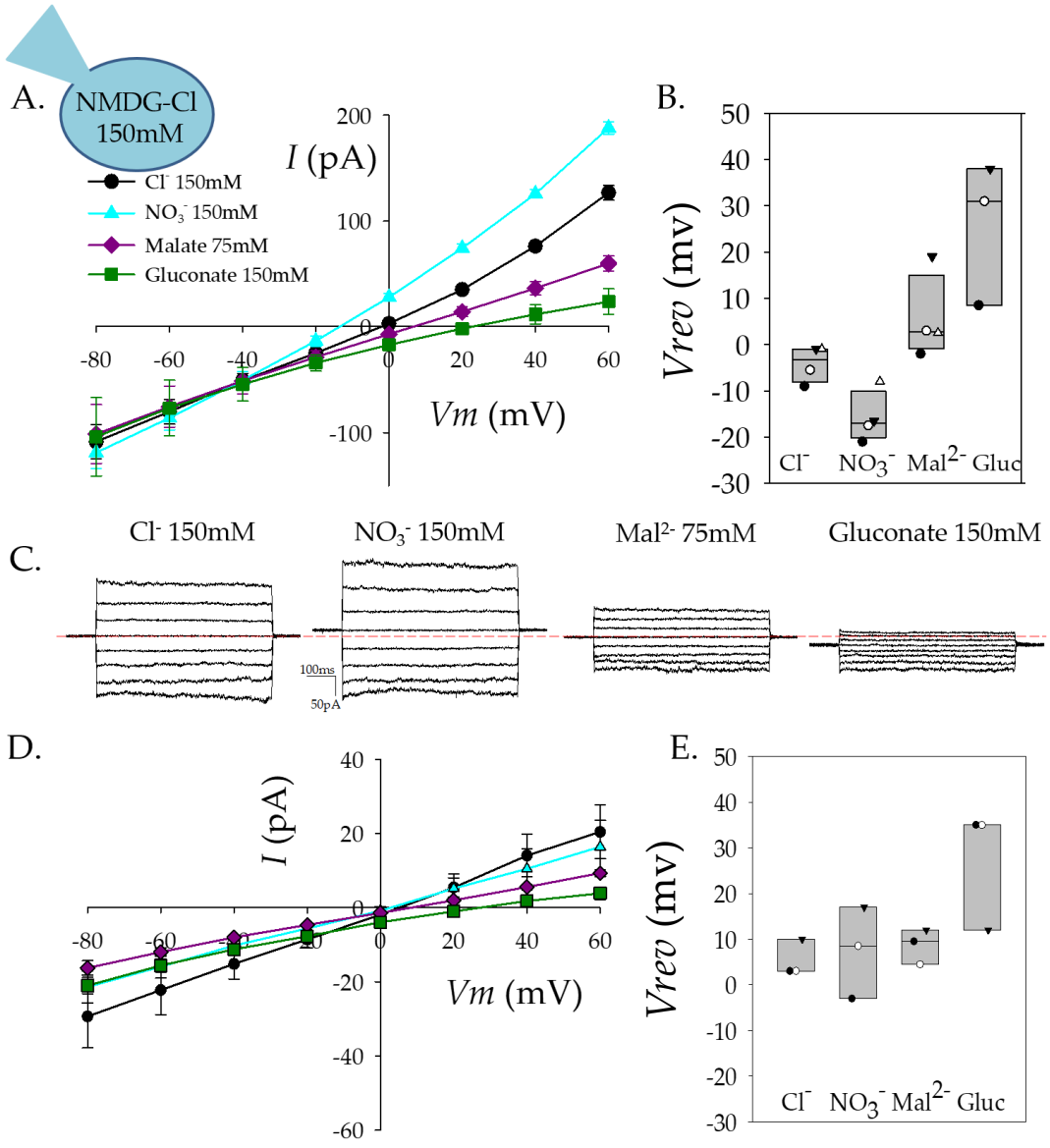

Figure 20: Anion selectivity of *Pp*GLR1. A.) *I-V* curves of anion substitution experiments on *Pp*GLR1 expressing cells where extracellular Cl^- was exchanged for NO_3^- (n=4), Mal^{2-} (n=4), and gluconate (n=3). B.) Boxplots illustrate the median reversal potentials (*Vrev*) from each ion, Data points indicate individual experiments. C.) Representative current traces. D.) *I-V* curves for pCI empty vector control cells where extracellular Cl^- was exchanged for NO_3^- (n=3), Mal^{2-} (n=3), and gluconate (n=3) as in a. E.) Reversal potentials (*Vrev*) obtained from pCI transfected cells upon anion exchange. Solution set S8 was used in GLR and empty-vector control cells. Major charge carriers are indicated in the panel A inset.

Part 3: *Pp*GLR1 ligand profile

With at least a dozen proteinogenic amino acids thought the activate GLRs — the physiological relevant ligand of GLRs has remained uncertain. Instead, the breadth of GLR ligands has led to speculation that GLRs are associated with signaling as an amino acid sensor. The finding of a constitutive channel activity questions the overall significance of ligand-gating. Since glutamate (Glu) still possesses the ability to modulate the current properties, it was prudent to screen potential ligands that may be more effective or serve specific physiological roles. Using the Ca^{2+} imaging protocol of figure 17, changes in cytosolic Ca^{2+} concentration ($[Ca^{2+}]$cyt) could be used as a read-out for the an experimental ligand's ability interact with *Pp*GLR1.

Ligand Profile of *Pp*GLR1 determined by YC3.6 imaging

As determined before, a basal Ca^{2+} flux was observed in *Pp*GLR1 expressing COS-7 cells without the presence of any amino acid (Figure 17). Only the addition of Ca^{2+} to *Pp*GLR1 expressing cells was required to elevate $[Ca^{2+}]$cyt. All twenty proteinogenic acids plus other several candidates were then tested by treating cells with

the experimental ligand prior to addition of Ca^{2+} (Figure 21). Time course traces were analyzed on the peak signal (the difference from the baseline to maximal YC3.6 ratio independent of time) as well as the integrated area below the curve (indicting the overall magnitude of Ca^{2+} flux). As in patch clamp recordings, Glu potentiated [Ca^{2+}]cyt as indicated by an increase in the YC3.6 ratio. Three other "effectors" were also found to be more potent than Glu for elevating [Ca^{2+}]cyt, including; 1-aminocyclopropane-1-carboxylic acid (ACC), reduced glutathione (GSH), and dithiothreitol (DTT)(Figure 21).

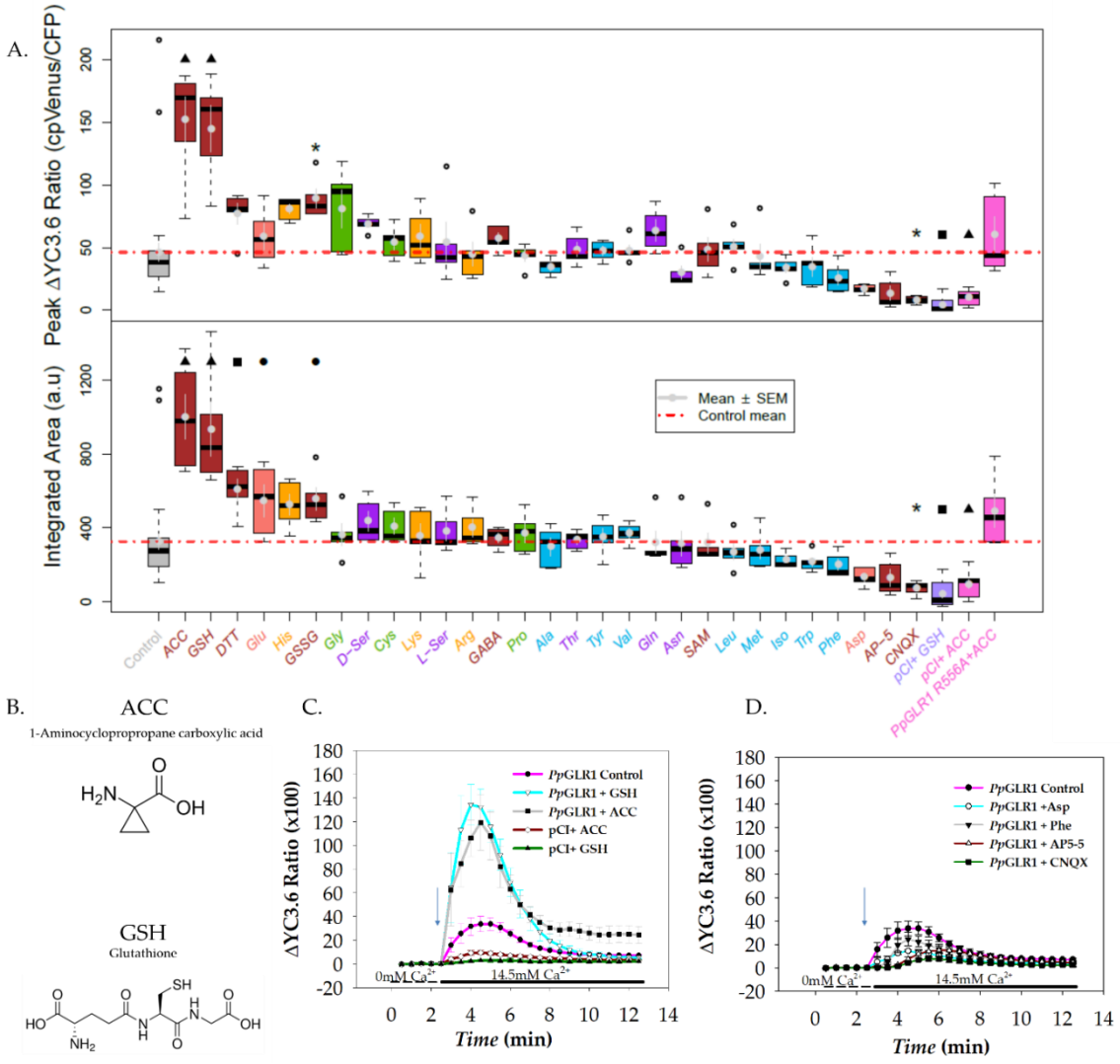

Figure 21: Ligand Profile of *Pp*GLR1 determined by YC3.6 imaging. A.) Panel of agonists and antagonists determined by peak YC3.6 signal (top) and integrated area below the curve (bottom). Box plots follow standard design; the top of box is 75th percentile; the bottom of box is 25th percentile; horizontal gray bar is median; gray whiskers show the maximum and minimum value within 1.5× the interquartile range) with outliers (open circles) and mean (solid black circles) ± SE Statistical significance was determined using Dunnett's test (solid black circle $P < 0.1$, $*P < 0.05$, solid black triangles $P < 0.001$). B.) Molecular structures of 1-aminocyclopropane-1-carboxylic acid (ACC) and glutathione (GSH). C.) and D.) Time course traces of the change in YC3.6 signal from *Pp*GLR1 expressing COS-7 cells showing response to Ca^{2+} (14.5mM), agonists (C), or antagonists (D). Arrow designates time of Ca^{2+} application. n=31 for *Pp*GLR1 control cells (no ligand), n=5 for all *Pp*GLR1 treatments, n=10 for pCI controls. AP-5 and CNQX were administered at 200μM, all other potential ligands were tested at 500μM.

Other agonists identified were His, oxidized glutathione (GSSG), D-Ser, and Gly (Figure 22). Time course analysis of the YC3.6 ratio revealed distinct Ca^{2+} signatures among the different agonists and most strikingly between the primary neurotransmitters (Glu, Gly, D-Ser) suggesting different possible molecular interactions (Figure 22). Gly evoked a distinctive Ca^{2+} response displaying a sharp increase in the YC3.6 ratio and a fast decay. Alternatively, Glu produced a slower and longer increase in YC3.6 ratio. D-Ser yielded an elevation of $[Ca^{2+}]$cyt with a signature not matching either Glu or Gly, but similar to His and GSSG. Of the "effectors", the small molecules (ACC, Glu, His, D-Ser, Gly) are likely to be canonical ligands that fit the amino acid binding pocket. GSH, GSSG, and DTT are expected to be allosteric regulators acting outside of the amino acid binding pocket.

*Pp*GLR1 antagonists were also elucidated as part of the ligand screening when cytosolic Ca^{2+} responses below the amino acid free control level were found (Figure 21A,D). The antagonists included Asp, Phe, CNQX (6-Cyano-7-nitroquinoxaline-2,3-dione), and AP-5 (D-(-)-2-Amino-5-phosphonopentanoic acid).

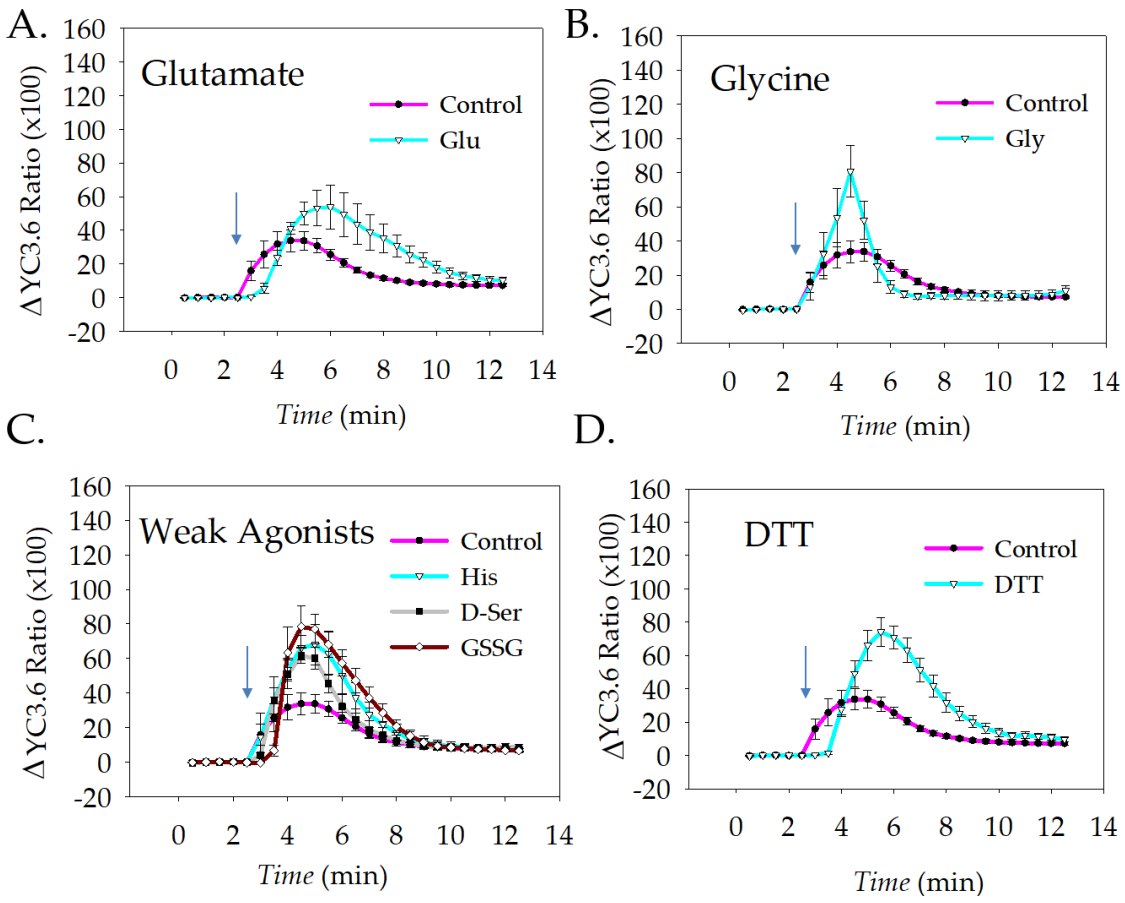

Figure 22: Ligand elicited Ca^{2+} signatures. Time course of changes in $[Ca^{2+}]$cyt within *Pp*GLR1 expressing COS-7 cells reported by YC3.6 for various proposed agonists. Arrow designates time of Ca^{2+} application. Error bars represent SE.

Molecular basis of *Pp*GLR1 ligand gating

As evidence of ligand-gating, a single residue of R556 was found to be critical for the ACC potentiation of $[Ca^{2+}]$cyt. The Arg at position 556 of *Pp*GLR1 is in the S1 segment and is found in 100% all GLR and iGluR sequences. In crystalized GluN1 LBDs, the α-carboxy group of ACC forms a salt bridge with the conserved Arg (294). In GluA2, the same Arg serves as the primary anchor for the α-carboxyl group of Glu essentially serving as a hook(205, 214). Mutagenesis of the conserved Arg in GluA1 and GluA4 abolished ligand binding and, consequently, the ligand-gated currents(295, 296).

When the *Pp*GLR1 R556 was mutated to an Ala (R556A), background Ca^{2+} elevations were unaffected but the ACC evoked Ca^{2+} response was severely attenuated, suggesting an interaction between ACC and R556 was necessary for the observed ACC evoked elevations in $[Ca^{2+}]$cyt (Figure 23A,B). This data establishes a molecular manipulation of the LBD altering the ACC effect on GLRs resulting in a functionally defective ionotropic receptor.

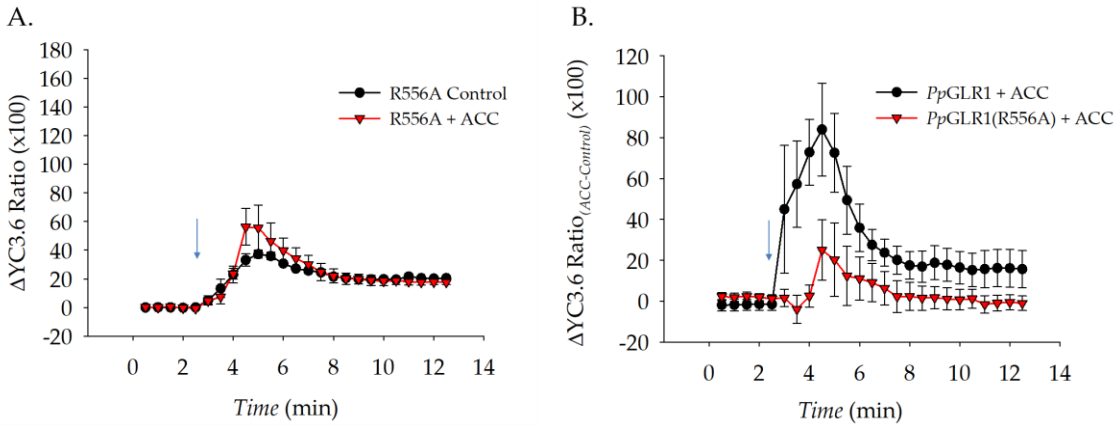

Figure 23: R556 is a critical residue for ACC-induced $[Ca^{2+}]$cyt elevations in COS-7 cells reported by YC3.6. A.) Change in YC3.6 ratio in control conditions (no ACC) and when treated with 500µM ACC B.) ACC-induced changes in $[Ca^{2+}]$cyt reported by YC3.6 comparing wild-type *Pp*GLR1 and R556A mutant. Background signal of *Pp*GLR1 and *Pp*GLR1(R556A) mutant channel was subtracted from the total ACC induced signal to normalize the ACC-induced signal from potential differences in basal flux. Arrow designates time of Ca^{2+} application. Error bars show SE, n=5 each treatment.

Part 4: *Pp*GLR1 multimodal gating integrates ligand, Ca^{2+} permeation, and voltage sensitivity, and CNIH

Patch clamp solutions:
A detailed list of the internal and external solutions used for patch clamp experiments in this chapter 2 part 4 can be found in Table 6 (pg. 144). The major charge carriers are indicated within each main figure.

The identification of an anion permeability for *Pp*GLR1 was a startling finding. An anion selectivity for what is thought to be a cation or Ca^{2+} channel would instigate a paradigm shift for considering how GLRs participate in plant cell signaling. Yet, the observed Ca^{2+} permeability complicates GLR mediated ion transport. Continuing an investigation of the gating properties of *Pp*GLR1, the newly acquired pharmacological toolkit can more precisely evaluate the ion selectivity and channel gating properties. The use of ACC as an agonist and Asp as an antagonist provides specificity to authenticate proposed *Pp*GLR1 currents. Determining the ion selectivity between permeable cations and anions, especially between Ca^{2+} and anions, is paramount to informing on the physiological roles of plant GLRs. Ca^{2+} responses and electrical membrane potential changes are tightly coupled and often difficult to separate. Establishing the ion selectivity and describing the molecular basis of the channel workings can offer biophysical evidence to separate GLRs contribution to Ca^{2+} and electrical signaling. In order to solidify the ion permeability, standard electrophysiology solutions intended to clearly separate cation from anion currents were established. This separation becomes difficult when attempting to mimic physiological ion gradients. When anions are concentrated

cytosolically and Ca^{2+} is concentrated extracellularly, the E_{anion} and $E_{Ca^{2+}}$ are indistinguishable by polarization. They both occur at positive voltages and carry a conventional "inward" current. Hence, ion permeability and then selectivity was investigated through the use of bi-ionic solutions pairing one cation and a counter-anion on the extracellular side. When cations and anions are both placed extracellularly the equilibrium potentials move in opposite directions, due to opposite charges, allowing for one to designate what current is derived from an anion or a cation. Extracellular cations yield a positive equilibrium potential and carry an "inward current". Extracellular anions yield a negative equilibrium potential and carry an "outward current". This experimental design affords the ability to identify what is anionic current and what is cation current. Because plant cells exist at resting membrane potentials never reaching positive voltages, characterizing a channel at non-physiological voltages at first appears flawed. However, preliminary evidence suggests *Pp*GLR1 is a non-rectifying ion channel. This means the ion channel will mediate passive currents according to electrochemical driving forces without any biophysical discrimination on the direction of ion flux. Once ion selectivity can be established, physiological ion conditions can be investigated to check gating properties.

Ligand-gating in moss protoplasts

In bi-ionic $BaCl_2$ solutions, the presence of outward Cl^- currents were only observed in WT protoplasts and lost in the *glr1* and *glr1/2* KO lines (Figure 19). The outward Cl^- currents of WT plants were also sensitive to known *Pp*GLR1 ligands— Asp and ACC— authenticating them as genuine *Pp*GLR1 currents (Figure 24). Although the

effect on the current amplitude appears anomalous as both agonists and antagonists decreased the current. Nonetheless, GLR operation in protoplasts is consistent with the ligand induced rundown described in heterologous expression. The use of ligand pharmacology supports the interpretation that anion transport was mediated through an amino-acid sensitive receptor.

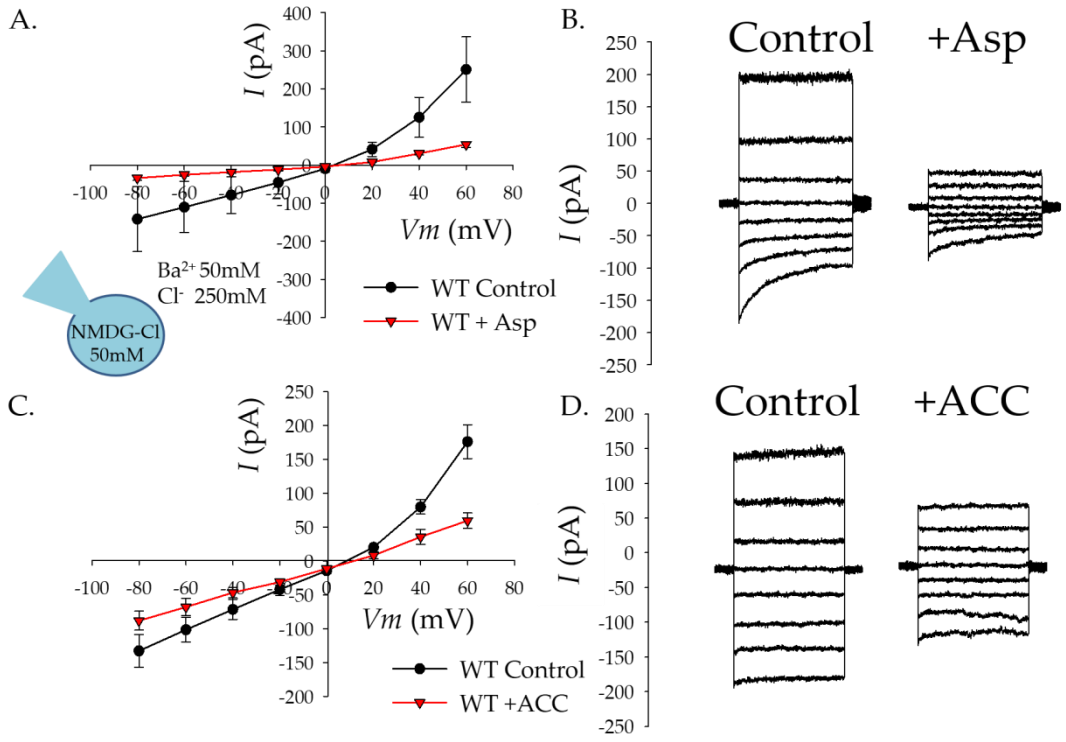

Figure 24: Rundown of Cl^- current in moss protoplasts evoked by GLR pharmacology. A.) and C.) *I-V* curves from whole-cell patch clamp recordings of WT moss protonema protoplasts before (black, circles) and after (red, upside-down triangles) ligand treatment (Asp or ACC, 500μM). Error bars represent SE. Asp, n=4. ACC, n=3. B.) and D.) Representative traces of from corresponding *I-V* curve. Data was generated with solution set S7. Major charge carriers are indicated in the inset between A and C.

***Pp*GLR1 properties assayed in heterologous system**

Figure 25 shows typical currents recording in standard $Ca(NO_3)_2$ solutions (standard solution 9). *Pp*GLR1 expressing cells display substantial outward background currents that could be washed-out when replaced with calcium gluconate, confirming the pipette seal resistance did not contribute to leak current (Figure 25 A,B). Empty-vector transfected control cells displayed no current indicating endogenous anion currents are an unlikely factor under these experimental conditions (Figure 25,C). As another control, ACC and Glu produced the anomalous rundown of the outward anion currents needed to reaffirm their sensitivity to GLR pharmacology (Figure 26).

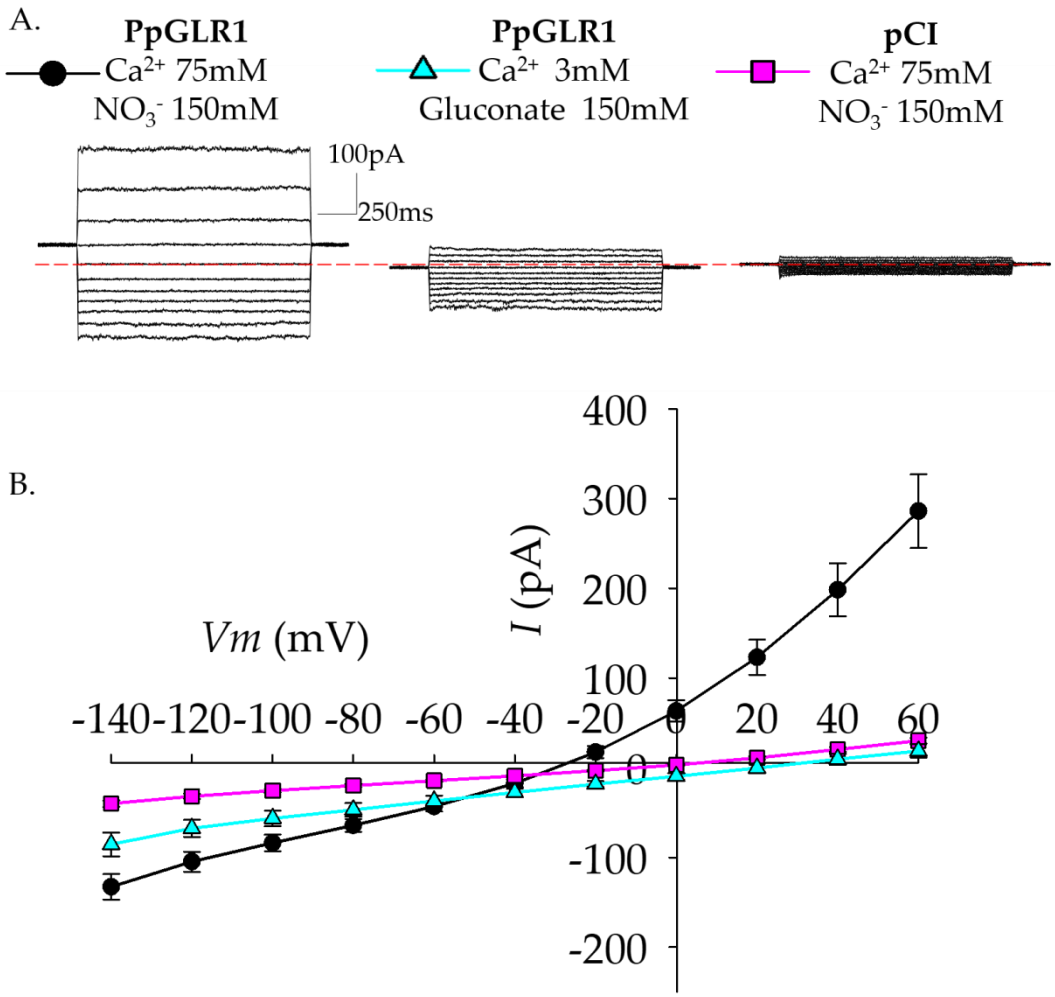

Figure 25: *Pp*GLR1 expressing COS-7 cells conduct an anionic current abolished by the perfusion of gluconate and are not observed in control cells. A) Example traces obtained from whole-cell recordings with major charge carriers indicated above corresponding traces. B) Corresponding *I-V* curve, *Pp*GLR1+ NO_3^- (n=23, solution (9), Gluconate (n=4, solution S10), pCI + NO_3^- (n=10, solution S9). Error bars represent SE.

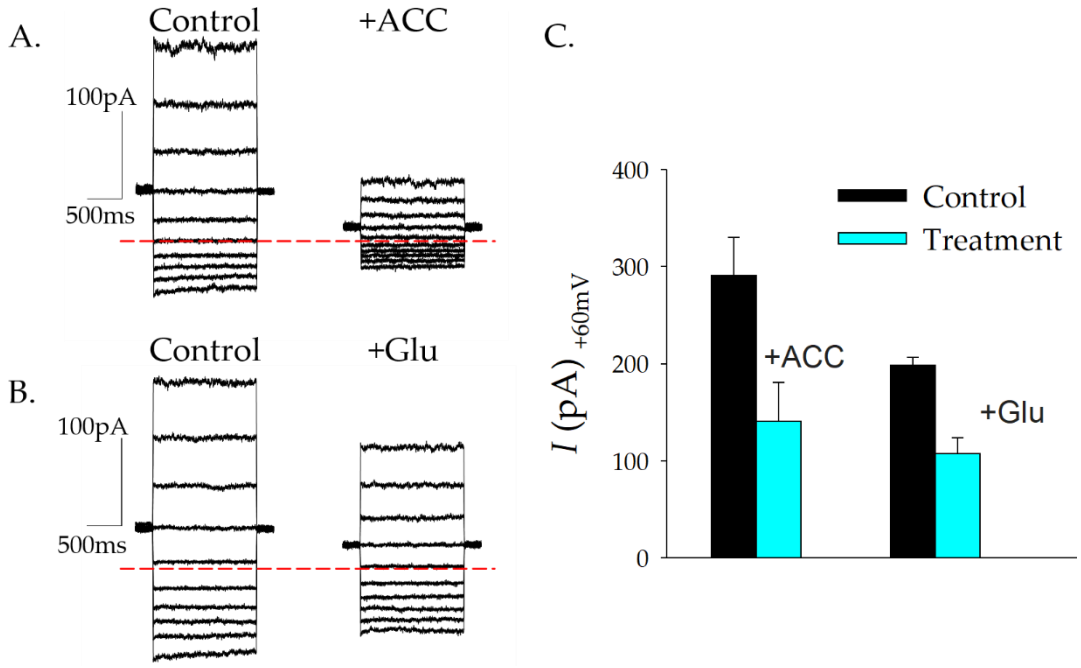

Figure 26: Rundown of NO_3^- current in *Pp*GLR1 expressing COS-7 cells evoked by GLR pharmacology. A. and B.) Representative current traces obtained from whole-cell recordings before (control) and after administering respective ligand (+) in standard solution set 9 where the major charge carrier consisted of 75mM $Ca(NO_3)_2$ located extracellularly. C.) Summary bar graphs indicating current at +60mV before (black) and after ligand treatment (cyan) (500µM). ACC, n=4. Glu, n=3. Error bars represent SE.

To further characterize the contribution of NO_3^- and Ca^{2+} to the total whole-cell current, bulk perfusions successively substituting each ion were completed (Figure 27). From conditions of 75mM $Ca(NO_3)_2$, a large reduction of Ca^{2+} ions resulted in a marginal shift of the reversal potential (*Vrev*). The lack of shift in the *Vrev* suggests Ca^{2+}

contributes little to the membrane permeability and that *Pp*GLR1 is selective for NO_3^-. Likewise, washing NO_3^- concentrations from 150mM to 6mM removes the outward current yet maintains a *Vrev* resembling the ENO_3^-. Keeping 6mM NO_3^- in the extracellular solution clamped the ENO_3^- to 0mV; therefore, a substantial Ca^{2+} permeability could be identified if the *Vrev* exceeded 0mV to more positive voltages. Here, the *Vrev* reached a maximally polarized value of +33mV, and averaging +14.15 mV $\pm$ 3.07 where ECa^{2+} =+168mV. Lopsided gradients favoring a driving force for either the NO_3^- current or the Ca^{2+} current both reflected a *Vrev* mirroring the ENO_3^-. Rather Ca^{2+} has a different effect as a permeant blocker. Reduction of [Ca^{2+}] augmented the overall current amplitude along the voltage spectrum of -140mV to +60mV, suggesting Ca^{2+} has a direct regulatory role on *Pp*GLR1 anion currents (Figure 27).

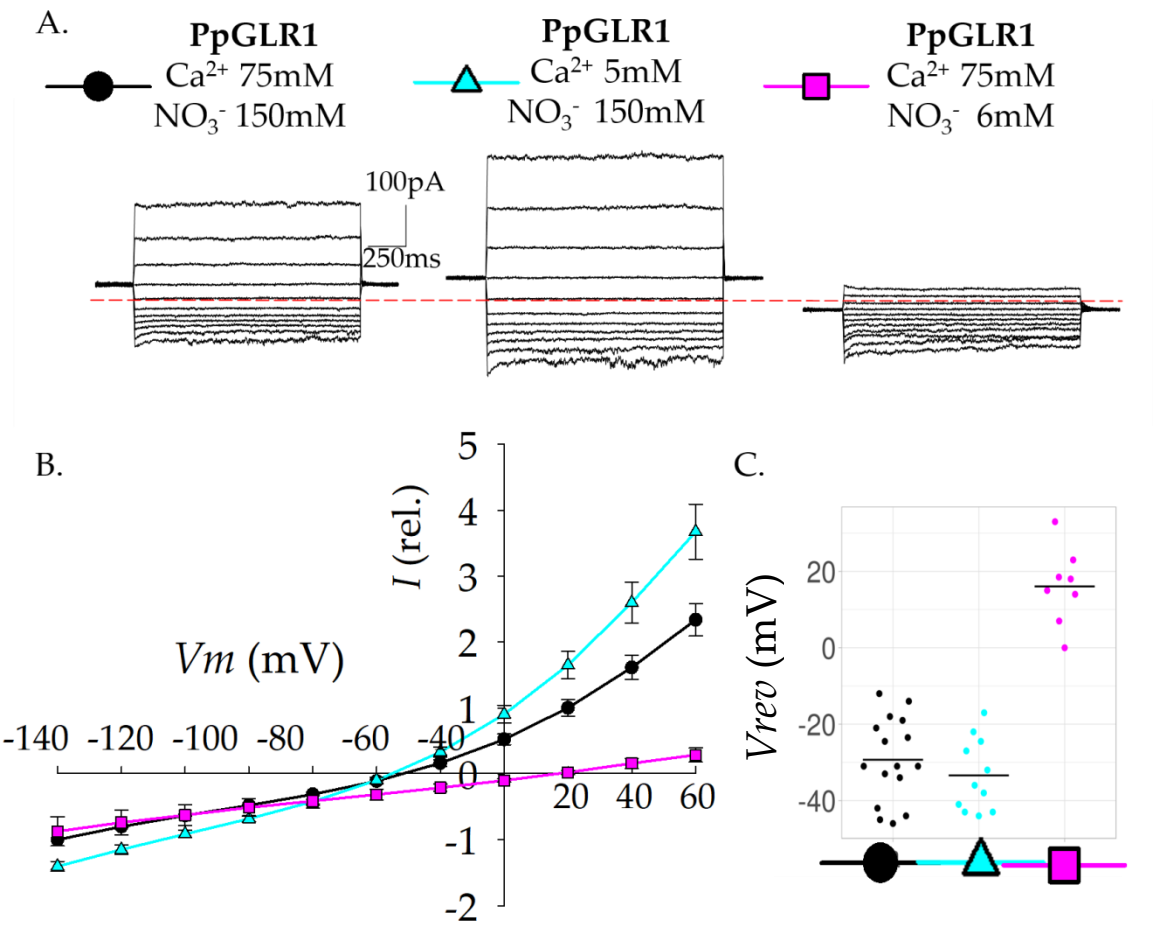

Figure 27: *Pp*GLR1 is selective to NO_3^-, and Ca^{2+} weakly contributes to the *Vrev*. A.) Example whole-cell current recordings from a single cell showing both anionic and Ca^{2+} current. Major charge carriers are indicated above representative trace. B.) Corresponding *I-V* curve. Ca^{2+} 75mM. NO_3^- 150mM (black circles; is solution set S9. Perfusions were balanced with $NMDG^+$ for removal of Ca^{2+} , S11, or gluconate for the removal of NO_3^-, S12). Error bars show SE. C.) Scatter plot depicting *Vrev* of individual replicates; n= 15, n= 9, n= 8 respectively. Mean value denoted by the bar.

The initial ion selectivity assay left several open questions. One, what accounts for the discrepancy between the *Vrev* and ENO_3^- if Ca^{2+}'s low permeability seemingly contributes little to the *Vrev*? With the defined NO_3^- gradient, ENO_3^- equals -80mV, and the *Vrev*s only measured -28.3±2mV (n=28). The only available data driven interpretation is that Ca^{2+} may contribute little to the *Vrev*, but to a sufficient degree

preventing a completely selective anion channel. To challenge this hypothesis, instead of changing the Ca^{2+} concentration, a higher internal NO_3^- concentration of 50mM was loaded into the cytosol of *Pp*GLR1 expressing COS-7 cells moving ENO_3^- to -40mV. The expected outcome was that the *Vrev* would also shift +40mV, the difference in ENO_3^- between S9 and S14. The observed result was that the *Vrev* was left unaffected by the higher internal NO_3^- concentration and now matched ENO_3^- . The average *Vrev* was measured at -23.2 $\pm$ 4.1mV (Supplemental Table 1; Supplemental Figure 1). Currents along the entire voltage range tested were also susceptible to Asp (2mM) with 43$\pm$6% (n=5) decrease for the currents recorded at +60mV, lending pharmacological evidence that the currents were mediated by *Pp*GLR1. Thus, a second interpretation explaining the discrepancy of *Vrev* to ENO_3^- is that the ion permeation may be concentration dependent. The next outstanding question from initial selectivity assays looks at the Ca^{2+} dependent inhibition.

Exploring the Ca^{2+} dependent inhibition, experiments in Ca^{2+} imaging with YC3.6 showed incubating *Pp*GLR1 expressing cells with Ca^{2+} (5mM) prevented successive applications of Ca^{2+} to boost $[Ca^{2+}]$cyt (Supplemental Figure 2). Basal $[Ca^{2+}]$cyt were already elevated compared to when incubated with EGTA, Mg^{2+}, or Ba^{2+} (5mM). Like EGTA, incubation of Mg^{2+} or Ba^{2+} did not prevent the elevation of $[Ca^{2+}]$cyt when prompted with external Ca^{2+} (Supplemental Figure 2).

As increasing the Ca^{2+} electrochemical gradient by perfusion of high external concentrations had an inhibitory effect on anionic currents, so did hyperpolarizing the membrane. In independent experiments, *Pp*GLR1 expressing cells in standard solutions

(solution S9) were exposed to a holding potential of 0mV and applied a series of voltage steps of 1.5secs from -140mV to +60mV in 20mV increments, or from -80mV to +60mV in 20mV increments until steady-state currents were achieved. *Pp*GLR1 expressing cells yielded stronger current amplitudes when avoiding exposure to hyperpolarized potentials (-100mV, -120mV, -140mV;Figure 28). The impact the test-pulse polarization has on the current amplitude illustrates the channel is not voltage-independent. Thus far, all whole-cell recordings used to determine the cation permeability have maintained a holding potential of 0mV, so I challenged a *Pp*GLR1 voltage-sensitivity by toggling the holding potential within the single recording. The ideal holding potential was found by allowing the cell's free-running voltage to equilibrate in current-clamp mode when injecting zero pA (Figure 28C). Because *Pp*GLR1 is the most heavily expressed ion channel on the plasma membrane during heterologous expression, the resting membrane voltage is largely determined by the permeability of *Pp*GLR1. By not imposing a membrane voltage, ion flux through *Pp*GLR1 is also expected to equilibrate. Allowing the cell to rest at its free-running voltage potentiated the outward anion current when applying a test pulse (Figure 28B). On the other hand, membrane hyperpolarization forced an irreversible rundown, compromising future studies (Supplemental Figure 3). The impact membrane hyperpolarization has on current amplitude demonstrates the constitutive background current is a product of the 0mV holding potential.

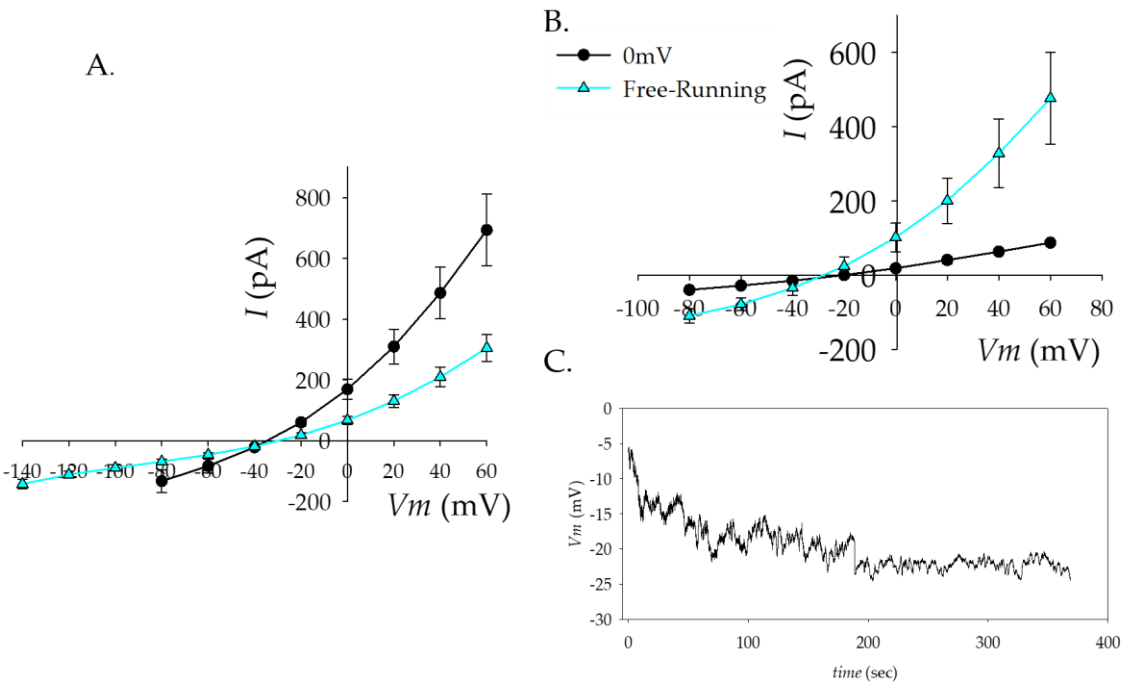

Figure 28: Impact of test-pulse pulse polarization and holding potential on whole-cell current amplitudes of *Pp*GLR1 expressing COS-7 cells. A.) *I-V* curve illustrating the result of different voltage protocols in standard solution S9. Test pulses clamping *Pp*GLR1 expressing cells to hyperpolarized potentials (-140 to -100mV) to +60mV (cyan, triangles; n=22) results in a smaller current amplitudes along the entire voltage spectrum compared to when test pulses are contained from -80mV to +60mV (black, circles; n=6). B.) *I-V* curve of *Pp*GLR1 expressing COS-7 cells under two different holding potentials: 0mV (black, circles) or the cell's free-running voltage (cyan, triangles; n=3). C.) Representative current clamp recording illustrating the equilibration of membrane potential. Error bars represent SE.

The voltage-sensitivity result was interpreted to hypothesize that the membrane hyperpolarization pulls Ca^{2+} into the pore exerting its "blocking" action. Further evidence that anions and Ca^{2+} occupy the same pore comes from a Gd^{3+} induced anion current rundown (data shown in Chapter 2, Figure 39).

Insights on Ca^{2+} permeation offered some hints on the molecular mechanisms determining GLR gating. By weakening the Ca^{2+} electrochemical gradients (low

extracellular Ca^{2+} and a depolarized *Vm*), ACC produced the canonical current increase expected of an agonist. *Pp*GLR1 transfected cells bathed in 1mM Ca^{2+} with 150mM NO_3^- and clamped +40mV for 5min to fully equilibrate before adding ACC (500μM) saw ACC application potentiate outward NO_3^- currents (Figure 29). The average time for the current amplitude to re-stabilize was 9.1±0.7min (Supplemental Figure 4). The R556A mutant defective in ligand-binding still produced a background current but was not potentiated by ACC. Control cells remained silent in these experimental conditions (Figure 29A,B). ACC-induced currents once achieving a steady-state amplitude at +40mV could be further potentiated upon successive iterations of 1.5 sec voltage steps from -80mV to +60mV culminating in saturated currents shown in the *I-V* with representative traces (Figure 29C,D). The *Vrev* before and after ACC potentiation remained constant, indicating the Ca^{2+} permeability was not significantly increased relative to the anion permeability (Figure 29, C). Prior to ACC, the average *Vrev* was -28.3±2mV (n=28). From nine cells potentiated by ACC where a *Vrev* measurement was taken, the average *Vrev* was -31.08±4.98mV. In the subset that could be further potentiated to saturating levels, the *Vrev* was measured at -28mV± 1.2 before runup and -32.75±2.72mV when steady state currents were achieved — for an average shift of -4.75±1.7 mV (n=4) (Table 2).

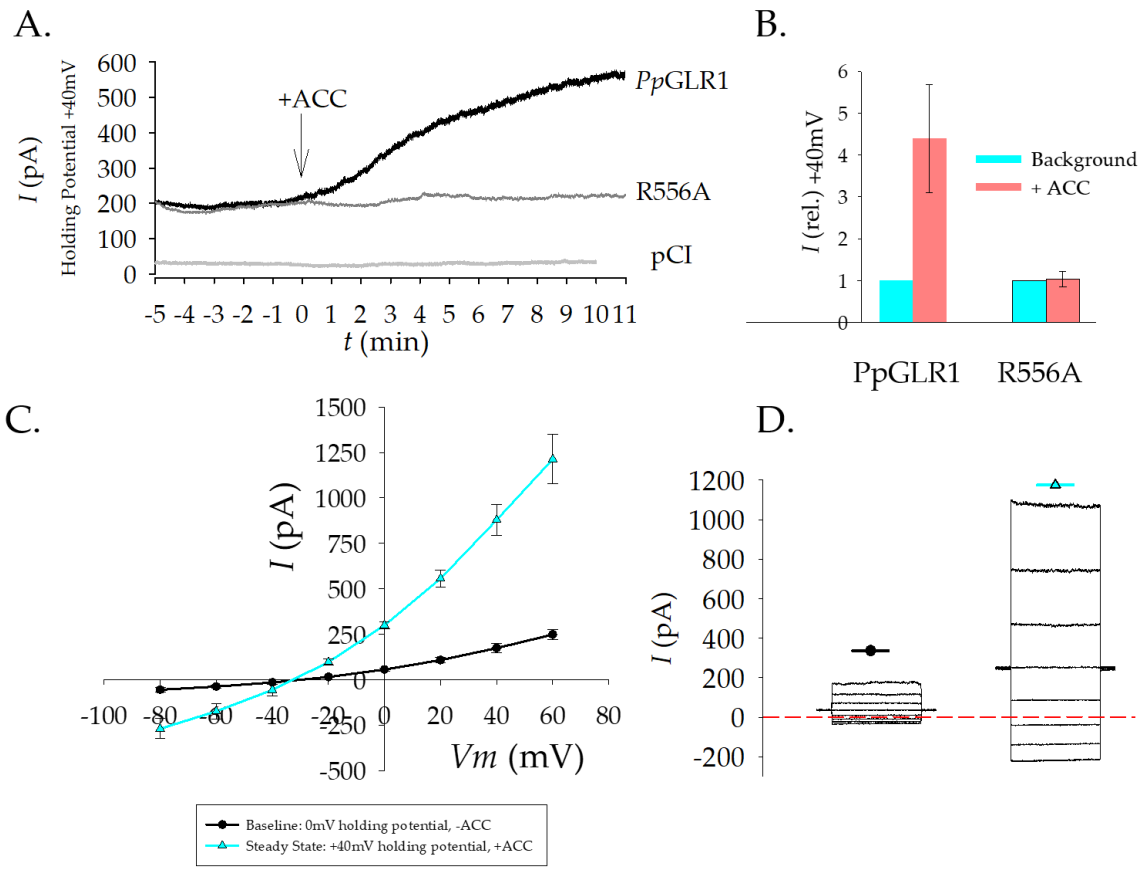

Figure 29: *Pp*GLR1 NO_3^- current is potentiated by ACC. A.) Representative current trace from *Pp*GLR1, *Pp*GLR1 (R556A), and pCI control cell from a holding potential of +40mV when applying ACC (500μM) and B.) Summary bar graphs depicting the relative increase in current amplitude at +40mV after ACC perfusion. *Pp*GLR1, n=13. R556A, n= 3 C.) *I-V* curve of *Pp*GLR1 steady-state currents before (black, circles) and after ACC, n=4. D.) Representative current traces corresponding to *I-V* curve shown in (C). Data generated in solution set S13.

Alternatively, steady-state currents at +40mV could be rundown with hyperpolarizing test pulses by either; applying short 1.5 sec pulses of -140mV, or long 30sec exposures of -100mV (Figure 30). The continual decay over the time period of 30sec illustrates the slow gating kinetics of the *Pp*GLR1. A rundown of the current did

not result in a change of ion selectivity either. In this subset of five cells, ACC activated currents established a *Vrev* of -31.08 +4.98mV prior to hyperpolarizing pulses and -31.72±6.51mV after rundown was completed —for an average shift of -0.02±0.62mV (Table 2).

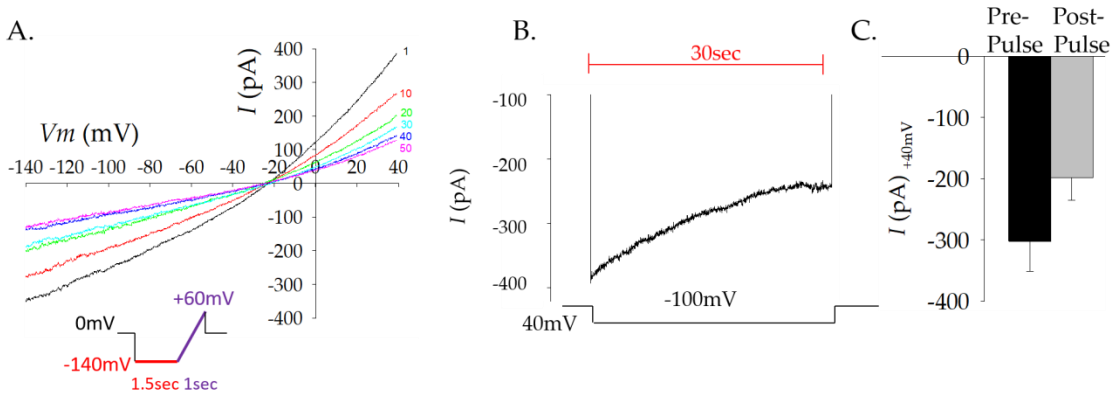

Figure 30: *Pp*GLR1 currents from COS-7 cells potentiated by ACC could be rundown by hyperpolarization. A.) *I-V* curve plotted from a representative whole-cell recording for n=5, biological replicates. Voltage protocol shown in the inset was repeated every 5sec and every tenth ramp is graphed for simplicity, numerical annotation indicates ramp number. B.) ACC potentiated currents also displayed a slow decay when clamped to -100mV for 30sec. Voltage protocol show below current trace. C.) Difference in steady state current recorded at +40mV before (pre-pulse) and after (post-pulse) a single 30sec exposure at -100mV corresponding to trace shown in B, n=5. Error bars represent SE. Data generated in solution set S13.

Table 2: *Vrev* measurements from *Pp*GLR1 transfected cells in various ion channel states; background currents without ACC, with ACC (500μM), after runup by depolarizing pulses in the presence of ACC (corresponding to currents shown in Figure 29), or after current rundown in the presence of ACC after hyperpolarizing pulses (corresponding to currents in Figure 30).

Condition	*Vrev* (mV)
Background	-28.3 (n=28)
+ACC	-31.08 (n=9)
+ACC / runup	-32.75 (n=4)
+ACC / rundown	-31.72 (n=5)

Although ACC did not change the ion selectivity to favor a Ca^{2+} selective channel, we have not excluded the possibility ACC potentiated currents confer a greater overall Ca^{2+} flux (as may be expected from ligand screening assay performed by Ca^{2+} imaging). Because the permeability of Ca^{2+} is too low to be reflected by *Vrev* analysis, the ENO_3^- was exploited instead. In bi-ionic solutions comprised of only Ca^{2+} and NO_3^-, a bona fide Ca^{2+} current could be found by holding the membrane voltage to NO_3^-'s equilibrium potential of -80mV. At an ion's equilibrium potential, that ion has zero net current, and therefore any changes in the measured current amplitude must come from another ion. In these bi-ionic conditions, the only other possibility is Ca^{2+}. When clamping to -80mV, ACC (500μM) perfusion potentiated an inward current (Figure 31). Of eight cells; two spontaneously in/deactivated reducing the current amplitude, four in/deactivated instigated by supplemental Ca^{2+} (1mM), and two cells were not challenged for in/deactivation. A split population of cells expressing *Pp*GLR1 that showed various

in/deactivation behaviors suggests the Ca^{2+} dependent inhibition threshold could be approximately 1mM extracellular Ca^{2+}. Notably, prior to ACC perfusion, cells were clamped to -80mV for 1-2min in an attempt to achieve an equilibrated channel state. During this period, currents inactivated.

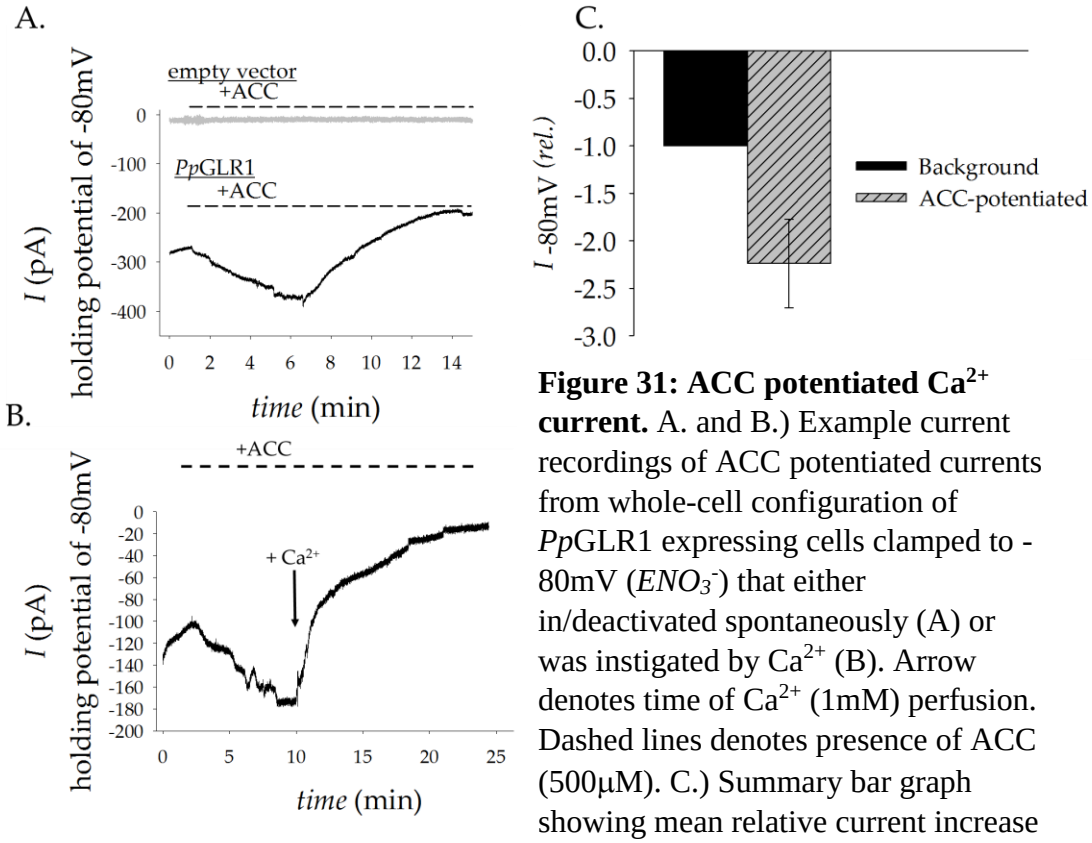

Figure 31: ACC potentiated Ca^{2+} current. A. and B.) Example current recordings of ACC potentiated currents from whole-cell configuration of *Pp*GLR1 expressing cells clamped to -80mV (ENO_3^-) that either in/deactivated spontaneously (A) or was instigated by Ca^{2+} (B). Arrow denotes time of Ca^{2+} (1mM) perfusion. Dashed lines denotes presence of ACC (500µM). C.) Summary bar graph showing mean relative current increase from n=8. Solution Set S13 was used. Error bars represent SE.

Impact of CNIH on *Pp*GLR1 gating

Patch clamp solutions:

A detailed list of the internal and external solutions used for patch clamp experiments in this chapter 2 part 4 for figures 32, 33, and 34 can be found in Table 7 (pg. 145). The major charge carriers are described in the main text and depicted in Figure 32B.

Interactions between *At*CNIHs and *At*GLRs have critical roles for receptor trafficking that underlie Ca^{2+} homeostasis(71). In the heterologous system, *At*CNIHs were obligatory to record an ionic current suggesting they may have additional roles in ion channel gating, a satisfactory conclusion compared to the work of Tapken *et al.*, 2008(277) who found *At*GLRs on the plasma membrane but were not functional ion channels. Although *Pp*GLR1 does not need the presence of CNIH like *At*GLRs do, two CNIHs are found in *P. patens* genome. Since *Pp*GLR1 has the ability to go to the plasma membrane independently of CNIH, we asked if *Pp*CNIHs could modify *Pp*GLR1 gating.

Because we are attempting to add a new component to the ion channel that is physiologically present with *Pp*GLR1, we also modified our experimental conditions to mimic the natural ion current directions (standard solution set S14). The anion is now loaded into the pipette (dialyzing into the cytosol) and carries an "inward" current. Ca^{2+} remained extracellular and also presents an "inward" current. Moreover, a particular challenge with a constitutively active current is the need to assess the portion of leak current from a given patch. These ionic conditions are experimentally advantageous to monitor the presence of artefactual leak currents as all ionic currents must be inward. Outward current would indicate a pipette leak.

By co-expressing *Pp*GLR1 with *Pp*CNIHa in COS-7 cells, the *Pp*GLR1 mediated background currents were substantially augmented by the auxiliary protein's presence, suggesting *Pp*CNIHa interacts with *Pp*GLR1, an effect very similar to the one observed of *At*CNIHs on *At*GLRs (Figure 32).

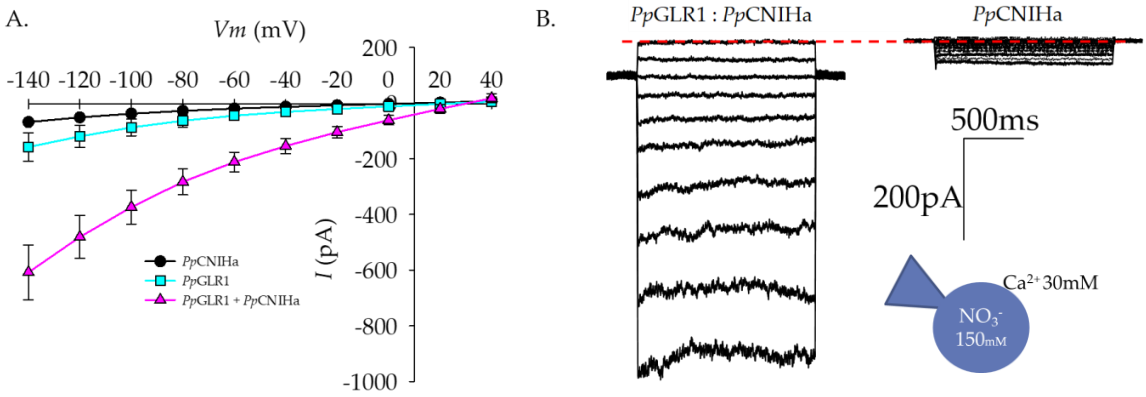

Figure 32: *Pp*GLR1 current amplitude is enhanced by co-expression with *Pp*CNIHa. A.) *I-V* curve and B.) representative current traces from whole-cell patch clamp experiments on singularly expressing *Pp*GLR1 (n=4) or *Pp*CNIHa (n=3), or co-transfected *Pp*GLR1:*Pp*CNIHa (n=6) in COS-7 cells. Error bars represent SE. Data generated with standard solution set S15. Major charge carriers are depicted panel B.

If *At*CNIHs/ *At*GLRs and *Pp*CNIHs/ *Pp*GLRs interactions derive from a common ancestral interaction, we can expect conserved molecular mechanisms. To test this hypothesis, *At*CNIH4 was co-expressed with *Pp*GLR1. The background current remained intact, but the current potentiation in response to exogenous Glu (1mM, 5mM) was sensitized and subsequently inhibited by Gd^{3+} (1mM) (Figure 33 and Figure 34). The action of a gene encoded by *Arabidopsis* on GLR1 from *P.patens* is suggestive of an evolutionarily conserved function of CNIH proteins in glutamate receptor channel gating. Although both *Pp*CNIHa and *At*CNIH4 enhanced channel activity; *Pp*CNIHa enhanced the steady-state current and *At*CNIH4 enhanced the ligand-gating. Even among *At*CNIHs,

of which there five genes, it is uncertain if all CNIHs fulfill the same function. Some *At*CNIHs are speculated to be involved in trafficking (bringing more channels to the plasma membrane) while others are thought to be more involved in channel gating (playing an active role in opening or closing the channel)(71). If, or how, various CNIHs operate in different capacities remains an open question.

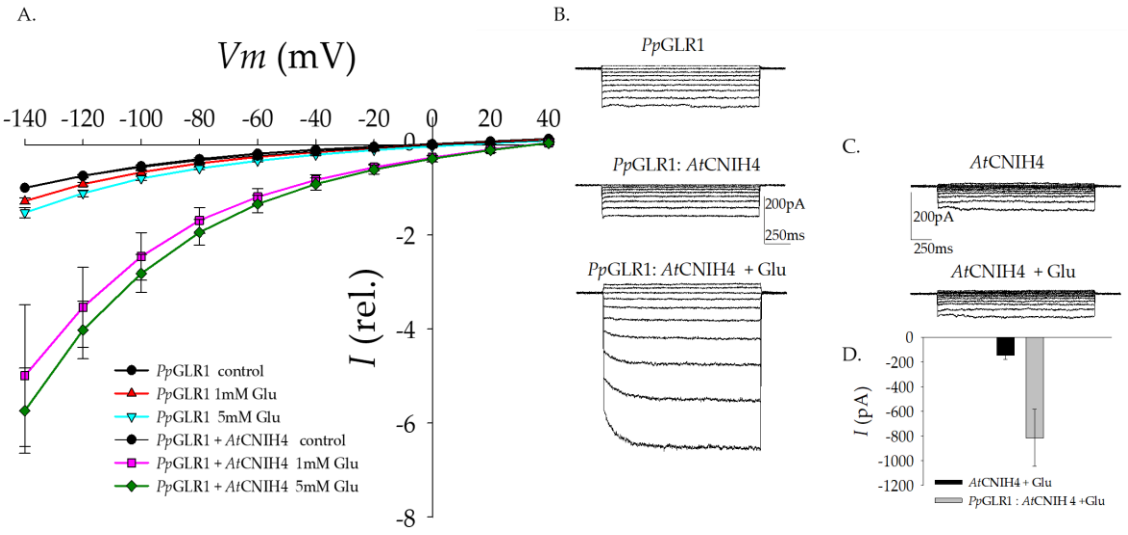

Figure 33: *At*CNIH4 co-expression with *Pp*GLR1 sensitizes Glu potentiation. A.) *I-V* curve reporting relative current amplitude potentiation by Glu (1 and 5mM) on singularly expressing *Pp*GLR1 (n=5) , or *At*CNIH4 (n=3), or co-expressing *Pp*GLR1:*At*CNIH4 (1mM, n=3; 5mM, n=4) in COS-7 cells. B.) and C.) Representative current traces from whole-cell patch clamp experiments corresponding to A. D.) Summary bar graph illustrating the mean Glu potentiated current amplitude of singularly expressing *At*CNIH4 or co-expressing *At*CNIH4 with *Pp*GLR1.Error bars represent SE. Data generated with standard solution set S15.

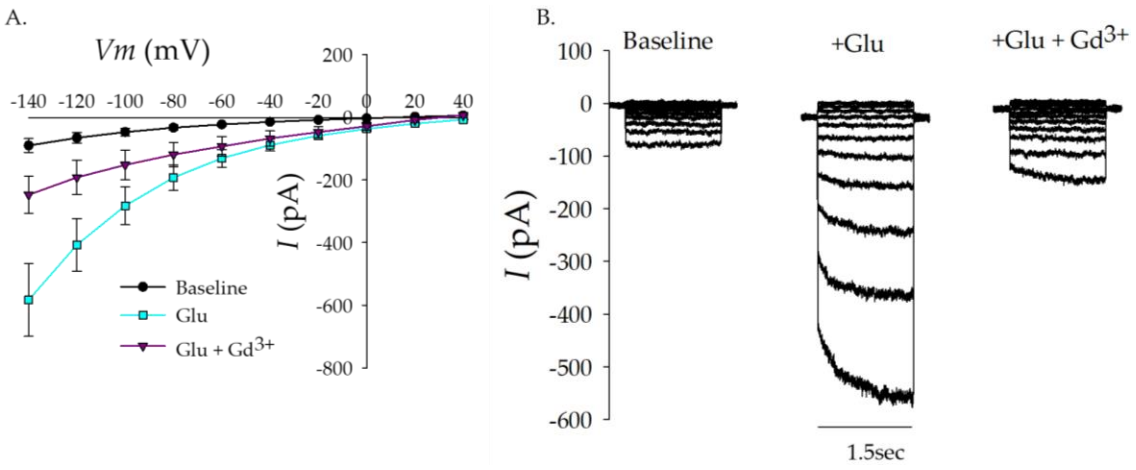

Figure 34: Glu potentiated currents from *Pp*GLR1:*At*CNIH4 co-expressing COS-7 cells are inhibited by Gd^{3+}. A.) *I-V* curve reporting current amplitude potentiation by Glu (5mM) on co-expressing *Pp*GLR1:*At*CNIH4 are inhibited by Gd^{3+} (500μM)(n=3). Error bars represent SE. B.) Representative current traces from whole-cell patch clamp experiments corresponding to A. Data generated with standard solution set S15.

The disadvantage to this ionic solutions is the inability to draw conclusions on the ion selectivity as all currents present as inward. I therefore turned to Ca^{2+} imaging with YC3.6 in COS-7 cells. Applying Glu to *Pp*GLR1 or *Pp*GLR1:*At*CNIH4 expressing cells showed no discernable difference suggesting the overall Ca^{2+} signal was not enhanced by *At*CNIH4 (Supplemental Figure 5).

In the next section, a gating function independent of the ligand and LBD interaction will be pursued as the primary means of opening and closing the channel. Three independent results from *Pp*GLR1 and *At*GLRs, in addition to the LBD mutagenesis, encourage the study of constitutively active currents over ligand-induced currents. First, ligand-induced runup or rundown did not alter the ion selectivity. ACC potentiated distinct *Pp*GLR1 anion currents with no palpable shift in the *Vrev* toward

ECa^{2+}. In conditions of high Ca^{2+}, ACC and Glu induced rundown occurred at all voltages, including the inward currents able to be carried by Ca^{2+} suggesting an overall increase of Ca^{2+} permeation is unlikely. Second, currents either as background currents mediated by *Pp*GLR1 potentiated by co-expression with *Pp*CNIHa or Glu-potentiated currents in *Pp*GLR1/*At*CNIH4 co-expressed cells likewise saw no increased capability to elevated [Ca^{2+}]cyt. Lastly, the broader implications of the background currents are observed in the heteromerization studies of clade 3 *At*GLRs. As obligatory heteromers displaying a spectrum of gating tendencies, there were two dominant subunits. One dominant channel subunit was *At*GLR3.7. *At*GLR3.7 did promote ligand activated currents, but is not a functional homomer. The other dominant subunit was *At*GLR3.2 forced larger background currents insensitive to ligands suggesting the constitutive gating mode is prevalent throughout *P.patens* and *Arabidopsis.*

Part 5: Ion selectivity and gating is determined by the channel pore

Patch clamp solutions:
A detailed list of the internal and external solutions used for patch clamp experiments in this chapter 2 part 5 can be found in Table 8 (pg. 146). The major charge carriers are indicated within each main figure.

While *Pp*GLR1 was able to conduct a Ca^{2+} current (Figure 15), chapter 2 part 2 demonstrated that anions are permeant. From the same experiments in Figure 15 that demonstrate the Ca^{2+} permeability, reversal potential (*Vrev*) analysis shows a discrepancy compared to the predictions for a selective cationic channel — indicative that another ion species is more permeable than Ca^{2+}. In Figure 15, the average *Vrev* of *Pp*GLR1 expressing COS-7 cells in 70mM Ca^{2+} within a fixed Cl^- gradient was +29.9 $\pm$ 8.3mV

(with a ECl^-=+7 mV ECa^{2+}= +169mV). To estimate a relative permeability ratio of Ca^{2+} compared to Cl^- ($P\ Ca^{2+}/\ Cl^-$)— supposing *Pp*GLR1 conforms to the ion independence assumptions allowed by the Goldman-Hodgkin-Katz (GHK) formality— the GHK equation (Equation 4) according to Lewis (1979)(297) was fitted to the shift in *Vrev* when exchanging the bathing [Ca^{2+}] from 3mM to 10mM, 30mM and 70mM. The average *Vrev* shift between 3mM and 70mM Ca^{2+} measured 21.4 $\pm$ 8mV. Permeability ratios were individually calculated and then averaged to approximate the $PCa^{2+}/\ Cl^-$= 0.23$\pm$0.21 (n=4).

Challenging an anion selectivity of *Pp*GLR1

To challenge if *Pp*GLR1 is therefore a predominantly anion selective channel, we were motivated to perform the opposite perfusion by increasing [Cl^-] in a fixed gradient of Ca^{2+} (15mM). As expected, raising the [Cl^-] in the extracellular solution from 30mM to 60mM, and 120mM dramatically increased the outward current amplitude (Figure 35). Analysis of the current-voltage (*I-V*) curves revealed the measured *Vrev* ,which shifted from 0.17$\pm$1.3mV to -29.07$\pm$4.30mV when exchanging 30mM for 120mM Cl^-, closely tracked the predicted Nernstian ECl^- (Figure 35D). Additionally, Cl^- currents in *Pp*GLR1 expressing COS-7 cells were abolished by the antagonist Asp (1mM), validating that *Pp*GLR1 mediated the Cl^- current (Figure 35A,B). Again, with the assumption *Pp*GLR1 conforms to the ion independence allowed by the GHK formality, the GHK equation was fitted to the shift in *Vrev* purely as an estimation referencing the *Vrev*. Individually calculated permeability ratios were then averaged to approximate the $P\ Ca^{2+}/\ Cl^-$

=0.20±0.12 (*n*=3), a value equivalent to the one deduced from previous experiments perfusing different [Ca^{2+}] (Figure 15; *P* Ca^{2+}/ Cl^-=0.23±0.2).

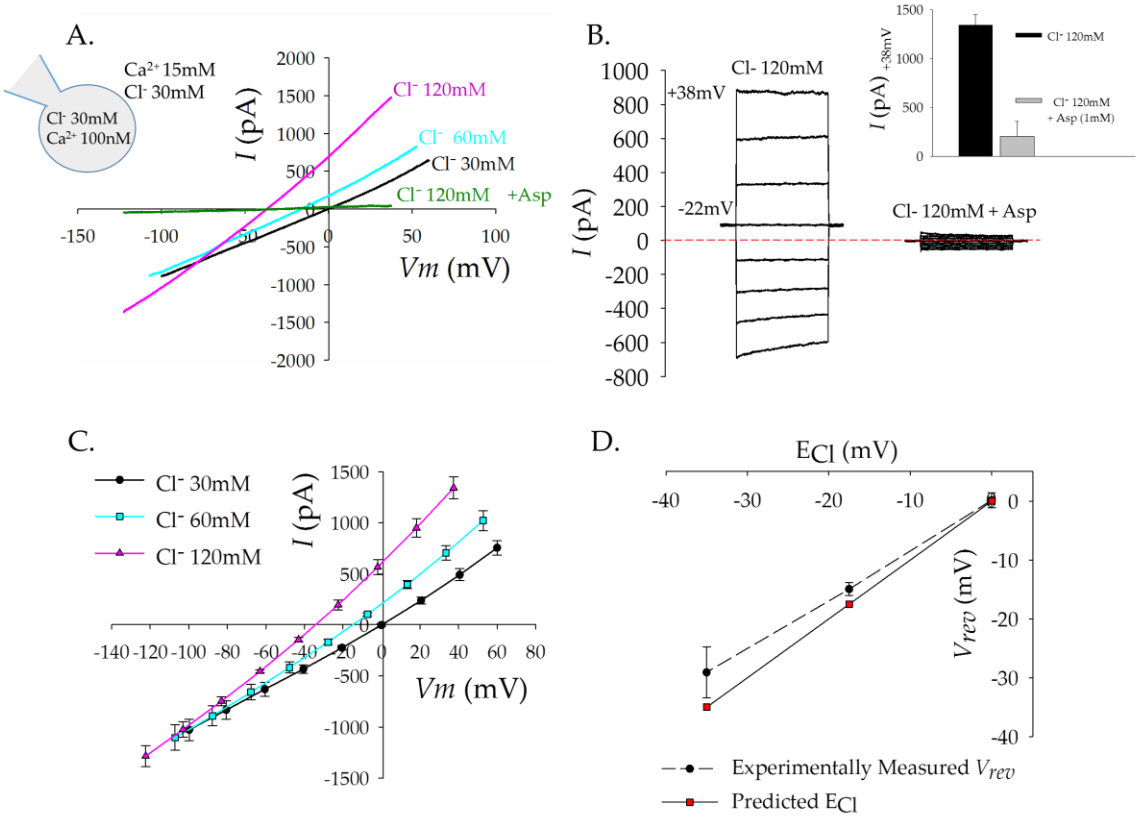

Figure 35: *Pp*GLR1 is selective for Cl^- over Ca^{2+}. A.) Representative ramp traces (obtained from whole-cell patch clamp) plotted as an *I-V* curve from a *Pp*GLR1 expressing COS-7 cell upon perfusion of Cl^- in a fixed gradient of Ca^{2+}. B.) Representative steady-state current traces before and after the addition of Asp (1mM), inset in upper right corner displays statistics of current rundown observed at +38mV (n=3). C.) Average *I-V* curve of Cl^- perfusion. n=3 for all conditions. D.) Reversal potentials (*Vrev*) of *Pp*GLR1 expressing cells (black circles, dashed line; n=3) under various [Cl^-] compared to calculated Nernst potentials (red squares; solid line). Error bars indicate SE. Data was obtained with solution S16 (major charge carriers are illustrated in panel A inset). Data in panel A,C, D was collected from the following fast ramp voltage protocol: From a holding potential of 0mV, a 0.5sec pulse of -120mV was applied before ramping from -120mV to +60mV over 2sec. Ramps were repeated every 15sec, cells were re-clamped to a holding potential of 0mV between ramps. Data in panel B was collected from a typical voltage step protocol applying test pulses of 1.5sec from -80mV to +60mV (before correction of liquid junction potentials) in +20mV steps.

Vrevs were also tracked to ENO_3^- upon perfusion of NO_3^- in a Ca^{2+} gradient. Perfusion of high extracellular [NO_3^-] also resulted in a leftward shift of the *Vrev* mirroring the shift observed by the Cl^- perfusion, likewise indicating a preference for NO_3^- over Ca^{2+} (Figure 36). Intriguingly, a modified voltage protocol ramping from -60mV to +60mV minimizing exposure to negative voltages was required to observe the increase in outward current. From the independent anion perfusions, when the final extracellular Cl^- and NO_3^- concentration reached 120mM, equivalent with an equilibrium potential of -35 mV, the *Vrev* of *Pp*GLR1 expressing cells subjected to the Cl^- perfusion was measured at -29.07$\pm$4.31mV (n=3). Similarly, the cells subjected to a NO_3^-perfusion measured a *Vrev* of -26.06 $\pm$ 3.37mV(n=5) (Figure 36D). In solution set S17, non-expressing control cells showed minimal current at+60mV averaging 39.04$\pm$10.78pA (n=5), revealing that endogenous ion channels from COS-7 cells did not mediate a NO_3^- current under our experimental conditions (Figure 36B). As a control for validating the authenticity of NO_3^- currents that were recorded, all cells patched were routinely exposed to +60mV steps to check for inactivating currents(298).

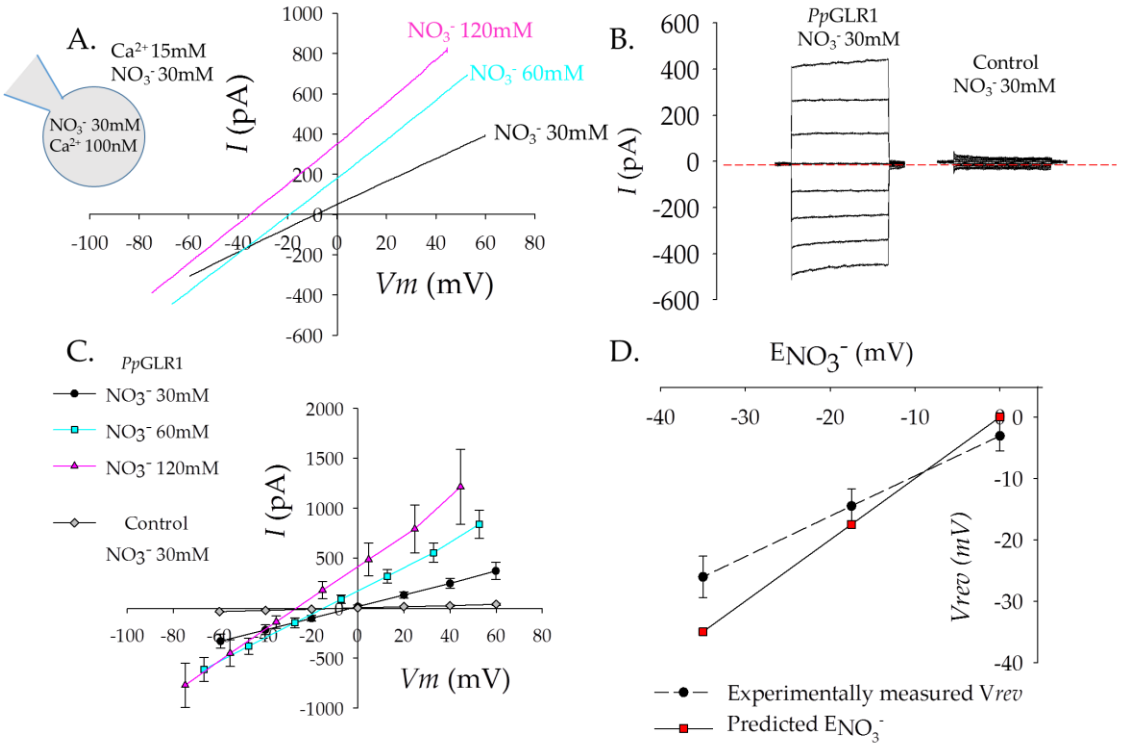

Figure 36: *Pp*GLR1 is selective for NO_3^- over Ca^{2+}. A.) Representative ramp traces (obtained from whole-cell patch clamp) plotted as an *I-V* curve from a *Pp*GLR1 expressing COS-7 cell upon perfusion of NO_3^- in a fixed gradient of Ca^{2+}. B.) Representative steady-state current trace from a *Pp*GLR1 transfected cell and an empty vector transfected control cell illustrating the continued observation that COS-7 cells show minimal endogenous current under our experimental conditions (Both genotypes, n=5). C.) Average *I-V* curve of NO_3^- perfusion on *Pp*GLR1 transfected cells. n=5 for all conditions. D.) Reversal potentials (*Vrev*) of *Pp*GLR1 expressing cells (black circles, dashed line; n=5) under various NO_3^-concentrations compared to calculated Nernst potentials (red squares; solid line). Error bars indicate SE. Data was obtained with solution S17 (major charge carriers are illustrated in panel A inset). Data in panel A,C, D was collected from the following fast ramp voltage protocol: From a holding potential of 0mV, a 0.5sec pulse of -60mV was applied before ramping from -60mV to +60mV over 2sec. Ramps were repeated every 15sec, cells were re-clamped to a holding potential of 0mV between ramps. Data in panel B was collected from a typical voltage step protocol applying test pulses of 1.5sec from -80mV to +60mV (before correction of liquid junction potentials) in +20mV steps.

Besides Ca^{2+}, monovalent cations also play important roles in membrane transport. To test if *Pp*GLR1 is also preferential to monovalent anions over monovalent

cations, I selected to quantify the relative permeability of NO_3^- compared to Na^+ (PNO_3^-/Na^+) because COS-7 cells show no detectable endogenous currents for either of the ions(67). To approximate PNO_3^-/Na^+, the shift in *Vrev* was measured when exchanging from a symmetric extracellular and pipette (internal) $NaNO_3$ solutions (150mM), to asymmetric $NaNO_3$ solutions with a diluted extracellular solution (30mM). In these bi-ionic solutions, the Nernst equation predicts that a channel favorable to cations will have a *Vrev* shift to the left toward negative potentials when diluting $NaNO_3$; ENa^+ moves from 0mV to -40mV. If the channel is favorable to anion permeation, then the *Vrev* will predictably shift to the right toward positive voltages when diluting $NaNO_3$; ENO_3^- moves from 0mV to +40mV. Experimentally, a clear shift of +17.7±1.7mV (n=9) toward ENO_3^- was consistently observed upon exchanging 150mM for 30mM $NaNO_3$. (Figure 37; Table 3). The estimated PNO_3^-/Na^+ equaled 3.3+0.4.

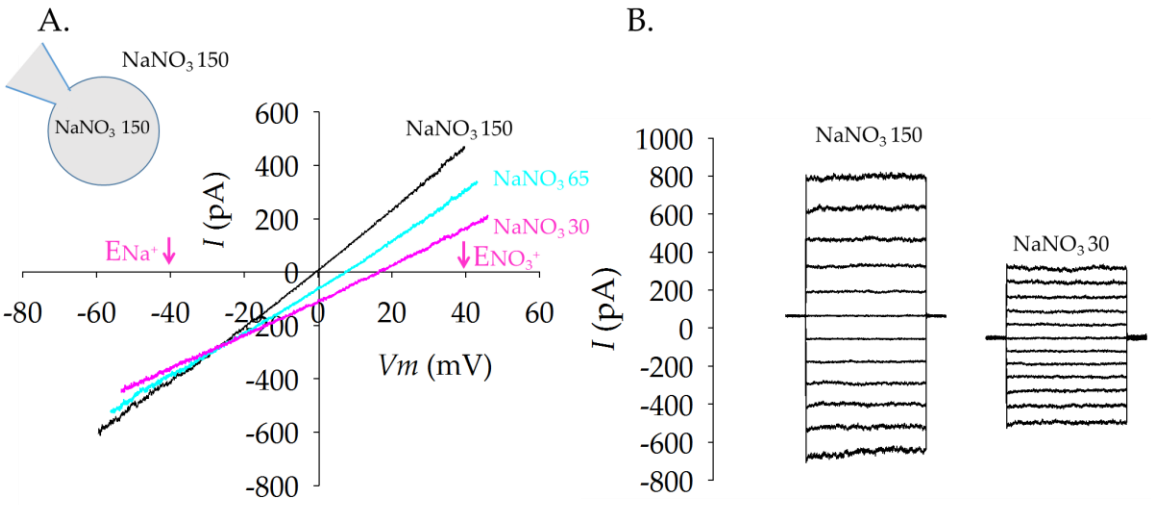

Figure 37: *Pp*GLR1 is selective for NO_3^- over Na^+. A.) Representative ramp traces from a *Pp*GLR1 expressing COS-7 cell plotted as an *I-V* curve. Whole-cell patch clamp currents were recorded upon dilution of extracellular [$NaNO_3$] from 150mM (black), 65mM (cyan), and 30mM (pink). B.) Representative steady-state current traces in *Pp*GLR1 transfected cells under 150mM or 30mM $NaNO_3$. $NaNO_3$ dilution experiments

utilized solution set S18 (major charge carriers before dilution are illustrated in panel A inset). Data in panel A was collected from voltage ramps with a 0.5sec pulse of -60mV applied before ramping from -60mV to +60mV over 2sec. Ramps were repeated every 15sec, in the meantime, cells were reset to a holding potential of 0mV. Data in panel B was collected from a typical voltage step protocol applying test pulses of 1.5sec from -60mV to +50mV in +10mV steps. Arrows labeled with ENO_3^- or ENa^+ indicate the equilibrium potential for the given ion in the asymmetric conditions with $NaNO_3$ 30mM as the extracellular solution. In symmetric 150mM $NaNO_3$, both ENO_3^- and ENa^+ are 0mV.

Targeted mutagenesis of the *Pp*GLR1 selectivity filter

To begin appreciating the molecular basis for the anion selectivity of plant GLRs, we looked at sequence alignments of GLRs compared to iGluRs concentrating on the residues flanked by the signature WGP pore loop motif. The residues aligning the predicted GLR pore— particularly in the selectivity filter— are poorly conserved to iGluRs, and several GLRs show several positively charged residues which would be favorable for anions penetrating through (Figure 38). To test if the unconserved selectivity filter may be responsible for the different ion selectivity, a chimeric channel was engineered by swapping out the predicted *Pp*GLR1 selectivity filter and cytoplasmic entry residues for those from the Ca^{2+} permeable (Q-form) GluA2 (Figure 38).

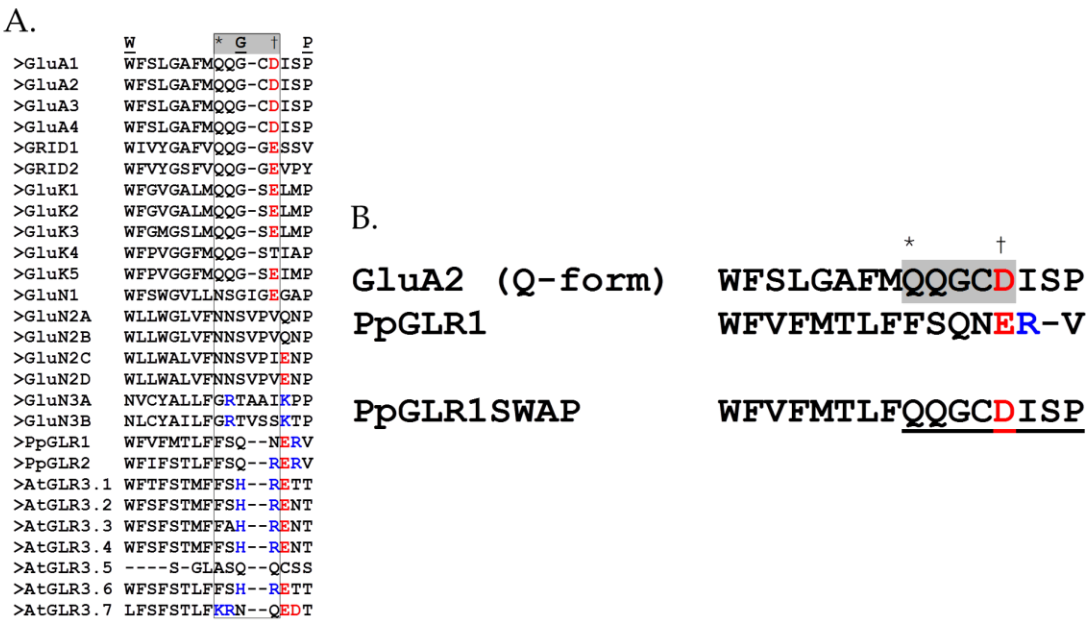

Figure 38: Design of a GLR-iGluR pore chimera. A.) Alignment of iGluR and GLR sequences encoding the pore domain using Clustal Omega. B.) top; Alignment of amino acid sequences from the Ca^{2+} permeable GluA2 (Q-form) channel and *Pp*GLR1 using AlignMe(299). bottom; A *Pp*GLR1-GluA2 chimera, named *Pp*GLR1$_{SWAP}$, was engineered by swapping out the amino acid residues native to the *Pp*GLR1 selectivity filter for the amino acids encoding the cation selective and Ca^{2+} permeable GluA2. Asterisk (*) denotes the Q/R/N site, dagger denotes the cytoplasmic entry point. In A, the boxed residues, or in B, the grey shaded area, highlights the predicted selectivity filter. Red residues signify a negatively charged residue, blue residues signify a positively charged residue.

The pore chimera (*Pp*GLR1$_{SWAP}$) and the non-mutated *Pp*GLR1 (*Pp*GLR1) were expressed in COS-7 cells and evaluated for its relative permeability of Ca^{2+} compared to NO_3^-. A Ca^{2+} permeability was first measured in the Ca^{2+}/NO_3^- bi-ionic condition (Solution S9), where only NO_3^- can drive outward currents and Ca^{2+} predominantly drives the inward currents. *Vrev* analysis and current amplitudes suggest the *Pp*GLR1$_{SWAP}$ had gained a Ca^{2+} permeability over *Pp*GLR1 (Figure 39). When compared to currents recorded in *Pp*GLR1 expressing cells, *Pp*GLR1$_{SWAP}$ inward currents were greater,

suggesting an increase in Ca^{2+} permeability. In agreement, *Vrev* of *Pp*GLR1$_{SWAP}$ currents (-11.5mV±4.5, *n*=6) was shifted to the right compared to *Pp*GLR1 currents (-34mV±7,*n*=3), showing that the chimera had gained Ca^{2+} permeability. Currents in both the *Pp*GLR1 and *Pp*GLR1$_{SWAP}$ were sensitive to Gd^{3+}, a classical Ca^{2+} channel pore blocker, lending credence to the hypothesis that both the anion and the Ca^{2+} ion bind in the same pore (Figure 39).

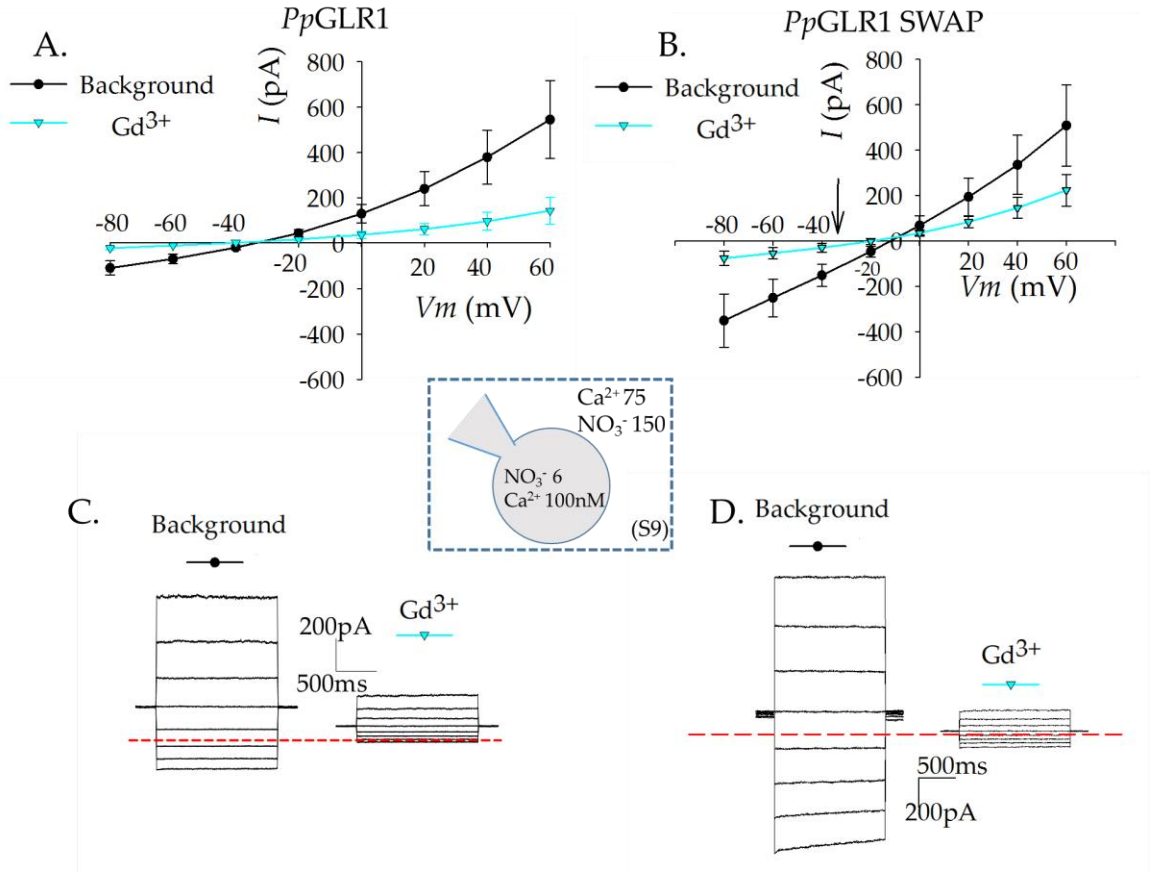

Figure 39: *Pp*GLR1$_{SWAP}$ demonstrates a gain in Ca^{2+} permeability. A.) and B.) *I-V* curve obtained from whole-cell patch clamp experiments on *Pp*GLR1 or *Pp*GLR1$_{SWAP}$ expressing COS-7 cells. Outward NO_3^- currents from both channels are sensitive to Gd^{3+} (1mM). *Pp*GLR1$_{SWAP}$ currents revealed augmented Ca^{2+} permeability indicated by the larger inward currents and rightward shift of the reversal potential (*Vrev*). Arrow in B denotes the average *Vrev* measured in *Pp*GLR1 expressing cells. *Pp*GLR1, n=3. *Pp*GLR1$_{SWAP}$, n=6. Error bars represent SE. C. and D.) Representative traces

corresponding to *I-V* curve in A and B, respectively. Data was generated in solution set S9 (major charge carriers are diagramed in the dotted box), and collected from a typical voltage step protocol applying 1.5sec test pulses from -80mV to +60mVin +20mV steps, the holding potential in between test pulses was 0mV.

To further examine this hypothesis, the voltage dependency of Gd^{3+} inhibition was investigated (Supplemental Figure 6). Gd^{3+} (1mM) was found to be ineffective when cells received 1.5sec voltage pulses of +80 and +100mV. Tail current analysis revealed a minor voltage sensitivity. In the presence of Gd^{3+}, tail currents measured at -100mV were inhibited after 1.5sec test pulses from -80 to 0mV; only after potentials depolarized of 0mV did currents recover (Supplemental Figure 6). Although the differences in relative current change are small, they may be proportional to the short test pulses, which overall is congruent with the slow kinetics of channel previously reported (Shown in Chapter 2 part 4, Figure 30).

Because an anion current was still observed in *Pp*GLR1$_{SWAP}$ we further evaluated the NO_3/Na selectivity in $NaNO_3$ dilution experiments and found the *Pp*GLR1$_{SWAP}$ mutant also gained a Na^+ permeability comprising the background currents compared to *Pp*GLR1. In cells expressing *Pp*GLR1$_{SWAP,}$ the shift of the *Vrev* upon dilution of $NaNO_3$ was largely mitigated to average only 6mV (Figure 40; Table 3). It is possible that the slightly positive *Vrev* was partially contributed to by the extracellular Ca^{2+} given the greater permeability to Ca^{2+} ions. To support the conclusion that the lack of shift in the *Vrev* was due to a gain in Na^+ current, the total current amplitude was analyzed to reveal the *Pp*GLR1$_{SWAP}$ also gained current amplitude in the presence of $NaNO_3$, similar to the

observation that *Pp*GLR1$_{SWAP}$ expression yielded larger inward currents carried by Ca^{2+} (Figure 42).

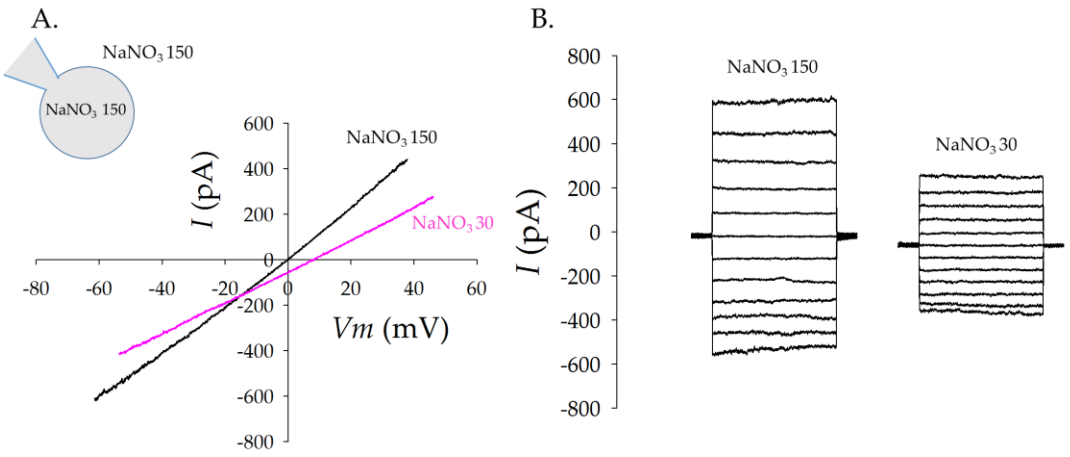

Figure 40: *Pp*GLR1$_{SWAP}$ losses selectivity for NO_3^- over Na^+. A.) Representative ramp traces from a *Pp*GLR1$_{SWAP}$ expressing COS-7 cell obtained from whole-cell patch clamp plotted as an *I-V* curve upon dilution of extracellular [$NaNO_3$] from 150mM (black) to 30mM (pink). B.) Representative steady-state current traces from a *Pp*GLR1$_{SWAP}$ transfected cell under 150mM or 30mM $NaNO_3$. $NaNO_3$ dilution experiments utilized solution set S18 (major charge carriers prior to dilution are illustrated in panel A inset). Data in panel A was collected from voltage ramps with a 0.5sec pulse of -60mV applied before ramping from -60mV to +60mV over 2sec. Ramps were repeated every 15sec, in the meantime, cells were reset to a holding potential of 0mV. Data in panel B was collected from a voltage step protocol applying test pulses of 1.5sec from -60mV to +50mV in +10mV steps.

The only mostly conserved residue in the pore swap was E647 supplying the only negative charged in the predicted selectivity filter of GLRs. The mutations of E647A still yielded background currents but no shift in the *Vrev* reflected a non-selective channel (Figure 41; Table 3). E647R was then tested to challenge if the electrostatics of this residue determined selectivity. E647R transfected cells yield no discernable currents (Figure 42).

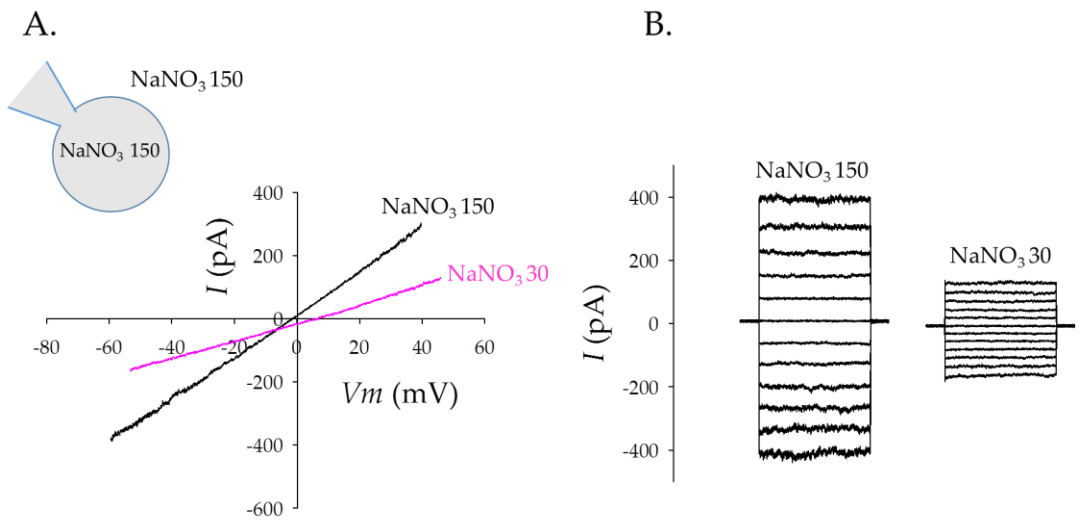

Figure 41: *Pp*GLR1 (E647A) is non-selective for NO_3^- over Na^+. A.) Representative ramp traces from a *Pp*GLR1 (E647A) expressing COS-7 cell obtained from whole-cell patch clamp plotted as an *I-V* curve upon dilution of extracellular [$NaNO_3$] from 150mM (black), 65mM (cyan), and 30mM (pink). B.) Representative steady-state current traces from a *Pp*GLR1 (E647A) transfected cell under 150mM or 30mM $NaNO_3$. $NaNO_3$ dilution experiments utilized solution set S18 (major charge carriers prior to dilution are illustrated in panel A inset). *I-V* curve in panel A was plotted from voltage ramps where 0.5sec pulse of -60mV was applied before ramping from -60mV to +60mV over 2sec. Ramps were repeated every 15sec, in the meantime, cells were reset to a holding potential of 0mV. Representative traces in panel B were collected from a voltage step protocol applying 1.5sec test pulses from -60mV to +50mV in +10mV steps.

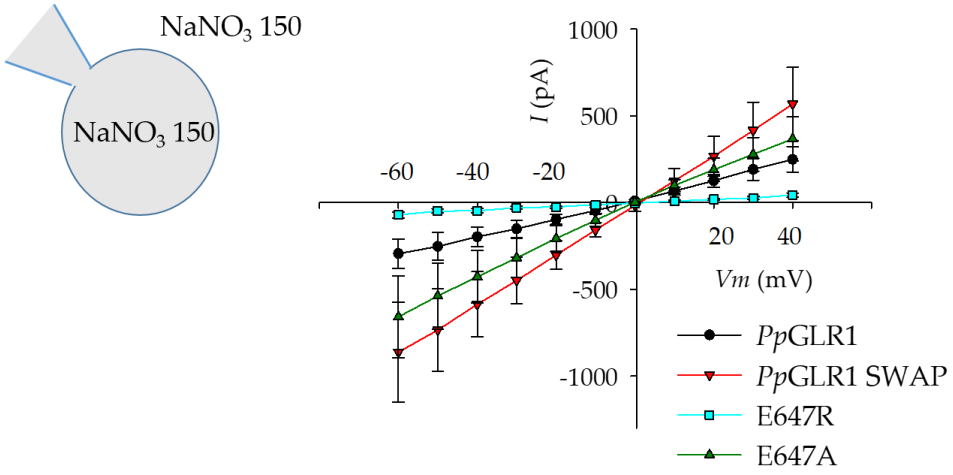

Figure 42: Current amplitudes recorded from *Pp*GLR1 genotypes under asymmetric 150mM [$NaNO_3$]. *I-V* curve of *Pp*GLR1 (n=9), *Pp*GLR1$_{SWAP}$ (n=5),

*Pp*GLR1$_{E647R}$ (n=6), and *Pp*GLR1 $_{E647A}$ (n=5) expressing COS-7 cells obtained from whole-cell recordings illustrating differences in average current amplitude.

Table 3. Reversal potentials *Pp*GLR1 and *Pp*GLR1 mutants measured in symmetric 150mM $[NaNO_3]_o$ and asymmetric $[NaNO_3]_o$.

Channel (filter motif)	V*rev*(mV) $[NaNO_3]_o$ 150mM	V*rev* (mV) $[NaNO_3]_o$ 65mM	V*rev*(mV) $[NaNO_3]_o$ 30mM	|Δ| (mV)
*Pp*GLR1 **FSQN-ERV**	-1.3 ±0.8 (n=9)	4.8 ± 1.5	16.4 ± 1.5 (n=9)	17.7 ±1.7 (n=9)
*Pp*GLR1$_{SWAP}$ **QQGCDISP**	2.3±2.4 (n=5)	n.d	8.4 ± 2.4 (n=5)	6.1 ± 1.4 (n=5)
*Pp*GLR1(E647A) **FSQN-ARV**	-0.5±0.4 (n=5)	n.d	0.8.±2.2 (n=5)	1.3±2.3 (n=5)

Ion selectivity of *At*GLR3.2 and *At*GLR3.4

*At*GLRs show a different selectivity filter compared to *Pp*GLR1 (Figure 38). *At*GLRs have two positively charged residues in the predicted pore selectivity filter—one more than *Pp*GLR1— hinting that *At*GLRs may also be conducive to anion permeation, so the ion selectivity of *At*GLRs was also investigated. *At*GLR3.2 was selected as a model *At*GLR because in heteromerization studies (See Introduction) found it was a dominant subtype of heteromeric combinations that drove a constitutively active gating mode. Under the same $NaNO_3^-$ dilution experiments, cells co-expressing *At*GLR3.2 with *At*CNIH1 and *At*CNIH4 (as determined to be the obligatory complex) displayed a shift in the *Vrev* from 0.5±0.3 to 24.1±2.6mV (Figure 43; Table 4).

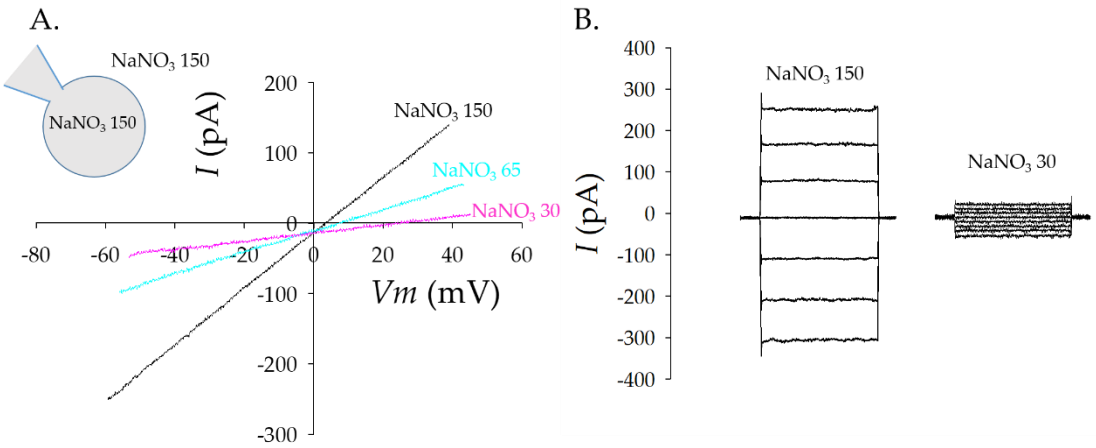

Figure 43: *At*GLR3.2 is selective for NO_3^- over Na^+. A.) Representative ramp traces from an *At*GLR3.2 expressing COS-7 cell obtained from whole-cell patch clamp plotted as an *I-V* curve. *At*GLR3.2 mediated background currents carried by NaNO3 solutions were diluted from 150mM (black) to 65mM (cyan), and 30mM (pink). B.) Representative steady-state current traces of *At*GLR3.2 transfected cells under 150mM or 30mM $NaNO_3$. $NaNO_3$ dilution experiments utilized solution set S18 (major charge carriers prior to dilution are illustrated in panel A inset). *I-V* curve A was collected from voltage ramps with a 0.5sec pulse of -60mV before ramping from -60mV to +60mV over 2sec. Ramps were repeated every 15sec, in the meantime, cells were reset to a holding potential of 0mV. Data in panel B was collected from a typical voltage step protocol where test pulses were applied for 1.5sec from -60mV to +60mV in +20mV steps.

*At*GLR3.4 shows demonstrably different ion channel properties, so we also challenged the ion selectivity of *At*GLR3.4. COS-7 cells transfected with *At*GLR3.4 with two CNIHs (*At*CNIH1 and *At*CNIH4) presented minimal background current prior to applying a ligand in the form of Asn (1mM), which activated macroscopic currents. Dilution of extracellular $NaNO_3$ solutions on cells expressing Asn activated current indicated *At*GLR3.4 was permeable to anions but showed little selectivity for anions over cations indicated by an 8.6$\pm$2.9mV shift in the *Vrev* (Figure 44; Table 4). We further controlled the anion permeability by challenging *At*GLR3.4 mediated currents from solution set S9 featuring bi-ionic $Ca(NO_3)_2$ conditions. Here, the Asn potentiation of

outward current confirmed the anion permeability of *At*GLR3.4 and further supported an increase of Ca^{2+} current reflected in the inward current (Figure 45).

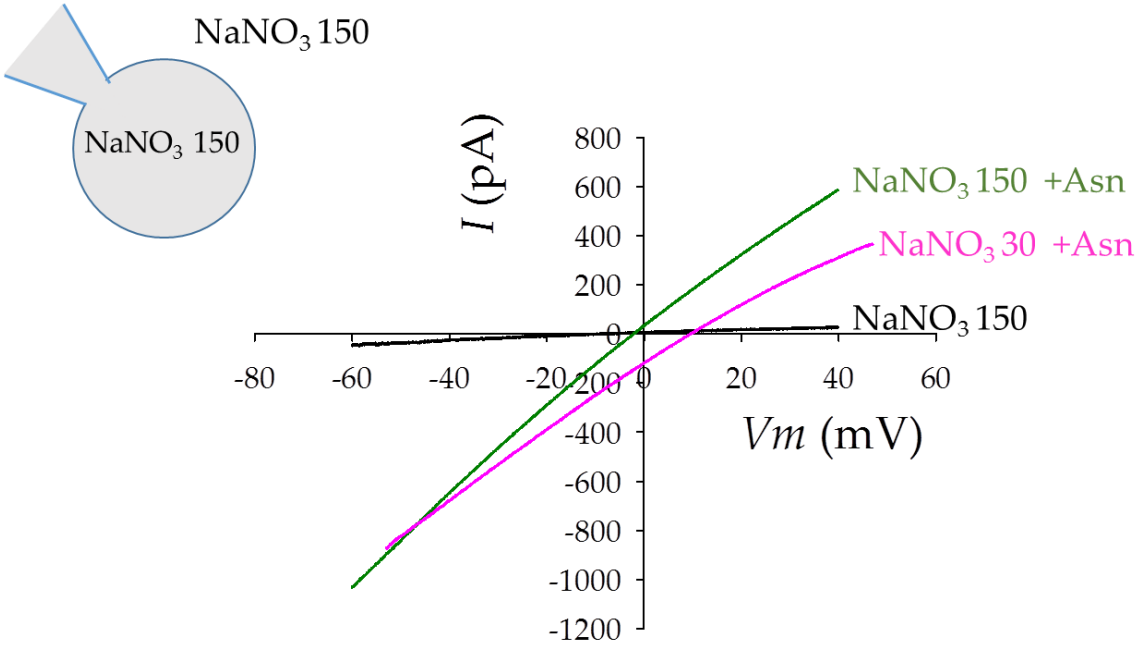

Figure 44: *At*GLR3.4 is permeable to NO_3^-, but largely non-selective to NO_3^- compared to Na^+. Representative ramp traces from an *At*GLR3.4 expressing COS-7 cell obtained from whole-cell patch clamp plotted as an *I-V* curve. *At*GLR3.4 mediated currents were activated by exogenous Asn perfusion (1mM) and extracellular $NaNO_3$ concentrations were diluted from 150mM (green) to 30mM (pink) in the continued presence of Asn. Control currents prior to Asn perfusion are shown in the black line. *Juan Barbosa-Caro performed the experiment. I designed the experiment.*

Table 4. Reversal potentials measured in symmetric 150mM $[NaNO_3]_o$ and asymmetric $[NaNO_3]_o$ from *P.patens* and *Arabidopsis* GLR expressing COS-7 cells. *Pp*GLR1 and *At*GLR3.2:*At*CNIH1/4 demonstrated substantial background currents. *At*GLR3.4:*At*CNIH1/4 currents were evoked by the application of Asn (1mM). *Juan Barbosa-Caro performed the experiment for AtGLR3.4:CNIH1/4*

Channel (filter motif)	V*rev*(mV) $[NaNO_3]_o$ 150mM	V*rev* (mV) $[NaNO_3]_o$ 65mM	V*rev*(mV) $[NaNO_3]_o$ 30mM	|Δ| (mV)
*Pp*GLR1 **FSQN-ERV**	-1.3 ±0.8 (n=9)	4.8 ± 1.5	16.4 ± 1.5 (n=9)	17.7 ±1.7 (n=9)
*At*GLR3.2 :*At*CNIH1/4 **FSHRE-NT**	0.5±0.3 (n=4)	11.8±1.3 (n=3)	24.6±2.6 (n=4)	24.1±2.6 (n=4)
*At*GLR3.4 :*At*CNIH1/4 **FSHRE-NT**	-3.4±05 (n=4)	n.d	5.15±3.1 (n=4)	8.6±2.9 (n=4)

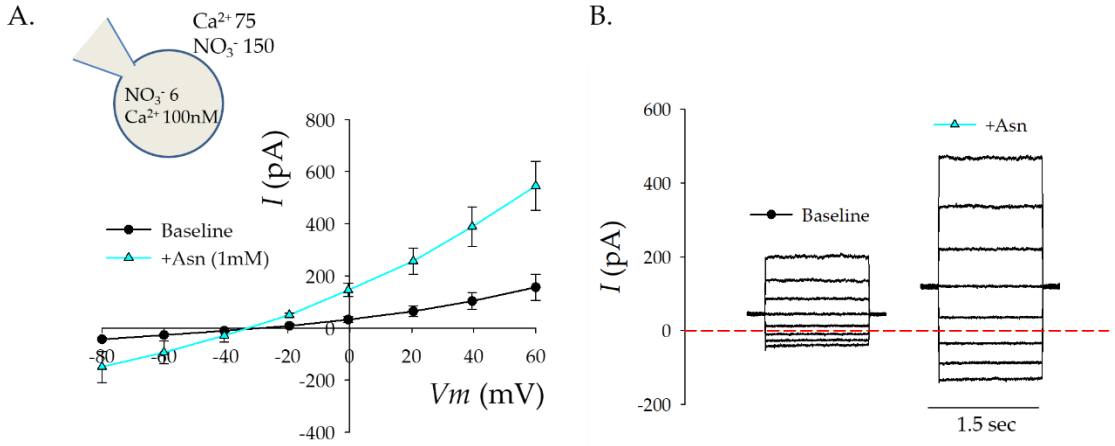

Figure 45: *At*GLR3.4 mediated NO_3^- currents are potentiated by Asn. A.) *I-V* curve obtained from whole-cell patch clamp on *At*GLR3.4 + *At*CNIH1 / 4 co-transfected COS-7 cells before (black, circles) and after the addition of Asn (1mM) (cyan, triangles), n=3. B.) Representative current traces corresponding to *I-V* curve shown in A. Major charge carriers are indicated in the panel A inset. Voltage step protocol used consisted of 1.5sec test pulses from -80mV to +60mV in +20mV steps, with a holding potential of 0mV. *I designed the experiment. Juan Barbosa-Caro and I performed the experiment.*

*Pp*GLR1$_{SWAP}$ lends a gain-of-function in ligand gating

Returning to test the hypothesis that molecular properties outside the LBD could play an active role in channel gating, *Pp*GLR1$_{SWAP}$ emerged as a prime candidate. The hypothesis that the pore may be a gate stemmed from the impact permeable ions played on whole-cell current amplitudes —particularly through two mechanisms typically independent of ligand binding in the extracellular domain, the effect Ca^{2+} dependent inhibition and hyperpolarization inactivated currents. Under the asymmetric $NaNO_3$ ionic solutions used to verify the anion selectivity of *Pp*GLR1 and the new Na^+ permeability of *Pp*GLR1$_{SWAP}$, ACC was also administered to evaluate if the ligand gating was altered or ligand-induced current composition was any different than the background current. These ion conditions mimic the chemical gradients of physiological conditions where there is anion efflux and Ca^{2+} influx. When patched directly in asymmetric $NaNO_3$ solutions, *Pp*GLR1 displayed small current amplitudes, and ACC marginally potentiated an inward current compared to empty vector control cells (pCI). ACC did not affect outward currents on either *Pp*GLR1 or pCI transfected cells. (Figure 46A, Figure 47). *Pp*GLR1$_{SWAP}$ demonstrated large steady-state background currents and were further potentiated by ACC, demonstrating a gain-of-function for ligand-gating (Figure 46B). Particularly relevant was the outward current measured, which under our conditions is primarily carried by Na^+, confirming that the ion selectivity had been altered by swapping the selectivity filter (Figure 47). Under these experimental conditions, the ACC evoked current potentiation achieved a steady-state level in 4.3 ± 0.36min (Figure 46C). Overall, *Pp*GLR1$_{SWAP}$ conserved the plant GLR gating feature that is characterized by a

background activity in the absence of ligand. But, its ligand-gating was strengthened by the change in pore composition (Figure 46).

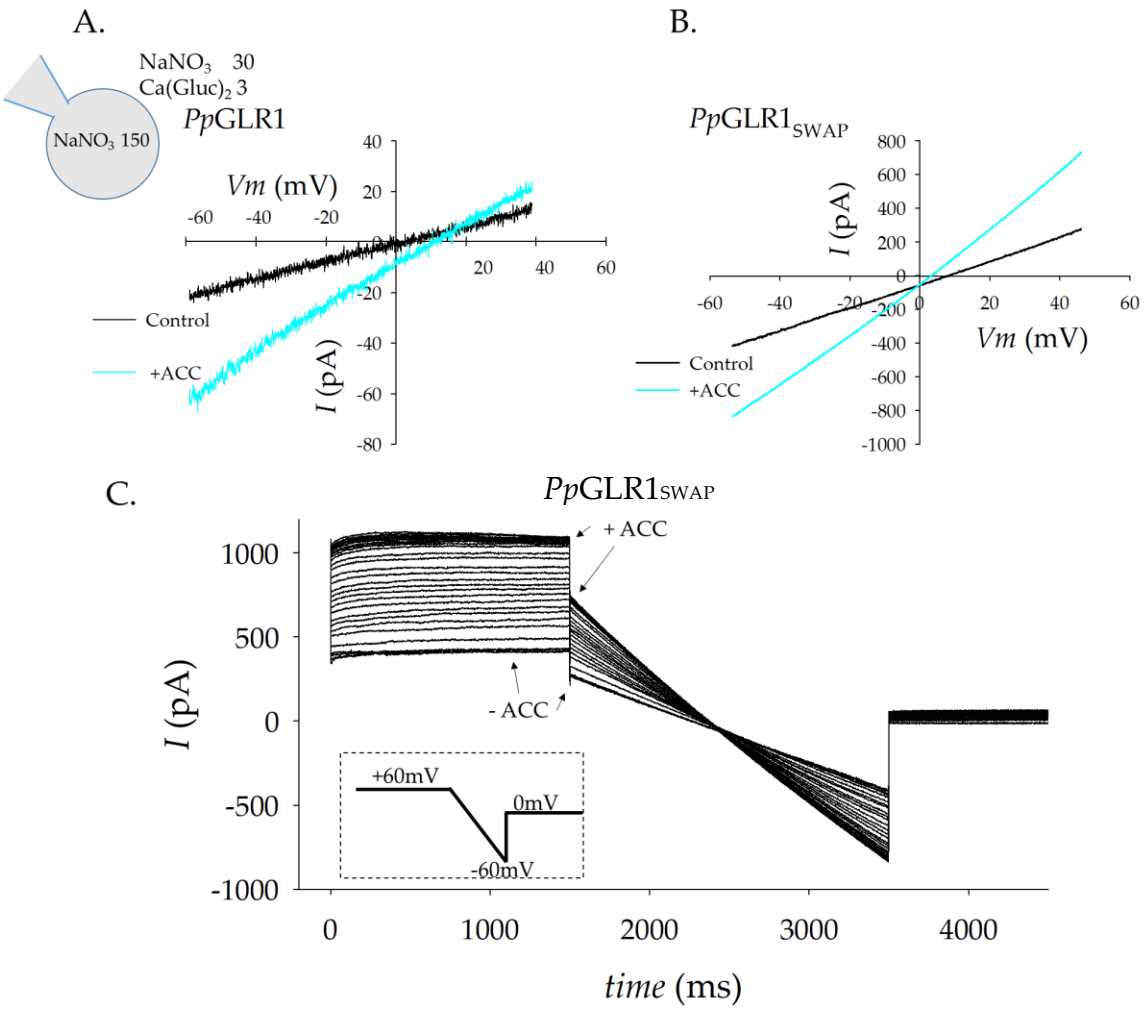

Figure 46: *Pp*GLR1$_{SWAP}$ demonstrates a gain-of-function in ligand-gating. A.) and B.) Representative ramp traces from *Pp*GLR1 or *Pp*GLR1$_{SWAP}$ expressing COS-7 cells obtained from whole-cell patch clamp plotted as *I-V* curve upon perfusion of ACC (500μM). C.) Representative current trace illustrating potentiation kinetics of ACC induced currents from *Pp*GLR1$_{SWAP}$. Data in all panels was collected from voltage ramps applying a 1.5sec pulse of +60mV before ramping from +60mV to -60mV over 2sec. Ramps were repeated every 15sec, in the meantime, cells were reset to a holding potential of 0mV. Inset of panel C illustrates the voltage protocol used. Experiments utilized solution set S19 (major charge carriers prior to dilution are illustrated in panel A inset).

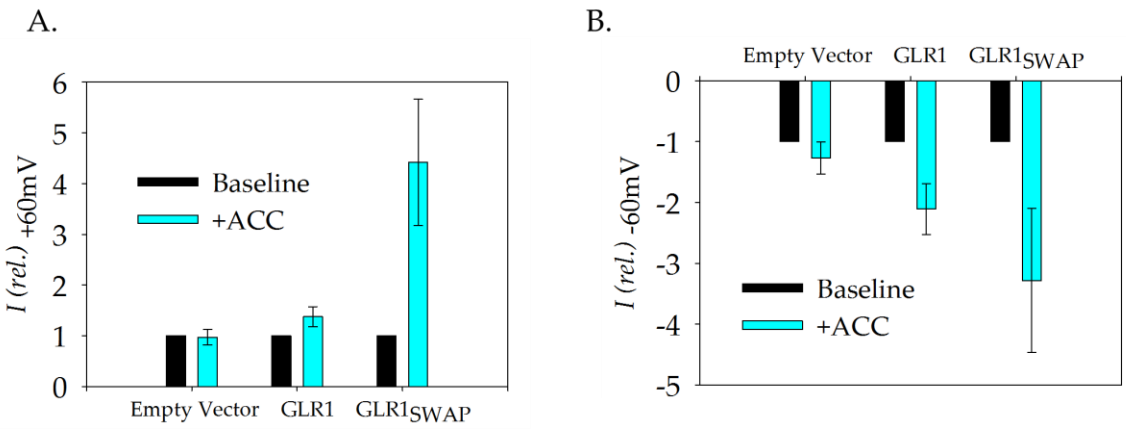

Figure 47: Summary of ACC-potentiation currents at -60mV and +60mV from empty vector control cells, *Pp*GLR1, and *Pp*GLR1$_{SWAP}$. A.) Average relative current increases recorded at +60mV. B.) Average relative current increases recorded at -60mV. Experiments utilized solution set S19. Error bars indicate SE. At both voltages, empty vector, n=6; *Pp*GLR1, n=4; *Pp*GLR1$_{SWAP}$, n=5.

Part 6: *At*GLR3.2 LBD structure determination

Copyright Notice:

Figures 48 and 49 are reproduced from Gangwar *et al.*, 2020.

Gangwar SP , Green MN , Michard E, Simon AA, Feijó JA, Sobolevsky AI. (2020). The Structure of the Arabidopsis Glutamate Receptor, GLR 3.2, Ligand-Binding Domain. **Structure**, 28:1-9.

The plant GLR LBD's molecular properties were further addressed in structure determination efforts purifying the *At*GLR3.2 LBD. In fact, purified LBDs of both *At*GLR3.2 , as well as the recently published *At*GLR3.3(274), showed a core amino acid pocket that coordinated binding of amino acids. In the case of the *At*GLR3.3, the same seven ligand – LBD residue interactions coordinated the binding of Glu, Gly, Met, and Cys. The sulfur containing ligands, Cys and Met, took advantage of additional interactions yielding a higher binding affinity over Glu and Gly(274).

X-ray crystallography of *At*GLR3.2 LBDs

The structure of *At*GLR3.2 elaborated on the structural mechanism underlying the apparent promiscuity of ligand binding by analyzing LBDs bound to Met or Gly (Figure 48 B,C)(273). Crystalized *At*GLR3.2 LBDs showed the conserved Arg (at position 133 of the purified LBD used for structure determination in Figure 48, or position 551 in the full-length protein used for electrophysiological experiments in Figure 49)— the corresponding to the residue mutated in *Pp*GLR1(Figure 48D)— interacted with both amino acids successfully bound in complex with the LBD (Met and Gly) (Figure 48) (273). Here, the guanidinium group of the conserved Arg133 in upper lobe formed two hydrogen bonds with the ligand. The backbone amines of Ala128 and Tyr178 also hydrogen bonded to the ligand's carboxyl group, while the backbone carbonyl oxygen of Asp126, the carboxyl group of Glu218, and the hydroxyl group of Tyr221 coordinated the ligand's amino group. (Figure 48 B,C). The thioether group of methionine brought specificity to methionine binding through additional coordination by the hydroxyl group of Tyr221, the guanidinium group of Arg57, and the amide group of Gln174 (Figure 48 C). These interactions with the thioether group are missing in the case of glycine, which lacks the bulky side chain(273). While a core set of LBD residues coordinated both Met and Gly binding through the amino and amide groups, the smaller R-group of Gly (only consisting of a hydrogen atom) fit into the same binding pocket as Met (with a bulky R-group) with the help of water molecules to fill excess space (Figure 48 B).

In addition to being a functional amino acid binding pocket, the *At*GLR3.2 LBD was always found in the closed clamshell configuration bound by Met or Gly. The absence of an open clamshell configuration shows a structural comprehension of ligand

binding, and functional ligand-gating, of GLRs remains limited —albeit rapidly growing— and makes *At*GLR3.2 an informative target to test hypothesizes on ligand-gating (Figure 48A). Replicating the same Arg mutation in *At*GLR3.2 (R551A) as performed in *Pp*GLR1 (R556A),(Figure 23) resulted in a similar observation in that the ligand potency was altered (Figure 49). Curiously, Ca^{2+} imaging in COS-7 cells showed cytosolic Ca^{2+} levels without stimulation by any ligand were higher in *At*GLR3.2 (R551A) mutant compared to the non-mutated channel. Adding Met or Gly to the *At*GLR3.2 (R551A) then resulted in a lower elevation of $[Ca^{2+}]cyt$ (Figure 49). This suggests Met or Gly could seemingly still bind to the receptor, but with a different effect.

The interpretation available from synthesizing the results of *Pp*GLR1 and *At*GLR3.2 for appreciating the larger context of ligand-gating in plant GLRs is expanded upon in the discussion section (pg. 117).

A.

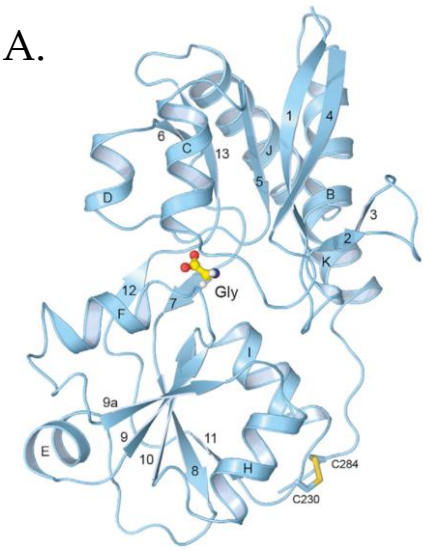

Figure 48. *At*GLR3.2 ligand-binding domain structure. A) Crystal structures of isolated *At*GLR3.2 LBD (S1S2) in complex with glycine adopts a bilobed clamshell configuration (PDB: 6VEA). Glycine is in ball-and-stick representation. Highly conserved cysteines, C230 and C284, are connected by disulfide bonds and shown in sticks. B-C) Close-up views of the ligand-binding pocket with bound glycine PDB: 6VEA (B) and methionine (PDB: 6VE8) (C). Residues involved in ligand binding are shown in sticks. Water molecules in B are illustrated as green balls. Interactions between the ligands and the binding pocket residues are indicated by dashed lines. D.) Alignment of S1 segment of *Pp*GLR1 and *At*GLR of clade 3 using amino acid position of the full length protein. *Gangwar SP, Green MN, and Sobolevsky AI performed the protein purification and structure determination.*

B.

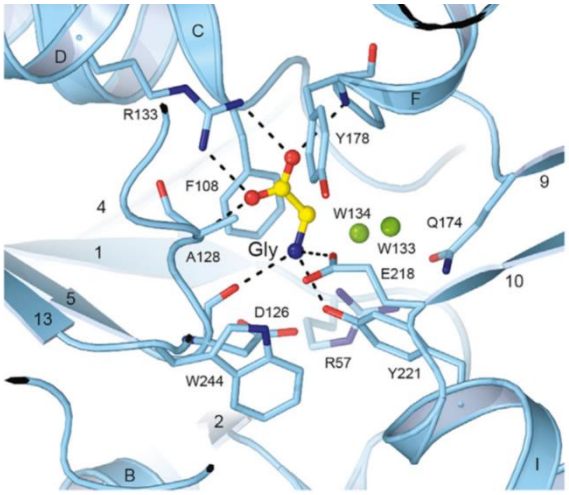

C.

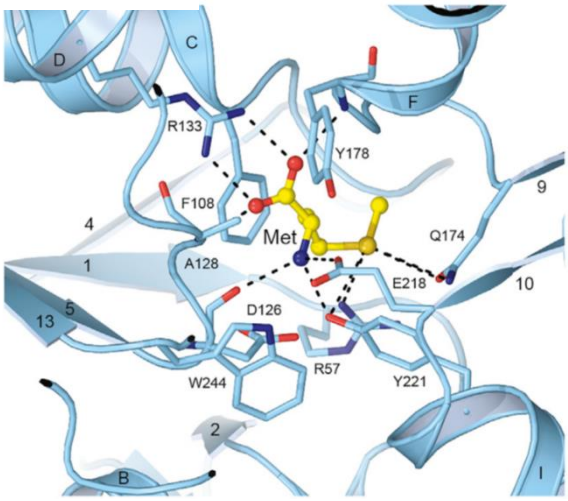

D.

S1

```
PpGLR1    PLVIGVPNRVGYKEFVESSVDSNNRTAFRGFCIDVFQQALSNLPYAVSYYFTSFGDGNSTPSYDALVDEIAEKK-FDAVVGDVTITTKRSMSVDFTQPFTTSGLVVVVPV 576
AtGLR3.1  RLRIGVPDRASFKDFVSRVN--GSSNKVQGYCIDVFEAAVKLLSYPVPHEFIFFGDGLTNPNYNELVNKVTTGVDFDAVVGDIAIVTKRTRIVDFTQPYIESGLVVVAPV 602
AtGLR3.2  RLRIGVPDRASFKEFVSRLD--GS-NKVQGYAIDVFEAAVKLISYPVPHEFVLFGDGLKNPNFNEFVNNVTTGV-FDAVVGDIAIVTKRTRIVDFTQPYIESGLVVVAPV 572
AtGLR3.3  ELKIGVPLRVSYKEFVSQIR--GTENMFKGFCIDVFTAAVNLLPYAVPVKFIPYGNGKENPSYTHMVEMITTGN-FDGVVGDVAIVTNRTKIVDFTQPYAASGLVVVAPF 571
AtGLR3.4  PLRIGVPNRVSYTDYVSKDK--N-PPGVRGYCIDVFEAAIELLPYPVPRTYILYGDGKRNPSYDNLVNEVVADN-FDVAVGDITIVTNRTRYVDFTQPFIESGLVVVAPV 598
AtGLR3.5  PLKIGVPNRVSYKNYASKDK--N-PLGVKGFCIDIFEAAIQLLPYPVPRTYILYGDGKKNPSYDNLISEVAANI-FDVAVGDVTIITNRTKFVDFTQPFIESGLVVPSSG 586
AtGLR3.6  HLRIGVPNRYRFEEVVSV----KSNGMITGFCVDVFIAAINLLPYAVPFELVAFGNGHDNPSNSELVRLITTGV-YDAGVGDITITTFRTKMADFTQPYVESGLVVVAPV 561
AtGLR3.7  PLVIGVPNRVGYKEFVESSVDSNNRTAFQGFCIDVFIEALKFVPYSVPYIFEPFGNGHSSPNYNHLIQMVTDGV-YDAAVGDIAIVPSRSKLVDFSQPYASTGLVVVIPA 564
```

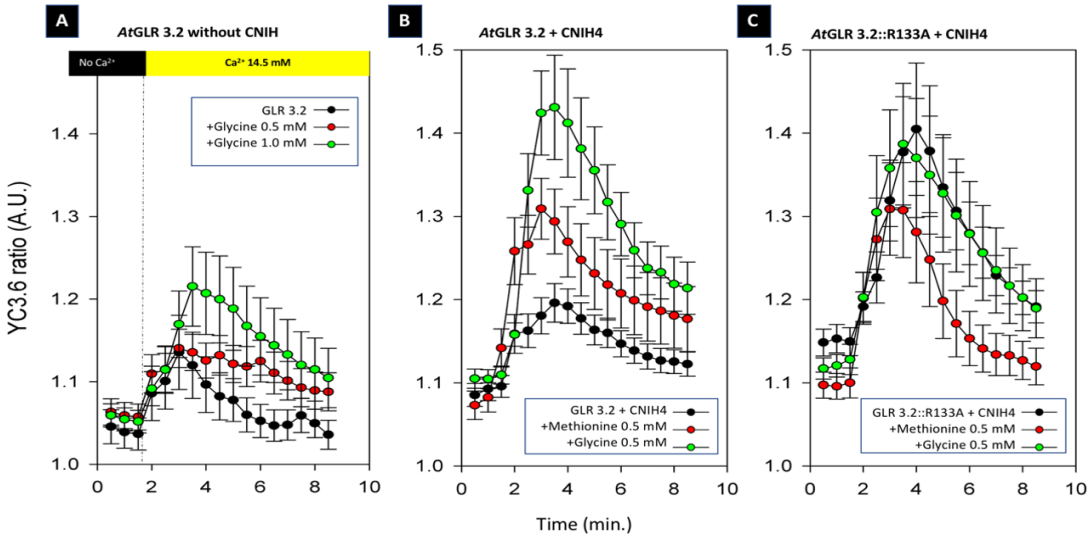

Figure 49. **Effect of a point mutation in ligand gating of *At*GLR3.2.** The effect of a point mutation,R133A, (R551A in full length structure) in the LBD on *At*GLR3.2 channel gating was assayed by the transfection of mammalian COS-7 cells expressing a Ca^{2+} indicator (YC3.6). **A**, Expression of wild-type channel alone, shows its Ca^{2+} conductance to be gated by Glycine (Gly) at 1.0 mM. The experimental sequence is shown on the top black/yellows bar. Cells are Ca^{2+}-starved with EGTA and then perfused with 14.5 mM Ca^{2+}. In the absence of ligand (black dots) a slight increase occurs in $[Ca^{2+}]$cyt. When the experiment is done in the presence 0.5 mM Gly, this elevation is slightly, but significantly, prolonged ($p<0.01$), but in the presence of 1.0 mM Gly there is a visible and statistical significant elevation of $[Ca^{2+}]$cyt ($p<10^{-6}$ to control and $p=0.01$ to 0.5 mM). **B**, Simultaneous expression of *At*GLR3.2 and *At*CNIH4 renders the channel gated by both Met (red) and Gly (green) at 0.5 mM in comparison to the control ($p<0.01$ for all comparisons). However, when the critical residue 133 is substituted from Arginine to Alanine (**C**) the channel behaves as being constitutively open (black; compare with black control in **B**) (All statistics obtained by two-way ANOVA with TukeyHSD). *Michard E and I designed the experiment. Michard E performed the Ca^{2+} imaging. I completed the targeted mutagenesis.*

Outlook on gating properties

The appearance of two prominent gating modes in GLRs in the form of a background current and ligand potentiated current is not entirely a consequence of a gating mechanism dependent on the pore— since *Pp*GLR1$_{SWAP}$ also displays a background current— nor can it be solely dependent on the LBD if only one structural

conformation can be captured. Thus, the connections between structural domains may play a role in ion conduction remains elusive for the moment necessitating structure determination studies encapsulating four structural layers of glutamate receptors; TMD, LBD, ATD, and C-terminus would be necessary to appreciate the causal relationships between functional units. Beyond what could be resolved in this present thesis, several additional parameters require further attention to appreciate GLR gating. The role of the gate domain is among the primary candidates. In fact the gate motif comprises the most highly conserved portion of the GLR and iGluR sequences (300). Another parameter is the linkers connecting the LBD to the TMD.

The gate of glutamate receptors is known to form the upper portion of the ion conduction pathway as well as to link the opening of the pore to the receptor (229). The third transmembrane region, M3, forms a gate, and a polypeptide linker connects M3 to the LBD. A highly conserved SYTANLAAF motif in every iGluR, sometimes referred to as the lurcher motif, characterizes this gate. A helical bundle crossing and a largely hydrophobic patch are two properties of this motif that have garnered the most attention. On the cell membrane's external side, the SYTANLAAF motif forms helical bundle crossing that in a resting channel occludes the ion pathway to the pore(204). The amino acids with hydrophobic side chains (Y, A, L, A, A, F) comprise the hydrophobic patch. During iGluR gating, the critical action taking place occurs as the LBD clamshells move and exert a strain on the helical bundle crossing to splay open the entrance to the pore.

Mutagenesis within the hydrophobic patch of the gate motif has greatly advanced various hypotheses regarding the structure-function of the gate. Namely, the lurcher

mutant for which motif bears the name, converting the third Ala to a Thr, has become a widely referenced model for glutamate receptor function. Mice heterozygous for the lurcher allele experienced Purkinje cell death during postnatal developed while homozygous mice died shortly after birth. In electrophysiological experiments, the lurcher mutant resulted in a constitutively open channel (301). The mutant gating properties are proposed to result from an enhanced ligand sensitivity where contamination conditions activate the channel. Remarkably, altering the gate changes the nature of the ligand as to whether it is an agonist or antagonist. In this mutant, CNQX can activate currents, while Gly and D-Ser inactivate currents (302–304). Above all, this switch in pharmacological action points toward the suggestion that ligand gating properties encompass more than clamshell closure.

In plants, the low conservation in the SYTANLAAF motif has raised hypothesizes that a constitutively active channel may be predicted(300, 305). Preliminary experiments tested this mutation by mimicking the conserved motif in *At*GLR1.2. The mutant channel bearing the entire SYTANLAAF motif still presented a background current, unresponsive to the amino acid D-Ser (the expected ligand for this channel(72)), but blocked by Gd^{3+} suggesting a background current is still a channel feature independent of the SYTANLAAF motif (Figure 50).

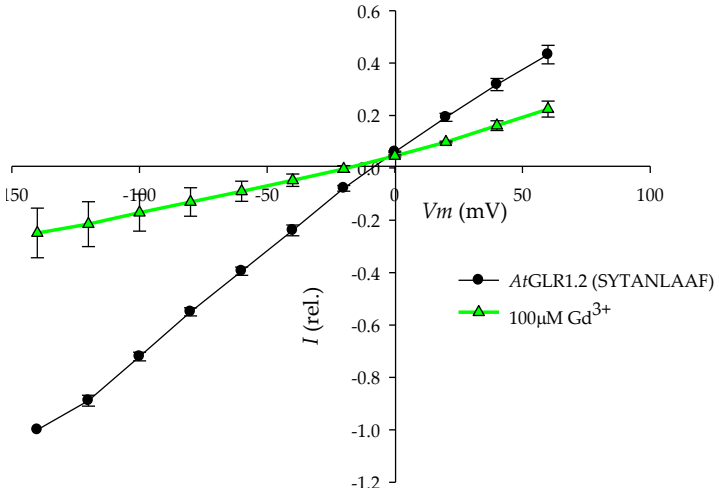

Figure 50: *I-V* curve of *At*GLR1.2 (SYTANLAAF) currents expressed in COS-7 cells. *At*GLR1.2 mutagenized in the gate domain shows a background currents and is inhibited by Gd^{3+} 100µM (n=2).

Located peripheral to the LBD, the S2-TMD linkers are active components of the gating process that work to communicate LBD movement to the TMD. In AMPARs, M3-S2 electrostatics play a role in adopting a unique configuration between closed and desensitized states(306). In NMDAR, mutagenesis studies constraining M3-S2, M4-S2 and pre-M1 linkers dramatically reduced ion channel open probability in an inter- and intrasubunit specific manner(307, 308). Characteristics of these linkers in plant GLRs have yet to be explored.

Supplemental Figures

Supplemental Table 1: *Vrevs* measured from *Pp*GLR1 expressing COS-7 cells loaded with different internal NO_3^- concentrations compared to ENO_3^-. $|\Delta|$ is calculated to equal the absolute difference in the predicted ENO_3^- and the *Vrev*.

Internal $[NO_3^-]$ mM	Bath $[NO_3^-]$ mM	Internal $[Ca^{2+}]$ nM	Bath $[Ca^{2+}]$ mM	E_{NO3-} (mV)	*Vrev* (mV)	$\|\Delta\|$ (mV)	n
6	150	100	75	-81.2	-28.3 ±2	52.9	28
50	150	100	75	-27.7	-23.2 ±4	4.5	5

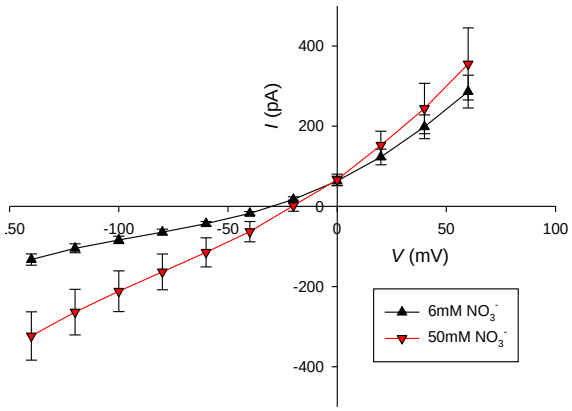

Supplemental Figure 1: Effect of internal anion concentration on *Vrev*. *I-V* curve from obtained from whole-cell patch clamp on *Pp*GLR1 expressing COS-7 loaded with different internal NO_3^- concentrations 6mM corresponding to solution set S9 (black, upwards-triangle) or 50mM corresponding to S14 (red, down facing triangles), and the same external solution consisting of 75mM Ca^{2+} and 150mM NO_3^-.

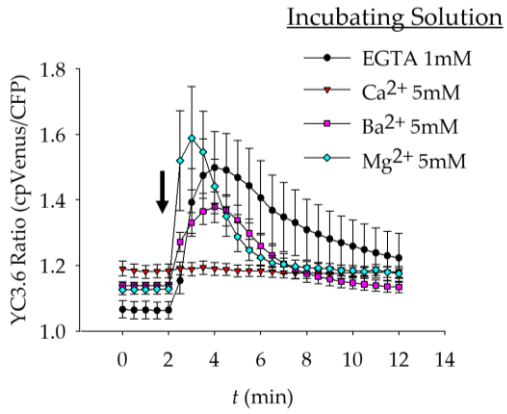

Supplemental Figure 2: Ca^{2+} dependent inhibition demonstrated in Ca^{2+} imaging by YC3.6. Incubation of *Pp*GLR1 expressing COS-7 cells with Ca^{2+} (5mM, n=17), but not EGTA (1mM, n=11), Mg^{2+} (5mM, n=11), or Ba^{2+} (5mM, n=14), prevents an elevation of $[Ca^{2+}]$cyt by successive Ca^{2+} (14.5mM) treatment. Error bars represent SE.

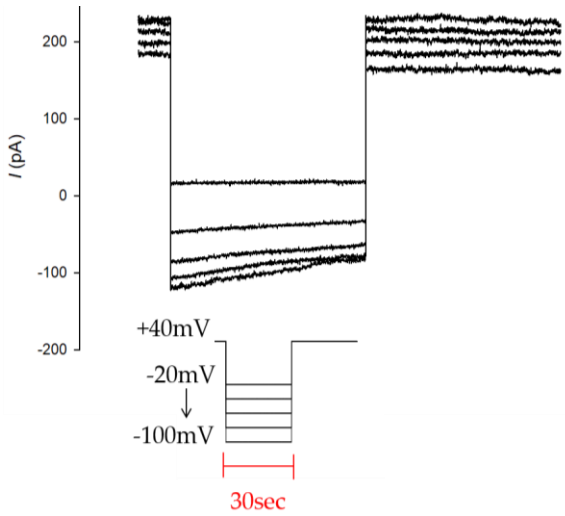

Supplemental Figure 3: Representative current trace depicting *Pp*GLR1 currents that display a slow and irreversible rundown of the steady-state currents upon hyperpolarizing the membrane. *Pp*GLR1 expressing COS-7 cells were clamped to a holding potential of +40mV and stepped the membrane voltage from -20mV to -100mV in -20mV increments. 30sec exposures from -40mV to -100mV (all hyperpolarized to the *Vrev*) lowered the steady-state current. Data generated in solution set S13.

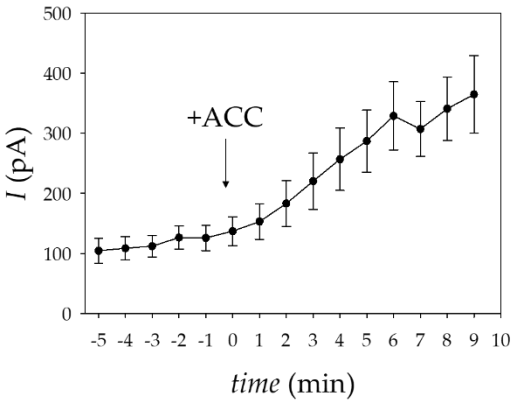

Supplemental Figure 4: Average time course of ACC potentiation. *Pp*GLR1 expressing COS-7 cells were clamped to a holding potential of +40mV and applied 500mM ACC (n=13). Error bars represent SE. Experiments were performed in solution set S13.

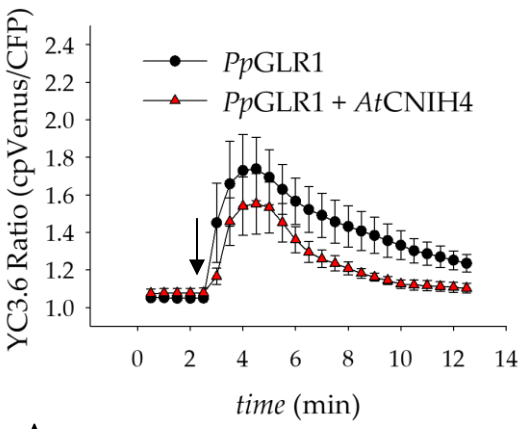

Supplemental Figure 5: Elevations in $[Ca^{2+}]$cyt mediated by *Pp*GLR1 are independent of *At*CNIH4 expression. YC3.6 reported $[Ca^{2+}]$cyt elevations induced by Glu (1mM) in *Pp*GLR1 expressing cells (n=8) and *Pp*GLR1 transfected cells co-expressing *At*CNIH4 (n=7). Arrow indicates time of Ca^{2+} (14.5mM) application. Glu was pre-incubated for the duration of the experiment. Error bars represent SE.

A.

B.

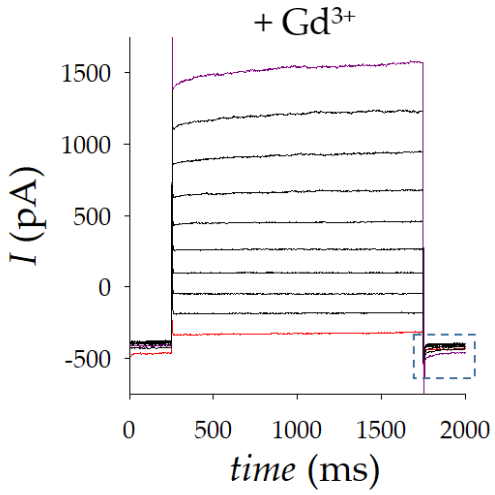

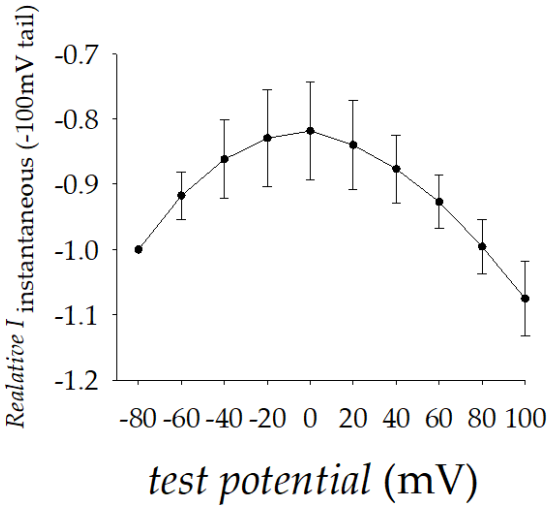

C.

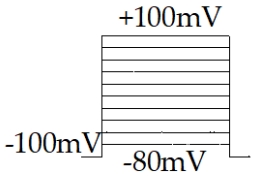

Supplemental Figure 6: Voltage dependency of Gd^{3+}. A.) Example current trace from a *Pp*GLR1 expressing COS-7 cell in solution set S9 + 1mM Gd^{3+}. B.) Tail currents designated in dashed box from A are plotted in relative current amplitude (n=4). C.) Voltage protocol imposed; cells were stepped from -80mV to +100mV in +20mV increments. Each voltage step (test potential) lasted 1.5sec. A holding potential of -100mV was imposed for 0.25sec before and after each test pulse.

Chapter 3 Discussion

Summary

Plant GLRs are differentiated from their mammalian counterparts by non-canonical ligand gating properties and ion selectivity. This thesis has dissected certain ion channel properties of *Pp*GLR1 and proposes evolutionary conservations of function between glutamate receptors encoded in the genomes of *P.patens, Arabidopsis,* and also mammals.

The quantity of coding sequences encoding Glutamate Receptor –Like genes (GLRs) has greatly expanded along the succession of land plants. The moss *P.patens*— representative of the bryophytes— encodes only two genes while *Arabidopsis thaliana*— the model flowering plant— encodes twenty genes. This expansion in the quantity of genes coincides with a functional diversification in which *At*GLRs are obligatory heteromers and display channel gating properties along a wide spectrum from being constitutively active to highly responsive to exogenous amino acids (Unpublished, Erwan Michard). To address the functional diversification of *At*GLRs, I turned to *Pp*GLR1 as it is exclusively expressed as the sole glutamate receptor in the vegetative tissue of *P.patens* and is a functional homomeric ion channel with a role in light-signal transduction. This result has broad implications to plant GLRs as it points out a conservation of function at the physiological level between a single homomeric ion channel and a biophysically diversified group of twenty channels. *Pp*GLR1's function as a physiological homomeric ion channel permitted a basic characterization then afforded the ability to map the

attributes CORNICHON homolog proteins (CNIHs) add to the channel, and finally investigate the structure-function relations without compounding, and potentially uninformative, variables.

Despite possessing a homologous ligand binding domain to iGluRs, *Pp*GLR1 demonstrated a palette of amino acids and peptides that outperformed Glu in Ca^{2+} imaging experiments evaluating the effectiveness of potential ligands and allosteric regulators. Other standard amino acids were also identified as agonists and antagonists. The most effective agonist determined by Ca^{2+} imaging was ACC. An effect confirmed by whole-cell patch clamp finding ACC reliably modulated the current amplitude in *Pp*GLR1 expressing COS-7 cells and moss protoplasts. Mutagenesis of a highly conserved residue (R556) in the ligand binding domain —known to enable ligand binding— disrupted the ligand-gating function of *Pp*GLR1 in COS-7 cells, demonstrating a ligand gating characteristic of the channel. The mutation also left a basal activity of the ion channel unaffected, opening further questions about whether ligand binding is the primary channel gating feature. ACC indeed evoked a gating response, but stimuli in the transmembrane domain, including the extracellular Ca^{2+} concentrations and membrane voltage, show an ability to exert strong governing roles on ion permeation. We also reveal that CNIHs have a conserved role during glutamate receptor gating as both *Pp*CNIH and *At*CNIH amplify *Pp*GLR1 current.

Reconciling that glutamate receptor's homology is based on a conserved amino acid binding pocket, we demonstrated that the pore confers distinctive biophysical properties to plant GLRs not observed in iGluRs. Through ion selectivity experiments

and targeted mutagenesis of the pore, we demonstrated it bestows an anion permeability and is a direct player governing channel gating. Mutagenesis of the pore increased the relative cation permeability and allowed for ACC-gated cation currents under conditions where the wild-type *Pp*GLR1was unresponsive to ACC.

Two *At*GLRs investigated, *At*GLR3.2 and *At*GLR3.4, which both require co-expression of *At*CNIH proteins to form functional ion channels, represent the bookends of the gating spectrum. *At*GLR3.2 is a constitutively active channel demonstrating a background current, and *At*GLR3.4 is ligand-gated being silent prior to perfusion of amino acids. However, both ion channels show a high anion permeability demonstrating the ion permeability is the main channel property conserved from *P.patens* to *Arabidopsis.*

Autophagy's relation to membrane transport

Autophagy is a highly conserved catabolic process based on the principal ATG-related genes needed for bulk degradation and recycling of intracellular material. In plants, unwanted cytoplasmic content is engulfed by a lipid membrane that seals off to form an enclosed structure, called the autophagosome, and is delivered to the vacuole to be broken down. Autophagy processes occur at basal levels essential to cellular homeostasis and development, but activity can also be enhanced by abiotic stress to use carbon and nitrogen reserves(309). Under these stress conditions, autophagy is known to degrade chloroplasts(309, 310). The evaluation of a GLR related role in senescence provides an experimental setup for future studies into the molecular mechanism of

autophagy and, more generally, the plant's adaptation to the dark. To the best of my knowledge, no plant ion channel has been directly linked to autophagy processes.

In mammals, autophagy is known to have roles associated with sexual reproduction, but also aging and neurodegeneration, among others (311, 312). For these roles, autophagy requires highly intricate Ca^{2+} signaling networks set off by Ca^{2+} transport through IP_3R, Ca_vs, TRPs, and iGluRs(313–318). A variety of other ion channel classifications — including K^+, Cl^-, and Na^+ channels — also have regulatory roles in autophagy in all stages of the autophagic process. The integration of ion signaling remains an undeveloped area of research(319). iGluR involvement of autophagy is a special case because only a channel mutant— known as the lurcher mutant ($GluR\delta2^{LC}$)— which in mice leads to pronounced neurodegeneration from Purkinje cell death in the cerebellum(301, 320) is responsible for autophagy. Electrophysiology recordings showed $GluR\delta2^{LC}$ — which harbors a single point mutation in the gate motif — renders the channel constitutively open. Therefore, the hyperactivity of the channel possibly activates the autophagy pathway. The relation autophagy to membrane excitability through the command of membrane potential and Ca^{2+} signaling provided a rationale to investigate the biophysical properties of GLRs to a greater extent, which becomes the main thesis in its evolutionary context.

Plant GLRs have a conserved role in light-signal transduction.

By identifying a light-signal transduction phenotype with a homomeric GLR from *P.patens,* we find a physiological conservation of function wrapped inside the functional

diversification that occurs with the evolution of land plants. We can now expect the characterization of *Pp*GLR1 to inform on hypothesizes of angiosperm GLRs. When plant GLRs were discovered in *Arabidopsis*' genome, they were phenotypically characterized by impaired light-signal transduction. *Arabidopsis* seedlings treated with the iGluR antagonist DNQX (6,7-dinitroquinoxaline-2,3-dione) showed elongated hypocotyls and a loss of chlorophyll (155). Additional pharmacological studies supported a link between *At*GLRs and light-signal transduction. For example, the Glu analog BMAA [S(1)-β-methyl-α, β-diaminopropionic acid] —known to be an agonist for NMDARs(321) and neurotoxin associated with Amyotrophic Lateral Sclerosis (ALS) and dementia— found in the seeds of the false sago palm tree (*Cycas circinalis*) also caused an elongation of *Arabidopsis* hypocotyls that was reversible by L-Glu when plants were growing in the light (322, 323). However, BMAA inhibited hypocotyl length on dark grown seedlings implicating a light-specific response. Genetic screens searching for BMAA insensitive mutants discovered a mutation on another protein, Proteosomal Regulatory Particle AAA-ATPase-3 known to be involved in protein degradation(324).

Light and dark regimes have a pronounced effect on Ca^{2+} homeostasis with the current model of light mediated Ca^{2+} signaling postulating that under light conditions the chloroplasts are loaded with Ca^{2+} and discharge it into the cytosol upon transition to the dark, triggering cytosolic-based signaling cascades(325). Besides Ca^{2+}, a plant cell's oxidative status also undergoes a considerable shift under photosynthetic regimes that can impact cell signaling. Specifically in *P.patens,* glutathione (GSH) was found to be essential for redox homeostasis, and GSH availability was highly responsive to light. The

responsiveness of GSH was even pinned to the cell's photosynthetic status related to electron transport chain efficiency. Interestingly, the light to dark transition had an oxidizing effect in chloroplast stroma over the time range of minutes. Over a long-term exposure of 44 days in the dark, *glutathione reductase* gene knockout plants showed complete senescence, but plants were viable upon light recovery(326). A similar result to the observed dark treated *glr1* plants. The hypothesis that GSH and *Pp*GLR1 can interact was challenged relative to other plausible channel modulators where GSH was evaluated to be an effective agonist of channel activity (Chapter 2 part 3; Figure 21). The relationship between GSH and *Pp*GLR1 opens the door to explore both oxidative stress in plants as well as its potential relationship to autophagy.

Possible roles of experimental ligands

Several of the identified *Pp*GLR1 ligands may have potential physiological roles related to channel activity or help decipher channel function. The GSH concentration in the *P.patens* gametophore is known to be highly responsive to alternating light-dark conditions (326). Also known to activate iGluRs, GSH is a neuromodulator in the central nervous system, technically considered an antagonist. It is able to displace Glu binding by sharing a binding site with the agonist creating a dose dependent activation or inhibition (327, 328). Interestingly, GSH has two roles on iGluRs. It is a ligand that is able to bind to the extracellular receptor, but also has reducing functions where it is an important antioxidant buffering reactive oxygen species. The antioxidant properties are

highly conserved in plants and found to be involved in Ca^{2+} signaling(267, 329, 330). To ask if a reducing function of GSH on *Pp*GLR1 is sufficient to elevate [Ca^{2+}]cyt, I also checked if DTT could perform similarly. DTT is a common chemical reducing agent and is not expected to undergo binding to the receptor. Known to potentiate Glu/Gly activations of NMDARs, DTT reduces extracellular cysteine residues(331, 332). DTT's ability to elevate [Ca^{2+}]cyt suggests GLRs may be involved in sensing the oxidative environment, thereby expanding the extracellular receptor's potential sensing roles. ACC was the most potent ligand in elevating [Ca^{2+}]cyt. ACC is not known to be synthesized in mammalian tissues but is a partial agonist at the Gly/D-Ser site of NMDARs(294, 333, 334). On the other hand, in plants, ACC is a precursor in the synthesis of the central plant hormone ethylene(335). ACC has been long used to gauge ethylene-specific responses due to ACC's rapid conversion to ethylene, both spontaneously and by ACC OXIDASE proteins. Importantly, a function for ACC signaling was found in the ovular sporophytic tissue and involved in pollen tube attraction associated with Ca^{2+} signaling (336). Identifying an ACC-specific signal—acting through GLRs— raises the point that the meaning of GLR-ligand interaction has a specificity in physiological function. As a non-proteinogenic amino acid, the effectiveness of ACC promotes the discussion if the most physiologically relevant ligands exist in a new class beyond the standard twenty amino acids. The effectiveness of GSH (as well as GSSG and DTT) also show allosteric modulation is an important parameter regulating GLRs. Intriguingly, all three potent effectors on GLR mediated Ca^{2+} responses (ACC, GSH, and DTT) are found under reduced conditions of low oxidative stress.

The genetic dissection of ACC revealed that *Arabidopsis* plants with an octuple knockout mutant of *ACC synthase genes (acs)* displayed a reduced seed set as a consequence of impaired pollen tube attraction(336). In clever semi-in vivo assays, *acs* octuple mutant plants failed to attract pollen tubes toward the ovule. Pollen tube attraction could be rescued by exogenous application of ACC to mutant ovules illustrating an ACC signaling function. Although ACC was not found to be a chemoattractant itself, ACC promoted the secretion of the LURE1.2 peptide which is sufficient for chemoattraction(336),(337). Promotion of LURE1.2 secretion by ACC could also be performed in an *ein2* mutant line that disrupts the ethylene signal transduction pathways, showing ACC signaling was independent of ethylene signaling.

The other identified agonists may also inform on the channel function and physiological roles. The amino acid His has not been considered as a signaling amino acid directly related to Ca^{2+} or electrical signaling. It is generally known for roles in plant growth and development such that *Arabidopsis* plants defective in His synthesis experience aborted seeds(338). His is also unique among amino acids for a role in acid-base catalysis due to a pKa=6, permitting it to alternate between protonated and unprotonated states around physiological conditions. Intriguingly, His is transported across the plasma membrane by the Lysine Histidine Transporter 1 (LHT1). LHT1 also has an affinity to transport ACC (339). Whether LHT1 transport of His and ACC to the apoplast impacts GLR gating remains to be investigated. The action of oxidized GSSG, which is a dimer of two Glu-Gly-Cys tripeptides, complements the dual role of GSH as both a ligand and a reducing agent. As a DTT potentiation of $[Ca^{2+}]$cyt likely indicates a

reducing action on disulfide bonds in the extracellular receptor, the effect of GSSG suggests a ligand binding capacity of the tripeptide. Gly and D-Ser are mutually exclusive co-agonists that promote NMDAR activation, occupying one binding site. In addition to D-Ser being among the classical iGluR agonists, it also has an acknowledged physiological role in pollen tube growth(72). Recently, the structure of *At*GLR3.3 LBD revealed the possibility that D-Ser may fit into the amino acid binding pocket(274).

So far, the ligand profile for *Pp*GLR1 bears a resemblance to the profile of NMDARs given by the action of ACC, GSH, DTT, Glu, Gly, D-Ser, Phe, and Asp, which all work on both receptor families. However, the classic iGluR antagonists of CNQX (the AMPAR specific antagonist) and AP-5 (the NMDAR specific antagonist) inhibit similarly. Phe and Asp both present intriguing cases as receptor antagonists. Phe is a NMDAR antagonist(340), and Asp is also a known agonist of NMDARs.

It should be noted that the results of the ligand screening assay were intended to indicate the best ligands acting on *Pp*GLR1. We elected to use a competitive concentration of 500μM to identify the best ligands, not all the ligands. It is likely that some amino acids that elicited a small response at 500μM may be found to be clear agonists at higher concentrations.

Non-canonical ligand-gating

iGluR gating is indeed dependent on a mandatory ligand binding needed to close a clamshell-like LBD and open the ion channel pore. Still, clamshell closure alone does not directly indicate ion conduction. In other words, ligand binding to iGluRs does not

dictate a channel gating scenario analogous to an on-off situation. When adopting a resting configuration, known as the "apo" configuration, the receptor is free of Glu, and the clamshell-like LBD is fully open. Upon Glu binding, "holo" LBDs can adopt a pre-active state, partially closing the clamshell— but still leaving the pore occluded. With sufficient energy, the clamshell completely closes and drives either a conducting open channel or a non-conducting channel in a desensitized state as the LBD's flop and the pore collapses(215).

Structure determination of isolated GLR LBDs in the "holo" configuration indicates a similar closed clamshell-like LBD when bound to an amino acid that insinuates comparable channel gating models of GLRs and iGluRs(273). Mutagenesis of a conserved residue (R551A in *At*GLR3.2 and R556A in *Pp*GLR1) further suggests a common property in LBD associated actions in the channel gating. However, electrophysiological data incompatible with this interpretation — because of a constitutively active background current without exogenous ligands — indicates additional factors may be at play. Ligand regulation may even take on a different action. The *At*GLR binding affinity for several amino acids determined to be in the low to sub-micromolar range (ranging from 0.33μM to 5.5μM for Cys, Met, Glu, Ala, Asn, L-Ser, Gly as determined by thermophoresis) is also incompatible with the physiological amino acid concentrations found in the plant cell apoplast(273, 274). Estimations of Glu and other amino acid concentrations fall into the millimolar range, approximately the concentration needed to potentiate a macroscopic GLR current (256, 341). In some instances, apoplastic Glu found between 50mM and 100mM at wounding sites was

speculated to be needed for signaling(117, 342). Therefore, it could be surmised that GLRs are forced into a complete ligand-binding domain occupancy state, jeopardizing the physiological relevance of a dynamic or fast amino acid-gating quintessential of iGluRs. Taken together, a GLR ligand-gating function does not fit the classical iGluR-like model. It is worth noting that in our experiments and those of Tapken *et al.,* (2013) and Vincill *et al.,* (2012), no clear and obvious desensitization has been observed after amino acid potentiation(272, 278). This sort of mechanism may possibly be needed to endure long term exposures to changes in amino acid concentrations. A still undetermined non-canonical ligand-gating scheme needs to resolve the triple discrepancy between; biochemically calculated amino acid binding affinities (submicromolar), the dose-response of electrophysiological patch-clamp recordings (micromolar to millimolar), and the nature of the physiological amino acids both in specificity and free concentration (millimolar to tens of millimolar). Since we can always expect an amino acid to be bound to the receptor, the outstanding question posits; how does a permanently closed clamshell contribute to constitutively active currents?

To evaluate this question, we will revert our viewpoint to again consider comparable ligand gating schemes of iGluRs and GLRs and then challenge the assumption's validity. With this perspective, two lines of evidence based on the structure determination efforts initially suggest that the two gating modes could be related. First, crystalized LBDs are only formed in the "holo" or ligand-bound state with a closed clamshell. Further, the inability to obtain an "apo" or ligand-free state suggests a conformational instability when an amino acid is absent. In light of the high binding

affinities for amino acids, it is a valid hypothesis that the LBD clamshell is closed, in essence, by contamination. The contamination would force GLR LBDs into a closed clamshell configuration —and an open ion channel. A plausible mechanism without apparent receptor desensitization. Such a mechanism is not precisely as it is defined by fast iGluR signaling, but fundamentally is an ion channel gating mechanism primarily dependent on the stimulus provided by a mandatory ligand binding.

Since there are two modes of GLR gating, one designated by a constitutive activity and the other evoked by a ligand— it stands to further question if a mutation in the LBD that impacts ligand gating also impacts the constitutive active mode. Here, the incompatibilities to the canonical iGluR gating scheme are again evident. If ligand binding was impaired, then the basal Ca^{2+} flux and background current would also be expected to be abolished(295, 296). This was not the experimental observation. *Pp*GLR1(R556A) still produced an elevation of $[Ca^{2+}]$cyt in control conditions (in the absence of exogenous ACC) comparable to the WT channel as well as a background current recorded in patch clamp. A background current divorced of normal ligand-induced gating supports the notion that ion conductance can be independent of the ligand-gating. Additionally, the background current produced from a holding potential of 0mV also suggests there may be gating features operating independently of exogenous ligand-binding. Typical ligand binding is not expected to be affected by membrane voltage or ion conditions. Yet, the ligand's ability to transduce a current rundown or runup dependent on the ionic conditions and membrane voltage lends new hypotheses that other

molecular properties are the primary determinants of ion conductance instead of the ligand-LBD interactions.

Alternatively, another interpretation for the increased background activity in the *At*GLR3.2 R551A mutation is that the clamshell's spontaneous closure facilitates an open channel state. Importantly, as basal Ca^{2+} responses without an amino acid were augmented in R551A over the non-mutated receptor, the mutant is expected to have a fully closed clamshell. Met and Gly still evoked an effect on the mutant but are likely partial agonists; therefore, other ligands would be expected to mimic a clamshell closure to the fullest extent seen in the R551A mutant. The logic outlined here is in accordance with our work on the ligand diversity suggestive that an unappreciated class of molecules may be physiological ligands by demonstrating a role for non-proteinogenic amino acids to be more effective than standard proteinogenic amino acids in initiating ion channel gating(336). In this line of reasoning, if Met and Gly still bind into a fully closed clamshell, then proteinogenic amino acids binding to GLR LBDs may constitute a purpose other than ion channel activation. Establishing the role of amino acids in GLR mediated signaling bears a formidable challenge. Still to be considered is what happens when different amino acids replace each other in the binding site. It would be relevant to appreciate the competition between ACC and Glu binding to probe the agonistic versus antagonistic properties.

Voltage-sensitive gating

Voltage sensitive gating is a common mechanism in excitable animal cells. Voltage sensitive channels often contain a specific voltage sensing transmembrane domain that moves to open the channel pore. The voltage-sensitive properties of *Pp*GLR1 are different in the sense that GLRs do not encode a voltage-sensing domain. Voltage sensing from voltage-sensor-less channels has been described to minimally require a space to sense an electrical field. The pore can fulfill this role as a cavity where ions flow through to affect channel activity(343, 344). The mechanism proposed by our data posits that Ca^{2+} plays a particularly important role in the channel deactivation. Extracellular Ca^{2+} has previously been shown to reduce NMDAR currents but in a voltage-independent manner(345). Voltage-dependent inhibition of NMDARs has also been extensively characterized in the form of a Mg^{2+} block where a depolarization is necessary to eject blocking Mg^{2+} ions for a Ca^{2+} current. In our conditions, Mg^{2+} was always maintained constant, and the perfusion of Ca^{2+} ions was sufficient to augment or reduce ion conductance. Notably, our patch pipette contained 3mM Mg^{2+}, which is also precise to the established physiological concentration.

What does the voltage-sensitivity mean for ion channel gating under physiological conditions? The current rundown was most apparent when the holding potential was more hyperpolarized than the *Vrev*. Therefore, at resting membrane voltages in the plant cell, the *Pp*GLR1 background current should be expected to be minimal, and the channel would open when the *Vm* depolarizes to the equivalent *Vrev*. A channel most active during a depolarization fits the classic mechanism where a voltage-dependent Ca^{2+}

permeable channel couples the *Vm* with Ca^{2+} signaling. However, there is no physiological evidence available to make such a conclusion. Interestingly, transcriptomic analysis illustrates the genes related to voltage-dependent Ca^{2+} signaling exist in moss, albeit to a much lower extent than in animals, but are missing in angiosperms(284). Depolarization activated Ca^{2+} uptake has likewise been reported in moss protoplasts(167). Given the loss of genetic material specifically designated for voltage-dependent signaling in *Arabidopsis*, it remains undetermined if the diversification of *At*GLRs compensates for signaling functions. The striking aspect of the voltage regulation is that *Pp*CNIHa and *At*CNIH4 seem to lower the voltage sensitivity where current amplitudes at hyperpolarized voltages (-140mV) are larger.

Co-opting ion selectivity conserves electrical signaling functions

We postulate the difference in ion selectivity and channel gating between GLRs and iGluRs is an adaptive mechanism to suit the different cellular environments and membrane properties between animals and plants. Glu's brief binding to AMPARs opens the channel for a Na^{+} current to initiate a rapid depolarization of the post-synaptic membrane. An anion selective GLR thus co-opts the means necessary to drive a membrane depolarization in plant cells and points toward an evolutionary conservation of function for controlling membrane voltage.

We have previously outlined that a functional diversification takes place between GLRs in *P.patens* and *Arabidopsis*. *Pp*GLR1 is a functional homomeric ion channel. *At*GLRs constitute a family of ion channels requiring heteromerization, bringing a

breadth of gating properties from those with a constitutive background current and those more potentiated by amino acids. Despite the differences in ion channel assembly and gating, the high anion permeability factor defining the ion selectivity is a characteristic conserved between *P.patens* and *Arabidopsis*. Fitting the overall evolution in plant membrane transport, plant GLRs exemplify the trend that anion permeable channels in plants diversified, and the need for Na^+ selective channels was lost.

Structure-Function: GLR gating properties rely on the pore structure

The commanding role the GLR pore takes to co-opt the ion selectivity and determine ion conduction demarcates the biophysical properties of GLRs from iGluRs. Our electrophysiological results allow us to make several inferences about GLR structure-function centered around the pore. (1) First, GLR ligand-gating intimately depends on the pore's conformation. Ligand binding to the extracellular receptor alone is not a sufficient stimulus to dictate ion conduction. Stimuli in the TMD elicit conformational changes downstream of the LBD that over-ride an agonist's presence. We show that ligand binding changes the channel's properties in a way that can only be seen through the direct effect the ions within the permeation pathway exert. (2) Second, we can expect the pore to be a lower gate of plant GLRs harboring the molecular determinates of ion conduction and ion selectivity. This hypothesis is based on our results showing ionic conditions define ion flux such that the current amplitude is either potentiated (run-up) or inhibited (run-down) after applying a ligand. Additionally, we provide the molecular evidence through pore domain swap experiments that lend a gain-

of-function for ligand gating. Under our experimental conditions, the non-mutated pore remained non-conductive when the expressing cells were applied ACC. *Pp*GLR1$_{SWAP}$, a channel possessing the WT *Pp*GLR1 extracellular domains with a cationic GluA2 pore, was readily potentiated by ACC. (3) Perhaps the main distinguishing feature of GLRs is the presence of a background current. Importantly, our recordings suggest the currents that appear leaky are the result of a voltage-sensitivity compounded by slow kinetics. Our whole-cell patch clamp experiments use a holding potential of 0mV; yet when GLR expressing cells were clamped to -100mV, we observed a current decay over tens of seconds to minutes. Data suggest the current decay was due in part to block by permeant ions, but where they bind or if there is a physical closure of the pore is unclear.

The only determining hallmark of gating is the conformation of the pore itself. A minimum radius is needed for ion permeation, demonstrating whether the channel is open or closed. For iGluRs, the pore dilates when opening from a non-conducting to conducting state and subsequently constricts all while bound to Glu. It's unclear if the iGluR pore is an active component of the gating or passively forced by adjacent domains. Our ability to resolve GLRs exhibiting a background current suggests the GLR pore is already dilated and allows us to explore the pore's contribution to gating in different LBD states. Our data also suggests ACC binding drives conformational changes, but we show the pore plays a role in the mechanical coupling.

There is much more to learn about the molecular properties governing ion selectivity. Despite the gain of cation permeability, it was surprising that an anion permeability persisted given that the channels are homologous(346). However, it has

been documented that other chimeras between distantly related Na^+ and Ca^{2+} channels also did not entirely convert ion selectivity, illustrating the notion that pinpointing the molecular mechanism of ion selectivity encompasses a much larger and more general challenge to the ion channel field(347). We interpret the retention of anion permeability in *Pp*GLR1$_{SWAP}$ to imply that other transmembrane channel properties influence ion selectivity or that the chimeric channel's pore dimensions were amenable to less selectivity. The mutation of the only negatively charged residue in the *Pp*GLR1 selectivity filter (E647) also surprised us that it did not directly control cation selectivity. Instead, it may have played a structural role in ion permeation regulating the current amplitude.

Concluding remarks and perspective

Primitive roles for a conserved ligand-binding domain?

As we argue, the molecular evolution of the pore conserves an evolutionary function for commanding membrane voltage; the ligand binding domain may have diversified into separate signaling functions. Accommodating the demands of the synapse, the ligand-binding domain (LBD) is a leading factor specializing iGluR function. The iGluR LBD faces a well buffered synaptic cleft where Glu is released by exocytosis from the pre-synapse and recycled. This physiological specificity for Glu ensures the high fidelity of synaptic transmission(348). The early identification of a conserved glutamate receptor LBD in plant GLRs sparked the hypothesis that a primitive signaling mechanism existed before the divergence of plants and animals(275). Because GLRs indeed possess a structurally conserved amino acid binding pocket to the iGluR LBD, it is initially surprising the ligand gating of plant GLRs is so divergent. GLR-related currents— unlike iGluRs— have been demonstrated to be stimulated by a broad panel of ligands totaling more than a dozen, resembling more of the prokaryotic GluR0(230). The GLR LBD indeed accommodates a non-specific amino acid binding pocket already crystalized with four different amino acids suggesting GLRs never developed an amino acid specificity seen in mammals. By examining the origins of the LBD, it was discovered that the GLR and iGluR LBDs are homologous to the lysine-arginine-ornithine binding protein (LAOBP), a classification of bacterial periplasmic binding proteins (PBPs) that also include glutamate-binding proteins(349). PBPs are bilobed clamshell-like structures that have roles in ligand binding for active substrate

transport and chemotaxis with diverse amino acid specificities depending on the PBP gene. LAOBP has an affinity for at least four amino acids L-lysine, L-arginine, L-ornithine, and L-histidine(350, 351). The non-specific amino acid binding properties of the LBD are more similar to PBPs. The plant ATD is also homologous to another PBP, the LIVBP (leucine isoleucine valine binding protein)(349). It is still unknown if the plant ATD possesses a function ligand binding capacity, but dual amino acid sensors would be an innovative function for amino acid signaling(352). The hypothesis proposing a primitive signaling mechanism through the presence of a ligand-binding domain of glutamate receptors may still bear some merit. However, our electrophysiological data and reports on structure determination convincingly demonstrate a primitive role is divorced from Glu specificity.

Structure-function intersects with evolution and physiology.

The pivotal step in the evolution of glutamate receptors appears to have come with the fusion of the pore loop with bacterial amino acid binding proteins. Experimental data even supports the hypothesis that the pore loop is derived from an unknown K^+ channel creating a phylogenetic link between glutamate receptors and K^+ channels(232, 353, 354). While all glutamate receptors generally preserved the amino acid binding properties, it is increasingly apparent from an evolutionary perspective that the ion selectivity governed by the pore has greatly diversified with the kingdoms' divergence.

The bacterial glutamate receptor, GluR0 from *Synechocystis*, is only a three-transmembrane pass ion channel missing the M4 domain in addition to lacking an ATD

later developed in eukaryotes. GluR0 is a potassium selective ion channel(230). The freshwater rotifer *Adineta vaga* is thought to encode the first eukaryotic glutamate receptor with the modular architecture and 4-transmembrane pass channel like iGluRs. *Av*GluR is also a potassium selective ion channel(231, 355). Among mammals, iGluRs evolved to non-selective cation channels with permeability to Ca^{2+}. This thesis illustrates an ancestral K^+ channel may have also evolved into an anion channel. A recent study found a conserved activation mechanism exists between an iGluR extracellular domains and a viral K^+ channel pore supporting the pore's evolutionary origins(356). If so, our conclusions of the pore's contribution to gating may have a broader impact on all P-loop families fundamental to all cells and viruses' electrical properties.

New perspective on physiological roles

The electrophysiological characterization of *Pp*GLR1 holds potential to uncover new physiological roles of the GLR family. Anion currents from unidentified channels have been isolated from protoplasts across various species and cell types, including guard cells and parenchyma cells along the xylem. Putting forward the molecular identity of a new candidate family that may comprise those various currents supports efforts in plant physiology to improve understanding of intricate physiological processes. Although we have focused our attention on the importance of anion transport on the cellular electrical properties (previously outlined for roles in cell-cell communication and gas exchange), anion transport is not without consequence on agronomy related to plant osmotic

regulation and nutrition(357). Coupled with the information that *At*GLR activity is disguised by heteromerization that produces a functional diversification of ligand gating properties, heterogenic combinations may fulfill different physiological needs throughout various tissues, a fine tuning of GLR activity in the plant.

A new perspective to view physiology extends to mammals. Non-neuronal iGluRs in peripheral tissues, as well as sperm, are associated with clinical pathophysiology(7, 358, 359). Similar to plant cells, mammalian cells from peripheral tissues such as the pancreas also exist in cellular environments different from neurons, particularly in the context of free amino acids available in the blood. Typically assumed to function the same as neuronal iGluRs, our work provokes the argument that different physiological conditions could lead to adapted biophysical properties of non-neuronal iGluRs impacting human health.

Integrating the membrane transport network

Coalescing GLR activity into documented Ca^{2+} signaling roles involves the rest of the membrane transport network. Although Ca^{2+} permeable, attributing unexpected anion permeability and gating properties to GLRs reinforces the membrane transport network's connectivity. Ion channels do not work in isolation and unraveling one channel's properties inherently impacts how the entire network is interpreted.

Long-distance signaling, for example— because of GLR's heavy involvement— exemplifies the importance of integrating the membrane transport network. The propagation of a long-distance electrical signal like those induced by wounding and

herbivory needs a continual re-amplification(360) involving GLRs(17, 57) as well as two channels on the tonoplast; the K^+ channel TPK1 that modulates tonoplast excitability and the voltage-dependent- Ca^{2+} activated TPC1 able to release Ca^{2+} from vacuolar stores(79, 160, 361). The electrochemical coupling of the two membranes remains unknown, yet plasma membrane transport can alter the cytosol's ionic conditions, influencing the tonoplast's electrical properties. One proposed mechanism is by Ca^{2+} induced Ca^{2+} release (79). The Ca^{2+} induced Ca^{2+} release mechanism's plausibility ultimately depends on a tightly regulated initial Ca^{2+} stimulus to stay within a homeostatic range either by limiting the flux magnitude across the plasma membrane or through spatial constraints placing interacting channels in close proximity. According to our data, Ca^{2+} itself tightly regulates the weak Ca^{2+} permeability of *Pp*GLR1, as evidenced by the inhibitory effect Ca^{2+} has on the current amplitude.

With cells connected by a continuous plasma membrane and cytosolically joined by the plasmodesmata, the GLR mediated anion efflux across the plasma membrane would be predicted to both depolarize the plasma membrane and the adjacent cell propagating an electrical signal. The work of Mousavi *et al.*,(17) nicely illustrated the extensive involvement of GLRs in the transmission of electrical signals through undamaged tissue and that GLRs are less so involved in the initiation event occurring at damaged leaves. Assuming a ligand was needed for GLR channel activation troubled this result, especially as Glu's apoplastic elevations were discovered to only elevate locally(117). The biophysical properties of a background current we present alleviates this discrepancy. A genetic link has also begun to emerge connecting GLRs with the H^+-

pump AHA1(114), further implicating the interplay between membrane voltage and Ca^{2+} signaling.

What is essential to point out is that anion selectivity of plant GLRs— more than anything else— expands the capacity of signaling functions and impacts how they play on membrane voltage dynamics. The anion selectivity may make some channels highly depolarizing, but all GLRs do not need to drive the main depolarization to still impact membrane voltage. Some channels like *At*GLR3.4 with an approximately equal permeability of anion to cation would be predicated to minimize the maximal depolarization possible, effectively creating more of a stabilizing factor on the membrane voltage. An equal anion/cation permeability is rare among plant ion channels and brings new perspectives on cell signaling(362). Presumably, ones beneficial for Ca^{2+} permeation. Integrating GLRs into the remaining membrane transport network presents an enticing challenge. Ca^{2+} signaling is inseparable from electrical signaling, and the two must be compensated. The work presented here has characterized a major ion channel in Ca^{2+} signaling and takes a step toward evaluating a dynamic electro- Ca^{2+} system.

Methods

Mammalian cell culture

Cryo-preservation

Frozen COS-7 cells were bought from either ATCC or Sigma. Cells were initially defrosted according the manufacturer's instructions (ATCC; CRL1651). New cells were grown to confluence and partitioned into cryo-vials for long-term storage in liquid nitrogen in a freezing solution of Dulbecco's Modified Eagle Medium (DMEM) supplemented with 10% Fetal Bovine Serum (heat inactivated) and 5% DMSO. Subsequent defrosting of cell vials was also carried out according to the ATCC's instructions (https://www.atcc.org/products/all/CRL-1651.aspx#documentation).

COS-7 cell growth conditions

COS-7 cells were cultured in 25cm^2 flasks in Dulbecco's Modified Eagle Medium (DMEM; The complete formulation of DMEM is provided in the following hyperlink: https://www.thermofisher.com/us/en/home/technical-resources/media-formulation.45.html) —supplemented with 5% Fetal Bovine Serum (heat inactivated) and 1% Penicillin/ Streptomycin — stored in an incubator at 37°C and 5% CO_2. Cells were passaged every 7 days before reaching a stationary growth phase or 100% confluence. Cells are suitable for transient transfection were taken from low passage numbers (p1-4) 5-7 days after passage and when cells reached 80% confluence. Cells were plated into

35mm dishes at least 4hours, and maximally 32 hours prior to transfection at 50% confluence. In the event cells were plated 24 hours or more in advance of transfection the confluency of cells was adjusted to 30%.

COS-7 cell transfection

Expression of GLRs in COS-7 cells was achieved by transient transfection of cDNA using the transfection reagent, FuGENE HD (Promega). Cells were transfected with a cDNA: FuGene HD ratio of approximately 1:7. Or patch clamp experiments; 1.0μg of pCI-*Pp*GLR1 cDNA and 0.1μg of pEF1-YC 3.6 was mixed with 100μL sterile H_20. 7μL of FuGene HD was added to the cDNA and water mixture and incubated with for 5min at room temperature before pipetting the mixture directly to DMEM media in 35mm dishes. Transfection of all *Pp*GLR1 mutants used the same protocol. When co-transfecting *Pp*GLR1 and CNIH; 0.75μg pCI-*Pp*GLR1 cDNA and 0.25μg pcDNA3-*Pp*CNIHa or pCI-*At*CNIH4 was mixed with 01. μg pEF1-YC3.6 and 100μL H_20 and 7μL FuGene HD. For *At*GLR3.2/*At*CNIH1/*At*CNIH4 co-transfections: 0.5μg pcDNA3-*At*GLR3.2 cDNA was mixed with 0.25μg pCI-*At*CNIH1 and 0.25μg pCI-*At*CNIH4. Plasmids were mixed in 100μL and incubated with 3.5μL FuGENE HD. For Ca^{2+} imaging experiments the only adjustment to the protocol was the total amount of DNA. 1.5μg cDNA was transfected keeping *Pp*GLR1 to 1μg and increasing YC3.6 to 0.5μg of cDNA. Cells were re-suspended by trypsin treatment and transferred to coverslips in new 35mm petri dishes the following day. DMEM always needed to equilibrated to pH either

by using a fresh bottle or placing DMEM in vented flasks in the incubator (37˚C, 5% CO_2) overnight. Transfected cells were found to be expressing *Pp*GLR1 36-38 hours after transfection.

Patch-clamp

Glass Pipettes were pulled with a P97 or P1000 puller (Sutter Instrument) to a resistance of 3–5 MΩ for COS-7 cells, or to a resistance of 15 MΩ for protoplasts. Currents were recorded after establishing the whole-cell configuration and filtered at 1–2 kHz with a sampling frequency of 2–4 kHz using an Axopatch 200A amplifier, a DigiData 1322A AD-converter (Molecular Devices) and the latest version of WinWCP software (http://spider.science.strath.ac.uk/sipbs/software_ses.htm). All statistical analyses were done using SigmaPlot (v11.0, Systat Software Inc)

All electrophysiology solutions and voltage protocols are defined in the results where applicable. Voltage test pulses were typically run for 1.5sec unless otherwise stated. Cells were set to 0mV prior to and following each test pulse. Liquid junction potentials were corrected offline with Clampex 10.0. Pipette voltages could be corrected to actual command voltages with the formula:

$$Vc = Vp - LJP$$

Vc is the command voltage, Vp is the pipette voltage, and LJP is the Liquid Junction Potential. When using internal solutions devoid of Cl^-, a 3M KCL 1% agar bridge was fitted to the AgCl electrode.

Patch Clamp Solutions

Table 5: List of internal and external solution sets used in Chapter 2 part 2. Extracellular solutions are summarized in each figure or figure legend. Internal and external pH of S1-S6 was adjusted to 7.3 with BTP/HEPES. Osmolarity was adjusted 350 mOsmol kg^{-1} with D-mannitol with the exception of S7. S7 was adjusted to 500mOsmol kg^{-1} to be used with protonema protoplasts. Concentrations denoted by an asterisk (*) indicate units in nanomolar. All other concentrations are given by millimolar.

Set	Solution	Ca^{2+}	Mg^{2+}	Ba^{2+}	Na^{+}	$NMDG^{+}$	Cl^{-}	NO_3^{-}	$Gluc^{-}$	Mal^{2-}	BTP	HEPES	EGTA
S1	Internal	100*	3	0	0	0	8	0	0	0	-	10	5
	External	3	0	0	0	0	6	0	0	0	10	-	0
		10	0	0	0	0	6	0	14	0	10	-	0
		30	0	0	0	0	6	0	54	0	10	-	0
		70	0	0	0	0	6	0	134	0	10	-	0
S2	Internal	100*	3	0	0	0	8	0	0	0	-	10	5
	External	70	0	0	0	0	6	0	134	0	10	-	0
S3	Internal	100*	3	0	0	0	8	0	0	0	-	10	5
	External	10	0	0	0	0	10	0	10	0	10	-	0
		10	0	0	130	0	10	0	130	0	10	-	0
S4	Internal	100*	3	0	0	0	8	0	0	0	-	10	5
	External	30	0	0	0	0	0	0	60	0	10	-	0
S5	Internal	100*	3	0	0	0	8	0	0	0	-	10	5
	External	30	0	0	0	0	10	0	50	0	10	-	0
S6	Internal	100*	3	0	0	0	8	0	0	0	-	10	5
	External	30	0	0	0	0	0	10	50	0	10	-	0
S7	Internal	0	0	100*	0	50	50	0	0	0	10	-	5
	External	0	0	50	0	150	150	0	0	0	10	-	0
S8	Internal	100*	3	0	0	150	150	0	0	0	10	-	5
	External	3	0	0	0	150	150	0	0	0	10	-	0
		3	0	0	0	150	0	150	0	0	10	-	0
		3	0	0	0	75	0	0	0	75	10	-	0
		3	0	0	0	150	0	0	150	0	10	-	0

Table 6: List of internal and external solution pairs used Chapter 2 part 4. Experimental solutions are summarized in each figure or figure legend. Solution set S7 is reproduced here from Table 5 for clarity. Internal and external pH was adjusted to 7.3 with BTP or HEPES, respectively. Osmolarity was adjusted 350 mOsmol kg^{-1} with D-mannitol with the exception of S7. S7 was adjusted to 500mOsmol kg^{-1} for protonema protoplasts. Concentrations denoted by an asterisk (*) indicated units in nanomolar. All other concentrations are given by millimolar.

Set	Solution	Ca^{2+}	Mg^{2+}	Ba^{2+}	Na^{+}	$NMDG^{+}$	Cl^{-}	NO_3^{-}	$Gluc^{-}$	Mal^{2-}	BTP	HEPES	EGTA
S7	Internal	0	0	100*	0	50	50	0	0	0	10	-	5
	External	0	0	50	0	150	150	0	0	0	10	-	0
S9	Internal	100*	3	0	0	150	0	6	150	0	10	0	5
	External	75	0	0	0	0	0	150	0	0	10	-	0
S10	Internal	100*	3	0	0	150	0	6	150	0	10	0	5
	External	3	0	0	0	150	0	0	150	0	10	-	0
S11	Internal	100*	3	0	0	150	0	6	150	0	10	0	5
	External	5	0	0	0	140	0	150	0	0	10	-	0
S12	Internal	100*	3	0	0	150	0	6	150	0	10	0	5
	External	75	0	0	0	0	0	6	144	0	10	-	0
S13	Internal	100*	3	0	0	150	0	6	150	0	10	0	5
	External	1	0	0	0	150	0	150	0	0	10	-	0
S14	Internal	100*	3	0	0	150	0	50	100	0	10	0	5
	External	75	0	0	0	0	0	150	0	0	10	-	0

Table 7: List of internal and external solution pairs used in Chapter 2, part 4 for CNIH analysis. Internal and external pH adjusted to 7.3 with BTP or HEPES, respectively. Osmolarity was adjusted 350 mOsmol kg^{-1} with D-mannitol. Concentrations denoted by an asterisk (*) indicated units in nanomolar. All other concentrations are given by millimolar.

Set	Solution	Ca^{2+}	Mg^{2+}	Ba^{2+}	Na^{+}	$NMDG^{+}$	Cl^{-}	NO_3^{-}	$Gluc^{-}$	Mal^{2-}	BTP	HEPES	EGTA
S15	Internal	100*	3	0	0	150	8	150	0	0	10	0	5
	External	30	0	0	0	0	0	0	60	0	10	-	0

Table 8: List of internal and external solution pairs used in Chapter 2, part 5. Internal and external pH adjusted to 7.3 with BTP or HEPES, respectively. Osmolarity was adjusted 350 mOsmol kg^{-1} with D-mannitol. Concentrations denoted by an asterisk (*) indicated units in nanomolar. All other concentrations are given by millimolar.

Set	Solution	Ca^{2+}	Mg^{2+}	Ba^{2+}	Na^{+}	$NMDG^{+}$	Cl^{-}	NO_3^{-}	$Gluc^{-}$	Mal^{2-}	BTP	HEPES	EGTA
S9	Internal	100*	3	0	0	150	0	6	150	0	10	0	5
	External	75	0	0	0	0	0	150	0	0	10	-	0
S16	Internal	100*	3	0	0	19	30			0	10	0	5
	External	15	0	0	0	0	30	0	0	0	10	-	0
		15	0	0	0	30	60	0	0	0	10	-	0
		15	0	0	0	90	120	0	0	0	10	-	0
S17	Internal	100*	3	0	0	19	0	30		0	10	0	5
	External	15	0	0	0	0	0	30	0	0	10	-	0
		15	0	0	0	30	0	60	0	0	10	-	0
		15	0	0	0	90	0	120	0	0	10	-	0
S18	Internal	100*	3	0	150	0	6	150	4	0	10	0	5
	External	3	0	0	150	0	0	150	6	0	10	-	0
		3	0	0	65	0	0	65	0	0	10	-	0
		3	0	0	30	0	0	30	0	0	10	-	0
S19	Internal	100*	3	0	150	0	6	150	4	0	10	0	5
	External	3	0	0	30	0	0	30	0	0	10	-	0

Ca^{2+} imaging

Imaging was performed at room temperature using a DeltaVision Elite Deconvolution/TIRF microscope system (Olympus inverted IX-71) under a 60× water immersion lens (1.2NA UPLSAPO water lens/WD 0.28 mm). A xenon lamp from the DeltaVision system was used with a CFP excitation filter (438–424 nm). Two simultaneous emission records were captured: cpVenus emission (548–522 nm) and CFP emission (475–424 nm). The laser power was set to 2%. cpVenus and CFP acquisitions were recorded with 0.3 sec exposure time. Time-lapse acquisition was collected with a sampling interval of 30 sec.

Images were processed using ImageJ. Ratios were obtained after background subtraction and signal clipping using the "Ratio-plus" plug-in for ImageJ. In the ligand screening experiments, values were multiplied by a factor of one hundred to increase the signal:noise ratio. The signal of each channel was averaged in a circle in the middle of the cell (with 100–200 pixel diameter depending on the size of the cell). To standardize YC3.6 responses, the baseline values (five points prior to Ca^{2+} application) were averaged and then subtracted from each measurement recorded. The integrated area under the curve was calculated in SigmaPlot 11.0 (Systat Software Inc) by drawing a best-fit line and using the built in macro "Area Below Curves".

Ca^{2+} imaging solutions

Transfected COS-7 cells to be imaged were removed from DMEM and washed three times with a Ca^{2+}-free solution (1 mM EGTA, 10 mM Bis-Tris propane buffered to

pH 7.3 (HEPES), osmolarity of 335 mOsmol kg−1 with D-mannitol). Cells were imaged in the Ca^{2+}-free solution for 2.5 min before the addition of Ca^{2+} to a final concentration of 14.5 mM. For ligand screening experiments, the potential ligand was applied to the Ca^{2+}-free solution at the beginning of imaging session.

Mammalian Expression Constructs.

Table 9: Mammalian expression constructs used for transfection.

Construct Name (vector-cDNA)	Source
pCI-*Pp*GLR1	Ortiz-Ramirez et al., 2017
pcDNA3-*Pp*glr1-IRES-NES-YC3.6	This thesis (Lizzio, M.)
pcDNA3-*Pp*glr1-SWAP-IRES-NES-YC3.6	This thesis
pcDNA3-*At*GLR3.2	Wudick et al., 2018
pCI-*Pp*CNIHa	This thesis (Michard E.)
pCI-*At*CNIH4	Wudick et al., 2018
pCI-*At*CNIH1	Wudick et al., 2018
pCI-*Pp*GLR1 (R556A)	Dr. Caren Chang Lab (University of Maryland)
pCI-*Pp*GLR1 (E647A)	This thesis
pCI-*Pp*GLR1 (E647R)	This thesis
pcDNA3-*At*GLR3.2 (R551A)	Gangwar et al., 2020
pCI-*At*GLR1.2	This thesis (Lizzio, M.)
pCI-*At*GLR1.2 (SYTANLAAF)	This thesis
pEF1-YC3.6	Prof. Jörg Kudla Lab (University of Muenster, Germany)
pcDNA3-*At*GLR3.4	Lizzio, M. & I

Cloning

Table 10: Base vectors for cloning

Construct Name (vector-cDNA)	**Source**
pDONR207-*Pp*GLR1	Lizzio, M.
pcDNA3-Gateway-IRES-NES-YC3.6	Lizzio, M.
pGGC-XD-*Pp*GLR1-E647A-3P	Lizzio, M.
pGGC-XD-*Pp*GLR1-E647R-3P	Lizzio, M.
pDONR207-*Pp*GLR1-SWAP	Lizzio, M.
pDONR207-GoldenGate(SapI)	Lizzio, M.
pMOD_B2101	Cermak et al., 2017 (363)
pGGD000	Lampropoulos et al., 2013 (364)
pDS_EF1-XB-glr3.4-CFP	Dr. Edgar Spalding University of Wisconsin-Madison
pcDNA3	Invitrogen
pIRES	Clontech
pCambia-3300-Lat52-YC3.6	Kai Conrad University Wuerzburg, Germany
pK7FWG2	University of Ghent, Center for Plant Systems Biology

Targeted mutagenesis:

Constructs for GLR mutants with mammalian expression vectors were generated by PCRs each with overlapping mutagenic oligonucleotide primers listed in Table X.

Table 11: PCR design for targeted mutagenesis. DNA used as the template is located in the left column. Primers used for each reaction are located in the right column.

Final Construct Name: pcDNA3-*Pp*GLR1-SWAP-IRES-NES-YC3.6	
DNA template: pCI-*Pp*GLR1	Primer Name : Sequence 5' – 3': PCR #1 C180 F:CTCATGTGGCTGACCACCGG C181 R:CGGGCTAATATCGCAGCCCTGCTG GAAGAGAGTCATAAATACGAACCATAATG PCR #2 C182 F: CAGCAGGGCTGCGATATTAGCCCG AACAGCACTCTGGGTAGGGC C183 R: TGGTAAAAGCGCACTCAGTCGA
Final Construct Name: pCI-*Pp*GLR1 (E647A)	
DNA template: pGGC-XD-PpGLR1-E647A-3P	Primer Name : Sequence 5' – 3': PCR #1 **C180** F: CTCATGTGGCTGACCACCGG C183 R: TGGTAAAAGCGCACTCAGTCGA
Final Construct Name: pCI-*Pp*GLR1 (E647R)	
DNA template: pGGC-XD-PpGLR1-E647R-3P	Primer Name : Sequence 5' – 3': PCR #1 **C180** F: CTCATGTGGCTGACCACCGG C183 R: TGGTAAAAGCGCACTCAGTCGA
Final Construct Name: pCI-*At*GLR1.2 (SYTANLAAF)	
DNA template: pCI-*At*GLR1.2	Primer Name : Sequence 5' – 3': PCR #1 B608 F: GAGAGAAGGGTAGGATTCTGG B611 R: TTAATTGCCATTGTTTACTGCG PCR #2 B610 F: ATGAAGAGAGAAAACAACCTCG B609 R: GTCGTTGTGAGAAGTATATATTGACCG

Table 11, Continued;

Final Construct Name: pCI-*At*GLR3.2 (R133A)	
DNA Template: pcDNA3-*At*GLR3.2	Primer Name : Sequence 5' – 3': <u>PCR #1</u> C214: TGATACTGTCTGGATCATTGC TCGAGCTGTTAAGAGACTTCTAG C215: GAAATCCACAATCCTTGTTGC TTTCGTAACAATAGCTATGTCTCC <u>PCR #2</u> C216: GAGACATAGCTATTGTTACGAAAGC AACAAGGATTGTGGATTTCACTCAGC B518: atagggccctctagatgcatgctcgaG TCATATTGGTCTAGAAGGCT

PCRs were performed with under the following thermocycler conditions:

Step 1: 98˚C — 2min
Step 2: 98˚C — 30sec
Step 3: 54˚C — 15sec
Step 4: 72˚C — 15sec
Step 5: 72˚C — 5min
} 30x
Step 6: 4˚C — until ready to proceed

The PCR products were treated with Dpn1 overnight at 37˚C and the presence of PCR products was verified by gel electrophoresis. PCR products purified by Zymo Research: DNA Clean-up kit were inserted into a linearized vector backbone by Gibson Isothermal Assembly Method(365). The final vectors were transformed by electroporation into electro-competent 10β *E.coli* cells to be amplified on low salt LB agar (tryptone, 10g/L; yeast extract, 5g/L; NaCl, 0.5g/L; agar, 15g/L) incubated at 30°C.

DNA extraction was completed according to the manufacturer's instructions (Qiagen). All constructs were sequenced verified by GENEWIZ. The primers used for DNA sequencing are found in Table 12.

Specific Cloning Instructions

Specific Cloning instructions (provided by Lizzio M.) are detailed with labeled by full name and plasmid numerical code (pXXX) associated with the Feijó Lab plasmid database.

p766 – pDONR207-GoldenGate(SapI)

A DNA fragment containing the ccdb gene was amplified from pMOD_B2101 (Voytas Lab) with primer pair B988/B989. A BP Clonase II reaction was then performed with the purified PCR Product and pDONR207 to yield p766 (pDONR207-GoldenGate[SapI]).

p782 – pDONR207-PpGLR1(cDNA)

*Pp*GLR1 was amplified from p786 (pCI-*Pp*GLR1) via two PCRs with primer pairs C10/C11 and C12/C13 to remove an internal SapI site. The final entry clone pDONR207-*Pp*GLR1(cDNA) was constructed by performing a Golden Gate reaction with p766 (pDONR207-GoldenGate[SapI]) and the PCR products with SapI enzyme.

p886 pDONR207-*Pp*GLR1(cDNA) SWAP (GLUA2-Filter)

P782 (pDONR207-*Pp*GLR1) was digested with AgeI-HF, and SalI-HF. Two PCRs were performed with primer pairs C180/C181 and C182/C183 using pCI-*Pp*GLR1 as template. The PCR products were cloned into digested p782 via Gibson Isothermal Assembly to yield p866 pDONR207-*Pp*GLR1(cDNA) SWAP.

p910 pGGC-XD-*Pp*GLR1-E647R

*Pp*GLR1 was amplified from p786 (pCI-*Pp*GLR1) via two PCRs with primer pairs C231/C259 and C260/C232. The PCR products were cloned into, pGGD000 digested with HindII and EcoRI, via Gibson Isothermal Assembly to yield p910 pGGC-XD-*Pp*GLR1-E647R.

p908 pGGC-XD-*Pp*GLR1-E647A

*Pp*glr1 was amplified from p786 (pCI-*Pp*GLR1) via two PCRs with primer pairs C231/C271 and C272/C232. The PCR products were cloned into, pGGD000 digested with HindII and EcoRI, via Gibson Isothermal Assembly to yield p908 pGGC-XD-*Pp*GLR1-E647A.

p923 pCI-*Pp*GLR1-E647A(cDNA)

A fragment of *Pp*GLR1 containing the E647A mutation was amplified from p908 via PCR with primer pair C180/C183. The PCR product was cloned into, p786(pCI-*Pp*GLR1) digested with AgeI and SalI, via Gibson Isothermal Assembly to yield p923 pCI-*Pp*GLR1-E647A(cDNA).

p967 pCI-*Pp*GLR1-E647R(cDNA)

A fragment of *Pp*GLR containing the E647R mutation was amplified from p910 via PCR with primer pair C180/C183. The PCR product was cloned into, p786(pCI-*Pp*GLR1) digested with AgeI and SalI, via Gibson Isothermal Assembly to yield p967 pCI-*Pp*GLR1-E647R(cDNA).

p659 pCI-*At*GLR1.2-Full_Length

The long isoform of *At*GLR1.2 was PCR amplified from *Arabidopsis thaliana* cDNA with primer pair 5' –GAGCTAGCATGGTGAGAATTTGTATTCA – 3; and 5' –AAAGCGGCCGCCTATCGTCTGTTACGTTGAGC - 3'. The PCR product was cloned into pCI digested with NheI and NotI by standard T4 DNA Ligase.

p581 pcDNA3-*At*GLR3.4(cDNA)

The glr3.4 CDS was amplified by PCR from template pDS_EF1-XB-glr3.4-CFP with primer pair B579/B580. The resulting PCR product was cloned into pcDNA3 digested with NotI and XhoI via Gibson Isothermal Assembly to yield pcDNA3-*At*GLR3.4.

p729 pUC19-Gateway-IRES-NES-YC3.6.

The Gateway Destination ccdb-Chloramphenicol cassette from pK7FWG2 (Univ. Ghent) was PCR amplified with primer pair B955/B730. The IRES sequence from pIRES (Clontech) was PCR amplified with primer pair B731/B732. The calcium sensor with nuclear export signal, NES-YC3.6, was PCR amplified in two parts from pCambia-3300-Lat52-YC3.6 (Kai Konrad) via primer pairs B733/B796, and B797/B957. The four PCR products B955/B730, B731/B732, B733/B796, B797/B957 were cloned into pUC19 digested with EcoRI and HindIII via Gibson Isothermal Assembly yielding intermediate vector p729 pUC19-Gateway-IRES-NES-YC3.6.

p743 pcDNA3.1-Gateway-IRES-NES-YC3.6

The Gateway-IRES-NES-YC3.6 cassette was PCR amplified from p729 with primer pair B828/B830. A 4.5kB fragment was gel-extracted and purified. The gel extracted fragment was cloned into pcDNA3 digested with KpnI and XhoI via Gibson

Isothermal Assembly yielding the Gateway Destination Vector p743 pcDNA3.1-Gateway-IRES-NEW-YC3.6.

p789 pcDNA3-*Pp*GLR1-IRES-NES-YC3.6

An LR Clonase II reaction was performed with Entry Clone p782 – pDONR207-*Pp*GLR1(cDNA) and Destination Vector p743 pcDNA3.1-Gateway-IRES-NES-YC3.6 to yield p789 pcDNA3-*Pp*GLR1-IRES-NES-YC3.6.

p894 pcDNA3-*Pp*GLR1-SWAP-IRES-NES-YC3.6

An LR Clonase II reaction was performed with Entry Clone p886 pDONR207-*Pp*GLR1(cDNA) SWAP and Destination Vector p743 pcDNA3.1-Gateway-IRES-NES-YC3.6 to yield p894 pcDNA3-*Pp*GLR1 SWAP-IRES-NES-YC3.6.

***pCI-At*GLR1.2 (SYTANLAAF)**

pCI- *At*GLR1.2 cDNA was amplified by primer pairs of B608/B611 and B608/B611. Purified PCR products were inserted into a backbone created from digestion of pCI-*At*GLR1.2 plasmids at EcoRI restriction sites via Gibson Isothermal Assembly.

p715 pCI-*Pp*CNIHa

*Pp*CNIHa was PCR amplified from *P.patens* cDNA with primers 5'-AAACTCGAGATGGCTTCCGATCTCCTTCTGTGG- 3' and 5'-AAAGTCGACTCACATGTTTGCGTGGATCCCCG – 3'. The PCR product was cloned into pCI digested with XhoI and SalI by standard T4 DNA Ligase.

p897 pcDNA3-*At*GLR3.2 (R551A)

pcDNA3-*At*GLR3.2 was PCR amplified with overlapping mutagenic oligonucleotide primer sets C214/C215 and C216/B518. Inserts were ligated with a backbone of pcDNA3-*At*GLR3.2 linearized at XhoI restriction sites to construct the final mutant vector by Gibson Isothermal Assembly

Table 12: Primers for DNA Sequencing. Primers designed for each construct were also used for sequencing point mutants.

Construct: pCI-*Pp*GLR1	
Primer Name	Sequence 5' – 3'
B434_PPGLR1_seq_F354	GCAAGTGCCATTGGTGTCTT
B435_PPGLR1_seq_F759	TGTTACAGAGGCCATGACGA
B436_PPGLR1_seq_F1157	GTCCTGTGCAGCTGGATGA
B437_PPGLR1_seq_F1556	TCACCTCATTTGGTGATGGA
B438_PPGLR1_seq_F1953	CACTCTGGGTAGGGCTGTTC
B439_PPGLR1_seq_F2357	CACAGTTGGCCATTGATTTCT
B440_PPGLR1_seq_F2750	TCTCCTCTCCTGAGCAAATCA
B441_PPGLR1_seq_R445	CATCATCAGAATGAGTGACACG
Construct: pCI-*Pp*CNIHa	
Primer Name	Sequence 5' – 3'
CMV-Forward	CGCAAATGGGCGGTAGGCGTG
Construct: pCI-*At*GLR1.2	
Primer Name	Sequence 5' – 3'
B107_glr1-2-long-seq1-F	CTTAAGGACTTGGGAACAACTG
B108_p76F-glr1-2-long-seq	ATAATTTGGCCCGGTGGG
B109_glr1-2-long-seq2-F	GCTTCTCTACCCTTGTTTATGC
B442_Glr12_seq_R450	TTGGATCAAGTGAGTGTATTTGC
B443_Glr12_seq_F2357	CCCTATATAGATTCCGTGGTTTG
B501_ glr1-2 long F	GGAGTGCAAGCAATAATTGGC
Construct: pcDNA3-*At*GLR3.4	
Primer Name	Sequence 5' – 3'
B574_GLR3.4 seq Forward_4	CGCGGTTAAAGCAGCTATGG
B575_GLR3.4 seq Rev_1	GGAGATCATGTGAGCAATCCCTG
B576_GLR3.4 seq Forward_5	TCCTTATTTCCTCCGCACCAC
B577_GLR3.4 seq fwd_6	CCAACGATCCAAATCTGCAC
B404_GLR3.4_seq1.fwd	CAGAGACTTGTTGGTTTCTGT
B405_GLR3.4_seq2.fwd	ATCCAGGAGAAGTAACTAAGC
B406_GLR3.4_seq3.fwd	AGCTTCTCAACAATGTTCTTCT
Construct: pcDNA3-*At*GLR3.2	
B521_Atglr3-2_seq01-F	AGATTTCATACAAGGCTGTGC
B522_Atglr3-2_seq02-F	TTCGAGCTCAAACCAACATCTG
B523_Atglr3-2_seq03-F	GTGAGTACACTCGGTCGTGC
B531_GLR3.2_cDNA.fwd	GGATTTGCATTTCCAAGAGAC
B532_GLR3.2_cDNA.rev	TCATATTGGTCTAGAAGGCTTT

***P.patens* growth conditions**

Physcomitrium patens from the gransden strain was cultured for this study. Wild-type, *glr1* and *glr1/2* mutant plants were obtained from Ortiz-Ramirez et al., 2017. Protonema were grown on KNOPS agar or liquid KNOPS supplemented with 0.5g/L ammonium tartrate without glucose at room temperature under 16 hour light exposure and 8 hour dark exposure(366). *P.patens* plants were mechanically disrupted weekly to maintain the protonema stage. For gametophore development, 7 day old cultured protonema were transferred to autoclaved and fully hydrated Jiffy Peat Pellets (Jiffy-7 products) contained in sealed plant culture boxes. Sterile water was supplied to the boxes to leave one-third of the Peat Pellet submerged.

Protoplast generation

Protoplasts were prepared from protonema grown on solid KNOPS media 3 or 4 days after mechanical disruption. Protonema were collected and the cell wall was digested by incubating protonema in a solution of 500 mM D-mannitol supplemented with 1% driselase (Sigma-Aldrich) supernatant for 20-30 min at room temperature. Driselase supernatant was isolated by centrifuging the 1% solution for 5 min at 10,000 x g. Protoplasts were filtered through 50 μm mesh and pelleted by centrifugation 5 min at 250 x g. Pelleted proptoplasts were washed twice in 500 mM D-mannitol before being transferred to the extracellular solution used in patch-clamp recordings.

Chlorophyll measurements

Chlorophyll from *P.patens* gamephores was extracted by 100% DMSO heated to 60˚C for 30min(367, 368). Plant material was harvested from Jiffy Peat Pellets, cleaned, and allowed to dry over the course of the day. Plant material was portioned into 100mg fresh weight samples for incubation in 10mL DMSO. Absorbance at 645nM and 663nM were measured by a spectrophotometer (ThermoSpectronic: GENESYS 10uv) immediately after extraction. Total chlorophyll concentration was calculated according to Arnon's equation(369):

$$\text{Total Chl(g/L)} = 0.0202(A663) + 0.00802(A645).$$

Detection of Autophagy

To detect autophagy, moss protonema were mechanically disrupted and allowed to recover under growth conditions (liquid KNOPS supplemented with 0.5g/L ammonium tartrate without glucose; room temperature 16hour light and 8 hour dark) for 7 days. 7 day old protonema were collected and transferred to sterile microcentrifuge tubes and stored in the dark for 6days before adding pharmacological treatment, 100μM E-64d or 0.1μM concanamycin A. Differential Interference Contrast (DIC) microscopy images were taken under 60x magnification using a DeltaVision Elite Deconvolution/TIRF microscope system (Olympus inverted IX-71).

Structure Determination

Protein expression and purification (Gangwar *et al.*, 2020)(273)

The boundaries of the GLR3.2 ligand-binding domain (S1S2) were determined based on the sequence alignment with GluA2. The DNA encoding AtGLR3.2 residues, S420-V572 (S1) and P682-N811 (S2), were amplified using gene-specific primers and subcloned into the pET22b vector (Novagen) between NcoI and XhoI sites with a GT linker between S1 and S2. For purification purposes, an 8xHis affinity tag followed by a thrombin cleavage site (LVPRG) was introduced at N-terminal.

The construct pET22b carrying GLR3.2-S1S2 was transformed into *Escherichia coli* Origami B (DE3) cells and grown in LB media supplemented with 100 µg/ml ampicillin, 15 µg/ml kanamycin and 12.5 µg/ml tetracycline. The freshly inoculated culture was grown at 37°C until OD_{600} reached the value of 1.0-1.2. Then cells were cooled down to 20°C, induced with 250 µM IPTG, and incubated in the orbital shaker for another 20 hours at 20°C. Cells were harvested by centrifugation at 5488 g for 15 min at 4°C and the cell pellet was washed with the buffer containing 20 mM Tris pH 8.0 and 150 mM NaCl. For protein extraction, cells were resuspended in lysis buffer consisting of 20 mM Tris pH 8.0, 200 mM NaCl, 1 mM glutamate, 5 mM methionine, 1 mM βME, 1 mM PMSF, 100 µg/ml lysozyme, 5 mM $MgSO_4$ and DNAse. All purification steps were carried out in buffers supplemented with 1 mM glutamate and 5 mM methionine. The cells were disrupted by sonication and centrifuged at 18600 g in the Ti45 rotor for 1 hour at 4°C. The supernatant was mixed with His60 Ni superflow resin (Takara) and rotated for 2 hours at 4°C. The protein-bound resin was washed with the buffer containing 15

mM imidazole and the protein was eluted in 20 mM Tris pH 8.0, 150 mM NaCl, 1 mM glutamate, 5 mM methionine, 1 mM βME, and 200 mM imidazole. The protein was dialyzed overnight in the buffer containing 20 mM Tris pH 8.0, 75 mM NaCl, 1 mM glutamate, 5 mM methionine, 1 mM BME, and 4% (v/v) glycerol. After thrombin digest (1:500 w/w) at 22°C for 1-hour, the protein was further purified using ion-exchange Hi-Trap Q HP- (GE Healthcare). The protein quality was assessed by SDS-PAGE and analytical size-exclusion chromatography using the Superpose 10/300 column (GE Healthcare).

Crystallization and structure determination (Gangwar *et al.*, 2020)

Crystallization screening was performed with GLR3.2-S1S2 protein at a concentration of ~7 mg/ml using Mosquito robot (TTP Labtech) and sitting drop vapor diffusion in 96-well crystallization plates. Small needle-shaped crystals, which appeared after two weeks of incubating crystallization trays at 4°C and 20°C, were further optimized using the hanging drop method and 24-well crystallization plates. The best-diffracting long needle-shaped crystals of methionine-bound GLR3.2-S1S2 grew at 20°C in 0.1 M MES pH 6.5, 18% PEG MME 2K and 0.1 M ammonium sulfate. Crystals of glycine-bound GLR3.2-S1S2 grew in a similar condition but in the presence of 0.3 µl of 1M glycine that supplemented the 4 µl crystallization drop as an additive. The best-diffracting needle-shaped crystals of glycine-bound GLR3.2-S1S2 grew at 4°C in 22 % PEG 4K, 0.1 M ammonium acetate, and 0.1 M sodium acetate pH 4.6. All crystals were cryoprotected using 25% glycerol and flash-frozen in liquid nitrogen for data collection.

Crystal diffraction data were collected at the beamline 24-ID-C of the Advanced Photon Source and processed using XDS and Aimless as a part of the CCP4 suit.

The structure of methionine-bound GLR3.2-S1S2 was solved by molecular replacement using Phaser and a search probe generated by SWISS-MODEL homology modeling from the ligand-binding domain of NMDA receptor (PDB ID: 6MMS). The initial partial solution was used again as a search probe for subsequent rounds of molecular replacement, which ultimately resulted in a complete GLR3.2-S1S2 model. The model was refined by alternating cycles of building in COOT and automatic refinement in Phenix. The structure of glycine-bound GLR3.2-S1S2 was solved by molecular replacement using the methionine-bound GLR3.2-S1S2 structure as a search probe. Water molecules were added in Coot and Phenix refine. All structural figures were prepared in PyMol. The protein-ligand interaction plot was created using the Ligplot server.

Appendix A: Primer on electrophysiology

The patch-clamp technique

The patch clamp technique in voltage clamp mode was used extensively to study the electrical properties of cellular membranes(370). A biological cell can be modeled as a simple RC electrical circuit consisting of a resistor and a capacitor in parallel(13) (Figure 51A). The cell membrane acts as a capacitor with an insulating lipid bilayer sandwiched by conducting saline solutions on both sides. Ion channels can be represented as resistors that yield an ionic conductance across the membrane (R= 1/g). Lastly, the membrane potential quantifies an electrical difference across the membrane serving as a battery.

Ion channel research was revolutionized in 1974 by Erwin Neher and Bert Sakmann with the invention of the patch clamp technique(371). The patch clamp technique hacks into the RC circuit with a single electrode to control the membrane voltage and simultaneously measure electrical current. To do so, a glass pipette is pressed against a cell creating a high resistance “giga-Ohm” seal with the cell. Light suction ruptures a patch of the membrane to gain electrical access to the interior of cell entering a configuration known as “whole-cell”. Whole-cell configuration forms a larger electrical circuit in which the single electrode is continuous with the cell plasma membrane and connected to a microelectrode amplifier (Figure 51B).

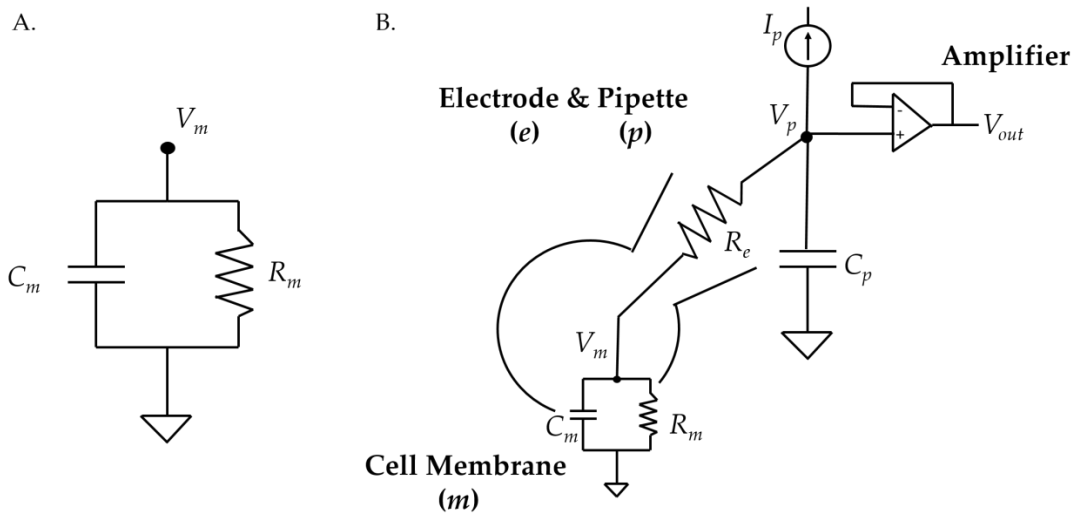

Figure 51: Electrical circuits in biology A.) A simplified electrical circuit represents a biological cell. There is an electrical difference, or "potential" , across the membrane (*Vm*) serving as a battery. The lipid bilayer of the membrane surrounded by conducting saline solutions defines a capacitor (*Cm*). The total electrical resistance of the membrane (*Rm*) is given by the sum of individual resistances of all ion channels that open and close for ion flux across the membrane. B.) Circuit diagram of the whole-cell configuration in voltage-clamp mode. Adapted from Barbour (2011)(372).

Once the electrode has gained access to the interior of the cell, the membrane voltage can then be "clamped" or set to a designated voltage in what is referred to as "voltage-clamp". A constant user-defined membrane voltage (V) and a constant resistance (R) given by the stable ion channel population allows Ohm's Law, V=IR, to be applied for monitoring current (I). The current measured here is the input from the amplifier in order to keep the plasma membrane to the user designated command potential (not the direct current across the membrane). Importantly, the amplifier can only register net current. Therefore, the movement of an anion (of a negative charge) and a cation (of a positive charge) in the same direction across the membrane results in no

difference in membrane voltage. This means no current is injected from the amplifier, so zero current is falsely registered.

Patch-clamp is a powerful method for determining ion selectivity. Ion selectivity analysis typically relies on the cell's reversal potential and each ion's equilibrium potential. The reversal potential (V*rev*) is the membrane voltage at which there is zero net current across the membrane. When current (*I*) is plotted on the y-axis against the membrane voltage (*Vm*) on the x-axis, the V*rev* is where the "*I-V* curve" crosses the x-axis (Figure 52).

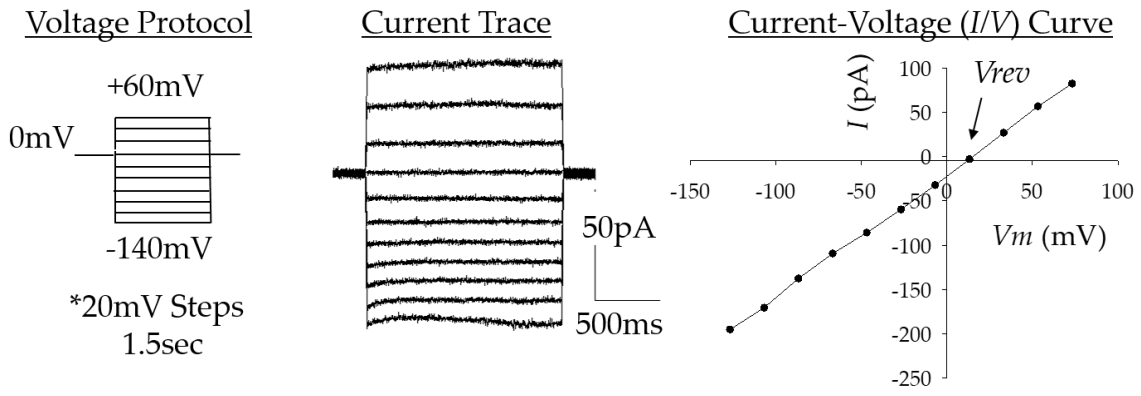

Figure 52: Construction of an *I-V* curve and identification of the *Vrev.*

An ion's equilibrium potential is the membrane voltage where the electrostatic and chemical gradients between the inside and outside of the cell are balanced. This equilibrium potential, often referred to as the Nernst potential, is calculated by Nernst equation (Equation 1).

$$E_{\text{ion}} = \frac{\text{RT}}{\text{zF}} \ln \frac{([\text{ion}]_{\text{o}})}{([\text{ion}]_{\text{i}})}$$

Equation 1: The Nernst equation solves for a given ion's equilibrium potential (E_{ion}). R is the ideal gas constant, T is absolute temperature in Kelvin, z is the ionic valence, F is the Faraday constant and [ion] are the ionic concentrations inside (i) and outside (o) the cell.

The advantage of patch clamp is that the internal and external ionic solutions can be experimentally designed to challenge particular channel properties. Thus, different solutions can be formulated to allow permeable ions to be paired with impermeable to ions thereby isolating specific ionic species. This, in turn, allows equilibrium potentials to be easily manipulated and make recordings amenable to the comparison of *Vrevs*. When recording only passive ion channels, the reversal potential is expected to be the sum of equilibrium potentials for each permeant ion. Therefore, if the reversal potential for the total net current across the membrane matches the equilibrium potential, then it is an indication that the membrane is highly permeable for that particular ionic species. Alternatively, the farther away V*rev* fits to E_{ion}, the less selective it is for that ion.

The overall membrane permeability is estimated by Goldman-Hodgkin-Katz (GHK) equation (Equation 2). This equation takes into account that several moving ions dictate the reversal potential to calculate the relative contribution one ion makes over another. Importantly, the GHK equation assumes that each permeating ion moves independently.

$$Vm = \frac{RT}{F} \ln\left(\frac{\Sigma P_{Cation} [Cation]_o + P_{Anion} [Anion]_i}{\Sigma P_{Cation} [Cation]_i + P_{Anion} [Anion]_o} \right)$$

Equation 2: GHK Equation. *Vm* is the membrane potential, R is the ideal gas constant, T is absolute temperature in Kelvin, F is the Faraday constant and [ion] are the ionic concentrations inside (i) and outside (o) the membrane. P is the permeability of a given ion.

To estimate a permeability ratio between a monovalent anion and cation, using NO_3^- and Na^+ as selected ions, the equation for PNO_3^-/Na^+ can be written as:

$$\Delta Vrev = \frac{RT}{F} \ln\left(\frac{[Na^+]_o + (P_{NO3}/ P_{Na})[NO_3^-]_i}{[Na^+]_i + (P_{NO3}/ P_{Na}) [NO_3^-]_o} \right)$$

Equation 3: GHK Equation for PNO_3^-/Na^+. *ΔVrev* is the shift in reversal potential between two ion concentrations. R is the ideal gas constant, T is absolute temperature in Kelvin, z is the ionic valence, F is the Faraday constant and [ion] are the ionic concentrations inside (i) and outside (o) the membrane.

To estimate a permeability ratio between a monovalent anion and divalent cation, several complications need to be considered to care for the different charges. Using Cl^- and Ca^{2+} as selected ions, the GHK equation requires further derivation to simplify equation for PCa^{2+}/Cl^- and can be written as follows according to Lewis (1979)(297) (with the assumption that $[Ca^{2+}]$cyt is negligible):

$$P_{Ca^{2+}/Cl^-} = \left(\frac{\{([Cl^-]_o\,(e^{V_{rev}F/RT}) - [Cl^-]_i)\,(1+e^{V_{rev}F/RT})\}}{4([Ca^{2+}]_o)} \right)$$

Equation 4: Simplified equation to estimate *PCa^{2+}/Cl$^-$*. *Vrev* is the reversal potential. R is the ideal gas constant, T is absolute temperature in Kelvin, F is the Faraday constant and [Cl^-] or [Ca^{2+}]are the ionic concentrations inside (i) and outside (o) the membrane.

Ion current conventions in patch clamp

Currents are described as either "inward" or "outward" currents based on the convention of a moving positive charge. A positive ion (cation) entering the cell is read as an inward current. A cation leaving the cell is read as an outward current. The movement of a negative charge (anion) is then, by convention, read as the inverse. An anion entering the cell is an outward current and an anion leaving the cell is an inward current. Whether an ion is entering or leaving the cell depends on its equilibrium potential. If the membrane potential is hyperpolarized more negative than the E_{ion}, then the current will be inward. For example, under most conditions, Ca^{2+} has a very positive ECa^{2+} and often exceeds +100mV, so Ca^{2+} is always read as an inward current. When the membrane potential is more depolarized to E_{ion}, then the current will be outward.

Ca^{2+} imaging

Genetically encoded Ca^{2+} indicators (GECI) provide the ability to monitor [Ca^{2+}]cyt as a function of fluorescence. Two classifications of GECI include ratiometric

probes and intensiometric probes. Ratiometric probes offer superior design over the intensiometric probes because they not biased by the protein expression level, heterogeneously distributed within the cytosolic volume, or compartmentalized where Ca2+ is not homeostatically regulated (e.g. ER).

In this work, the ratiometric GECI Yellow CaMeleon 3.6 (YC3.6) was used. YC3.6 has a binding affinity with a Kd of 250nM, conferring the detection of physiological Ca^{2+} concentrations(373). To report a Ca^{2+} signal, YC3.6 uses Förster Resonance Energy Transfer (FRET) technology with two fluorophores; a donor fluorophore (CFP) and an acceptor fluorophore (cpVenus) (Figure 53). A calmodulin (CaM) binding pocket binds free Ca^{2+}. During image acquisition, the donor CFP fluorophore is excited at a light wavelength of 415–445 nm and an emission spectra can be collected from the CFP (455–485 nm) and the acceptor cpVenus fluorophore (520–550 nm). When Ca^{2+} is unbound to the CaM domain, the acceptor and donor fluorophore are too far apart for an electron to transfer from the excited CFP fluorophore to the cpVenus fluorophore by FRET, therefore an emission signal is only detected from the donor (CFP). When Ca^{2+} binds to CaM, a conformational change pulls the acceptor and the donor closer together permitting the transfer of an electron from the donor to excite the acceptor fluorophore yielding a cpVenus fluorescence. The YC3.6 ratio (cpVenus/CFP) ratio is obtained by dividing the emission recorded for cpVenus (520–550 nm) by the one recorded for CFP (455–485 nm).

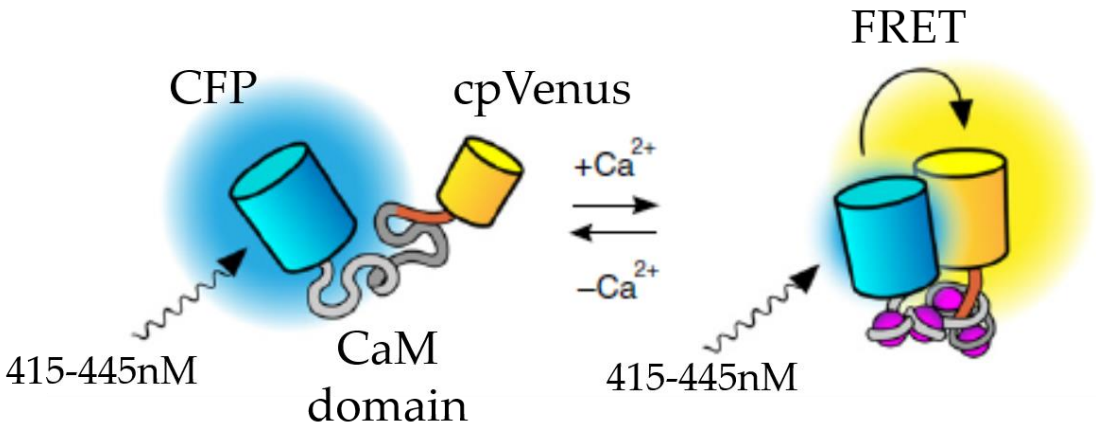

Figure 53: Diagram of FRET-based YC3.6 imaging. Adapted from Koldenkova *et al.*, 2013(374).

Appendix B: Ion signaling in pollen tubes

"Signaling with Ions: The Keystone for Apical Cell Growth and Morphogenesis in Pollen Tubes" emphasizes the membrane transport network annotating the ion channels transporters known to be involved in pollen tube growth and morphogenesis primarily focused on the ions' second messenger roles. With the introduction of the main thesis, a more nuanced perspective can allow the discussion that while second messenger functions are indeed prevalent, the electrical implications of "ion signaling" extend further into areas we have yet to fully grasp. "Ion signaling" can convey the concept that a single ion (particularly, H^+ or Ca^{2+}) may have two roles, including: 1.) its second messenger function and 2.) its electric signal.

Signaling with Ions: The Keystone for Apical Cell Growth and Morphogenesis in Pollen Tubes[1][OPEN]

Erwan Michard, Alexander A. Simon, Bárbara Tavares, Michael M. Wudick, and José A Feijó*

Department of Cell Biology and Molecular Genetics, University of Maryland, College Park, Maryland 20742–5815 (E.M., A.A.S., M.M.W., J.A.F.); and Instituto Gulbenkian de Ciência, Oeiras 2780–901, Portugal (B.T.)

ORCID IDs: 0000-0002-4048-8915 (B.T.); 0000-0002-4332-369X (M.M.W.); 0000-0002-1100-5478 (J.A.F.).

Pollen tubes (PTs) are one of the best characterized plant cell types in many respects. The identification of key players involved in tube growth offers the perspective of an integrative understanding of cell morphogenesis processes. One outstanding feature of PTs is their prominent dependence on ion dynamics to promote and regulate growth. Many reports have identified and characterized membrane transport proteins, such as channels, transporters, and pumps, as well as their regulatory mechanisms, some of which themselves are dependent on ions such as Ca^{2+} and H^+. The signaling network that governs growth is based on a strict spatial distribution of signaling molecules, including apical gradients of Ca^{2+}, H^+, and reactive oxygen species. A central role for ion homeostasis, and more generally membrane transport systems, is proposed to underlie the spatiotemporal establishment of the signaling network that controls the PT self-organization and morphogenesis. Here, we review the latest progress on understanding tube growth from the perspective of membrane transporters and ion homeostasis. The ongoing molecular characterization of the Ca^{2+}-signaling pathways, as well as the recent identification of female external cues and corresponding receptors on the pollen that control growth orientation, offer a firm biological context to boost the field even further.

POLLEN TUBES AS A TAILORED MODEL FOR STUDYING ION DYNAMICS AT THE CELL BIOLOGY LEVEL

Pollen tubes (PTs) have long been considered outstanding models for cell biology for a variety of reasons. On the one hand, they display dramatic features at the level of cell polarity, cytoskeleton dynamics, growth rates, membrane recycling, cell-cell interaction mechanisms, etc. (Cheung and Wu, 2007; Michard et al., 2009; Qin and Yang, 2011; Hepler, 2016). On the other hand, their study is backed up by extensive databases on transcriptomics and proteomics on practically all of its biological contexts (Honys and Twell, 2003; Pina et al., 2005; Borges et al., 2008; Qin et al., 2009; Boavida et al., 2011; Mayank et al., 2012; Pertl-Obermeyer et al., 2014; Lang et al., 2015). All these features define a unique cell type so evolutionarily streamlined to fast growth and sperm delivery (Williams, 2008) that it remained basically conserved as the only gametophyte developmental end product for male function since the

ADVANCES

- Pollen tube growth is strictly dependent on ion dynamics, and this property has been used to detect phenotypes of novel ion transport proteins.
- Ion fluxes and cytosolic gradients of concentration have been mechanistically associated with the action of specific transporters, especially for protons.
- GLR channels and CNGCs have been established as cation-transporting channels with a role in Ca^{2+} homeostasis and signaling in growing pollen tubes.
- Ca^{2+} and ROS signaling networks are interconnected and are key elements to regulate RHO GTPases, NADPH oxidases, and Ca^{2+} downstream signaling cascades.
- Specific temporal patterns of cytosolic Ca^{2+} have been implicated in various steps of fertilization, suggesting the existence of cell-cell communication events that are mediated by Ca^{2+} signaling.

[1] This work was supported by the National Science Foundation (grant no. MCB 1616437/2016) and the University of Maryland.

* Address correspondence to jfeijo@umd.edu.

[OPEN] Articles can be viewed without a subscription.
www.plantphysiol.org/cgi/doi/10.1104/pp.16.01561

Cretaceous (Rudall and Bateman, 2007). PTs in angiosperms can grow up to 4 $\mu m \cdot s^{-1}$ and are characterized by the periodic formation of callose plugs that isolate older parts of the tube to die so that growth can be maintained continuously restricted to the apical end (for review, see Boavida et al., 2005a, 2005b). In plants, PTs share the same type of apical growth mechanism with root hairs, a fact that is reflected at the molecular level by the existence of an apical signature in transcriptomics profiles (Becker et al., 2014). Root hairs, however, grow slower than PTs. In addition, root hair length is controlled through a signaling network involving ROOTHAIR DEFECTIVE SIX-LIKE (RSL) transcription factors (Honkanen and Dolan, 2016). In spite of those main differences, the apical growth of root hairs and PTs is characterized by apical exocytosis of new cell wall material, similar ion gradients, fluxes at the tip, and a mechanism depending on actin cytoskeleton supporting cell elongation (Gu and Nielsen, 2013; Ketelaar, 2013; Mendrinna and Persson, 2015; Mangano et al., 2016).

With so many peculiarities and extreme adaptations to function, the applicability of PT-specific mechanisms to other plant somatic cells, namely diffuse growing ones, is not always straightforward. This assumption is clearly reflected in the well-differentiated transcriptomic profiles between PTs and those of other organs and tissues (for snail-view representations, see Becker et al., 2003; Pina et al., 2005). The one feature in PTs that stands out the most is their strict dependence on ion dynamics to grow and sustain their functions (Michard et al., 2009). Different ions, namely calcium (Ca^{2+}), protons (H^+ or pH), and chloride (Cl^-), form stable/standing gradients of cytosolic concentration in the clear zone (Fig. 1). Of relevance, these spatial patterns and their temporal and spatial variations or choreographies, correlate remarkably well with the intracellular structure of PTs, be it the grading of organelle sizes defining the so-called clear zone, the cytoplasmic reverse fountain (Cheung and Wu, 2007; Hepler and Winship, 2015), and, to some extent, the definition of the membrane-recycling domains in the tip (Parton et al., 2001; Bove et al., 2008; Kost, 2008; Bloch et al., 2016; Wang et al., 2016; Fig. 1). The existence of these ion gradients as a putative central coordinating mechanism for cellular growth and morphogenesis in PTs has been conceptualized elsewhere (Feijó et al., 1995, 2001; Michard et al., 2009; Daminelli et al., 2017). Largely believed to be generated from plasma membrane (PM) activity, the ion choreography of PTs is easily traceable by noninvasive methods such as ion-specific vibrating probe electrophysiology and ion-specific probe imaging to show nearly perfect correlation with growth variations while also allowing one to score for very subtle phenotypes hardly detectable in other nongrowing cells (Michard et al., 2011).

Of relevance, growth rate, ion fluxes, and concentrations may oscillate in PTs, as well as during root hair growth. Some studies present the choreography of ion fluxes and intracellular ion concentrations by a relative lag time during a growth period in PT (for review, see Holdaway-Clarke and Hepler, 2003; Hepler et al., 2013) and root hair (Monshausen et al., 2007, 2008). In such studies, the minimum pH or maximum Ca^{2+} oscillations and growth peak display a time lag of a few seconds in both PT and root hairs, suggestive of similar regulation mechanisms of growth. Of note, the flux of Cl^- was found to be in phase with growth (Zonia et al., 2002). Nevertheless, different estimates of advances and delays have been collected in a variety of biological systems like lily (*Lilium longiflorum*), tobacco (*Nicotiana tabacum*), petunia (*Petunia hybrida*), less in Arabidopsis (*Arabidopsis thaliana*), using imaging techniques (differential interference contrast, wide-field or confocal fluorescence), and electrophysiology methods in such ways that comparisons of the published delays and proposed sequences of events are subject to potential distortions (Portes et al., 2015; Daminelli et al., 2017). Last but not least, correlation does not imply causation, and not much can be deduced from those studies, particularly because we do not know the kinetic properties of key reactions within the networks, such as molecular diffusion, protein phosphorylation, exocytosis, etc. (Daminelli et al., 2017)

Figure 1 highlights the peculiar correlation between ion dynamics and cell structure. Spatial correlations between features of the cytosolic gradients (Fig. 1, B, C, and E) and other cellular structures are conspicuous and easily observed at the level of zonation of organelles along the clear zone (Fig. 1A) or the actin cytoskeleton (Fig. 1D). Characterizing the transport molecules that generate these gradients may be a first step in their manipulation and eventually may test the hypothesis that spatial correlations are not a mere phenomenological coincidence but may actually be causal and part of a network of regulatory feedback loops. One first step in that direction is the establishment of a functional correlation between the transport molecules and the predicted outcome of their activity in terms of ion dynamics, whether at the level of cytosolic concentration or of membrane transport. One such example is also offered in Figure 1, where the localization of the H^+-ATPase NICOTIANA TABACUM AUTOINHIBITED H^+-ATPASE (NtAHA1) (Fig. 1F) correlates perfectly with the existence of intracellular pH domains (Fig. 1E) and extracellular H^+ fluxes (Fig. 1G; Certal et al., 2008; Michard et al., 2008). The fact that this crucial pump is segregated from the tip PM triggers a number of testable models and by itself already defines an experimental paradigm offered uniquely by PTs.

In Arabidopsis, more than 800 transporter transcripts have been identified in pollen using the ATH1 mRNA microarray (Pina et al., 2005; Bock et al., 2006), and this overrepresentation is confirmed by RNA sequencing in Arabidopsis and lily (Loraine et al., 2013; Lang et al., 2015). This is perhaps one of the reasons why PTs have been widely explored in recent years for phenotyping an increasing repertoire of channels, transporters, and pumps, rendering the vegetative cell of the PT likely one of the best studied cells in plants in terms of ion

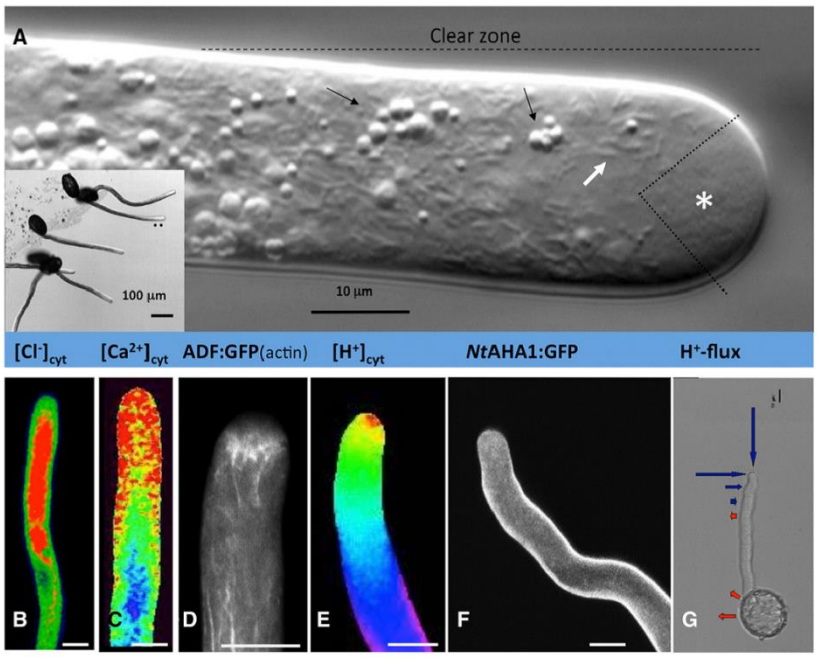

Figure 1. The ion dynamics regulatory paradigm of the PT structure is supported by strong spatial correlations. A, Lily PTs (differential interference contrast imaging) display the quintessence of the dramatic polarization of these cells. Actin-driven reverse-fountain cytoplasmic movement drives organelles to the tip by the periphery and back through the tube core. Yet, this back-turning movement occurs some 20 to 50 μm back from the tip, resulting in a pattern best described as if there is a size-sorting or sieving mechanism, first dispatching back big starch plastids (black arrows), then mitochondria (white arrow) and other larger endomembrane formations, and only allowing small exocytic vesicles to the very tip (asterisk). This pattern generates two clearly observable cytologic domains: the clear zone, defined by the absence of large plastids and many times seen at low magnification (double asterisk in the inset), and an inverted cone (Lancelle et al., 1987) of small vesicles that, contrary to the rest of the tube shank, move in a nonorganized Brownian-like motion (dashed lines on the tip). B to G, In tobacco PTs, these domains are remarkably correlated with cytosolic ion concentrations of Cl^- (B), Ca^{2+} (C), and H^+ (E) when live imaged with specific fluorescent genetic probes. The acidic tip (E) very closely defines the inverted cone and is also correlated with a lower concentration of Cl^-. In tobacco, the inverted cone also seems to be lined up by a concentration of small, highly dynamic actin filaments (D) that are often organized as a basket or fringe (Rounds et al., 2014). The clear zone is correlated with both the fading of the Ca^{2+} and the acidic gradients focused on the tip. The base of the clear zone also defines the appearance of the long actin filaments that support organelle streaming. A causal correlation between a specific transporter distribution and cytosolic concentration of an ion is best seen for H^+, where the localization of the most highly expressed P-type ATPase in tobacco, NtAHA1 (F; Certal et al., 2008), closely correlates with the extracellular H^+ fluxes (G; effluxes in red and influxes in blue) and cytosolic pH (E). H^+ effluxes, on the other hand, correlate with the presence of the chimeric NtAHA1::GFP protein, and influxes correlate with their absence on the tip. Last but not least, the acid tip (red in E) correlates with the largest influxes and the submembranar alkaline linings (purple in E) correlate with effluxes. Bars = 10 μm. (The image in A is by N. Moreno, adapted from Taiz et al. [2015] and Smith et al. [2009]; the image in B is adapted from Gutermuth et al. [2013]; the images in C and E are adapted from Michard et al. [2008]).

dynamics. Figure 2 and Table I summarize this accumulated knowledge. They incorporate not only genes that have already been characterized but also genes that can be predicted from transcriptomics, proteomics, and comparative physiology to play roles in PT growth. In this review, we focus on organizing or systematizing this growing repertoire, focusing on three different angles. (1) Is this knowledge sufficient to define regulatory mechanisms around a specific ion? (2) What are the downstream targets of specific ions? And (3) how do cellular processes feed back to regulate ion transport?

OPPOSING FORCES: TURGOR AND CELL WALL DEPOSITION

When growing PTs or root hairs stop in response to an osmotic shock, the exocytosis of vesicles ensuring cell wall deposition continues at the tip (Schroeter and

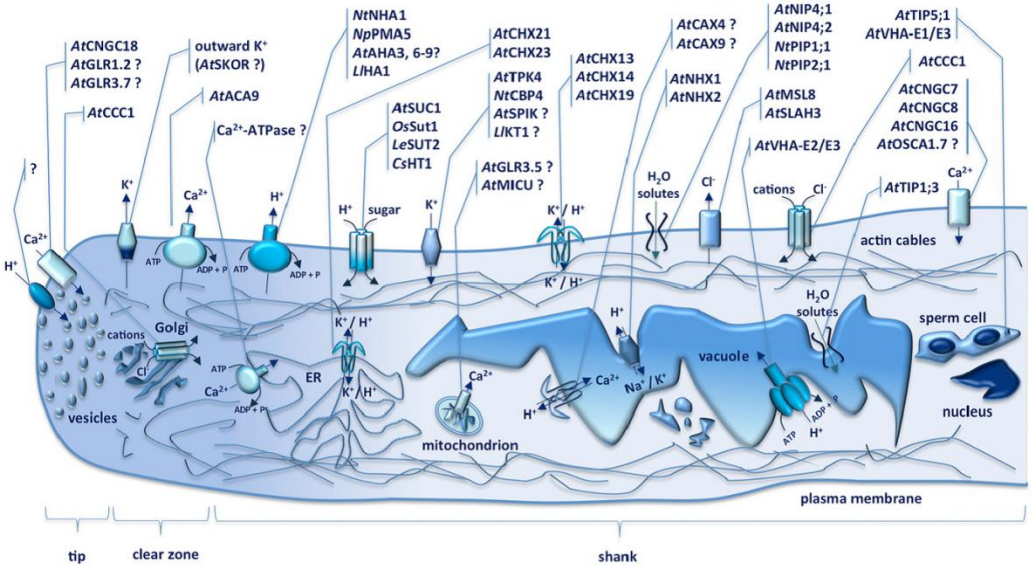

Figure 2. Molecular basis for the transmembrane transport in the PT. A schematic overview of ion and solute transport in the PT is shown. Gradients of different ion concentrations (e.g. H^+, Ca^{2+}, and Cl^-) differentiate the clear zone from the shank region and are essential for the polarized growth of the tube. We posit that, like cytosolic pH (Fig. 1), ion homeostasis along these gradients is reached by the integrated transport activity of a network of different transport molecules distributed between the tip, shank, and internal domains of the tube. Depicted on the images are the channels, transporters, and pumps that were either genetically described or putative but deemed to be essential from transcriptomic analysis (question marks) to form the ion choreography of a pollen tune (for details, see Table I). *At, Arabidopsis thaliana*; *Cs, Cucumis sativus*; *Le, Solanum lycopersicum*; *Ll, Lilium longiflorum*; *Np, Nicotiana plumbaginifolia*; *Nt, Nicotiana tabacum*; *Os, Oryza sativa*. (This image is not drawn to scale.)

Sievers, 1971; Li et al., 1996; Zerzour et al., 2009). Apparently, the main control of the apical growth process does not depend on turgor as much as on other plant cells (Cosgrove, 2014; Ali and Traas, 2016). Quantification of the opposing growth forces in lily PTs led to a difference of 2 orders of magnitude between the internal turgor pressure (approximately 0.3 MPa) and the cell wall elasticity (approximately 20–90 MPa; Vogler et al., 2012), clearly bringing other growth control mechanisms than turgor to the board. Supporting this concept, growth can be arrested by nonrelated turgor means, such as caffeine treatment (Li et al., 1996). Yet, despite the fact that there is no correlation between turgor and growth rate, a minimal turgor pressure of approximately 0.3 MPa is necessary to sustain PT growth in lily (Benkert et al., 1997). The general consensus is that turgor drives the PT growth by providing a minimal mechanical force necessary for cell wall elongation at the tip but that it plays no or a minor regulatory role. Various theoretical approaches have tried to bridge these opposing forces at work by modeling anisotropic-viscoplastic properties (Dumais et al., 2006), the incorporation of new cell wall material, particularly pectine esters, as a key factor in softening the wall by affecting polymer cross-links (Rojas et al., 2011), and finite element analysis methods (Fayant et al., 2010; Vogler et al., 2012). A discussion of the opportunities and caveats of these models is beyond the scope of this review, and here we focus on the facts that (1) turgor is a direct consequence of water transport driven by small solutes, notably ions, and (2) ions such as Ca^{2+} and H^+ are involved in the mechanical maturation of cell walls.

PTs can appropriately adjust turgor pressure by adapting to changes in external osmolarity (Benkert et al., 1997), but no osmosensor has yet been characterized. Mechanosensitive ion channels like the cation channel REDUCED HYPEROSMOLALITY-INDUCED $[Ca^{2+}]_i$ INCREASE1 (AtOSCA1) (Yuan et al., 2014) or the anion channel MECHANOSENSITIVE CHANNEL OF SMALL CONDUCTANCE-LIKE (AtMSL8) (Hamilton et al., 2015) offer a conceptual basis for a sensor, but so far the reported ion currents and phenotypes of these channels do not warrant that they may be acting in PT growth.

Several arguments can be raised regarding the role of aquaporins in facilitating water transport in PTs (Obermeyer, 2017). Pollen aquaporins of the SMALL BASIC INTRINSIC PROTEINS (SIP) and TONOPLAST INTRINSIC PROTEIN (TIP) clade have been located at endomembranes (Ishikawa et al., 2005; Wudick et al., 2014), while NOD26-LIKE INTRINSIC PROTEINS

Table I. *Summary of molecular data available on the physiological role of ion or turgor-related membrane transport proteins in PT growth, gathered by function (pumps, channels, cotransporters, and aquaporins) and selectivity (sugars, anions, potassium, and cations)*

For each transporter and corresponding genomic identifier, the molecular function and the biological system in which it has been established are indicated as well as the intracellular localization and the localization method(s) used. Physiological relevance is defined by phenotypes of knockdown or overexpressing lines, when available, or other physiological traits. Putative genes are indicated when (1) transcriptomics indicated pollen selective and high expression and (2) function has been defined for the gene family in other tissues. n/a, Not available.

Name	Locus Identifier	Function (System[a])	Localization[b] (Method[c])	Physiological Relevance[d]	Reference
Pumps					
NtAHA1	AY383599	P-type ATPase; proton pump (P)	PT, PM, shank (FP)	OX: slowed growth rate, callose plug deformation	Certal et al. (2008)
NpPMA5	AY772462 AY772468	P-type ATPase; proton pump (Y)	Shank PM (I)	?	Lefebvre et al. (2005)
LlHA1	AY029190	P-type ATPase; proton pump (P)	PG, PM (PC)	H^+ currents under patch clamp	Gehwolf et al. (2002)
AtAHA3	At5g57350	P3A-type ATPase; proton pump (P)	PM?	Expressed during pollen development (GUS); KO: lethal	Robertson et al. (2004)
AtAHA6 AtAHA7 AtAHA8 AtAHA9	At2g07560 At3g60330 At3g42640 At1g80660	P3A-type ATPase; proton pump?	PM?	Putative, based on expression levels (AHA8), homology with Nt and Ll, and pollen selective (AHA6, AHA7, and AHA9)	Pina et al. (2005); Bock et al. (2006); Lang et al. (2015)
AtACA9	At3g21180	P2B-type ATPase; calcium pump (Y)	PM (FP)	KO: partial male sterility	Schiott et al. (2004)
AtVHA-E1 AtVHA-E2 AtVHA-E3	At4g11150 At3g08560 At1g64200	Vacuolar H^+-ATPase (P)	E1, vacuoles and endosomes of sperm cell; E2, vegetative cell, pollen specific; E3, vegetative cell and sperm cell vacuole (FP)	E1, KO is embryo lethal; E2, KO has no phenotype; E3, partially redundant to E1, possible stress response implications	Strompen et al. (2005); Dettmer et al. (2010)
Suc transporters					
AtSUC1	At1g71880	Suc carrier (P)	PM, around callose plugs and cytoplasm near PT tip (FP)	KO: reduced pollen germination rate	Stadler et al. (1999); Sivitz et al. (2008)
OsSUT1	Os03g07480	Suc transporter (P)	?	KO: impaired germination rate	Hirose et al. (2010)
LeSUT2	Solyc11g017010	Suc transporter (P)	PT, PM (I)	AS: decreased amounts of soluble sugars, inhibited PT growth	Hackel et al. (2006)
CsHT1	GenBank HQ202746	Hexose transporter, high affinity for Glc (Y)	PM (FP)	OX: higher pollen germination rate, increased tube growth; AS: inhibited germination and elongation, fewer seeds	Cheng et al. (2015)
AtSWEET8/ AtRPG1	At5g40260	Suc transporter (P, H, Y)	PM (FP)	KO: male fertility phenotype, microsporogenesis, exine formation and cell integrity	Guan et al. (2008); Chen et al. (2010); Sun et al. (2013)
Anion channels and transporters					
AtSLAH3	At5g24030	Anion channel (P, O)	PM (FP)	Voltage clamp: regulated by AtCPK2 and AtCPK20	Gutermuth et al. (2013)
AtMSL8	At2g17010	Anion channel (O)	PM, endomembranes (FP)	WT: mechanosensitive; KO: improved germination;OX: inhibited germination (negatively regulates)	Hamilton et al. (2015)

(*Table continues on following page.*)

Table I. (*Continued from previous page.*)

Name	Locus Identifier	Function (System[a])	Localization[b] (Method[c])	Physiological Relevance[d]	Reference
AtCCC1	At1g30450	Cl^-/cation cotransporter (O)	PM, Golgi (FP)	Pollen expression; KO: aborted siliques, seed-set reduction	Colmenero-Flores et al. (2007); Kong et al. (2011); Henderson et al. (2015)
Potassium channels					
AtSPIK (AtAKT6)	At2g25600	K^+ channel (C)	PM (PC)	WT: voltage dependent, inward currents, CsCl inhibition; KO: disrupted pollen germination, slower tube growth, fertility affected	Mouline et al. (2002)
LilKT1	Gene n/a; protein A3RG92	K^+ channel (P, Y)	Cytoplasm, punctate; PM in tobacco epidermis (FP)	?	Safiarian et al. (2015)
AtTPK4	At1g02510	K^+ channel (P, O, Y)	PM (PC)	WT: regulated in pH, calcium-dependent manner	Becker et al. (2004)
AtSKOR	At3g02850	Outward-rectifying K^+ channel	?	Putative, pollen selective	Pina et al. (2005)
Cation channels and transporters					
AtCNGC7 AtCNGC8	At1g15990 At1g19780	Cation channel?	AtCNGC7: tip PM during tube emergence, PT shank during elongation (FP)	WT: pollen fertility, initiation of PT growth; double KO: male sterile	Tunc-Ozdemir et al. (2013a)
AtCNGC16	At3g48010	Cation channel?	?	WT: PT germination and growth during stress; KO: reduced competitive fitness, fewer seeds, low pollen transmission	Tunc-Ozdemir et al. (2013b)
AtCNGC18	At5g14870	Ca^{2+} permeation (E), nonselective cation channel (H)	PT apical PM (FP)	WT: Ca^{2+} influx; KO: sterile	Frietsch et al. (2007); Gao et al. (2016)
AtCAX4 AtCAX9	At5g01490 At3g14070	Cation/Ca^{2+} exchanger	Endomembranes	Putative, pollen selective	Pina et al. (2005); Morris et al. (2008)
AtGLR1.2	At5g48400	Cation channel, Ca^{2+} permeable (P)	Ca^{2+} influx at PT tip PM (VP)	WT: Ca^{2+} influx, PT growth, and morphogenesis; KO: AS, partial male sterility	Michard et al. (2011)
AtGLR3.7	At2g32400	Cation channel?	?	KO: decreased growth rate, partial male sterility	Michard et al. (2011)
AtGLR3.5	At2g32390	Cation channel?	Mitochondria, chloroplast (FP)	KO: disrupts the formation of mitochondria and Ca^{2+} uptake	Teardo et al. (2015)
AtOSCA1.7	At4g02900	Ca^{2+}-permeable? osmolarity gated?	PM?	?	Hou et al. (2014); Yuan et al. (2014)
AtMICU	At4g32060	Ca^{2+}-binding protein (P)	Mitochondria (I, FP)	KO: higher free Ca^{2+} in mitochondria, faster and higher Ca^{2+} accumulation in response to auxin and extracellular ATP	Stael et al. (2012); Wagner et al. (2015)
H^+/cation cotransporters					

(*Table continues on following page.*)

Table I. (*Continued from previous page.*)

Name	Locus Identifier	Function (System[a])	Localization[b] (Method[c])	Physiological Relevance[d]	Reference
AtCHX19	At3g17630	Cation channel?	PM (FP)	KO: *chx17/chx18/chx19* mutant pollen normal, reciprocal cross experiments indicate a largely male defect	Padmanaban et al. (2016)
AtCHX13	At2g30240	K^+ acquisition, high-affinity K^+ uptake (Y)	PM (FP)	Roots and seedlings: KO: sensitive to K^+ deficiency; OX: reduced sensitivity to K^+ deficiency; no pollen phenotype	Sze et al. (2004); Zhao et al. (2008)
AtCHX14	At1g06970	Low-affinity K^+ efflux (P, Y)	PM (FP)	KO and double KO *chx13/14*: root growth sensitive to high K^+; OX: root growth increase in high K^+; no pollen phenotype	Sze et al. (2004); Zhao et al. (2015)
AtCHX21	At2g31910 At1g05580	AtCHX23: K^+ uptake in a pH-dependent way (E)	Endomembranes (FP)	KO: PT navigation	Sze et al. (2004); Evans et al. (2011); Lu et al. (2011)
AtCHX23					
AtNHX1	At5g27150	Na^+/H^+ antiporter (P)	Vacuole (FP)	Double KO: pollen unaffected; regulates pH and K^+ homeostasis	Bassil et al. (2011)
AtNHX2	At3g05030				
Aquaporins					
AtNIP4;1	At5g37810	Water and nonionic solute channels (O)	AtNIP4;1, PM and intracellular vesicles in PT, pollen grains; AtNIP4;2, PM and intracellular vesicles of PT only (FP)	KO: fewer seeds, reduced pollen germination and PT length	Di Giorgio et al. (2016)
AtNIP4;2	At5g37820				
NtPIP1;1	AF440271	Water channels (O)	PM?	Pollen dehydration and dehiscence	Bots et al. (2005)
NtPIP2;1	AF440272				
AtTIP1;3	At4g01470	Regulation of water fluxes?, water and solute transport (O)	TP of vegetative cell (FP)	Double KO with AtTIP5;1 revealed poor seed development and silique growth	Soto et al. (2008); Wudick et al. (2014)
AtTIP5;1	At3g47440	Regulation of water fluxes?, water and solute transport (O)	TP of sperm cells (FP)	Double KO with AtTIP1;3 revealed poor seed development and silique growth	Soto et al. (2008); Wudick et al. (2014)

[a]C, COS cells; E, *Escherichia coli*; H, HEK cells; O, *Xenopus laevis* oocytes; P, plant; Y, yeast. [b]TP, Tonoplast. [c]FP, Fluorescent protein fusion; I, immunodetection; PC, patch clamp; VP, calcium-selective vibrating probe. [d]AS, Antisense line; KO, knockout line; OX, overexpression line; WT, wild-type line.

(NIP) aquaporins were localized in the pollen PM (Lang et al., 2015). Heterologous overexpression of PLASMA MEMBRANE INTRINSIC PROTEIN (AtPIP) aquaporins yielded an increase of the water permeability of lily pollen but no evident functional phenotype (Sommer et al., 2008). Aquaporins from the SIP, TIP, and NIP families were shown to transport water and/or solutes and appear to be involved in PT growth (Ishikawa et al., 2005; Soto et al., 2008; Di Giorgio et al., 2016) and fertilization (Wudick et al., 2014). Interestingly, although not expressed in pollen, it was reported recently that AtPIP2;1 also shows a nonselective cation channel activity (Byrt et al., 2016), a feature that might be found for other members of the aquaporin family.

Ion-driven osmotic changes induce electric potential shifts at the PM in addition to external pH along the PT, and osmoregulation depends on an active transport system driven by the proton pump, through 14-3-3 protein regulation (Pertl et al., 2010). Several H^+-ATPase pumps are expressed in pollen (Pina et al., 2005; Bock et al., 2006), with AtAHA8 being the most highly expressed and AtAHA6, AtAHA7, and AtAHA9 being pollen specific (Table I). In tobacco, a close homolog of AtAHA6 and AtAHA9, NtNHA1, was found to be localized on the PM but segregated from the tip and involved in tube growth and callose plug formation (Certal et al., 2008). These pumps are likely to energize the transport of other molecules that underlie turgor in PTs, such as sucrose (Stadler et al., 1999; Goetz et al., 2001). While not necessarily affecting only PT growth, the Arabidopsis AtSUC1 and rice (*Oryza sativa*) OsSUT1 sucrose transporters have defective male gametophyte phenotypes (Sivitz et al., 2008; Hirose et al., 2010). In cucumber (*Cucumis sativus*), the hexose transporter CsHT1 is necessary for PT growth (Cheng et al., 2015). Despite probably being related to microsporogenesis and exine pattern formation, mutants of the PM-localized sucrose transporter AtRPG1/AtSWEET8 display fertility defects (Guan et al., 2008; Chen et al., 2010; Sun et al., 2013).

However, and importantly, ion fluxes such as anions (Zonia et al., 2002) or K^+ may participate in turgor generation. K^+ inward conductivities have been recorded by patch clamp and voltage clamp in lily and Arabidopsis (Mouline et al., 2002; Griessner and Obermeyer, 2003; Becker et al., 2004). The inward rectifier AtSPIK channel is involved in PT growth (Mouline et al., 2002), and AtTPK4 mediates nonrectifying currents and also may participate in osmotic regulation of the PT (Becker et al., 2004). For anions, major solutes associated with water movement and turgor in animals and plants, only AtSLAH3 has been characterized in PTs (Gutermuth et al., 2013), but it only accounts for a small percentage of the total anion flux. Yet the demonstration of a role for anion channels in stomatal turgor regulation offers an analogy that could eventually serve as a conceptual template to screen for their identity in PTs (see Text Box 1; Fig. 3). High turgor pressure typically induces the bursting in both hyphea, another tip-growing cell (Money and Hill, 1997), and PTs (Benkert et al., 1997; Amien et al., 2010). The rupture point always being the tip suggests anisotropy in the cell wall mechanical properties, characterized by a stronger shank. In hyphae, the turgor pressure plays a minor role in polarization; rather, the apical localization of lytic enzymes that loosen the cell wall determines the growth rate and polarity (Money and Hill, 1997). Similarly, PT growth is sustained by the deposition of primary cell wall material at the apex; once deposited at the tip, the wall is subject to a maturation process that stiffens it, creating a gradient of viscosity/elasticity between the growing tip and the nongrowing tube (Hepler et al., 2013; Cosgrove, 2016). Despite discrepancies over the quantification of the mechanical properties of the cell wall (Fayant et al., 2010; Vogler et al., 2012), many biochemical data demonstrate its anisotropic composition and suggest a viscosity gradient along the tube (Steer and Steer, 1989; Geitmann, 2010; Chebli et al., 2012; Hepler et al., 2013). The primary cell wall of the PT deposited at the apex is essentially composed of pectin plus 2% to 3% cellulose (Aouar et al., 2010; Derksen et al., 2011). Pectins are exported as methyl esters and, in parallel, some pectin methylesterase enzymes (PME) are secreted by the PT and catalyze pectin deesterification. This pectin chemomechanical structure largely determines the growth of the tube, as revealed by pectinase treatment that affects growth properties and induces tube swelling (Parre and Geitmann, 2005) and by the PME mutant vanguard1 PTs, which are slower and burst precociously (Jiang et al., 2005). Both Ca_{21} and H_1 either cross-link pectin polymers to induce the formation of a gel or regulate the activity of PMEs, coordinating the stiffening of the cell wall (Bosch et al., 2005; Bosch and Hepler, 2005; Parre and Geitmann, 2005; Tian et al., 2006; Vieira and Feijó', 2016). pH regulation of root cell elongation has been demonstrated directly (Fendrych et al., 2016). Thus, while never directly demonstrated, the regulation of the excretion of these ions to the apoplast could have a regulatory role in the anisotropy of cell wall mechanics of PTs.

ION FLUXES AND GRADIENTS AT THE TIP: AN ELECTRIFYING AFFAIR?

The particular constitution and regulation of the tip domain of the PT PM is such that large extracellular ion fluxes and cytosolic gradients are formed (Fig. 1). Ion fluxes, and in particular the huge anion efflux at the tip (Zonia et al., 2002; Gutermuth et al., 2013), are expected to generate an osmotic gradient, an extracellular electric field, and, as discussed below, eventually a membrane voltage gradient along the length of the PM. In Arabidopsis, the accumulation of vesicles at the apex is enough to sustain a 30-s growth period (Ketelaar et al., 2008). It has been proposed that vesicles in the clear zone are governed mainly by Brownian dynamics because of the apparent disorganization of the actin cytoskeleton in this region (Kroeger et al., 2009). But the existence of such dramatic ion gradients also may play a role in the movement of vesicles by either electrostatic

BOX 1. Taming turgor, the force that sustains growth: lessons from guard cells

PT growth is sustained by a minimum turgor (0.3 MPa in lily; Benkert et al., 1997). The relative importance of turgor and wall mechanics for growth is wrapped in controversy, (Winship et al., 2011; Zonia and Munnik, 2011), but consensus exists around turgor providing the force underlying wall elongation. Turgor implies the accumulation of solutes, namely ions. So how are they transported? And how do ions regulate water flux and turgor?

Guard cells are arguably the best studied cellular system of turgor regulation in plants, relying on H^+, anions, and K^+ to move water in and out of the cell. Evidence for the same exists for PTs: H^+ fluxes are well documented (Feijó et al., 1999; Certal et al., 2008), and large anion fluxes of up to 60 nmol cm^{-2} s^{-1} (Zonia et al., 2002), anion conductivity (Tavares et al., 2011a), and a cytosolic anion gradient (Gutermuth et al., 2013) all have been characterized. Furthermore, K^+ currents and the underlying channels have long been observed in pollen (Obermeyer and Kolb, 1993; Mouline et al., 2002; Becker et al., 2004). So is it possible to establish a parallel between what is known about turgor regulation in guard cells and PT growth?

Similar events leading to the stomata **OPENING** are observable in pollen growth, with the efflux of H^+ in the **SHANK** coupling anion and K^+ influxes (Zonia et al., 2002; Domingos P, Dias PN, Tavares B, Portes MT, Konrad K, Wudick MW, Gilliham M, Bicho A, Feijó JA, unpublished data), which may indicate the water influx point. Conversely, as in stomatal **CLOSURE**, large effluxes of anions, and the influx of H^+ and Ca^{2+}, occur in the pollen **TIP**, the combined effect of which should result in the depolarization of the PM (Michard et al., 2009). We hypothesize that water flows at the pollen tip following the osmotic potential of anions (Cl^-/NO^{3-}) and K^+. This comparison implies that the mechanisms behind the temporal sequence of events in guard cells, leading to a transient water flow, could have been coopted in the PT, in the form of a spatial segregation of transport molecules between shank and tip, leading to the regulation of water transport and turgor necessary for growth (Fig. 3). This concept generates various testable hypotheses and gives ground to new channel discovery in PTs based on similarities with guard cells.

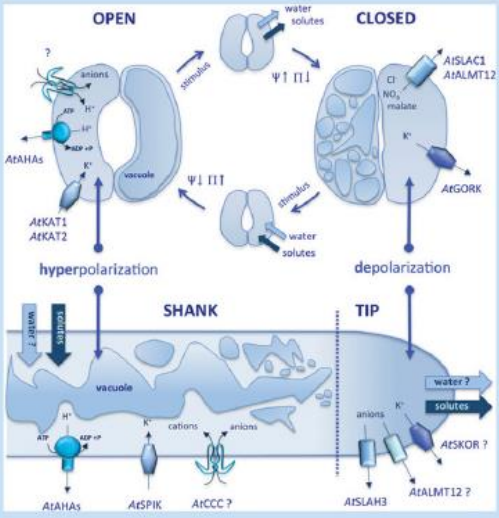

Figure 3. Schematic drawing illustrating the parallels between events leading to the regulation of guard cell (GC) movement (top) and putative mechanisms leading to PT water intake regulation and growth (bottom). Top, Stomatal opening and closing depend on GC turgor pressure regulation and are accompanied by morphological changes of the GC vacuoles. Stomatal opening (left) by stimuli such as light is sustained by solute influx that induces (1) water potential (Ψ) decrease, (2) turgor pressure (Π) increase, and (3) transient water influx. Main solute transporters are indicated in the scheme. H^+ pumps (AtAHA family) hyperpolarize the membrane and generate a H^+ gradient. K^+ enters through hyperpolarization-activated channels (mainly AtKAT1 and AtKAT2), and anions enter through an unidentified H^+/anion cotransporter. During stomatal closure (right), in response to dark or abscisic acid, for instance, solute efflux induces (1) an increase in Ψ, (2) a decrease in Π, and (3) a transient water efflux. The anion channels AtSLAC1 and AtALMT12 catalyze massive anion effluxes that contribute to a depolarization of the PM. Potassium moves out of the cell through the depolarization-activated AtGORK channel. Bottom, The transport system at the shank of the PT is similar to the one involved in the opening of GCs: the activity of H^+ pumps (AtAHAs) couples the influx of K^+ and anions. The hyperpolarization-activated potassium channel involved (AtSPIK) is homologous to AtKAT1/2. The transport system at the growing tip can be compared with the one active in a closing GC: a large anion efflux is induced by the AtSLAH3 channel (homologous to AtSLAC1), and the expression of the depolarization-activated AtSKOR channel (homologous to AtGORK) in pollen may facilitate K^+ efflux. From this comparison of GC and PT, we propose testable hypotheses regarding membrane electric polarization along the PT as well as on water fluxes.

or osmotic influence. PM voltage has been determined to be around −130 mV when measured on the shank of PTs (Mouline et al., 2002; Griessner and Obermeyer, 2003; Becker et al., 2004), a resting potential slightly more negative than the K^+ equilibrium (Mouline et al., 2002). This hyperpolarization is likely driven by H^+-ATPase activity (Lang et al., 2014). Unfortunately, the apical voltage remains unknown, since it is not possible to impale an electrode at the tip without provoking tube burst. Theoretically, apical membrane potential can be inferred to be more positive compared with the shank, since large passive ion fluxes at the tip have a depolarizing effect. Furthermore, H^+-ATPases are excluded from the tip (Certal et al., 2008; Michard et al., 2009), where there is high NADPH oxidase activity (Potocky et al., 2007). This kind of oxidase was proposed recently to generate electrochemical fluxes of ions on their own (Segal, 2016). Voltage at the tip PM and at the shank PM tend to equilibrate to the same value by charge fluxes along the membrane through the

equivalent of an electrical circuit, implying electrical resistance of the cytosol and capacitance of the membrane (Hille, 2001; Michard et al., 2009). Thus, a combination of high enough resistance of the cytosol and strong charge flux density across the PM at the tip could induce a membrane voltage gradient between the tip and the shank, supporting the notion of electrostatic movement of charges. Exocytic vesicles have long been found to bear a negative surface charge (Heslop-Harrison and Heslop-Harrison, 1982), and the existence of electrostatic fields in plant cells was recently proposed to underlie cell identity and signaling, namely by regulating the transfer of proteins from endomembrane to PM on the basis of charge alone (Simon et al., 2016). In animals, membrane depolarization promotes the vesicle exocytosis of pancreas β-cells (Yang et al., 2014; Cardenas and Marengo, 2016). If differential conditions of cytosolic resistance exist, then theoretically such mechanisms also could play a role in vesicle migration and fusion in PTs.

But other cues for polarity could come from anion fluxes. Large anion conductivity has been recorded in both Arabidopsis and tobacco (Tavares et al., 2011a, 2011b) with effluxes up to 60 $nmol \cdot cm^{-2} \cdot s^{-1}$ (Zonia et al., 2002), resulting in an anion gradient (Gutermuth et al., 2013; Fig. 1B). The anion channel AtSLAH3 is partly responsible for this conductance (Gutermuth et al., 2013), but other anion channels expressed in the PT may be involved (Tavares et al., 2011a), like members from the AtALMT family (Meyer et al., 2010). The existence of a gradient and fluxes of anions of such magnitude has been proposed to be physically sufficient to create conditions for an osmotic gradient strong enough to generate thrust for vesicles to move toward a minimum osmotic potential at the apex through the process of osmophoresis (Lipchinsky, 2015). While proposed on theoretical grounds, the existence of biophysical mechanisms for the vectorial movement of vesicles in the clear zone is an exciting new prospect calling for experimental validation.

Although the direction of potassium fluxes in the tip is still debated, anion fluxes must be compensated by cation efflux (Michard et al., 2009). K^+ outward currents have been recorded by patch clamp (Griessner and Obermeyer, 2003) but remain unaccounted for in terms of the channel generating them. The SKOR K^+ channel is known to be expressed in pollen (Pina et al., 2005) and constitutes a good candidate for that function. Other channels, namely nonselective cationic channels, as well as transporters from the cation-proton antiporter family also could play a role in anion flux compensation (see below).

The Ca^{2+} Affair

A Ca^{2+} gradient in which intensity correlates with growth rate has long been described in PTs (Reiss and Herth, 1985; Obermeyer and Weisenseel, 1991; Rathore et al., 1991; Pierson et al., 1994, 1996; Malho et al., 1995; Michard et al., 2008; Iwano et al., 2009; Fig. 1C). When the tube is reversibly stopped by caffeine or low temperature, the Ca^{2+} gradient dissipates and the Ca^{2+} influx is lowered to a basal level; regrowth reconstitutes the Ca^{2+} gradient and influx (Pierson et al., 1996). Ca^{2+} channel activity was early deduced by quenching with Mn^{2+} (Malho et al., 1995). Several types of channels permeable to Ca^{2+} have been characterized by patch clamp either as inward rectifiers in Arabidopsis and pear (*Pyrus communis*; Wang et al., 2004; Shang et al., 2005; Wu et al., 2010, 2014) or with no clear rectification in tobacco (Michard et al., 2011). Among the 20 cyclic nucleotide-gated channels (CNGCs) in plants, at least CNGC7, CNGC8, CNGC16, and CNGC18 are expressed in pollen (Pina et al., 2005; Bock et al., 2006; Kaplan et al., 2007). Some CNGC channels have been presented as inward-rectifying channels when expressed in HEK cells or oocytes (Leng et al., 1999, 2002; Ma et al., 2007). The disruption of AtCNGC18, localized in the subapical membrane, induces male sterility due to defective PT growth (Frietsch et al., 2007). AtCNGC18 was recently shown to drive inward cationic currents activated by cAMP/cGMP in an animal heterologous system (Gao et al., 2016). AtCNGC7, which localizes at the flank of the growing tip, and AtCNGC8 have weaker phenotypes, but the double knockout is male sterile (Tunc-Ozdemir et al., 2013a). Lastly, AtCNGC16 only plays a role under stress conditions (Tunc-Ozdemir et al., 2013b). In animals, CNGCs have calmodulin (CaM)-binding domains with regulatory functions, a mechanism recently confirmed for AtCNGC12 in plants (DeFalco et al., 2016). In tobacco, the Glutamate receptor agonist D-Ser induces a Ca^{2+} current while the antagonist CNQX inhibits the Ca^{2+} conductivity of PT protoplasts (Michard et al., 2011). This finding led to the description of PT growth phenotypes for the Arabidopsis Glutamate receptor-like (GLR) mutants *glr1.2* and *glr3.7*. Additional GLRs also are expressed in PTs (Pina et al., 2005; Bock et al., 2006) and may be involved in Ca^{2+} homeostasis. In accordance, other plant GLRs have been localized on the PM, and AtGLR3.4 has been shown to induce Ca^{2+} accumulation in HEK cells (Meyerhoff et al., 2005; Tapken and Hollmann, 2008; Teardo et al., 2010; Vincill et al., 2013). Interestingly, GLRs heterodimerize, as demonstrated by the sensitivity profile to amino acids in knockout plants (Stephens et al., 2008), yeast two-hybrid analysis (Price et al., 2013; Vincill et al., 2013), or FRET (Vincill et al., 2013). Utilizing a chimera strategy by introducing the pore of plant AtGLR1.1 and AtGLR1.4 into the animal GluR1 channel demonstrated low Ca^{2+} permeability and low rectification with nonselective cation pores (Tapken and Hollmann, 2008). Other Ca^{2+}-permeable channels are putatively active in pollen on the basis of transcriptomics/proteomics, namely the annexins (Lee et al., 2004; Zhu et al., 2014) and the mechanosensitive channel AtOSCA1 (Yuan et al., 2014).

One common point of the Ca^{2+}-permeable channels identified so far is their weak selectivity: they appear to be nonselective cation channels rather than Ca^{2+}-selective channels. Their gating also is still poorly

defined. While CNGCs open in response to cAMP and cGMP in HEK cells, no data are available in situ. GLR channel activity is modulated by amino acids with low specificity, as shown by the different responses to Gly, Glu, and D-Ser (Michard et al., 2011). AtGLR1.4 and AtGLR3.4 induce nonselective cationic currents in response to a broad range of amino acids in mammalian cells (Tapken and Hollmann, 2008; Vincill et al., 2013; Tapken et al., 2013). Clearly, a common ligand-gated system for Ca^{2+} homeostasis is still missing in plant biology.

H^+ Signaling, the Missing Link?

H^+ has long been proposed to act in signaling cascades in plants (Felle, 2001) and has even been identified as a bona fide neurotransmitter (Beg et al., 2008). In PTs, H^+ gradients also have been correlated with growth, with an acidic tip and alkaline subapical or submembranar region in tobacco and lily (Feijó et al., 1999; Certal et al., 2008; Michard et al., 2008). H^+ influx at the apex and efflux at the shank have been recorded and participate in the establishment of the gradient (Feijó et al., 1999; Certal et al., 2008; Michard et al., 2008). This is particularly clear in lily, where an alkaline band in the subapical region coincides with a maximum proton efflux (Feijó et al., 1999). Interestingly, this pattern is different in tobacco. PTs from this species do not display a distinct alkaline band (Michard et al., 2008). Accordingly, the H^+ effluxes along tobacco tubes do not display a maximum in the subapical zone as they do in lily but look rather constant along the tube (Certal et al., 2008). To the best of our knowledge, no H^+ or H^+-permeable channels have been characterized in plants. Anion channels have been discussed as participating in the establishment of pH gradients (Fernie and Martinoia, 2009). In addition to the endogenous permeability of the membrane bilayer to H^+ (Gutknecht, 1987), H^+ symporters or antiporters may be involved in H^+ fluxes. PTs express 18 genes from the putative cation-H^+ antiporter CHX family, with at least six genes expressed in the vegetative cell (Sze et al., 2004). Recently, CHX19 was localized in pollen PM (Padmanaban et al., 2017), while other GFP chimeras usually localize to the endomembrane system (see below; Table I).

THE SHANK OF THE PT: JUST SUPPORTING AND BUFFERING?

H^+ (pH) and Ca^{2+} gradients seem to depend on at least three components to be established: (1) influxes at the tip; (2) a cytoplasmic component including buffering by proteins and endomembrane transport activity; and (3) efflux at the shank. This section deals with the latter two.

The PT membrane appears to play an important role in the gradient establishment by its H^+- and Ca^{2+}-ATPase activity. PM H^+-ATPases play a major role in pH regulation (Sanders et al., 1981). The tobacco proton pump, NtAHA1, is specifically excluded from the PT tip, as shown by a GFP fusion (Certal et al., 2008). Early studies demonstrated that the inhibition of Ca^{2+} pumps using vanadate and compound 48/80 induces the increase of intracellular Ca^{2+} (Obermeyer and Weisenseel, 1991). Pharmacological studies on a Ca^{2+}-ATPase reconstituted in proteoliposomes showed that it can act as a bona fide Ca^{2+}/H^+ exchanger (Luoni et al., 2000). The fact that in PTs there is a high tip Ca^{2+} concentration and a low pH also could be dependent, at least in part, on the activity of this pump. The calcium pump AtACA9 is expressed specifically in pollen, and the knockout plant of this transporter displays a defect in pollen growth (Schiott et al., 2004). A major role is suspected to be played by 14-3-3 proteins due to their regulation of the C-terminal activity of all H^+-ATPases, and their proteomics repertoire has been described (Pertl et al., 2011). Yet, the large diversity and the lack of genetic studies still hinder their true mechanistic impact on the pH regulation of PTs.

H^+ and Ca^{2+} are highly buffered in the cytoplasm. pH homeostasis is largely ensured by metabolic regulation through the classical pH-STAT pathway (Smith and Raven, 1979; Sakano, 2001). Ca^{2+} interacts with many proteins in the cytosol that lower its diffusion coefficient (White and Broadley, 2003). In addition, H^+ and Ca^{2+} fluxes from and into internal stores are accepted to play a major role in the dynamics of those ions inside the cell, but there are no quantifications or mechanisms described. While the role of H^+ and Ca^{2+} influxes at the tip in generating H^+ and Ca^{2+} gradients is well defined, the role of cytosol and endomembrane proteins that are possibly major players in shaping the gradients is only vaguely known.

Several PM transporters are expressed in apical vesicles, including the P-type H^+-ATPases that may participate in local pH regulation (Certal et al., 2008). These H^+ pumps were recently associated with the rapid alkalinization factor (RALF) and the important receptor-like kinase FERONIA in roots (Haruta et al., 2014). Pollen expresses a number of RALFs (Pina et al., 2005), and a role of RALFs in PT growth regulation has long been described (Covey et al., 2010). Given that both FERONIA and its male counterpart ANXUR have disruptive fertilization phenotypes (for review, see Li et al., 2016), this functional relationship between RALFs and the H^+-ATPases could have consequences for pH regulation in PTs as well.

Cation-H^+ antiporters, from the CPA1 and CPA2 family, may play a role in controlling intracellular pH. CPA1 is typically localized in endomembranes, and some of them are expressed in pollen (Sze et al., 2004). From this family, Na^+(CATION)/H^+ EXCHANGER (AtNHX1) and AtNHX2 control cell expansion, pH homeostasis, and K^+ accumulation in the vacuole (Bassil et al., 2011). AtCHXs are expected to modulate pH by catalyzing H^+- and K^+-coupled fluxes. AtCHX13 and AtCHX14, both expressed in pollen, are PM transporters involved in K^+ homeostasis (Sze et al.,

2004; Zhao et al., 2008, 2015). CHX13 is a high-affinity K^+ influx transporter (Zhao et al., 2008), while AtCHX14 is a low-affinity efflux K^+ transporter in yeast and plant cells that operates in a pH-dependent manner (Zhao et al., 2008, 2015). Other AtCHXs, notably AtCHX21 and AtCHX23, have been characterized to play a role in pollen navigation through the ovary, resulting in male-transmitted sterility of the double knockout *chx21/23*, although PTs grow normally in vitro and in vivo (Evans et al., 2011; Lu et al., 2011). AtCHX23 increases yeast tolerance to high potassium in a pH-dependent manner, suggesting that it is an H^+/K^+ antiporter, and recent structure-function studies on AtCHX17 opened the way for understanding the integrated physiological function of this pollen overrepresented transporter family (Czerny et al., 2016). Recently, *CHX17* and *CHX19* were localized in PT vegetative and sperm cells, respectively, *CHX19* being addressed to the PM (Padmanaban et al., 2017). The triple mutant displays a fertility phenotype as well as a compromised pollen cell wall formation that could affect germination, tube burst, as well as gamete function (Padmanaban et al., 2017).

Ca^{2+} internal stores may also be essential in the establishment of the calcium gradient. In the absence of the canonical ligand-operated Ca^{2+}-buffering mechanisms as described for animal cells, namely IP3 receptors and G-coupled receptors, the repertoire of possible candidates in plants include the CAX (cation-H^+ exchangers) and TPC (two-pore channels) families. TPC was recently involved in the propagation of Ca^{2+} signals in roots (Choi et al., 2014), but no male phenotypes have been described. Measurement of Ca^{2+} in the endoplasmic reticulum (ER) showed that an inhibition of growth in parallel with a decrease in ER Ca^{2+} occurred when the ER Ca^{2+}-ATPase was inhibited (Iwano et al., 2009). Some GLRs are expressed in endomembranes and may participate in Ca^{2+} signaling (Teardo et al., 2011, 2015). Experimental evidence also is suggestive of a role for the Arabidopsis mitochondrial channel uniporter regulator MICU, a Ca^{2+}-binding protein that modulates the mitochondrial Ca^{2+} accumulation (Stael et al., 2012). Interestingly, MICU is expressed in PTs (Wang et al., 2008b). Mitochondrial membrane charge shifts at the clear zone of PTs (Colaço et al., 2012) have been speculated to play a role in cytosolic Ca^{2+} homeostasis and in the definition of the Ca^{2+} gradient at the tip.

Reactive oxygen species (ROS) also have been long implicated in ion dynamics regulation in PTs. The subject has been reviewed elsewhere (Wudick and Feijó, 2014; Mangano et al., 2016), so it will only be alluded to briefly here. Tip-localized ROS in growing PTs have been described in Arabidopsis (Potocky et al., 2007), and double mutants of the pollen-expressed H and J members of respiratory burst oxidase homolog (Rboh) have PT phenotypes and altered Ca^{2+} gradient features (Liu et al., 2009; Boisson-Dernier et al., 2013; Kaya et al., 2014, 2015; Lassig et al., 2014). Plastids and mitochondria positioned in the subapical region are other possible sources of ROS (Mittler et al., 2011). In lily, abundant accumulations of ROS have been linked to mitochondria (Cardenas et al., 2006). This competing view of tip-localized ROS raises questions about ROS concentrations in the shank as either free cytosolic or localized to subcellular vesicles. Hydrogen peroxide was recently implicated in the regulation of K^+ and Ca^{2+} conductivities in lily pollen protoplast (Breygina et al., 2016). The possible integration of these pathways is illustrated in Text Box 2 (Zhou et al., 2014; Zhao et al., 2013; Xu et al., 2006; Mahs et al. 2013; Kaya et al., 2015; Garcia-Mata et al., 2010).

DECODING THE ION CODE: DOWNSTREAM MECHANISMS OF INTEGRATION OF ION SIGNALING

Various Ca^{2+} sensor proteins are known, some of them with activity in PTs. The most prominent are within the Ca^{2+}-binding EF-hand superfamily, which consists of calmodulin, calmodulin-like (CML) and calcineurin B-like (CBL) proteins, CBL-interacting protein kinases (CIPK), and finally the Ca^{2+}-dependent protein kinases (CDPK; abbreviated CPK in Arabidopsis; Zhou et al., 2015a). CaM, CML, and CBL have been demonstrated previously to serve as sensor relays that lack enzymatic activity, while CIPK and CDPK are responders. Each of these proteins contains a special helix-loop-helix motif known as the EF-hand that enables Ca^{2+} binding (Konrad et al., 2011; Steinhorst and Kudla, 2013).

The CPK family appears to have the most diverse array of targets by interacting with actin and also other membrane proteins (Curran et al., 2011). Of the 34 CPKs present in the genome of Arabidopsis, 12 members (CPK2, CPK4, CPK6, CPK11, CPK14, CPK16, CPK17, CPK20, CPK24, CPK26, CPK32, and CPK34) are expressed in pollen (Honys and Twell, 2003; Hrabak et al., 2003; Harper et al., 2004; Pina et al., 2005). Five of these have been characterized: AtCPK17 and AtCPK34 show very strong PT growth phenotypes; therefore, these proteins must play important roles, which were hypothesized to regulate Ca^{2+} channel activity (Myers et al., 2009). The expression of the 12 pollen Arabidopsis CPKs was analyzed by transient expression in tobacco PTs, revealing differential localizations: CPK4, CPK11, and CPK26 are cytosolic; CPK16, CPK24, and CPK32 seem to localize preferentially in the generative cell membrane; while the others localize to the PM of the PT: CPK2 and CPK20 specifically at the tip, CPK17 and CPK34 in the subapical zone (Gutermuth et al., 2013). Furthermore, AtCPK2 and AtCPK20 were shown to interact and activate the conductivity of the anion channel AtSLAH3. Taken together with the countercorrelation between the levels of cytosolic Ca^{2+} and Cl^-, these data are suggestive of a feedback regulation loop that could underlie the control of growth as an interplay between these two ions, AtSLAH3 and a yet unknown depolarization-activated Ca^{2+} channel (Gutermuth et al., 2013).

CMLs sense free cytosolic Ca^{2+} and are likely integral targets of Ca^{2+} signaling. There are over 50 AtCMLs expressed within pollen that share the highly

BOX 2. Integrating pathways: mission impossible?

All things are connected, and any exercise of linking different pathways is perennial by nature but often useful to develop hypotheses on their functional interfaces. Figure 4 represents one such exercise based on the available data. Ca^{2+} is known to activate AtCPK32, which in turn activates the Ca^{2+}-permeable channel AtCNGC18; overexpression of AtCPK32 also produces Ca^{2+} accumulation and unpolarized growth (Zhou et al., 2014). AtCPK11 and AtCPK24 inhibit inward K^+ currents via the Shaker channel AtSPIK (Zhao et al., 2013). AtCPK2 and AtCPK20 activate the anion channel AtSLAH3, and this interaction is suggestive of a growth regulatory feedback loop involving a yet uncharacterized depolarization-activated Ca^{2+} channel (Gutermuth et al., 2013). Overexpression of AtCIPK19 led to increased apical Ca^{2+} and loss of polarity, whereas the loss-of-function mutant hindered growth (Zhou et al., 2015a). In root hairs, CBL1 and CBL9 were shown to interact with CIPK23 to target the Shaker-type K^+ channel AKT1 (Xu et al., 2006). In PTs, Mahs et al. (2013) identified a similar role for CBL1 and CBL9 as Ca^{2+} sensors that show overexpression and knockout phenotypes of disturbed K^+ homeostasis, leading to the speculation that CBL1 and CBL9 may interact with an unknown CIPK to regulate a Shaker-type K^+ channel homologous to AKT1, SPIK. In PTs, AtCBL2 and AtCBL3 interact with AtCIPK12 on the tonoplast, implicating the vacuole in Ca^{2+} homeostasis and signaling (Steinhorst et al., 2015). CaM and CPKs have been identified as interacting partners to enable H^+-ATPases (Pertl-Obermeyer et al., 2014). ROS regulate Ca^{2+} influxes through Ca^{2+}-permeable channels in root hairs, while in PTs, Ca^{2+} has been shown to regulate the activity of the ROS-producing proteins AtRbohH and AtRbohJ (Wu et al., 2010; Kaya et al., 2015; for review, see Wudick and Feijó, 2014). The outward K^+ channel AtSKOR responds to hydrogen peroxide (Garcia-Mata et al., 2010). In PT experiments in which AtRbohH and AtRbohJ activity was manipulated, AtSPIK and AtSKOR have been suggested to be regulated by ROS (Lassig et al., 2014). Cytosolic pH affects the activity of many proteins, yet specific regulation of tube PM transporters by pH has not been reported so far. Given the existence of defined gradients of acidity on the tip and alkalinity either cytoplasmic or submembranar (Fig. 1), pH could regulate differentially evenly distributed channels or be involved in processes to regulate the differential localization of channels, one or the other contributing to the stabilization of cell polarity at the tip.

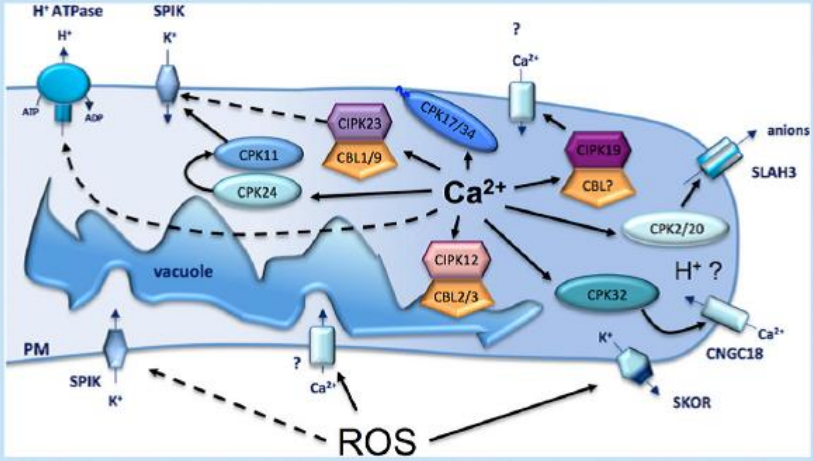

Figure 4. Schematic overview of signaling networks based on ion secondary messengers that participate in establishing ion homeostasis. Solid lines represent supported findings, while dashed lines represent ongoing hypotheses. Question marks indicate the likely presence of proteins whose molecular identities are still to be determined. We have represented the main transporters here: proton pumps, inward K^+ channel AtSPIK on the tube, calcium channels (unknown and AtCNGC18), outward potassium channel AtSKOR, and AtSLAH3 anion channel on the tip (for details, see Fig. 2; Table I).

conserved EF-hand binding motif and up to 75% amino acid identity with CaM (Bender and Snedden, 2013). Pharmacological evidence of the action of CaM in PTs of Arabidopsis seems to implicate hyperpolarization-activated Ca^{2+} channels, suggestive of a closed feedback loop dependent on H^+-ATPase activity (Sun et al., 2009). More recently, a function was identified for AtCML24 in PT growth, acting on the interface between the actin cytoskeleton and Ca^{2+} (Yang et al., 2014). Given the relevance of AtCNGCs in PT growth, the recent description of CaM regulation of AtCNGC12 (DeFalco et al., 2016) opens the possibility that such a protein also may also be involved as a decoder of Ca^{2+} signals in PTs, as previously suggested by injection experiments (Moutinho et al., 1998; Rato et al., 2004).

CIPKs are Ser/Thr kinases that couple with CBLs in the Ca^{2+} signaling network (Edel and Kudla, 2015; Mao

Table II. *Cytoskeleton effects linked to Ca^{2+}, H^+, or ROS signaling*

Second Messenger	Downstream Target(s)	Cytoskeleton Effects (*species*)	References
Ca^{2+}	ROP1 → RIC1, RIC3, RIC4	1. F-actin severing 2. Capping barbed ends (*At*) F-actin disassembly 1. F-actin assembly 2. Increases exocytosis of vesicles (*Nt*, *At*)	Zhou *et al.*, 2015; Gu *et al.*, 2005
	*At*MDP25	F-actin severing (*At*)	Qin *et al.*, 2014
	*At*MAP18	F-actin severing (*At*)	Zhu *et al.*, 2013
	Myosin XI?	Low Ca^{2+} (~0.1μM) generates cytoplasmic streaming. Near 1μM Ca^{2+}, streaming ability inhibited (*Ll*).	Yokota *et al.*, 1999; Tominaga *et al.*, 2012
	Profilin	1. Increased Ca^{2+} results in increased depolymerization (*Zm*, *Pr*) 2. Increasing Ca^{2+} sequesters profilin to block function (*Zm*, *Pr*)	Kovar *et al.*, 2000 Snowman *et al.*, 2002
	Villin2, 5?	Present in apical and sub-apical region. Actin severing, collar formation. (*At*)	Qu *et al.*, 2013
	*Ll*ABP29	Binds and aids F-actin severing. Overexpression inhibited germination and tube growth (*Ll*)	Xiang *et al.*, 2007
	*Ld*ABP41	F-actin severing (*Ld*)	Fan *et al.*, 2004
	*Pr*ABP80 (gelsolin-like)	F-actin severing, barbed end capping (*Pr*)	Huang *et al.*, 2004
H^+	*Ll*LIM1	F-actin bundle assembly and stabilization (*Ll*)	Wang *et al.*, 2008
	Actin-Depolymerizing Factor (ADF) and Actin-Interacting Protein (AIP)?	Active at alkaline pH to promote actin depolymerization (*Nt*). AIP proposed to work cooperatively with ADF (*Ll*).	Chen *et al.*, 2002; Lovy-Wheeler *et al.*, 2006
ROS	Ca^{2+} → CIPK → ?	Phosphorylation of actin depolymerizing agents? No evidence ROS acts directly on cytoskeleton.	Chen *et al.*, 2002; Wudick *et al.*, 2014

et al., 2016). The AtCBL-AtCIPK complex has been heavily implicated in abiotic stress tolerance by adjusting the levels of K^+ through AtAKT1 (Manik et al., 2015). Of the 26 different CIPKs identified within the Arabidopsis genome, AtCIPK10, AtCIPK11, AtCIPK12, AtCIPK14, and AtCIPK19 are strongly expressed in PTs (Konrad et al., 2011; Zhou et al., 2015a). They display an even distribution throughout the cytosol while being weakly expressed in other tissues (Zhou et al., 2015a). Different AtCBL/AtCIPK pairs have been implicated in the activation of various kinds of channels (for review, see Steinhorst and Kudla, 2013), and in PTs, AtCBL2 and AtCBL3 were described to interact with AtCIPK12 in the tonoplast, with phenotypic consequences at the level of growth and PT morphogenesis, implicating the vacuole in Ca^{2+} homeostasis and signaling (Steinhorst et al., 2015). A possible integration of these pathways is offered in Figure 4.

CYTOSKELETON AND ION DYNAMICS

PT growth is accredited to actin polymerization (Vidali and Hepler, 2001; Cardenas et al., 2008). Yet, a collective look at actin dynamics suggests an alternative perspective for normal growth: it is rapid actin turnover, the continuous assembly and disassembly of actin, that is important variable. Are signaling gradients, and not strict concentrations, important by themselves through dynamic mechanisms such as the polymerization/depolymerization of actin? Possible interactions between H^+ and Ca^{2+} and actin related

proteins have been systematized previously (Feijó et al., 2004; Hepler, 2016) and are summarized in Table II. One prominent candidate for interaction with Ca^{2+} is the GTPase Rho family of plants (ROPs). Primarily tip localized, members such as the pollen-specific AtROP1 have been demonstrated to mediate F-actin and Ca^{2+} signaling (for review, see Cheung and Wu, 2008; Qin and Yang, 2011). The best characterized ROP downstream effector are the family of ROP-interactive CRIB-containing proteins (RICs) that show a diverse range of responses. Opposing pathways of AtRIC3 and AtRIC4 produced starkly different consequences on F-actin. AtRIC3 leads to F-actin disassembly, specifically at the tip of PTs, promoting the accumulation of tip-localized Ca^{2+}. Conversely, AtRIC4 in response to Ca^{2+} promotes F-actin assembly (Gu et al., 2005). Additionally, recent studies investigating the apical PM-localized AtRIC1 add to the importance of RIC to regulate actin (Zhou et al., 2015b). Similar to AtRIC3, AtRIC1 binds to and severs F-actin in the presence of Ca^{2+}. The *ric1* knockout mutant was characterized by an accumulation of actin at the fringe and increased PT growth rate (Zhou et al., 2015b). Despite multiple pieces of evidence and phenotypes, a consensual mechanism for ROP GTPases in PT growth is still debated.

A number of actin-binding proteins, such as LlABP29 and LdABP41, respond in a Ca^{2+}-sensitive manner to contribute to F-actin regulation (Fan et al., 2004; Xiang et al., 2007). Also, villins, which are known to be Ca^{2+} responsive (Yokota et al., 2005), have been found to be major players in the actin turnover in PTs (Qu et al., 2013). Further details of ABPs have been reviewed recently (Fu, 2015; Hepler, 2016). Of note, there are no reports of ion regulatory dependencies for the ABP family of formins, which have emerged as major regulators of actin organization in PTs (Cheung et al., 2010). Like all proteins, formin action should be dependent on pH, but the range of pH variations in the PT tip was never associated with their regulation.

Despite contradictory evidence for a crucial role of microtubules in PTs, microtubule-destabilizing protein (MDP) binding activity was found to be augmented by high Ca^{2+} in Arabidopsis. Yet, remarkably, its action seems to be to sever actin instead of tubulin. AtMDP25 is localized in the subapical region on the PM, corresponding to the highest concentrations of Ca^{2+}, where it directly binds to and severs actin filaments, and its knockout resulted in an increased PT growth rate but, paradoxically, reduced fertilization (Qin et al., 2014). Moreover, MICROTUBULE-ASSOCIATED PROTEIN18 demonstrates similar actin-severing functions, as it is also localized on the subapical PM (Zhu et al., 2013). At this point, it is difficult to develop a mechanism integrating actin and microtubule interaction, but some evidence exists that they may cooperate in order to regulate the mechanical properties of PTs (Gossot and Geitmann, 2007).

H^+ also may be involved in the cytoskeleton and exocytosis regulation. Of relevance, alkalinization or acidification treatment of growing PTs showed that pH may control actin dynamics in lily PTs, eventually through the ADF-cofilin complex (Lovy-Wheeler et al., 2006). Other evidence of H^+ targeting the cytoskeleton comes from studies on the actin-binding protein LILIM1, which is essential for F-actin bundle assembly and protection against latruncalin B-mediated depolymerization and exhibits preference for activity under low pH and low calcium concentrations (Wang et al., 2008a).

CONCLUSION

PTs have been the source of relevant information of channel identity and function, mostly due to their strict dependence on ion dynamics and favorable cell biology. The aspects covered in this review show not

OUTSTANDING QUESTIONS

- What are the channels and transporters that sustain the cytosolic gradients of Ca^{2+} and anions in PTs?
- Are specific choreographies of ion dynamics associated with the spatial and temporal coordination of cellular processes that lead to growth and morphogenesis of the pollen tube?
- How are ions, especially K^+ and anions, associated with the generation of turgor and regulation of wall synthesis?
- What is the contribution of the endomembrane system and vacuole to ion homeostasis in the cytosol? And how are the ion transports to these compartments regulated?
- Is there a ligand-based regulatory mechanism that coordinates the activity of ligand-gated channels for the regulation of ion cytosolic concentration, especially for Ca^{2+}?
- What are the targets of the cytosolic pH gradient at the tip?
- How do the multiple downstream target families of Ca^{2+} (CPKs, CIPKs, and CMLs) interact to produce specific responses?

only significant advances in the repertoire of known ion transport proteins but also significant advances in downstream regulatory targets that may elucidate the very fundamental levels of organization of a living cell. Also in that respect, PTs offer unique features to bridge to biophysics, specifically at the levels of electrochemistry and biomechanics. Most of the studies covered refer to in vitro PT growth phenotypes, eventually backed up by in vivo phenotyping, but several pieces of evidence suggest that ion dynamics mechanisms can actually be involved in various steps of the progamic phase of reproduction. Examples of this centrality come from recent demonstrations of the influence of pollen Ca^{2+}-ATPases (Iwano et al., 2014) and GLRs (Iwano et al., 2015) on the self-incompatibility of *Brassica* spp. and the suite of articles that defined the emergence of an ion-mediated signaling model during PT-embryo sac interaction, either through K^+ in maize (*Zea mays*; Amien et al., 2010) or the putative existence of Ca^{2+} signatures in Arabidopsis (Iwano et al., 2012; Denninger et al., 2014; Hamamura et al., 2014; Ngo et al., 2014). The context of cell-cell communication during reproduction is suggestive that PTs have evolved for fast reaction signaling in the form of chemotaxis, growth turns, growth rate alterations, and bursting; therefore, it is likely that the repertoire of basic mechanisms that transduce information through ion dynamics will be increased, benefited by the plethora of new imaging methods and genetic probes continuously being developed.

Received October 12, 2016; accepted November 19, 2016; published November 28, 2016

LITERATURE CITED

Ali O, Traas J (2016) Force-driven polymerization and turgor-induced wall expansion. Trends Plant Sci **21:** 398–409

Amien S, Kliwer I, Marton ML, Debener T, Geiger D, Becker D, Dresselhaus T (2010) Defensin-like ZmES4 mediates pollen tube burst in maize via opening of the potassium channel KZM1. PLoS Biol **8:** e1000388

Aouar L, Chebli Y, Geitmann A (2010) Morphogenesis of complex plant cell shapes: the mechanical role of crystalline cellulose in growing pollen tubes. Sex Plant Reprod **23:** 15–27

Bassil E, Tajima H, Liang YC, Ohto MA, Ushijima K, Nakano R, Esumi T, Coku A, Belmonte M, Blumwald E (2011) The *Arabidopsis* Na^+/H^+ antiporters NHX1 and NHX2 control vacuolar pH and K^+ homeostasis to regulate growth, flower development, and reproduction. Plant Cell **23:** 3482–3497

Becker D, Geiger D, Dunkel M, Roller A, Bertl A, Latz A, Carpaneto A, Dietrich P, Roelfsema MR, Voelker C, et al (2004) AtTPK4, an Arabidopsis tandem-pore K^+ channel, poised to control the pollen membrane voltage in a pH- and Ca^{2+}-dependent manner. Proc Natl Acad Sci USA **101:** 15621–15626

Becker JD, Boavida LC, Carneiro J, Haury M, Feijo JA (2003) Transcriptional profiling of Arabidopsis tissues reveals the unique characteristics of the pollen transcriptome. Plant Physiol **133:** 713–725

Becker JD, Takeda S, Borges F, Dolan L, Feijo JA (2014) Transcriptional profiling of Arabidopsis root hairs and pollen defines an apical cell growth signature. BMC Plant Biol **14:** 197

Beg AA, Ernstrom GG, Nix PN, Davis MW, Jorgensen EM (2008) Protons act as a transmitter for muscle contraction in C. elegans. Cell **132:** 149–160

Bender KW, Snedden WA (2013) Calmodulin-related proteins step out from the shadow of their namesake. Plant Physiol **163:** 486–495

Benkert R, Obermeyer G, Bentrup FW (1997) The turgor pressure of growing lily pollen tubes. Protoplasma **198:** 1–8

Bloch D, Pleskot R, Pejchar P, Potocky M, Trpkosova P, Cwiklik L, Vukasinovic N, Sternberg H, Yalovsky S, Zarsky V (2016) Exocyst SEC3 an phosphoinositides define sites of exocytosis in pollen initiation and growth. Plant Physiol **172:** 980–1002

Boavida LC, Becker JD, Feijo JA (2005a) The making of gametes in higher plants. Int J Dev Biol **49:** 595–614

Boavida LC, Borges F, Becker JD, Feijo JA (2011) Whole genome analysis of gene expression reveals coordinated activation of signaling and metabolic pathways during pollen-pistil interactions in Arabidopsis. Plant Physiol **155:** 2066–2080

Boavida LC, Vieira AM, Becker JD, Feijo JA (2005b) Gametophyte interaction and sexual reproduction: how plants make a zygote. Int J Dev Biol **49:** 615–632

Bock KW, Honys D, Ward JM, Padmanaban S, Nawrocki EP, Hirschi KD, Twell D, Sze H (2006) Integrating membrane transport with male gametophyte development and function through transcriptomics. Plant Physiol **140:** 1151–1168

Boisson-Dernier A, Lituiev DS, Nestorova A, Franck CM, Thirugnanarajah S, Grossniklaus U (2013) ANXUR receptor-like kinases coordinate cell wall integrity with growth at the pollen tube tip via NADPH oxidases. PLoS Biol **11:** e1001719

Borges F, Gomes G, Gardner R, Moreno N, McCormick S, Feijo JA, Becker JD (2008) Comparative transcriptomics of Arabidopsis sperm cells. Plant Physiol **148:** 1168–1181

Bosch M, Cheung AY, Hepler PK (2005) Pectin methylesterase, a regulator of pollen tube growth. Plant Physiol **138:** 1334–1346

Bosch M, Hepler PK (2005) Pectin methylesterases and pectin dynamics in pollen tubes. Plant Cell **17:** 3219–3226

Bots M, Feron R, Uehlein N, Weterings K, Kaldenhoff R, Mariani T (2005) PIP1 and PIP2 aquaporins are differentially expressed during tobacco anther and stigma development. J Exp Bot **56:** 113–121

Bove J, Vaillancourt B, Kroeger J, Hepler PK, Wiseman PW, Geitmann A (2008) Magnitude and direction of vesicle dynamics in growing pollen tubes using spatiotemporal image correlation spectroscopy and fluorescence recovery after photobleaching. Plant Physiol **147:** 1646–1658

Breygina MA, Abramochkin DV, Maksimov NM, Yermakov IP (2016) Hydrogen peroxide affects ion channels in lily pollen grain protoplasts. Plant Biol (Stuttg) **18:** 761–767

Byrt CS, Zhao M, Kourghi M, Bose J, Henderson SW, Qiu J, Gilliham M, Schultz C, Schwarz M, Ramesh SA, et al (2016) Non-selective cation channel activity of aquaporin AtPIP2;1 regulated by Ca^{2+} and pH. Plant Cell Environ (in press)

Cardenas AM, Marengo FD (2016) How the stimulus defines the dynamics of vesicle pool recruitment, fusion mode, and vesicle recycling in neuroendocrine cells. J Neurochem **137:** 867–879

Cardenas L, Lovy-Wheeler A, Kunkel JG, Hepler PK (2008) Pollen tube growth oscillations and intracellular calcium levels are reversibly modulated by actin polymerization. Plant Physiol **146:** 1611–1621

Cardenas L, McKenna ST, Kunkel JG, Hepler PK (2006) NAD(P)H oscillates in pollen tubes and is correlated with tip growth. Plant Physiol **142:** 1460–1468

Certal AC, Almeida RB, Carvalho LM, Wong E, Moreno N, Michard E, Carneiro J, Rodriguez-Leon J, Wu HM, Cheung AY, et al (2008) Exclusion of a proton ATPase from the apical membrane is associated with cell polarity and tip growth in *Nicotiana tabacum* pollen tubes. Plant Cell **20:** 614–634

Chebli Y, Kaneda M, Zerzour R, Geitmann A (2012) The cell wall of the Arabidopsis pollen tube: spatial distribution, recycling, and network formation of polysaccharides. Plant Physiol **160:** 1940–1955

Chen CY, Wong EI, Vidali L, Estavillo A, Hepler PK, Wu HM, Cheung AY (2002) The regulation of actin organization by actin-depolymerizing factor in elongating pollen tubes. Plant Cell **14:** 2175–2190

Chen LQ, Hou BH, Lalonde S, Takanaga H, Hartung ML, Qu XQ, Guo WJ, Kim JG, Underwood W, Chaudhuri B, et al (2010) Sugar transporters for intercellular exchange and nutrition of pathogens. Nature **468:** 527–532

Cheng J, Wang Z, Yao F, Gao L, Ma S, Sui X, Zhang Z (2015) Down-regulating CsHT1, a cucumber pollen-specific hexose transporter, inhibits pollen germination, tube growth, and seed development. Plant Physiol **168:** 635–647

Cheung AY, Niroomand A, Zou Y, Wu HM (2010) A transmembrane formin nucleates subapical actin assembly and controls tip-focused growth in pollen tubes. Proc Natl Acad Sci USA **107:** 16390–16395

Cheung AY, Wu HM (2007) Structural and functional compartmentalization in pollen tubes. J Exp Bot **58:** 75–82

Cheung AY, Wu HM (2008) Structural and signaling networks for the polar cell growth machinery in pollen tubes. Annu Rev Plant Biol **59:** 547–572

Choi WG, Toyota M, Kim SH, Hilleary R, Gilroy S (2014) Salt stress-induced Ca waves are associated with rapid, long-distance root-to-shoot signaling in plants. Proc Natl Acad Sci USA **111:** 6497–6502

Colaço R, Moreno N, Feijó JA (2012) On the fast lane: mitochondria structure, dynamics and function in growing pollen tubes. J Microsc **247:** 106–118

Colmenero-Flores JM, Martinez G, Gamba G, Vazquez N, Iglesias DJ, Brumos J, Talon M (2007) Identification and functional characterization of cation-chloride cotransporters in plants. Plant J **50:** 278–292

Cosgrove DJ (2014) Plant cell growth and elongation. *In* eLS. John Wiley & Sons, Chichester, UK, doi/10.1002/9780470015902.a0001688.

Cosgrove DJ (2016) Plant cell wall extensibility: connecting plant cell growth with cell wall structure, mechanics, and the action of wall-modifying enzymes. J Exp Bot **67:** 463–476

Covey PA, Subbaiah CC, Parsons RL, Pearce G, Lay FT, Anderson MA, Ryan CA, Bedinger PA (2010) A pollen-specific RALF from tomato that regulates pollen tube elongation. Plant Physiol **153:** 703–715

Curran A, Chang IF, Chang CL, Garg S, Miguel RM, Barron YD, Li Y, Romanowsky S, Cushman JC, Gribskov M, et al (2011) Calcium-dependent protein kinases from Arabidopsis show substrate specificity differences in an analysis of 103 substrates. Front Plant Sci **2:** 36

Czerny DD, Padmanaban S, Anishkin A, Venema K, Riaz Z, Sze H (2016) Protein architecture and core residues in unwound alpha-helices provide insights to the transport function of plant AtCHX17. Biochim Biophys Acta **1858:** 1983–1998

Daminelli DSC, Portes MT, Feijó JA (2017) One thousand and one oscillators at the pollen tube tip: the quest for a central pacemaker revisited. *In* G Obermeyer, JA Feijó, eds, Pollen Tip Growth: From Biophysical Aspects to Systems Biology. Springer-Verlag, Heidelberg, Germany (in press)

DeFalco TA, Marshall CB, Munro K, Kang HG, Moeder W, Ikura M, Snedden WA, Yoshioka K (2016) Multiple calmodulin-binding sites positively and negatively regulate *Arabidopsis* CYCLIC NUCLEOTIDE-GATED CHANNEL12. Plant Cell **28:** 1738–1751

Denninger P, Bleckmann A, Lausser A, Vogler F, Ott T, Ehrhardt DW, Frommer WB, Sprunck S, Dresselhaus T, Grossmann G (2014) Male-female communication triggers calcium signatures during fertilization in Arabidopsis. Nat Commun **5:** 4645

Derksen J, Janssen GJ, Wolters-Arts M, Lichtscheidl I, Adlassnig W, Ovecka M, Doris F, Steer M (2011) Wall architecture with high porosity is established at the tip and maintained in growing pollen tubes of Nicotiana tabacum. Plant J **68:** 495–506

Dettmer J, Liu TY, Schumacher K (2010) Functional analysis of Arabidopsis V-ATPase subunit VHA-E isoforms. Eur J Cell Biol **89:** 152–156

Di Giorgio JA, Bienert GP, Ayub ND, Yaneff A, Barberini ML, Mecchia MA, Amodeo G, Soto GC, Muschietti JP (2016) Pollen-specific aquaporins NIP4;1 and NIP4;2 are required for pollen development and pollination in *Arabidopsis thaliana*. Plant Cell **28:** 1053–1077

Dumais J, Shaw SL, Steele CR, Long SR, Ray PM (2006) An anisotropic-viscoplastic model of plant cell morphogenesis by tip growth. Int J Dev Biol **50:** 209–222

Edel KH, Kudla J (2015) Increasing complexity and versatility: how the calcium signaling toolkit was shaped during plant land colonization. Cell Calcium **57:** 231–246

Evans AR, Hall D, Pritchard J, Newbury HJ (2011) The roles of the cation transporters CHX21 and CHX23 in the development of Arabidopsis thaliana. J Exp Bot **63:** 59–67

Fan X, Hou J, Chen X, Chaudhry F, Staiger CJ, Ren H (2004) Identification and characterization of a Ca^{2+}-dependent actin filament-severing protein from lily pollen. Plant Physiol **136:** 3979–3989

Fayant P, Girlanda O, Chebli Y, Aubin CE, Villemure I, Geitmann A (2010) Finite element model of polar growth in pollen tubes. Plant Cell **22:** 2579–2593

Feijó JA, Costa SS, Prado AM, Becker JD, Certal AC (2004) Signalling by tips. Curr Opin Plant Biol **7:** 589–598

Feijó JA, Malhó RM, Obermeyer G (1995) Ion dynamics and its possible role during in vitro germination and tube growth. Protoplasma **187:** 155–167

Feijó JA, Sainhas J, Hackett GR, Kunkel JG, Hepler PK (1999) Growing pollen tubes possess a constitutive alkaline band in the clear zone and a growth-dependent acidic tip. J Cell Biol **144:** 483–496

Feijó JA, Sainhas J, Holdaway-Clarke T, Cordeiro MS, Kunkel JG, Hepler PK (2001) Cellular oscillations and the regulation of growth: the pollen tube paradigm. BioEssays **23:** 86–94

Felle HH (2001) pH: signal and messenger in plant cells. Plant Biol **3:** 577–591

Fendrych M, Leung J, Friml J (2016) TIR1/AFB-Aux/IAA auxin perception mediates rapid cell wall acidification and growth of Arabidopsis hypocotyls. eLife **5:** e19048

Fernie AR, Martinoia E (2009) Malate: jack of all trades or master of a few? Phytochemistry **70:** 828–832

Frietsch S, Wang YF, Sladek C, Poulsen LR, Romanowsky SM, Schroeder JI, Harper JF (2007) A cyclic nucleotide-gated channel is essential for polarized tip growth of pollen. Proc Natl Acad Sci USA **104:** 14531–14536

Fu Y (2015) The cytoskeleton in the pollen tube. Curr Opin Plant Biol **28:** 111–119

Gao QF, Gu LL, Wang HQ, Fei CF, Fang X, Hussain J, Sun SJ, Dong JY, Liu H, Wang YF (2016) Cyclic nucleotide-gated channel 18 is an essential Ca^{2+} channel in pollen tube tips for pollen tube guidance to ovules in Arabidopsis. Proc Natl Acad Sci USA **113:** 3096–3101

Garcia-Mata C, Wang J, Gajdanowicz P, Gonzalez W, Hills A, Donald N, Riedelsberger J, Amtmann A, Dreyer I, Blatt MR (2010) A minimal cysteine motif required to activate the SKOR K^+ channel of Arabidopsis by the reactive oxygen species H_2O_2. J Biol Chem **285:** 29286–29294

Gehwolf R, Griessner M, Pertl H, Obermeyer G (2002) First patch, then catch: measuring the activity and the mRNA transcripts of a proton pump in individual Lilium pollen protoplasts. FEBS Lett **512:** 152–156

Geitmann A (2010) How to shape a cylinder: pollen tube as a model system for the generation of complex cellular geometry. Sex Plant Reprod **23:** 63–71

Goetz M, Godt DE, Guivarc'h A, Kahmann U, Chriqui D, Roitsch T (2001) Induction of male sterility in plants by metabolic engineering of the carbohydrate supply. Proc Natl Acad Sci USA **98:** 6522–6527

Gossot O, Geitmann A (2007) Pollen tube growth: coping with mechanical obstacles involves the cytoskeleton. Planta **226:** 405–416

Griessner M, Obermeyer G (2003) Characterization of whole-cell K^+ currents across the plasma membrane of pollen grain and tube protoplasts of Lilium longiflorum. J Membr Biol **193:** 99–108

Gu F, Nielsen E (2013) Targeting and regulation of cell wall synthesis during tip growth in plants. J Integr Plant Biol **55:** 835–846

Gu Y, Fu Y, Dowd P, Li S, Vernoud V, Gilroy S, Yang Z (2005) A Rho family GTPase controls actin dynamics and tip growth via two counteracting downstream pathways in pollen tubes. J Cell Biol **169:** 127–138

Guan YF, Huang XY, Zhu J, Gao JF, Zhang HX, Yang ZN (2008) RUPTURED POLLEN GRAIN1, a member of the MtN3/saliva gene family, is crucial for exine pattern formation and cell integrity of microspores in Arabidopsis. Plant Physiol **147:** 852–863

Gutermuth T, Lassig R, Portes MT, Maierhofer T, Romeis T, Borst JW, Hedrich R, Feijo JA, Konrad KR (2013) Pollen tube growth regulation by free anions depends on the interaction between the anion channel SLAH3 and calcium-dependent protein kinases CPK2 and CPK20. Plant Cell **25:** 4525–4543

Gutknecht J (1987) Proton/hydroxide conductance and permeability through phospholipid bilayer membranes. Proc Natl Acad Sci USA **84:** 6443–6446

Hackel A, Schauer N, Carrari F, Fernie AR, Grimm B, Kuhn C (2006) Sucrose transporter LeSUT1 and LeSUT2 inhibition affects tomato fruit development in different ways. Plant J **45:** 180–192

Hamamura Y, Nishimaki M, Takeuchi H, Geitmann A, Kurihara D, Higashiyama T (2014) Live imaging of calcium spikes during double fertilization in Arabidopsis. Nat Commun **5:** 4772

Hamilton ES, Jensen GS, Maksaev G, Katims A, Sherp AM, Haswell ES (2015) Mechanosensitive channel MSL8 regulates osmotic forces during pollen hydration and germination. Science **350:** 438–441

Harper JF, Breton G, Harmon A (2004) Decoding Ca^{2+} signals through plant protein kinases. Annu Rev Plant Biol **55:** 263–288

Haruta M, Sabet G, Stecker K, Minkoff BB, Sussman MR (2014) A peptide hormone and its receptor kinase regulate plant cell expansion. Science **343:** 408–411

Henderson SW, Wege S, Qiu J, Blackmore DH, Walker AR, Tyerman SD, Walker RR, Gilliham M (2015) Grapevine and Arabidopsis cation-chloride cotransporters localize to the Golgi and trans-Golgi network and indirectly influence long-distance ion transport and plant salt tolerance. Plant Physiol **169:** 2215–2229

Hepler PK (2016) The cytoskeleton and its regulation by calcium and protons. Plant Physiol **170:** 3–22
Hepler PK, Rounds CM, Winship LJ (2013) Control of cell wall extensibility during pollen tube growth. Mol Plant **6:** 998–1017
Hepler PK, Winship LJ (2015) The pollen tube clear zone: clues to the mechanism of polarized growth. J Integr Plant Biol **57:** 79–92
Heslop-Harrison J, Heslop-Harrison Y (1982) The growth of the grass pollen tube. 1. Characteristics of the polysaccharide particles (P-particles) associated with apical growth. Protoplasma **112:** 71–80
Hille B (2001) Ion Channels of Excitable Membranes, Ed 3, Sinauer Associates, Inc. Sunderland, Massachusetts
Hirose T, Zhang Z, Miyao A, Hirochika H, Ohsugi R, Terao T (2010) Disruption of a gene for rice sucrose transporter, OsSUT1, impairs pollen function but pollen maturation is unaffected. J Exp Bot **61:** 3639–3646
Holdaway-Clarke T, Hepler PK (2003) Control of pollen tube growth: role of ion gradients and fluxes. New Phytol **159:** 539–563
Honkanen S, Dolan L (2016) Growth regulation in tip-growing cells that develop on the epidermis. Curr Opin Plant Biol **34:** 77–83
Honys D, Twell D (2003) Comparative analysis of the Arabidopsis pollen transcriptome. Plant Physiol **132:** 640–652
Hou C, Tian W, Kleist T, He K, Garcia V, Bai F, Hao Y, Luan S, Li L (2014) DUF221 proteins are a family of osmosensitive calcium-permeable cation channels conserved across eukaryotes. Cell Res **24:** 632–635
Hrabak EM, Chan CW, Gribskov M, Harper JF, Choi JH, Halford N, Kudla J, Luan S, Nimmo HG, Sussman MR, et al (2003) The Arabidopsis CDPK-SnRK superfamily of protein kinases. Plant Physiol **132:** 666–680
Huang S, Blanchoin L, Chaudhry F, Franklin-Tong VE, Staiger CJ (2004) A gelsolin-like protein from Papaver rhoeas pollen (PrABP80) stimulates calcium-regulated severing and depolymerization of actin filaments. J Biol Chem **279:** 23364–23375
Ishikawa F, Suga S, Uemura T, Sato MH, Maeshima M (2005) Novel type aquaporin SIPs are mainly localized to the ER membrane and show cell-specific expression in Arabidopsis thaliana. FEBS Lett **579:** 5814–5820
Iwano M, Entani T, Shiba H, Kakita M, Nagai T, Mizuno H, Miyawaki A, Shoji T, Kubo K, Isogai A, et al (2009) Fine-tuning of the cytoplasmic Ca^{2+} concentration is essential for pollen tube growth. Plant Physiol **150:** 1322–1334
Iwano M, Igarashi M, Tarutani Y, Kaothien-Nakayama P, Nkayama H, Moriyama H, Yakabe R, Entani T, Shimosato-Asano H, Ueki M, et al (2014) A pollen coat-inducible autoinhibited Ca^{2+}-ATPase expressed in stigmatic papilla cells is required for compatible pollination in the Brassicaceae. Plant Cell **26:** 636–649
Iwano M, Ito K, Fujii S, Kakita M, Asano-Shimosato H, Igarashi M, Kaothien-Nakayama P, Entani T, Kanatani A, Takehisa M, et al (2015) Calcium signalling mediates self-incompatibility response in the Brassicaceae. Nat Plants **1:** 15128
Iwano M, Ngo QA, Entani T, Shiba H, Nagai T, Miyawaki A, Isogai A, Grossniklaus U, Takayama S (2012) Cytoplasmic Ca^{2+} changes dynamically during the interaction of the pollen tube with synergid cells. Development **139:** 4202–4209
Jiang L, Yang SL, Xie LF, Puah CS, Zhang XQ, Yang WC, Sundaresan V, Ye D (2005) VANGUARD1 encodes a pectin methylesterase that enhances pollen tube growth in the *Arabidopsis* style and transmitting tract. Plant Cell **17:** 584–596
Kaplan B, Sherman T, Fromm H (2007) Cyclic nucleotide-gated channels in plants. FEBS Lett **581:** 2237–2246
Kaya H, Iwano M, Takeda S, Kanaoka MM, Kimura S, Abe M, Kuchitsu K (2015) Apoplastic ROS production upon pollination by RbohH and RbohJ in Arabidopsis. Plant Signal Behav **10:** e989050
Kaya H, Nakajima R, Iwano M, Kanaoka MM, Kimura S, Takeda S, Kawarazaki T, Senzaki E, Hamamura Y, Higashiyama T, et al (2014) Ca^{2+}-activated reactive oxygen species production by *Arabidopsis* RbohH and RbohJ is essential for proper pollen tube tip growth. Plant Cell **26:** 1069–1080
Ketelaar T (2013) The actin cytoskeleton in root hairs: all is fine at the tip. Curr Opin Plant Biol **16:** 749–756
Ketelaar T, Galway ME, Mulder BM, Emons AMC (2008) Rates of endocytosis in Arabidopsis root hairs and pollen tubes. J Microsc **231:** 265–273
Kong XQ, Gao XH, Sun W, An J, Zhao YX, Zhang H (2011) Cloning and functional characterization of a cation-chloride cotransporter gene OsCCC1. Plant Mol Biol **75:** 567–578
Konrad KR, Wudick MM, Feijo JA (2011) Calcium regulation of tip growth: new genes for old mechanisms. Curr Opin Plant Biol **14:** 721–730
Kost B (2008) Spatial control of Rho (Rac-Rop) signaling in tip-growing plant cells. Trends Cell Biol **18:** 119–127
Kovar DR, Drobak BK, Staiger CJ (2000) Maize profilin isoforms are functionally distinct. Plant Cell **12:** 583–598
Kroeger JH, Daher FB, Grant M, Geitmann A (2009) Microfilament orientation constrains vesicle flow and spatial distribution in growing pollen tubes. Biophys J **97:** 1822–1831
Lancelle SA, Cresti M, Hepler PK (1987) Ultrastructure of the cytoskeleton in freeze-substituted pollen tubes of Nicotiana alata. Protoplasma **140:** 141–150
Lang V, Pertl-Obermeyer H, Safiarian MJ, Obermeyer G (2014) Pump up the volume: a central role for the plasma membrane H^+ pump in pollen germination and tube growth. Protoplasma **251:** 477–488
Lang V, Usadel B, Obermeyer G (2015) De novo sequencing and analysis of the lily pollen transcriptome: an open access data source for an orphan plant species. Plant Mol Biol **87:** 69–80
Lassig R, Gutermuth T, Bey TD, Konrad KR, Romeis T (2014) Pollen tube NAD(P)H oxidases act as a speed control to dampen growth rate oscillations during polarized cell growth. Plant J **78:** 94–106
Lee S, Lee EJ, Yang EJ, Lee JE, Park AR, Song WH, Park OK (2004) Proteomic identification of annexins, calcium-dependent membrane binding proteins that mediate osmotic stress and abscisic acid signal transduction in *Arabidopsis*. Plant Cell **16:** 1378–1391
Lefebvre B, Arango M, Oufattole M, Crouzet J, Purnelle B, Boutry M (2005) Identification of a Nicotiana plumbaginifolia plasma membrane H^+-ATPase gene expressed in the pollen tube. Plant Mol Biol **58:** 775–787
Leng Q, Mercier RW, Hua BG, Fromm H, Berkowitz GA (2002) Electrophysiological analysis of cloned cyclic nucleotide-gated ion channels. Plant Physiol **128:** 400–410
Leng Q, Mercier RW, Yao W, Berkowitz GA (1999) Cloning and first functional characterization of a plant cyclic nucleotide-gated cation channel. Plant Physiol **121:** 753–761
Li C, Wu HM, Cheung AY (2016) FERONIA and her pals: functions and mechanisms. Plant Physiol **171:** 2379–2392
Li YQ, Zhang HQ, Pierson ES, Huang FY, Linskens HF, Hepler PK, Cresti M (1996) Enforced growth-rate fluctuation causes pectin ring formation in the cell wall of Lilium longiflorum pollen tubes. Planta **200:** 41–49
Lipchinsky A (2015) Osmophoresis: a possible mechanism for vesicle trafficking in tip-growing cells. Phys Biol **12:** 066012
Liu P, Li RL, Zhang L, Wang QL, Niehaus K, Baluska F, Samaj J, Lin JX (2009) Lipid microdomain polarization is required for NADPH oxidase-dependent ROS signaling in Picea meyeri pollen tube tip growth. Plant J **60:** 303–313
Loraine AE, McCormick S, Estrada A, Patel K, Qin P (2013) RNA-seq of Arabidopsis pollen uncovers novel transcription and alternative splicing. Plant Physiol **162:** 1092–1109
Lovy-Wheeler A, Kunkel JG, Allwood EG, Hussey PJ, Hepler PK (2006) Oscillatory increases in alkalinity anticipate growth and may regulate actin dynamics in pollen tubes of lily. Plant Cell **18:** 2182–2193
Lu Y, Chanroj S, Zulkifli L, Johnson MA, Uozumi N, Cheung A, Sze H (2011) Pollen tubes lacking a pair of K^+ transporters fail to target ovules in *Arabidopsis*. Plant Cell **23:** 81–93
Luoni L, Bonza MC, De Michelis MI (2000) H^+/Ca^{2+} exchange driven by the plasma membrane Ca^{2+}-ATPase of Arabidopsis thaliana reconstituted in proteoliposomes after calmodulin-affinity purification. FEBS Lett **482:** 225–230
Ma W, Yoshioka K, Berkowitz GA (2007) Cyclic nucleotide gated channels and Ca-mediated signal transduction during plant innate immune response to pathogens. Plant Signal Behav **2:** 548–550
Mahs A, Steinhorst L, Han JP, Shen LK, Wang Y, Kudla J (2013) The calcineurin B-like Ca^{2+} sensors CBL1 and CBL9 function in pollen germination and pollen tube growth in Arabidopsis. Mol Plant **6:** 1149–1162
Malho R, Read ND, Trewavas AJ, Pais MS (1995) Calcium channel activity during pollen tube growth and reorientation. Plant Cell **7:** 1173–1184
Mangano S, Juarez SP, Estevez JM (2016) ROS regulation of polar growth in plant cells. Plant Physiol **171:** 1593–1605
Manik SM, Shi S, Mao J, Dong L, Su Y, Wang Q, Liu H (2015) The calcium sensor CBL-CIPK is involved in plant's response to abiotic stresses. Int J Genomics **2015:** 493191

Mao J, Manik SM, Shi S, Chao J, Jin Y, Wang Q, Liu H (2016) Mechanisms and physiological roles of the CBL-CIPK networking system in Arabidopsis thaliana. Genes (Basel) **7:** E62

Mayank P, Grossman J, Wuest S, Boisson-Dernier A, Roschitzki B, Nanni P, Nuhse T, Grossniklaus U (2012) Characterization of the phosphoproteome of mature Arabidopsis pollen. Plant J **72:** 89–101

Mendrinna A, Persson S (2015) Root hair growth: it's a one way street. F1000Prime Rep **7:** 23

Meyer S, Mumm P, Imes D, Endler A, Weder B, Al-Rasheid KA, Geiger D, Marten I, Martinoia E, Hedrich R (2010) AtALMT12 represents an R-type anion channel required for stomatal movement in Arabidopsis guard cells. Plant J **63:** 1054–1062

Meyerhoff O, Muller K, Roelfsema MR, Latz A, Lacombe B, Hedrich R, Dietrich P, Becker D (2005) AtGLR3.4, a glutamate receptor channel-like gene is sensitive to touch and cold. Planta **222:** 418–427

Michard E, Alves F, Feijo JA (2009) The role of ion fluxes in polarized cell growth and morphogenesis: the pollen tube as an experimental paradigm. Int J Dev Biol **53:** 1609–1622

Michard E, Dias P, Feijó JA (2008) Tobacco pollen tubes as cellular models for ion dynamics: improved spatial and temporal resolution of extracellular flux and free cytosolic concentration of calcium and protons using pHluorin and YC3.1 CaMeleon. Sex Plant Reprod **21:** 169–181

Michard E, Lima PT, Borges F, Silva AC, Portes MT, Carvalho JE, Gilliham M, Liu LH, Obermeyer G, Feijo JA (2011) Glutamate receptor-like genes form Ca^{2+} channels in pollen tubes and are regulated by pistil D-serine. Science **332:** 434–437

Mittler R, Vanderauwera S, Suzuki N, Miller G, Tognetti VB, Vandepoele K, Gollery M, Shulaev V, Van Breusegem F (2011) ROS signaling: the new wave? Trends Plant Sci **16:** 300–309

Money NP, Hill TW (1997) Correlation between endoglucanase secretion and cell wall strength in oomycete hyphae: implications for growth and morphogenesis. Mycoologia **89:** 777–785

Monshausen GB, Bibikova TN, Messerli MA, Shi C, Gilroy S (2007) Oscillations in extracellular pH and reactive oxygen species modulate tip growth of Arabidopsis root hairs. Proc Natl Acad Sci USA **104:** 20996–21001

Monshausen GB, Messerli MA, Gilroy S (2008) Imaging of the Yellow Cameleon 3.6 indicator reveals that elevations in cytosolic Ca^{2+} follow oscillating increases in growth in root hairs of Arabidopsis. Plant Physiol **147:** 1690–1698

Mouline K, Very AA, Gaymard F, Boucherez J, Pilot G, Devic M, Bouchez D, Thibaud JB, Sentenac H (2002) Pollen tube development and competitive ability are impaired by disruption of a Shaker K^+ channel in Arabidopsis. Genes Dev **16:** 339–350

Moutinho A, Trewavas AJ, Malho R (1998) Relocation of a Ca^{2+}-dependent protein kinase activity during pollen tube reorientation. Plant Cell **10:** 1499–1510

Morris J, Hawthorne KM, Hotze T, Abrams SA, Hirschi KD (2008) Nutritional impact of elevated calcium transport activity in carrots. Proc Natl Acad Sci USA **105:** 1431–1435

Myers C, Romanowsky SM, Barron YD, Garg S, Azuse CL, Curran A, Davis RM, Hatton J, Harmon AC, Harper JF (2009) Calcium-dependent protein kinases regulate polarized tip growth in pollen tubes. Plant J **59:** 528–539

Ngo QA, Vogler H, Lituiev DS, Nestorova A, Grossniklaus U (2014) A calcium dialog mediated by the FERONIA signal transduction pathway controls plant sperm delivery. Dev Cell **29:** 491–500

Obermeyer G (2017) Water transport in pollen. *In* G Obermeyer, JA Feijó, eds, Pollen Tip Growth: From Biophysical Aspects to Systems Biology. Springer-Verlag, Heidelberg, Germany (in press)

Obermeyer G, Kolb HA (1993) K^+ channels in the plasma membrane of lily pollen protoplasts. Bot Acta **106:** 26–31

Obermeyer G, Weisenseel MH (1991) Calcium channel blocker and calmodulin antagonists affect the gradient of free calcium ions in lily pollen tubes. Eur J Cell Biol **56:** 319–327

Padmanaban S, Czerny DD, Levin K, Leydon RR, Su RT, Maugel TK, Zou Y, Chanroj S, Cheung AY, Johnson MA, et al (2017) Transporters involved in pH and K^+ homeostasis affect wall formation, male fertility and embryo development. J Exp Bot (in press)

Parre E, Geitmann A (2005) Pectin and the role of the physical properties of the cell wall in pollen tube growth of Solanum chacoense. Planta **220:** 582–592

Parton RM, Fischer-Parton S, Watahiki MK, Trewavas AJ (2001) Dynamics of the apical vesicle accumulation and the rate of growth are related in individual pollen tubes. J Cell Sci **114:** 2685–2695

Pertl H, Pockl M, Blaschke C, Obermeyer G (2010) Osmoregulation in Lilium pollen grains occurs via modulation of the plasma membrane H^+ ATPase activity by 14-3-3 proteins. Plant Physiol **154:** 1921–1928

Pertl H, Rittmann S, Schulze WX, Obermeyer G (2011) Identification of lily pollen 14-3-3 isoforms and their subcellular and time-dependent expression profile. Biol Chem **392:** 249–262

Pertl-Obermeyer H, Schulze WX, Obermeyer G (2014) In vivo cross-linking combined with mass spectrometry analysis reveals receptor-like kinases and Ca^{2+} signalling proteins as putative interaction partners of pollen plasma membrane H^+ ATPases. J Proteomics **108:** 17–29

Pierson ES, Miller DD, Callaham DA, Shipley AM, Rivers BA, Cresti M, Hepler PK (1994) Pollen tube growth is coupled to the extracellular calcium ion flux and the intracellular calcium gradient: effect of BAPTA-type buffers and hypertonic media. Plant Cell **6:** 1815–1828

Pierson ES, Miller DD, Callaham DA, van Aken J, Hackett G, Hepler PK (1996) Tip-localized calcium entry fluctuates during pollen tube growth. Dev Biol **174:** 160–173

Pina C, Pinto F, Feijo JA, Becker JD (2005) Gene family analysis of the Arabidopsis pollen transcriptome reveals biological implications for cell growth, division control, and gene expression regulation. Plant Physiol **138:** 744–756

Portes MT, Daminelli D, Moreno N, Colaço R, Costa S, Feijó JA (2015) The pollen tube oscillator: integrating biophysics and biochemistry into cellular growth and morphogenesis. *In* S Mancuso, S Shabala, eds, Rhythms in Plants: Phenomenology, Mechanisms, and Adaptive Significance. Springer-Verlag, Heidelberg, Germany, pp 121–156

Potocky M, Jones MA, Bezvoda R, Smirnoff N, Zarsky V (2007) Reactive oxygen species produced by NADPH oxidase are involved in pollen tube growth. New Phytol **174:** 742–751

Price MB, Kong D, Okumoto S (2013) Inter-subunit interactions between glutamate-like receptors in Arabidopsis. Plant Signal Behav **8:** e27034

Qin Y, Leydon AR, Manziello A, Pandey R, Mount D, Denic S, Vasic B, Johnson MA, Palanivelu R (2009) Penetration of the stigma and style elicits a novel transcriptome in pollen tubes, pointing to genes critical for growth in a pistil. PLoS Genet **5:** e1000621

Qin Y, Yang Z (2011) Rapid tip growth: insights from pollen tubes. Semin Cell Dev Biol **22:** 816–824

Qin T, Liu X, Li J, Sun J, Song L, Mao T (2014) *Arabidopsis* Microtubule-Destabilizing Protein 25 functions in pollen tube growth by severing actin filament. Plant Cell **26:** 325–339

Qu X, Zhang H, Xie Y, Wang J, Chen N, Huang S (2013) *Arabidopsis* villins promote actin turnover at pollen tube tips and facilitate the construction of actin collars. Plant Cell **25:** 1803–1817

Rathore KS, Cork RJ, Robinson KR (1991) A cytoplasmic gradient of Ca^{2+} is correlated with the growth of lily pollen tubes. Dev Biol **148:** 612–619

Rato C, Monteiro D, Hepler PK, Malho R (2004) Calmodulin activity and cAMP signalling modulate growth and apical secretion in pollen tubes. Plant J **38:** 887–897

Reiss HD, Herth W (1985) Nifedipine-sensitive calcium channels are involved in polar growth of lily pollen tubes. J Cell Sci **76:** 247–254

Robertson WR, Clark K, Young JC, Sussman MR (2004) An Arabidopsis thaliana plasma membrane proton pump is essential for pollen development. Genetics **168:** 1677–1687

Rojas ER, Hotton S, Dumais J (2011) Chemically mediated mechanical expansion of the pollen tube cell wall. Biophys J **101:** 1844–1853

Rounds CM, Hepler PK, Winship LJ (2014) The apical actin fringe contributes to localized cell wall deposition and polarized growth in the lily pollen tube. Plant Physiol **166:** 139–151

Rudall PJ, Bateman RM (2007) Developmental bases for key innovations in the seed-plant microgametophyte. Trends Plant Sci **12:** 317–326

Safiarian MJ, Pertl-Obermeyer H, Lughofer P, Hude R, Bertl A, Obermeyer G (2015) Lost in traffic? The K^+ channel of lily pollen, LilKT1, is detected at the endomembranes inside yeast cells, tobacco leaves, and lily pollen. Front Plant Sci **6:** 47

Sakano K (2001) Metabolic regulation of pH in plant cells: role of cytoplasmic pH in defense reaction and secondary metabolism. Int Rev Cytol **206:** 1–44

Sanders D, Hansen UP, Slayman CL (1981) Role of the plasma membrane proton pump in pH regulation in non-animal cells. Proc Natl Acad Sci USA **78:** 5903–5907

Schiott M, Romanowsky SM, Baekgaard L, Jakobsen MK, Palmgren MG, Harper JF (2004) A plant plasma membrane Ca^{2+} pump is required for normal pollen tube growth and fertilization. Proc Natl Acad Sci USA **101:** 9502–9507

Schroeter K, Sievers A (1971) Wirkung der Turgorreduktion auf den Golgi-Apparat und die Bildung der Zellwand bei Wurzelhaaren. Protoplasma **72:** 203–211

Segal AW (2016) NADPH oxidases as electrochemical generators to produce ion fluxes and turgor in fungi, plants and humans. Open Biol **6:** 160028

Shang ZL, Ma LG, Zhang HL, He RR, Wang XC, Cui SJ, Sun DY (2005) Ca^{2+} influx into lily pollen grains through a hyperpolarization-activated Ca^{2+}-permeable channel which can be regulated by extracellular CaM. Plant Cell Physiol **46:** 598–608

Simon MLA, Platre MP, Marquès-Bueño MM, Armengot L, Stanislas T, Caillaud MC, Jaillais Y (2016) A PtdIns(4)-driven electrostatic field controls cell membrane identity and signalling in plants. Nat Plants **2:** 1–10

Sivitz AB, Reinders A, Ward JM (2008) Arabidopsis sucrose transporter AtSUC1 is important for pollen germination and sucrose-induced anthocyanin accumulation. Plant Physiol **147:** 92–100

Smith AM, Coupland G, Dolan L, Harberd N, Jones J, Martin C, Sablowski R, Amey A (2009) Plant Biology. Garland Science, New York

Smith FA, Raven JA (1979) Intracellular pH and its regulation. Annu Rev Plant Physiol **30:** 289–311

Snowman BN, Kovar DR, Shevchenko G, Franklin-Tong VE, Staiger CJ (2002) Signal-mediated depolymerization of actin in pollen during the self-incompatibility response. Plant Cell **14:** 2613–2626

Sommer A, Geist B, Da Ines O, Gehwolf R, Schaffner AR, Obermeyer G (2008) Ectopic expression of Arabidopsis thaliana plasma membrane intrinsic protein 2 aquaporins in lily pollen increases the plasma membrane water permeability of grain but not of tube protoplasts. New Phytol **180:** 787–797

Soto G, Alleva K, Mazzella MA, Amodeo G, Muschietti JP (2008) AtTIP1;3 and AtTIP5;1, the only highly expressed Arabidopsis pollen-specific aquaporins, transport water and urea. FEBS Lett **582:** 4077–4082

Stadler R, Truernit E, Gahrtz M, Sauer N (1999) The AtSUC1 sucrose carrier may represent the osmotic driving force for anther dehiscence and pollen tube growth in Arabidopsis. Plant J **19:** 269–278

Stael S, Rocha AG, Wimberger T, Anrather D, Vothknecht UC, Teige M (2012) Cross-talk between calcium signalling and protein phosphorylation at the thylakoid. J Exp Bot **63:** 1725–1733

Steer MW, Steer JM (1989) Pollen tube tip growth. New Phytol **111:** 323–358

Steinhorst L, Kudla J (2013) Calcium: a central regulator of pollen germination and tube growth. Biochim Biophys Acta **1833:** 1573–1581

Steinhorst L, Mahs A, Ischebeck T, Zhang C, Zhang X, Arendt S, Schultke S, Heilmann I, Kudla J (2015) Vacuolar CBL-CIPK12 Ca^{2+}-sensor-kinase complexes are required for polarized pollen tube growth. Curr Biol **25:** 1475–1482

Stephens NR, Qi Z, Spalding EP (2008) Glutamate receptor subtypes evidenced by differences in desensitization and dependence on the GLR3.3 and GLR3.4 genes. Plant Physiol **146:** 529–538

Strompen G, Dettmer J, Stierhof YD, Schumacher K, Jurgens G, Mayer U (2005) Arabidopsis vacuolar H-ATPase subunit E isoform 1 is required for Golgi organization and vacuole function in embryogenesis. Plant J **41:** 125–132

Sun MX, Huang XY, Yang J, Guan YF, Yang ZN (2013) Arabidopsis RPG1 is important for primexine deposition and functions redundantly with RPG2 for plant fertility at the late reproductive stage. Plant Reprod **26:** 83–91

Sun W, Li S, Xu J, Liu T, Shang Z (2009) H^+-ATPase in the plasma membrane of *Arabidopsis* pollen cells is involved in extracellular calmodulin-promoted pollen germination. Prog Nat Sci **19:** 1071–1078

Sze H, Padmanaban S, Cellier F, Honys D, Cheng NH, Bock KW, Conejero G, Li X, Twell D, Ward JM, et al (2004) Expression patterns of a novel AtCHX gene family highlight potential roles in osmotic adjustment and K^+ homeostasis in pollen development. Plant Physiol **136:** 2532–2547

Taiz L, Zeiger E, Møller IM, Murphy A (2015) Plant Physiology and Development, Ed 6, Sinauer Associates, Inc. Sunderland, Massachusetts

Tapken D, Anschutz U, Liu LH, Huelsken T, Seebohm G, Becker D, Hollmann M (2013) A plant homolog of animal glutamate receptors is an ion channel gated by multiple hydrophobic amino acids. Sci Signal **6:** ra47

Tapken D, Hollmann M (2008) Arabidopsis thaliana glutamate receptor ion channel function demonstrated by ion pore transplantation. J Mol Biol **383:** 36–48

Tavares B, Dias PN, Domingos P, Moura TF, Feijo JA, Bicho A (2011a) Calcium-regulated anion channels in the plasma membrane of Lilium longiflorum pollen protoplasts. New Phytol **192:** 45–60

Tavares B, Domingos P, Dias PN, Feijo JA, Bicho A (2011b) The essential role of anionic transport in plant cells: the pollen tube as a case study. J Exp Bot **62:** 2273–2298

Teardo E, Carraretto L, De Bortoli S, Costa A, Behera S, Wagner R, Lo Schiavo F, Formentin E, Szabo I (2015) Alternative splicing-mediated targeting of the Arabidopsis GLUTAMATE RECEPTOR3.5 to mitochondria affects organelle morphology. Plant Physiol **167:** 216–227

Teardo E, Formentin E, Segalla A, Giacometti GM, Marin O, Zanetti M, Lo Schiavo F, Zoratti M, Szabo I (2011) Dual localization of plant glutamate receptor AtGLR3.4 to plastids and plasmamembrane. Biochim Biophys Acta **1807:** 359–367

Teardo E, Segalla A, Formentin E, Zanetti M, Marin O, Giacometti GM, Lo Schiavo F, Zoratti M, Szabo I (2010) Characterization of a plant glutamate receptor activity. Cell Physiol Biochem **26:** 253–262

Tian GW, Chen MH, Zaltsman A, Citovsky V (2006) Pollen-specific pectin methylesterase involved in pollen tube growth. Dev Biol **294:** 83–91

Tominaga M, Kojima H, Yokota E, Nakamori R, Anson M, Shimmen T, Oiwa K (2012) Calcium-induced mechanical change in the neck domain alters the activity of plant myosin XI. J Biol Chem **287:** 30711–30718

Tunc-Ozdemir M, Rato C, Brown E, Rogers S, Mooneyham A, Frietsch S, Myers CT, Poulsen LR, Malho R, Harper JF (2013a) Cyclic nucleotide gated channels 7 and 8 are essential for male reproductive fertility. PLoS ONE **8:** e55277

Tunc-Ozdemir M, Tang C, Ishka MR, Brown E, Groves NR, Myers CT, Rato C, Poulsen LR, McDowell S, Miller G, et al (2013b) A cyclic nucleotide-gated channel (CNGC16) in pollen is critical for stress tolerance in pollen reproductive development. Plant Physiol **161:** 1010–1020

Vidali L, Hepler PK (2001) Actin and pollen tube growth. Protoplasma **215:** 64–76

Vieira AM, Feijo JA (2016) Hydrogel control of water uptake by pectins during in vitro pollen hydration of Eucalyptus globulus. Am J Bot **103:** 437–451

Vincill ED, Clarin AE, Molenda JN, Spalding EP (2013) Interacting glutamate receptor-like proteins in Phloem regulate lateral root initiation in *Arabidopsis*. Plant Cell **25:** 1304–1313

Vogler H, Draeger C, Weber A, Felekis D, Eichenberger C, Routier-Kierzkowska AL, Boisson-Dernier A, Ringli C, Nelson BJ, Smith RS, et al (2012) The pollen tube: a soft shell with a hard core. Plant J **73:** 617–627

Wagner S, Behera S, De Bortoli S, Logan DC, Fuchs P, Carraretto L, Teardo E, Cendron L, Nietzel T, Fussl M, et al (2015) The EF-hand Ca^{2+} binding protein MICU choreographs mitochondrial Ca^{2+} dynamics in *Arabidopsis*. Plant Cell **27:** 3190–3212

Wang H, Zhuang X, Wang X, Law AHY, Zhao T, Du S, Loy MMT, Jiang L (2016) A distinct pathway for polar exocytosis in plant cell wall formation. Plant Physiol **172:** 1003–1018

Wang HJ, Wan AR, Jauh GY (2008a) An actin-binding protein, LILIM1, mediates calcium and hydrogen regulation of actin dynamics in pollen tubes. Plant Physiol **147:** 1619–1636

Wang Y, Zhang WZ, Song LF, Zou JJ, Su Z, Wu WH (2008b) Transcriptome analyses show changes in gene expression to accompany pollen germination and tube growth in Arabidopsis. Plant Physiol **148:** 1201–1211

Wang YF, Fan LM, Zhang WZ, Zhang W, Wu WH (2004) Ca^{2+}-permeable channels in the plasma membrane of Arabidopsis pollen are regulated by actin microfilaments. Plant Physiol **136:** 3892–3904

White PJ, Broadley MR (2003) Calcium in plants. Ann Bot (Lond) **92:** 487–511

Williams JH (2008) Novelties of the flowering plant pollen tube underlie diversification of a key life history stage. Proc Natl Acad Sci USA **105:** 11259–11263

Winship LJ, Obermeyer G, Geitmann A, Hepler PK (2011) Pollen tubes and the physical world. Trends Plant Sci **16:** 353–355

Wu J, Qin X, Tao S, Jiang X, Liang YK, Zhang S (2014) Long-chain base phosphates modulate pollen tube growth via channel-mediated influx of calcium. Plant J **79:** 507–516

Wu J, Shang Z, Wu J, Jiang X, Moschou PN, Sun W, Roubelakis-Angelakis KA, Zhang S (2010) Spermidine oxidase-derived H_2O_2 regulates pollen plasma membrane hyperpolarization-activated Ca^{2+}-permeable channels and pollen tube growth. Plant J **63:** 1042–1053

Wudick MM, Feijo JA (2014) At the intersection: merging Ca^{2+} and ROS signaling pathways in pollen. Mol Plant **7:** 1595–1597

Wudick MM, Luu DT, Tournaire-Roux C, Sakamoto W, Maurel C (2014) Vegetative and sperm cell-specific aquaporins of Arabidopsis highlight the vacuolar equipment of pollen and contribute to plant reproduction. Plant Physiol **164:** 1697–1706

Xiang Y, Huang X, Wang T, Zhang Y, Liu Q, Hussey PJ, Ren H (2007) ACTIN BINDING PROTEIN 29 from *Lilium* pollen plays an important role in dynamic actin remodeling. Plant Cell **19:** 1930–1946

Xu J, Li HD, Chen LQ, Wang Y, Liu LL, He L, Wu WH (2006) A protein kinase, interacting with two calcineurin B-like proteins, regulates K^+ transporter AKT1 in Arabidopsis. Cell **125:** 1347–1360

Yang SN, Shi Y, Yang G, Li Y, Yu J, Berggren PO (2014) Ionic mechanisms in pancreatic beta cell signaling. Cell Mol Life Sci **71:** 4149–4177

Yokota E, Muto S, Shimmen T (1999) Inhibitory regulation of higher-plant myosin by Ca^{2+} ions. Plant Physiol **119:** 231–240

Yokota E, Tominaga M, Mabuchi I, Tsuji Y, Staiger CJ, Oiwa K, Shimmen T (2005) Plant villin, lily P-135-ABP, possesses G-actin binding activity and accelerates the polymerization and de-polymerization of actin in a Ca^{2+}-sensitive manner. Plant Cell Physiol **46:** 1690–1703

Yuan F, Yang H, Xue Y, Kong D, Ye R, Li C, Zhang J, Theprungsirikul L, Shrift T, Krichilsky B, et al (2014) OSCA1 mediates osmotic-stress-evoked Ca^{2+} increases vital for osmosensing in Arabidopsis. Nature **514:** 367–371

Zerzour R, Kroeger J, Geitmann A (2009) Polar growth in pollen tubes is associated with spatially confined dynamic changes in cell mechanical properties. Dev Biol **334:** 437–446

Zhao J, Cheng NH, Motes CM, Blancaflor EB, Moore M, Gonzales N, Padmanaban S, Sze H, Ward JM, Hirschi KD (2008) AtCHX13 is a plasma membrane K^+ transporter. Plant Physiol **148:** 796–807

Zhao J, Li P, Motes CM, Park S, Hirschi KD (2015) CHX14 is a plasma membrane K-efflux transporter that regulates K^+ redistribution in Arabidopsis thaliana. Plant Cell Environ **38:** 2223–2238

Zhao LN, Shen LK, Zhang WZ, Zhang W, Wang Y, Wu WH (2013) Ca^{2+}-dependent protein kinase11 and 24 modulate the activity of the inward rectifying K^+ channels in *Arabidopsis* pollen tubes. Plant Cell **25:** 649–661

Zhou L, Lan W, Chen B, Fang W, Luan S (2015a) A calcium sensor-regulated protein kinase, CALCINEURIN B-LIKE PROTEIN-INTERACTING PROTEIN KINASE19, is required for pollen tube growth and polarity. Plant Physiol **167:** 1351–1360

Zhou L, Lan W, Jiang Y, Fang W, Luan S (2014) A calcium-dependent protein kinase interacts with and activates a calcium channel to regulate pollen tube growth. Mol Plant **7:** 369–376

Zhou Z, Shi H, Chen B, Zhang R, Huang S, Fu Y (2015b) *Arabidopsis* RIC1 severs actin filaments at the apex to regulate pollen tube growth. Plant Cell **27:** 1140–1161

Zhu J, Yuan S, Wei G, Qian D, Wu X, Jia H, Gui M, Liu W, An L, Xiang Y (2014) Annexin5 is essential for pollen development in Arabidopsis. Mol Plant **7:** 751–754

Zhu L, Zhang Y, Kang E, Xu Q, Wang M, Rui Y, Liu B, Yuan M, Fu Y (2013) MAP18 regulates the direction of pollen tube growth in *Arabidopsis* by modulating F-actin organization. Plant Cell **25:** 851–867

Zonia L, Cordeiro S, Tupy J, Feijo JA (2002) Oscillatory chloride efflux at the pollen tube apex has a role in growth and cell volume regulation and is targeted by inositol 3,4,5,6-tetrakisphosphate. Plant Cell **14:** 2233–2249

Zonia L, Munnik T (2011) Understanding pollen tube growth: the hydrodynamic model versus the cell wall model. Trends Plant Sci **16:** 347–352

Appendix C: Membrane transport under salt stress

The discussion of the ionic basis in electrical signaling from the main text was restricted to ideal conditions when Na^+ is absent. This is not an entirely physiological scenario; therefore membrane transport events impacting cell signaling under salt-stress should not be neglected. We outline that a Na^+ permeability changes the membrane potential, Na^+ sensing alters Ca^{2+} permeability, and reactive oxygen species play an integral signaling role and impact cell health.

Appendix C presents an excerpt from:

Michard, E. and Simon AA. (2020) Melatonin's antioxidant properties protect plants under salt stress. **Plant, Cell & Environment.** 43:2587–2590.

Salt stress starts by Na^+ entry into the cell through non-selective cation channels. If Na^+ influx exceeds extrusion through transporters at the plasma membrane (PM) or tonoplast, the cytosolic $[Na^+]$ increases, and the $[K^+]/[Na^+]$ ratio decreases. Na^+ influx depolarizes the PM triggering K^+ efflux through non-selective cation channels and voltage-sensitive outward K^+ channels, further decreasing the $[K^+]/[Na^+]$ ratio. The adaptation to NaCl stress implies the activation of ion transporters through post-translational or transcriptional regulations that re-establish a homeostatic $[K^+]/[Na^+]$ ratio (Wu, Zhang, Giraldo & Shabala, 2018). The ion transport system that maintains a high $[K^+]/[Na^+]$ ratio is under the control of a signaling network involving H_2O_2 and Ca^{2+}. Na^+

is sensed possibly by the newly described Na^+ sensor glucuronosyltransferase for glycosyl inositol phosphorylceramide (GIPC) sphingolipids (Jiang, Zhou, Tao, Yuan, Liu *et al.* 2019), which activates Ca^{2+} channels and increases Ca^{2+} influx into the cytosol. The increase in cytosolic Ca^{2+} upregulates Na^+/H^+ antiporters in the plasma membrane and the tonoplast through the well-established SOS pathway, which involves Ca^{2+}-sensing CBLs and CBL-interacting protein kinases (CIPKs) (Manishankar, Wang, Koster, Alatar & Kudla, 2018). Ca^{2+} increase in the cytosol triggers RBOH activity, possibly through direct interaction of EF-hands present on RBOH enzymes, and though Ca^{2+}-dependent phosphorylation (Ogasawara, Kaya, Hiraoka, Yumoto, Kimura, Kadota, Hishinuma, Senzaki, Yamagoe, Nagata, Nara, Suzuki, Tanokura & Kuchitsu, 2008). RBOH activity directly induces the formation of H_2O_2 that is eventually converted into other ROS, for example by the Fenton reaction. H_2O_2 induces a transcriptional up-regulation of K^+ transporters and up- and down- regulation of signaling proteins. In parallel, H_2O_2 and Ca^{2+} also directly target ion transporters for post-translational regulation. The transporters newly transcribed or targeted by H_2O_2/Ca^{2+}-regulation contribute to maintain a high $[K^+]/[Na^+]$ ratio.

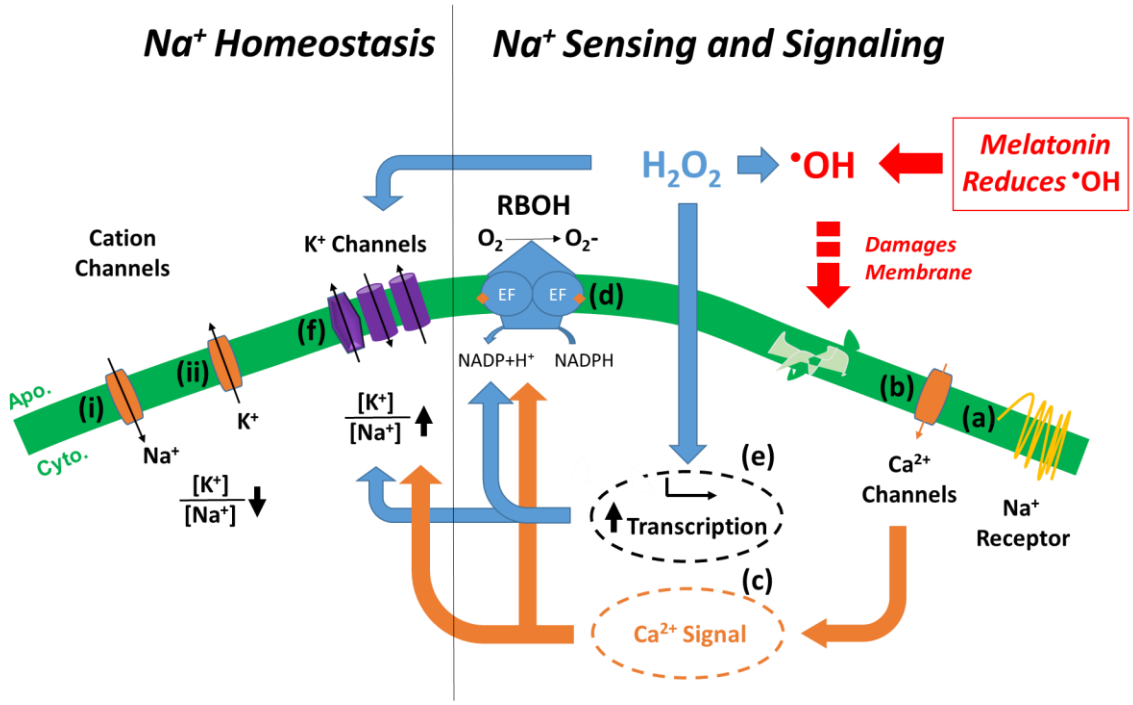

Figure 1: Molecular responses to salt stress in rice root apex cells, and ameliorating effects of melatonin. Possible molecular mechanism of melatonin-mediated salt stress amelioration (see text for details). One important factor that confers to halophyte their salt tolerance compared to glycophytes is the ability to maintain a high $[K^+]/[Na^+]$ ratio in the cytosol. Note that in addition to the Na^+-specific stress response addressed here, salt stress has a Cl^- component that was omitted for simplicity. **(i)** Na^+-permeable channels of unknown nature take up Na^+ into the cell. Glutamate receptor-like channels, cyclic-nucleotide gated channels or annexins could be involved. **(ii)** Na^+ influx depolarizes the plasma membrane, and K^+ leaks out of the cell through unidentified channels, possibly non-selective channels as well as depolarization-activated K^+ channels such as GORK. **(a)** Extracellular Na^+ is sensed, possibly by GIPC sphingolipids. **(b)** Unidentified channels permeable to Ca^{2+} induce Ca^{2+} influx. **(c)** The Ca^{2+} signal triggers the so-called Salt Overly Sensitive (SOS) signaling pathway to maintain ion homeostasis. **(d)** Respiratory Burst Oxidase Homologs (RBOH) activity is activated by Ca^{2+}. The Fenton reaction ($Fe^{2+} + H_2O_2 \rightarrow Fe^{3+} + {}^{\bullet}OH + OH^-$) and Haber-Weiss Reaction ($O_2^{\bullet-} + H_2O_2 \rightarrow O_2 + {}^{\bullet}OH + OH^-$) participate in the formation of ${}^{\bullet}OH$ that is scavenged in the presence of melatonin. **(e)** H_2O_2 induces transcriptional regulation of membrane transporters, including K^+ transporters, through an unknown pathway. **(f)** Transporter regulation helps to maintain a high $[K^+]/[Na^+]$ ratio. The activity of the following membrane transporters is potentially increased: plasma membrane H^+-ATPases, tonoplast H^+-ATPases/H^+-PPases, K^+ transporters such as AKT, HAK, SKOR (known to be regulated by redox), Na^+/H^+ exchangers (NHX), and the Na^+/H^+ antiporter Salt Overly Sensitive 1 (SOS1). Those transporters may also be the direct target of ROS by oxidation of cysteines.

References

Wu H., Zhang X., Giraldo J.P. & Shabala S. (2018) It is not all about sodium: revealing tissue specificity and signalling roles of potassium in plant responses to salt stress. *Plant and Soil*, **431**, 1-17.

Jiang Z., Zhou X., Tao M., Yuan F., Liu L., Wu F., Wu X., Xiang Y., Niu Y., Liu F., Li C., Ye R., Byeon B., Xue Y., Zhao H., Wang H.N., Crawford B.M., Johnson D.M., Hu C., Pei C., Zhou W., Swift G.B., Zhang H., Vo-Dinh T., Hu Z., Siedow J.N. & Pei Z.M. (2019) Plant cell-surface GIPC sphingolipids sense salt to trigger Ca(2+) influx. *Nature*, **572**, 341-346.

Manishankar P., Wang N., Koster P., Alatar A.A. & Kudla J. (2018) Calcium Signaling during Salt Stress and in the Regulation of Ion Homeostasis. *J Exp Bot*. **69**, 4215–4226.

Ogasawara Y., Kaya H., Hiraoka G., Yumoto F., Kimura S., Kadota Y., Hishinuma H., Senzaki E., Yamagoe S., Nagata K., Nara M., Suzuki K., Tanokura M. & Kuchitsu K. (2008) Synergistic activation of the Arabidopsis NADPH oxidase AtrbohD by Ca^{2+} and phosphorylation. *J Biol Chem*, **283**, 8885-8892.

References

1. S. G. Carriedo, S. L. Sensi, H. Z. Yin, J. H. Weiss, AMPA exposures induce mitochondrial Ca2+ overload and ROS generation in spinal motor neurons in vitro. *J. Neurosci.* **20**, 240–250 (2000).

2. S. J. Liu, R. S. Zukin, Ca2+-permeable AMPA receptors in synaptic plasticity and neuronal death. *Trends Neurosci.* **30**, 126–134 (2007).

3. Q. Zhou, M. Sheng, NMDA receptors in nervous system diseases. *Neuropharmacology* **74**, 69–75 (2013).

4. L. Volk, S.-L. Chiu, K. Sharma, R. L. Huganir, Glutamate Synapses in Human Cognitive Disorders. *Annu. Rev. Neurosci.* **38**, 127–149 (2015).

5. E. C. Twomey, *et al.*, Mechanisms of Channel Block in Calcium-Permeable AMPA Receptors. *Neuron*, 1–13 (2018).

6. J. B. Amin, G. R. Moody, L. P. Wollmuth, From bedside-to-bench: What disease-associated variants are teaching us about the NMDA receptor. *J. Physiol.* **0**, 1–20 (2020).

7. A. D. Hogan-Cann, C. M. Anderson, Physiological Roles of Non-Neuronal NMDA Receptors. *Trends Pharmacol. Sci.* **37**, 750–767 (2016).

8. J. Marquard, *et al.*, Characterization of pancreatic NMDA receptors as possible drug targets for diabetes treatment. *Nat. Med.* **21**, 363–376 (2015).

9. S. Gill, J. Veinot, M. Kavanagh, O. Pulido, Human Heart Glutamate Receptors—Implications for Toxicology, Food Safety, and Drug Discovery. *Toxicol. Pathol.* **35**, 411–417 (2007).

10. L. P. Wollmuth, Ion permeation in ionotropic glutamate receptors: still dynamic after all these years. *Curr. Opin. Physiol.* **2**, 36–41 (2018).

11. R. Reski, J. Parsons, E. L. Decker, Moss-made pharmaceuticals: From bench to bedside. *Plant Biotechnol. J.* **13**, 1191–1198 (2015).

12. E. L. Decker, R. Reski, Mosses in biotechnology. *Curr. Opin. Biotechnol.* **61**, 21–27 (2020).

13. B. Hille, Ion Channel Excitable Membranes. *Sunderl. Massachusetts USA*, 1–37 (2001).

14. Y. Kirichok, G. Krapivinsky, D. E. Clapham, The mitochondrial calcium uniporter is a highly selective ion channel. *Nature* **427**, 360–364 (2004).

15. B. Li, M. R. Tadross, R. W. Tsien, Sequential ionic and conformational signaling by calcium channels drives neuronal gene expression. *Science.* **351**, 863–867 (2016).

16. P. Marhavý, *et al.*, Single-cell damage elicits regional, nematode-restricting ethylene responses in roots. *EMBO J.* **38**, e100972 (2019).

17. S. A. R. Mousavi, A. Chauvin, F. Pascaud, S. Kellenberger, E. E. Farmer, GLUTAMATE RECEPTOR-LIKE genes mediate leaf-to-leaf wound signalling. *Nature* **500**, 422–426 (2013).

18. J. Kang, S. Mehta, F. J. Turano, Regulates Abscisic Acid Biosynthesis and Signaling to Control Development and Water Loss. *Plant Cell Physiol* **45**, 1380–1389 (2004).

19. A. L. Hodgkin, A. F. Huxley, Currents Carried by Sodium and Potassium Ions through the Membrane of the Giant Axon of Loligo. *J. Physiol* **116**, 449–472 (1952).

20. A. L. Hodgkin, A. F. Huxley, Propagation of electrical signals along giant nerve fibres. *J. Physiol.* **104**, 176–195 (1952).

21. A. L. Hodgkin, A. F. Huxley, Resting and action potentials in single nerve fibres. *J. Physiol.* **104**, 176–195 (1945).

22. A. L. Hodgkin, A. F. Huxley, A quantitative description of membrane current and its application to conduction and excitation in nerve. *J. Physiol.* **117**, 500–544 (1952).

23. A. L. Hodgkin, A. F. Huxley, The dual effect of membrane potential on sodium conductance in the giant axon of Loligo. *J. Physiol.* **116**, 497–506 (1952).

24. A. L. Hodgkin, A. F. Huxley, The components of membrane conductance in the giant axon of Loligo. *J. Physiol.* **116**, 473–496 (1952).

25. M. Levin, Large-scale biophysics: ion flows and regeneration. *Trends Cell Biol.* **17**, 261–270 (2007).

26. W. A. Catterall, Voltage-Gated Calcium Channels. *Cold Spring Harb. Perspect. Biol.*, 1–24 (2011).

27. L. R. Mills, *et al.*, N-type Ca2+ channels are located on somata, dendrites, and a subpopulation of dendritic spines on live hippocampal pyramidal neurons. *J. Neurosci.* **14**, 6815–6824 (1994).

28. R. W. Tsien, C. F. Barrett, A Brief History of Gdcium Channel Discovery (2005).

29. and B. S. Spruston, N., Y. Schiller, G. Stuart, Activity dependent action potential invasion and calcium influx into hippocampal CAl dendrites. *Science.* **268**, 297–300 (1995).

30. M. Naraghi, E. Neher, Linearized buffered Ca2+ diffusion in microdomains and its implications for calculation of [Ca2+] at the mouth of a calcium channel. *J. Neurosci.* **17**, 6961–6973 (1997).

31. D. E. Clapham, Calcium Signaling. *Cell* **131**, 1047–1058 (2007).

32. J. Burdon-Sanderson, Electrical phenomena in the leaf of Dionaea muscipula. *Proc. R. Soc. London* **21**, 495–496 (1873).

33. Umrath K., Untersuchungen über Plasma und Plasmas- trömungen an Characeen. IV. Potentialmessungen an Nitella mucronata mit besonderer Berücksichtigung der Erregungser- scheinungen. *Protoplasma* **9**, 576–597 (1930).

34. A. L. Nastuk, W. L., Hodgkin, The electrical activity of single muscle fibers. *J. Cell. Compo Physiol.* **35**, 39–73 (1950).

35. H. J. Curtis, K. S. Cole, Transverse electric impedance of nitella. *J. Gen. Physiol.* **21**, 189–201 (1937).

36. S. Shabala, I. Newman, Light-induced changes in hydrogen, calcium, potassium, and chloride ion fluxes and concentrations from the mesophyll and epidermal tissues of bean leaves. Understanding the ionic basis of light-induced bioelectrogenesis. *Plant Physiol.* **119**, 1115–1124 (1999).

37. M. H. Cho, E. P. Spalding, An anion channel in Arabidopsis hypocotyls activated by blue light. *Plant Biol.* **93**, 8134–8138 (1996).

38. E. P. Spalding, Ion channels and the transduction of light signals. *Plant, Cell Environ.* **23**, 665–674 (2000).

39. M. Koselski, K. Trebacz, H. Dziubinska, E. Krol, Light- and dark-induced action potentials in Physcomitrella patens. *Plant Signal. Behav.* **3**, 13–18 (2008).

40. S. Stoelzle, T. Kagawa, M. Wada, R. Hedrich, P. Dietrich, Blue light activates calcium-permeable channels in Arabidopsis mesophyll cells via the phototropin signaling pathway. *Proc. Natl. Acad. Sci. U. S. A.* **100**, 1456–1461 (2003).

41. O. Meyerhoff, *et al.*, AtGLR3.4, a glutamate receptor channel-like gene is sensitive to touch and cold. *Planta* **222**, 418–427 (2005).

42. A. Carpaneto, *et al.*, Cold transiently activates calcium-permeable channels in Arabidopsis mesophyll cells. *Plant Physiol.* **143**, 487–494 (2007).

43. E. Krol, H. Dziubińska, K. Trebacz, Low-temperature-induced transmembrane potential changes in mesophyll cells of Arabidopsis thaliana, Helianthus annuus and Vicia faba. *Physiol. Plant.* **120**, 265–270 (2004).

44. S. Zimmermann, *et al.*, Receptor-mediated activation of a plant Ca2+-permeable ion channel involved in pathogen defense. *Proc. Natl. Acad. Sci. U. S. A.* **94**, 2751–2755 (1997).

45. H. H. Felle, M. R. Zimmermann, Systemic signalling in barley through action potentials. *Planta* **226**, 203–14 (2007).

46. D. J. Cosgrove, R. Hedrich, Stretch-activated chloride, potassium, and calcium channels coexisting in plasma membranes of guard cells of Vicia faba L. *Planta* **186**, 143–153 (1991).

47. V. Kiep, *et al.*, Systemic cytosolic Ca2+ elevation is activated upon wounding and herbivory in Arabidopsis. *New Phytol.* **207**, 996–1004 (2015).

48. R. Hedrich, Ion channels in plants. *Physiol. Rev.* **92**, 1777–1811 (2012).

49. E. E. Farmer, Y. Q. Gao, G. Lenzoni, J. L. Wolfender, Q. Wu, Wound- and mechanostimulated electrical signals control hormone responses. *New Phytol.* **227**, 1037–1050 (2020).

50. T. Cuin, I. Dreyer, E. Michard, The Role of Potassium Channels in Arabidopsis thaliana Long Distance Electrical Signalling: AKT2 Modulates Tissue Excitability While GORK Shapes Action Potentials. *Int. J. Mol. Sci.* **19**, 926 (2018).

51. B. P. Bean, The action potential in mammalian central neurons. *Nat. Rev. Neurosci.* **8**, 451–465 (2007).

52. J. Fromm, S. Lautner, Electrical signals and their physiological significance in plants. *Plant, Cell Environ.* **30**, 249–257 (2007).

53. E. Ermolayeva, H. Hohmeyer, E. Johannes, D. Sanders, Calcium-dependent membrane depolarisation activated by phytochrome in the moss Physcomitrella patens. *Planta* **199**, 352–358 (1996).

54. P. Favre, R. D. Agosti, Voltage-dependent action potentials in Arabidopsis thaliana. *Physiol. Plant.* **131**, 263–272 (2007).

55. T. M. Shimmen T, Mimura T, Kikuyama M, Characean Cells as a Tool for Studying Electrophysiological Characteristics of Plant Cells. *Cell Struct. Funct.* **19**, 263–278 (1994).

56. E. M. Ruszala, *et al.*, Land plants acquired active stomatal control early in their

evolutionary history. *Curr. Biol.* **21**, 1030–1035 (2011).

57. C. T. Nguyen, A. Kurenda, S. Stolz, A. Chételat, E. E. Farmer, Identification of cell populations necessary for leaf-toleaf electrical signaling in a wounded plant. *Proc. Natl. Acad. Sci.* **115**, 10178–10183 (2018).

58. M. R. Zimmermann, H. Maischak, A. Mithöfer, W. Boland, H. H. Felle, System potentials, a novel electrical long-distance apoplastic signal in plants, induced by wounding. *Plant Physiol.* **149**, 1593–1600 (2009).

59. M. R. Zimmermann, A. Mithöfer, T. Will, H. H. Felle, A. C. U. Furch, Herbivore-triggered electrophysiological reactions: Candidates for systemic signals in higher plants and the challenge of their identification. *Plant Physiol.* **170**, 2407–2419 (2016).

60. G. Thiel, E. A. . MacRobbie, M. . Blatt, Membrane Transport in Stomatai Guard Cells: The Importance of Voltage Control. *Membr. Biol.* **126**, 1–18 (1992).

61. D. Gradmann, M. . Blatt, G. Thiel, Electrocoupling of Ion Transporters in Plants. *Membr. Biol.* **136**, 327–332 (1993).

62. J. I. Schroeder, B. U. Keller, Two types of anion channel currents in guard cells with distinct voltage regulation. *Proc. Natl. Acad. Sci. U. S. A.* **89**, 5025–5029 (1992).

63. M. Jezek, M. R. Blatt, The Membrane Transport System of the Guard Cell and Its Integration for Stomatal Dynamics. *Plant Physiol.* **174**, pp.01949.2016 (2017).

64. E. Michard, A. A. Simon, B. Tavares, M. M. Wudick, J. A. Feijó, Signaling with ions: The keystone for apical cell growth and morphogenesis in pollen tubes. *Plant Physiol.* **173**, 91–111 (2017).

65. R. D. Hoffmann, *et al.*, Plasma membrane H+-ATPases sustain pollen tube growth and fertilization. *Nat. Commun.* **11**, 1–15 (2020).

66. M. J. Berridge, M. D. Bootman, H. L. Roderick, Calcium Signalling: Dynamics, Homeostasis and Remodelling. *Nat. Rev. Mol. Cell Biol.* **4**, 517–529 (2003).

67. C. Ortiz-Ramírez, *et al.*, Glutamate receptor-like channels are essential for chemotaxis and reproduction in mosses. *Nature* **549**, 91–95 (2017).

68. C. . Brokaw, Calcium and Flagellar Response during the Chemotaxis of Bracken Spermatozoids. *J. Cell. Physiol.* **83**, 151–158 (1973).

69. S. P. Cook, C. J. Brokaw, C. H. Muller, D. F. Babcock, Sperm chemotaxis: Egg peptides control cytosolic calcium to regulate flagellar responses. *Dev. Biol.* **165**,

10–19 (1994).

70. D. S. C. Damineli, M. T. Portes, J. A. Feijó, Oscillatory signatures underlie growth regimes in Arabidopsis pollen tubes: computational methods to estimate tip location, periodicity, and synchronization in growing cells. *J. Exp. Bot.* (2017).

71. M. M. Wudick, *et al.*, CORNICHON sorting and regulation of GLR channels underlie pollen tube Ca2+ homeostasis. *Science.* **360**, 533–536 (2018).

72. E. Michard, *et al.*, Glutamate receptor-like genes form Ca2+ channels in pollen tubes and are regulated by pistil D-serine. *Science* **332**, 434–437 (2011).

73. G. B. Monshausen, M. A. Messerli, S. Gilroy, Imaging of the Yellow Cameleon 3.6 Indicator Reveals That Elevations in Cytosolic Ca2+ Follow Oscillating Increases in Growth in Root Hairs of Arabidopsis. *Plant Physiol.* **147**, 1690–1698 (2008).

74. C. S. Bascom, L. J. Winship, M. Bezanilla, Simultaneous imaging and functional studies reveal a tight correlation between calcium and actin networks. *Proc. Natl. Acad. Sci.* **115**, E2869–E2878 (2018).

75. W. G. Choi, M. Toyota, S. H. Kim, R. Hilleary, S. Gilroy, Salt stress-induced Ca2+ waves are associated with rapid, long-distance root-to-shoot signaling in plants. *Proc. Natl. Acad. Sci. U. S. A.* **111**, 6497–6502 (2014).

76. T. C. Xiong, *et al.*, Imaging long distance propagating calcium signals in intact plant leaves with the BRET-based GFP-aequorin reporter. *Front. Plant Sci.* **5**, 1–13 (2014).

77. P. . Shacklock, N. . Read, A. J. Trewavas, Cytosolic free calcium mediates red light.induced photo morphogenesis. *Nature* **358**, 753–755 (1992).

78. M. K. Meena, *et al.*, The Ca2+ Channel CNGC19 Regulates Arabidopsis defense against Spodoptera Herbivory. *Plant Cell* **31**, tpc.00057.2019 (2019).

79. T. R. Vincent, *et al.*, Interplay of Plasma Membrane and Vacuolar Ion Channels, Together with BAK1, Elicits Rapid Cytosolic Calcium Elevations in Arabidopsis during Aphid Feeding. *Plant Cell* **29**, tpc.00136.2017 (2017).

80. M. Charpentier, *et al.*, Nuclear-localized cyclic nucleotide–gated channels mediate symbiotic calcium oscillations Myriam. *Science.* **352**, 1102–5 (2016).

81. M. Kwaaitaal, R. Huisman, J. Maintz, A. Reinstädler, R. Panstruga, Ionotropic glutamate receptor (iGluR)-like channels mediate MAMP-induced calcium influx in *Arabidopsis thaliana*. *Biochem. J.* **440**, 355–373 (2011).

82. M. R. Knight, A. K. Campbellt, S. M. Smith, A. J. Trewavas, Transgenic plant aequorin reports the effects of touch and cold-shock and elicitors on cytoplasmic calcium. *Nature* **352**, 524–526 (1991).

83. N. H. Evans, M. R. McAinsh, A. M. Hetherington, M. R. Knight, ROS perception in Arabidopsis thaliana: The ozone-induced calcium response. *Plant J.* **41**, 615–626 (2005).

84. M. Storti, *et al.*, Systemic calcium wave propagation in physcomitrella patens. *Plant Cell Physiol.* **59**, 1377–1384 (2018).

85. M. R. McAinsh, C. Brownlee, A. M. Hetherington, Calcium ions as second messengers in guard cell signal transduction. *Physiol. Plant.* **100**, 16–29 (1997).

86. S. Kosuta, *et al.*, Differential and chaotic calcium signatures in the symbiosis signaling pathway of legumes. *Proc. Natl. Acad. Sci. U. S. A.* **105**, 9823–9828 (2008).

87. S. Behera, *et al.*, Cellular Ca 2+ signals generate defined pH signatures in plants. *Plant Cell* **30**, 2704–2719 (2018).

88. M. R. McAinsh, A. A. Webb, J. E. Taylor, A. M. Hetherington, Stimulus-induced oscillations in guard cell cytosolic free calcium. *Plant Cell* **7**, 1207–1219 (1995).

89. M. C. Martí, M. A. Stancombe, A. A. R. Webb, Cell-and stimulus type-specific intracellular free Ca2+ signals in Arabidopsis. *Plant Physiol.* **163**, 625–634 (2013).

90. A. N. Dodd, J. Kudla, D. Sanders, The Language of Calcium Signaling. *Annu. Rev. Plant Biol.* **61**, 593–620 (2010).

91. A. Costa, L. Navazio, I. Szabo, The contribution of organelles to plant intracellular calcium signalling. *J. Exp. Bot.* **69**, 4175–4193 (2018).

92. A. Costa, L. Navazio, I. Szabo, The contribution of organelles to plant intracellular Calcium signalling (2018) https:/doi.org/10.1093/jxb/ery185/4996169.

93. J. A. Feijó, M. M. Wudick, 'Calcium is life.' *J. Exp. Bot.* **69**, 4147–4150 (2018).

94. M. C. Bonza, *et al.*, Analyses of Ca2+ accumulation and dynamics in the endoplasmic reticulum of Arabidopsis root cells using a genetically encoded Cameleon sensor. *Plant Physiol.* **163**, 1230–1241 (2013).

95. H. Sze, F. Liang, I. Hwang, A. C. Curran, J. F. Harper, Diversity and Regulation of Plant Ca2+ Pumps: Insights from Expression in Yeast. *Annu. Rev. Plant Physiol. Plant Mol. Biol.* **51**, 433–462 (2000).

96. R. Lassig, T. Gutermuth, T. D. Bey, K. R. Konrad, T. Romeis, Pollen tube NAD(P)H oxidases act as a speed control to dampen growth rate oscillations during polarized cell growth. *Plant J.* **78**, 94–106 (2014).

97. T. Gutermuth, *et al.*, Pollen tube growth regulation by free anions depends on the interaction between the anion channel SLAH3 and calcium-dependent protein kinases CPK2 and CPK20. *Plant Cell* **25**, 4525–43 (2013).

98. T. Gutermuth, *et al.*, Tip-localized Ca 2 + -permeable channels control pollen tube growth via kinase-dependent R- and S-type anion channel regulation (2018) https:/doi.org/10.1111/nph.15067.

99. K. H. Edel, E. Marchadier, C. Brownlee, J. Kudla, A. M. Hetherington, The Evolution of Calcium-Based Signalling in Plants. *Curr. Biol.* **27**, R667–R679 (2017).

100. K. H. Edel, J. Kudla, Increasing complexity and versatility: How the calcium signaling toolkit was shaped during plant land colonization. *Cell Calcium* **57**, 231–246 (2015).

101. A. Costa, *et al.*, Ca2+-dependent phosphoregulation of the plasma membrane Ca2+-ATPase ACA8 modulates stimulus-induced calcium signatures. *J. Exp. Bot.* **68**, 3215–3230 (2017).

102. R. Hilleary, *et al.*, Tonoplast-localized Ca2+ pumps regulate Ca2+ signals during pattern-triggered immunity in Arabidopsis thaliana. *Proc. Natl. Acad. Sci. U. S. A.* **117**, 18849–18857 (2020).

103. X. Li, *et al.*, A distinct endosomal Ca2+/Mn2+ pump affects root growth through the secretory process. *Plant Physiol.* **147**, 1675–1689 (2008).

104. K. D. Hirschi, R. Zhent, K. W. Cunningham, P. A. Reat, G. R. Fink, CAX1, an H+/Ca2+ antiporter from Arabidopsis. *PNAS* **93**, 8782–8786 (1996).

105. N. H. Cheng, J. K. Pittman, B. J. Barkla, T. Shigaki, K. D. Hirschi, The Arabidopsis cax1 mutant exhibits impaired ion homeostasis, development, and hormonal responses and reveals interplay among vacuolar transporters. *Plant Cell* **15**, 347–364 (2003).

106. E. Teardo, *et al.*, Physiological characterization of a plant mitochondrial Calcium uniporter in Vitro and in Vivo. *Plant Physiol.* **173**, 1355–1370 (2017).

107. J. Golowasch, Neuronal Homeostasis: Voltage Brings It All Together. *Curr. Biol.* **29**, R641–R644 (2019).

108. C. A. Ryan, E. E. Farmer, Oligosaccharide signals in plants: A current assessment.

Annu. Rev. Plant Physiol. Plant Mol. Biol. **42**, 651–674 (1991).

109. H. Peña-Cortés, L. Willmitzer, J. J. Sánchez-Serrano, Abscisic acid mediates wound induction but not developmental-specific expression of the proteinase inhibitor II gene family. *Plant Cell* **3**, 963–972 (1991).

110. M. J. Evans, W. G. Choi, S. Gilroy, R. J. Morris, A ROS-assisted calcium wave dependent on the AtRBOHD NADPH oxidase and TPC1 cation channel propagates the systemic response to salt stress. *Plant Physiol.* **171**, 1771–1784 (2016).

111. Bose JCH., *Plant response as a means of physiological investigation.* (Longman, Green and Co, 1907).

112. D. C. Wildon, *et al.*, Electrical signalling and systemic proteinase inhibitor induction in the wounded plant. *Nature* **360**, 62–65 (1992).

113. L. F. Jaffe, Calcium waves. *Philos. Trans. R. Soc. B* **363**, 1311–1316 (2008).

114. A. Kumari, A. Chételat, C. T. Nguyen, E. E. Farmer, Arabidopsis H + -ATPase AHA1 controls slow wave potential duration and wound-response jasmonate pathway activation. *Proc. Natl. Acad. Sci.* **116**, 20226–20231 (2019).

115. H. M. Doherty, D. J. Bowles, The role of pH and ion transport in oligosaccharide-induced proteinase inhibitor accumulation in tomato plants. *Plant Cell Environ.* **13**, 851–855 (1990).

116. I. Bricchi, *et al.*, Separation of early and late responses to herbivory in Arabidopsis by changing plasmodesmal function. *Plant J.* **73**, 14–25 (2013).

117. M. Toyota, *et al.*, Glutamate triggers long-distance, calcium-based plant defense signaling. *Science.* **361**, 1112–1115 (2018).

118. E. B. Tucker, *et al.*, UV-A induces two calcium waves in Physcomitrella patens. *Plant Cell Physiol.* **46**, 1226–1236 (2005).

119. E. Suarez-Delgado, L. D. Islas, A novel origin for calcium selectivity. *Elife* **9**, e55216 (2020).

120. T. Nishiyama, *et al.*, The Chara Genome: Secondary Complexity and Implications for Plant Terrestrialization. *Cell* **174**, 448–464 (2018).

121. K. E. Helliwell, *et al.*, Alternative Mechanisms for Fast Na + /Ca 2+ Signaling in Eukaryotes via a Novel Class of Single-Domain Voltage-Gated Channels. *Curr. Biol.* **29**, 1503-1511.e6 (2019).

122. H. Sze, X. Li, M. G. Palmgren, Energization of plant cell membranes by H+-pumping ATPases: Regulation and biosynthesis. *Plant Cell* **11**, 677–689 (1999).

123. R. Poole, Energy Coupling For Membrane Transport. *Ann. Rev. Plant Physiol* **29**, 437–460 (1978).

124. L. Taiz, E. Zeiger, I. Møller, A. Murphy, *Plant Physiology and Development*, 6th Ed. (Sinauer Associates, Inc., 2015).

125. C. Plieth, B. Sattelmacher, U. P. Hansen, G. Thiel, The action potential in Chara: Ca2+ release from internal stores visualized by Mn2+-induced quenching of fura-dextran. *Plant J.* **13**, 167–175 (1998).

126. C. T. Gaffey, L. J. Mullins, Ion Fluxes During the Action Potential in Chara. *J. Physiol* **144**, 505–524 (1958).

127. M. Tazawa, T. Shimmen, T. Mimura, Membrane Control in the Characeae. *Ann. Rev. Plant Physiol* **38**, 95–117 (1987).

128. M. J. Beilby, Action Potential in Charophytes. *Int. Rev. Cytol.* **257**, 43–82 (2007).

129. U. Homann, G. Thiel, Cl− and K+ channel currents during the action potential in Chara. simultaneous recording of membrane voltage and patch currents. *J. Membr. Biol.* **141**, 297–309 (1994).

130. G. Lunevsky, VZ., Zherelova, OM., Vostrikov, IV., Berestovsky, Excitation of Characeae Cell Membranes as a Result of Activation of Calcium and Chloride Channels. *J. Membr. Bio* **72**, 43–58 (1983).

131. K. Trebacz, *et al.*, Cytoplasmic Ca2 + , K + , CI ', and NO , - Activities in the . at Rest and during Liverwort Conocephalum conicum 1 Action Potentials '. 1073–1084 (1994).

132. E. Johannes, E. Ermolayeva, D. Sanders, Red light-induced membrane potential transients in the moss Physcomitrella patens: ion channel interaction in phytochrome signalling. *J. Exp. Bot.* **48**, 599–608 (1997).

133. T. A. Cuin, I. Dreyer, E. Michard, The role of potassium channels in arabidopsis thaliana long distance electrical signalling: AKT2 modulates tissue excitability while GORK shapes action potentials. *Int. J. Mol. Sci.* **19**, 1–17 (2018).

134. R. Hedrich, V. Salvador-Recatalà, I. Dreyer, Electrical Wiring and Long-Distance Plant Communication. *Trends Plant Sci.* **21**, 376–387 (2016).

135. J. I. Schroeder, G. Allen, V. Hugouvieux, J. Kwak, D. Waner, Guard Cell Signal Transduction. *Annu Rev Plant Physiol. Plant Mol Biol* **52**, 627–658 (2001).

136. B. Kohler, K. Raschke, The Delivery of Salts to the Xylem . Three Types of Anion Conductance in the Plasmalemma of the Xylem Parenchyma of Roots of Barley 1. **122**, 243–254 (2000).

137. B. Tavares, P. Domingos, P. N. Dias, J. A. Feijó, A. Bicho, The essential role of anionic transport in plant cells: The pollen tube as a case study. *J. Exp. Bot.* **62**, 2273–2298 (2011).

138. S. K. Roberts, Plasma membrane anion channels in higher plants and their putative functions in roots. *New Phytol.* **169**, 647–666 (2006).

139. S. Meyer, *et al.*, AtALMT12 represents an R-type anion channel required for stomatal movement in Arabidopsis guard cells. *Plant J.* **63**, 1054–1062 (2010).

140. J. Negi, *et al.*, CO2 regulator SLAC1 and its homologues are essential for anion homeostasis in plant cells. *Nature* **452**, 483–486 (2008).

141. R. Hedrich, D. Geiger, Biology of SLAC1-type anion channels - from nutrient uptake to stomatal closure. *New Phytol.* (2017).

142. M. Gilliham, M. Tester, The Regulation of Anion Loading to the Maize. *Plant Physiol.* **137**, 819–828 (2005).

143. H. Barbier-Brygoo, *et al.*, Anion channels in higher plants: functional characterization, molecular structure and physiological role. *Biochim. Biophys. Acta* **1465**, 199–218 (2000).

144. D. Reboutier, *et al.*, A CFTR chloride channel activator prevents HrpN(ea)-induced cell death in Arabidopsis thaliana suspension cells. *Plant Physiol Biochem* **43**, 567–572 (2005).

145. E. Park, E. B. Campbell, R. MacKinnon, Structure of a CLC chloride ion channel by cryo-electron microscopy. *Nature* **541**, 500–505 (2017).

146. A. Accardi, C. Miller, Secondary active transport mediated by a prokaryotic homologue of ClC Cl-channels. *Nature* **427**, 803–807 (2004).

147. L. Leisle, *et al.*, Divergent Cl- and H+ pathways underlie transport coupling and gating in clc exchangers and channels. *Elife* **9**, 1–22 (2020).

148. A. De Angeli, *et al.*, The nitrate/proton antiporter AtCLCa mediates nitrate accumulation in plant vacuoles. *Nature* **442**, 939–942 (2006).

149. J. Du, W. Lü, S. Wu, Y. Cheng, E. Gouaux, Glycine receptor mechanism elucidated by electron cryo-microscopy. *Nature* **526**, 224–229 (2015).

150. Y. Ben-Ari, J. L. Gaiarsa, R. Tyzio, R. Khazipov, GABA: A pioneer transmitter that excites immature neurons and generates primitive oscillations. *Physiol. Rev.* **87**, 1215–1284 (2007).

151. S. A. Ramesh, *et al.*, GABA signalling modulates plant growth by directly regulating the activity of plant-specific anion transporters. *Nat. Commun.* **6**, 7879 (2015).

152. P. Domingos, *et al.*, Molecular and electrophysiological characterization of anion transport in Arabidopsis thaliana pollen reveals regulatory roles for pH, Ca2+ and GABA. *New Phytol.* **223**, 1353–1371 (2019).

153. K. L. Dennison, *et al.*, Functions of AKT1 and AKT2 potassium channels determined by studies of single and double mutants of Arabidopsis. *Plant Physiol.* **127**, 1012–1019 (2001).

154. M. . Hirsch, R. E. Lewis B.D. Spalding E.P. Sussman, A role for the AKT1 potassium c in plant nutrition. *Science.* **280**, 918–921 (1998).

155. H. M. Lam, *et al.*, Glutamate-receptor genes in plants. *Nature* **396**, 125–126 (1998).

156. S. Frietsch, *et al.*, A cyclic nucleotide-gated channel is essential for polarized tip growth of pollen. *Proc. Natl. Acad. Sci. U. S. A.* **104**, 14531–14536 (2007).

157. Q. F. Gao, C. F. Fei, J. Y. Dong, L. L. Gu, Y. F. Wang, Arabidopsis CNGC18 Is a Ca2+-Permeable Channel. *Mol. Plant* **7**, 739–743 (2014).

158. F. Yuan, *et al.*, OSCA1 mediates osmotic-stress-evoked Ca2+ increases vital for osmosensing in Arabidopsis. *Nature* **514**, 367–371 (2014).

159. K. Thor, *et al.*, The calcium-permeable channel OSCA1.3 regulates plant stomatal immunity. *Nature* **585** (2020).

160. J. Guo, W. Zeng, Y. Jiang, Tuning the ion selectivity of two-pore channels. *Proc. Natl. Acad. Sci. U. S. A.*, 201616191 (2017).

161. Y. Nakagawa, *et al.*, Arabidopsis plasma membrane protein crucial for Ca2+ influx and touch sensing in roots. *Proc. Natl. Acad. Sci. U. S. A.* **104**, 3639–3644 (2007).

162. D. Tran, *et al.*, A mechanosensitive Ca2+channel activity is dependent on the developmental regulator DEK1. *Nat. Commun.* **8**, 1–7 (2017).

163. A. A. Véry, J. M. Davies, Hyperpolarization-activated calcium channels at the tip of Arabidopsis root hairs. *Proc. Natl. Acad. Sci. U. S. A.* **97**, 9801–9806 (2000).

164. E. Kiegle, M. Gilliham, J. Haseloff, M. Tester, Hyperpolarisation-activated calcium currents found only in cells from the elongation zone of Arabidopsis thaliana roots. *Plant J.* **21**, 225–229 (2000).

165. J. Foreman, *et al.*, Reactive oxygen species produced by NADPH oxidase regulate plant cell growth. *Nature* **422**, 442–446 (2003).

166. Z. Pei, *et al.*, Calcium channels activated by hydrogen peroxide mediate abscisic acid signaling in guard cells. *Nature* **406**, 731–734 (2000).

167. K. S. Schumaker, M. J. Gizinski, Cytokinin stimulates dihydropyridine-sensitive calcium uptake in moss protoplasts. *Proc. Natl. Acad. Sci. U. S. A.* **90**, 10937–41 (1993).

168. H. Miedema, *et al.*, Two voltage-dependent calcium channels co-exist in the apical plasma membrane of Arabidopsis thaliana root hairs. *New Phytol.* **179**, 378–385 (2008).

169. H. Miedema, J. H. F. Bothwell, C. Brownlee, J. M. Davies, Calcium uptake by plant cells-channels and pumps acting in concert. *Trends Plant Sci.* **6**, 514–519 (2001).

170. L. Thion, *et al.*, Plasma membrane depolarization-activated calcium channels, stimulated by microtubule-depolymerizing drugs in wild-type Arabidopsis thaliana protoplasts, display constitutively large activities and a longer half-life in ton 2 mutant cells affected in the o. *Plant J.* **13**, 603–610 (1998).

171. P. Thuleau, J. M. Ward, R. Ranjeva, J. I. Schroeder, Voltage-dependent calcium-permeable channels in the plasma membrane of a higher plant cell. *EMBO J.* **13**, 2970–2975 (1994).

172. I. Dreyer, J. L. Gomez-Porras, D. M. Riaño-Pachón, R. Hedrich, D. Geiger, Molecular evolution of slow and quick anion channels (SLACs and QUACs/ALMTs). *Front. Plant Sci.* **3**, 1–12 (2012).

173. C. Lind, *et al.*, Stomatal guard cells co-opted an ancient ABA-dependent desiccation survival system to regulate stomatal closure. *Curr. Biol.* **25**, 928–935 (2015).

174. C. Cox, N. Bavi, B. Martinac, Origin of the Force: The Force-From-Lipids Principle Applied to Piezo Channels. *Curr. Top. Membr.* **79**, 59–96.

175. E. S. Haswell, E. M. Meyerowitz, MscS-like proteins control plastid size and shape in Arabidopsis thaliana. *Curr. Biol.* **16**, 1–11 (2006).

176. E. S. Haswell, R. Phillips, D. C. Rees, Mechanosensitive channels: What can they

do and how do they do it? *Structure* **19**, 1356–1369 (2011).

177. C. D. Pivetti, *et al.*, Two Families of Mechanosensitive Channel Proteins. *Microbiol. Mol. Biol. Rev.* **67**, 66–85 (2003).

178. A. Herdean, *et al.*, A voltage-dependent chloride channel fine-tunes photosynthesis in plants. *Nat. Commun.* **7**, 1–11 (2016).

179. H. C. Hartzell, Z. Qu, K. Yu, Q. Xiao, L. T. Chien, Molecular physiology of bestrophins: Multifunctional membrane proteins linked to best disease and other retinopathies. *Physiol. Rev.* **88**, 639–672 (2008).

180. K. Yu, *et al.*, Identification of a lipid scrambling domain in ANO6/TMEM16F. *Elife* **4**, 1–23 (2015).

181. S. Wege, *et al.*, The proline 160 in the selectivity filter of the Arabidopsis NO 3-/H+ exchanger AtCLCa is essential for nitrate accumulation in planta. *Plant J.* **63**, 861–869 (2010).

182. J. M. Ward, P. Maser, J. I. Schroeder, Plant Ion Channels: Gene Families, Physiology, and Functional Genomics Analyses. *Annu Rev Physiol* **71**, 59–82 (2009).

183. T. J. Jentsch, Discovery of CLC transport proteins: Cloning, structure, function and pathophysiology. *J. Physiol.* **593**, 4091–4109 (2015).

184. J. Lynch, Molecular structure and function of the glycine receptor chloride channel. *Physiol. Rev.* **84**, 1051–1095 (2004).

185. S. E. Murthy, *et al.*, OSCA/TMEM63 are an evolutionarily conserved family of mechanically activated ion channels. *Elife* **7**, 1–17 (2018).

186. A. Demuro, *et al.*, Subunit stoichiometry of human Orai1 and Orai3 channels in closed and open states. *Proc. Natl. Acad. Sci. U. S. A.* **108**, 17832–17837 (2011).

187. X. Sun, *et al.*, The Catsper channel and its roles in male fertility: A systematic review. *Reprod. Biol. Endocrinol.* **15**, 1–12 (2017).

188. A. E. McCarthy, C. Yoshioka, S. E. Mansoor, Full-Length P2X7 Structures Reveal How Palmitoylation Prevents Channel Desensitization. *Cell* **179**, 659–670 (2019).

189. W. A. Catterall, Voltage-gated sodium channels at 60: Structure, function and pathophysiology. *J. Physiol.* **590**, 2577–2589 (2012).

190. J. Lanner, G. DK, A. Joshi, H. SL, Ryanodine Receptors: Structure, Expression, Molecular Details, and Function in Calcium. *Cold Spring Harb Perspect Biol*

a003996, 1–21 (2010).

191. N. Burnashev, Z. Zhou, E. Neher, B. Sakmann, Fractional calcium currents through recombinant GluR channels of the NMDA, AMPA and kainate receptor subtypes. *J. Physiol.* **485**, 403–418 (1995).

192. A. B. MacDermott, M. L. Mayer, G. L. Westbrook, S. J. Smith, J. L. Barker, NMDA-receptor activation increases cytoplasmic calcium concentration in cultured spinal cord neurones. *Nature* **321**, 519–522 (1986).

193. N. Burnashev, A. Villarroel, B. Sakmann, Dimensions and ion selectivity of recombinant AMPA and kainate receptor channels and their dependence on Q / R site residues. 165–173 (1996).

194. L. P. Wollmuth, *et al.*, The Lurcher mutation identifies δ2 as an AMPA/kainate receptor-like channel that is potentiated by Ca2+. *J. Neurosci.* **20**, 5973–5980 (2000).

195. S. C. Gantz, K. Moussawi, H. S. Hake, Delta glutamate receptor conductance drives excitation of mouse dorsal raphe neurons. *Elife* **9**, 1–19 (2020).

196. A. Orth, D. Tapken, M. Hollmann, The delta subfamily of glutamate receptors: Characterization of receptor chimeras and mutants. *Eur. J. Neurosci.* **37**, 1620–1630 (2013).

197. R. Llinás, I. Z. Steinberg, K. Walton, Relationship between presynaptic calcium current and postsynaptic potential in squid giant synapse. *Biophys. J.* **33**, 323–352 (1981).

198. R. Schneggenburger, E. Neher, Intracellular calcium dependence of transmitter release rates at a fast central synapse. *Nature* **406**, 889–993 (2000).

199. T. C. Sudhof, J. Rizo, Synaptic Vesicle Exocytosis. *Cold Spring Harb. Perspect. Biol.* **3**, a005637 (2011).

200. A. C. Chin, R. A. Yovanno, T. J. Wied, A. Gershman, A. Y. Lau, D-Serine Potently Drives Ligand-Binding Domain Closure in the Ionotropic Glutamate Receptor GluD2. *Structure* **28**, 1168–1178 (2020).

201. D. Tapken, *et al.*, The low binding affinity of D-serine at the ionotropic glutamate receptor GluD2 can be attributed to the hinge region. *Sci. Rep.* **7**, 1–12 (2017).

202. M. Yuzaki, A. R. Aricescu, A GluD Coming-Of-Age Story. *Trends Neurosci.* **40**, 138–150 (2017).

203. M. Hollmann, A. O'Shea-Greenfield, S. W. Rogers, S. Heinemann, Cloning by

functional expression of a member of the glutamate receptor family. *Nature* **342**, 643–648 (1989).

204. A. I. Sobolevsky, M. P. Rosconi, E. Gouaux, X-ray structure, symmetry and mechanism of an AMPA-subtype glutamate receptor. *Nature* **462**, 745–56 (2009).

205. N. Armstrong, Y. Sun, G.-Q. Chen, E. Gouaux, Structure of a glutamate-receptor ligand-binding core in complex with kainate. *Nature* **395**, 913–917 (1998).

206. G. Ayalon, Y. Stern-Bach, Functional assembly of AMPA and kainate receptors is mediated by several discrete protein-protein interactions. *Neuron* **31**, 103–113 (2001).

207. A. N. Farina, *et al.*, Separation of domain contacts is required for heterotetrameric assembly of functional NMDA receptors. *J. Neurosci.* **31**, 3565–3579 (2011).

208. C. W. Christine, D. W. Choi, Effect of zinc on NMDA receptor-mediated channel currents in cortical neurons. *J. Neurosci.* **10**, 108–116 (1990).

209. A. Romero-Hernandez, N. Simorowski, E. Karakas, H. Furukawa, Molecular Basis for Subtype Specificity and High-Affinity Zinc Inhibition in the GluN1-GluN2A NMDA Receptor Amino-Terminal Domain. *Neuron* **92**, 1324–1336 (2016).

210. A. J. R. Plested, M. L. Mayer, Structure and Mechanism of Kainate Receptor Modulation by Anions. *Neuron* **53**, 829–841 (2007).

211. S. F. Traynelis, *et al.*, Glutamate Receptor Ion Channels: Structure, Regulation, and Function. *Pharmacol. Rev.* **62**, 405–496 (2010).

212. H. Mori, *et al.*, Role of the carboxy-terminal region of the GluRε2 subunit in synaptic localization of the NMDA receptor channel. *Neuron* **21**, 571–580 (1998).

213. G. J. Iacobucci, G. K. Popescu, Spatial coupling tunes NMDA receptor responses via Ca2+ diffusion. *J. Neurosci.*, 0901–19 (2019).

214. N. Armstrong, E. Gouaux, Mechanisms for activation and antagonism of an AMPA-sensitive glutamate receptor: Crystal structures of the GluR2 ligand binding core. *Neuron* **28**, 165–181 (2000).

215. E. C. Twomey, A. I. Sobolevsky, Structural Mechanisms of Gating in Ionotropic Glutamate Receptors. *Biochemistry* **57**, 267–276 (2018).

216. J. Luo, Y. Wang, R. P. Yasuda, A. W. Dunah, B. B. Wolfe, The majority of N-methyl-D-aspartate receptor complexes in adult rat cerebral cortex contain at least three different subunits (NR1/NR2A/NR2B). *Mol. Pharmacol.* **51**, 79–86 (1997).

217. W. Lü, J. Du, A. Goehring, E. Gouaux, Cryo-EM structures of the triheteromeric NMDA receptor and its allosteric modulation. *Science.* **355** (2017).

218. M. S. Horning, M. L. Mayer, Regulation of AMPA Receptor Gating by Ligand Binding Core Dimers. *Neuron* **41**, 379–388 (2004).

219. I. H. Greger, J. F. Watson, S. G. Cull-Candy, Structural and Functional Architecture of AMPA-Type Glutamate Receptors and Their Auxiliary Proteins. *Neuron* **94**, 713–730 (2017).

220. S. Chen, *et al.*, Activation and Desensitization Mechanism of AMPA Receptor-TARP Complex by Cryo-EM. *Cell* **170**, 1234-1246.e14 (2017).

221. J. Schwenk, *et al.*, Functional Proteomics Identify Cornichon Proteins as Auxiliary Subunits of AMPA Receptors. *Science.* **323**, 1313–1319 (2009).

222. I. D. Coombs, *et al.*, Cornichons modify channel properties of recombinant and glial AMPA receptors. *J. Neurosci.* **32**, 9796–9804 (2012).

223. A. L. Carbone, A. J. R. Plested, Superactivation of AMPA receptors by auxiliary proteins. *Nat. Commun.* **7**, 10178 (2016).

224. P. Brown, H. McGuire, D. Bowie, Stargazin and Cornichon-3 relieve polyamine block of AMPA receptors by enhancing blocker permeation. *J. Gen. Physiol.* **417**, TK-TK (2018).

225. I. Riva, C. Eibl, R. Volkmer, A. L. Carbone, A. J. R. Plested, Control of AMPA receptor activity by the extracellular loops of auxiliary proteins. *Elife* **6**, 1–22 (2017).

226. R. Wang, *et al.*, Evolutionary Conserved Role for TARPs in the Gating of Glutamate Receptors and Tuning of Synaptic Function. *Neuron* **59**, 997–1008 (2008).

227. T. Nakagawa, Structures of the AMPA receptor in complex with its auxiliary subunit cornichon. *Science.* **366**, 1259–1263 (2019).

228. N. F. Shanks, *et al.*, Differences in AMPA and Kainate Receptor Interactomes Facilitate Identification of AMPA Receptor Auxiliary Subunit GSG1L. *Cell Rep.* **1**, 590–598 (2012).

229. E. C. Twomey, M. V. Yelshanskaya, R. A. Grassucci, J. Frank, A. I. Sobolevsky, Channel opening and gating mechanism in AMPA-subtype glutamate receptors. *Nature* **549**, 60–65 (2017).

230. G. Q. Chen, C. Cul, M. L. Mayer, E. Gouaux, Functional characterization of a

potassium-selective prokaryotic glutamate receptor. *Nature* **402**, 817–821 (1999).

231. H. Janovjak, G. Sandoz, E. Y. Isacoff, A modern ionotropic glutamate receptor with a K+ selectivity signature sequence. *Nat. Commun.* **2**, 232–235 (2011).

232. T. Kuner, C. Beck, B. Sakmann, P. H. Seeburg, Channel-lining residues of the AMPA receptor M2 segment: structural environment of the Q/R site and identification of the selectivity filter. *J. Neurosci.* **21**, 4162–4172 (2001).

233. R. Dingledine, R. I. Hume, S. F. Heinemann, Structural determinants of barium permeation and rectification in non-NMDA glutamate receptor channels. *J. Neurosci.* **12**, 4080–4087 (1992).

234. N. Burnashev, *et al.*, Control by asparagine residues of calcium permeability and magnesium blockade in the NMDA receptor. *Science.* **257**, 1415–1419 (1992).

235. R. Schneggenburger, Altered voltage dependence of fractional Ca2+ current in N-methyl-D- aspartate channel pore mutants with a decreased Ca2+ permeability. *Biophys. J.* **74**, 1790–1794 (1998).

236. I. Pérez-Otaño, *et al.*, Assembly with the NR1 subunit is required for surface expression of NR3A-containing NMDA receptors. *J. Neurosci.* **21**, 1228–1237 (2001).

237. K. Williams, *et al.*, The selectivity filter of the N-methyl-D-aspartate receptor: A tryptophan residue controls block and permeation of Mg2+. *Mol. Pharmacol.* **53**, 933–941 (1998).

238. A. Ferrer-Montiel, J. Merino, R. Planells-Cases, W. Sun, M. Montal, Structural determinants of the blocker binding site in glutamate and NMDA receptor channels. *Neuropharmacology* **37**, 139–147 (1997).

239. J. Watanabe, C. Beck, T. Kuner, L. S. Premkumar, L. P. Wollmuth, DRPEER: a motif in the extracellular vestibule conferring high Ca2+ flux rates in NMDA receptor channels. *J. Neurosci.* **22**, 10209–10216 (2002).

240. J. Dai, H. X. Zhou, An NMDA receptor gating mechanism developed from MD simulations reveals molecular details underlying subunit-specific contributions. *Biophys. J.* **104**, 2170–2181 (2013).

241. J. B. Amin, X. Leng, A. Gochman, H. X. Zhou, L. P. Wollmuth, A conserved glycine harboring disease-associated mutations permits NMDA receptor slow deactivation and high Ca2+ permeability. *Nat. Commun.* **9** (2018).

242. L. P. Wollmuth, T. Kuner, B. Sakmann, Adjacent asparagines in the NR2-subunit of the NMDA receptor channel control the voltage-dependent block by

extracellular Mg 2+. *J. Physiol.* **506**, 13–32 (1998).

243. D. Ramos-Vicente, *et al.*, Metazoan evolution of glutamate receptors reveals unreported phylogenetic groups and divergent lineage-specific events. *Elife* **7**, 1–36 (2018).

244. C. Schuster, *et al.*, Molecular cloning of an invertebrate glutamate receptor subunit expressed in Drosophila muscle. *Science.* **254**, 112–114 (1991).

245. A. V. Maricq, E. Peckol, M. Driscoll, B. CI, Mechanosensory signalling in C. elegans mediated by the GLR-1 glutamate receptor. *Nature* **378**, 78–81 (1995).

246. T. Kano, *et al.*, Memory in Caenorhabditis elegans Is Mediated by NMDA-Type Ionotropic Glutamate Receptors. *Curr. Biol.* **18**, 1010–1015 (2008).

247. P. J. Brockie, D. M. Madsen, Y. Zheng, J. Mellem, A. V Maricq, Differential expression of glutamate receptor subunits in the nervous system of Caenorhabditis elegans and their regulation by the homeodomain protein UNC-42. *J. Neurosci.* **21**, 1510–22 (2001).

248. B. Lacombe, *et al.*, The Identity of Plant Glutamate Receptors. *Science.* **292**, 1486–1487 (2001).

249. M. M. Wudick, E. Michard, C. Oliveira Nunes, J. A. Feijó, Comparing plant and animal glutamate receptors: Common traits but different fates? *J. Exp. Bot.* **69**, 4151–4163 (2018).

250. S. De Bortoli, E. Teardo, I. Szabò, T. Morosinotto, A. Alboresi, Evolutionary insight into the ionotropic glutamate receptor superfamily of photosynthetic organisms. *Biophys. Chem.* (2016) https:/doi.org/10.1016/j.bpc.2016.07.004.

251. E. Teardo, *et al.*, Alternative Splicing-Mediated Targeting of the Arabidopsis GLUTAMATE RECEPTOR3.5 to Mitochondria Affects Organelle Morphology. *Plant Physiol.* **167**, 216–227 (2015).

252. E. D. Vincill, A. E. Clarin, J. N. Molenda, E. P. Spalding, Interacting glutamate receptor-like proteins in Phloem regulate lateral root initiation in Arabidopsis. *Plant Cell* **25**, 1304–1313 (2013).

253. E. Teardo, *et al.*, Dual localization of plant glutamate receptor AtGLR3.4 to plastids and plasmamembrane. *Biochim. Biophys. Acta - Bioenerg.* **1807**, 359–367 (2011).

254. S. J. Roy, *et al.*, Investigating glutamate receptor-like gene co-expression in Arabidopsis thaliana. *Plant, Cell Environ.* **31**, 861–871 (2008).

255. L. Gent, B. G. Forde, How do plants sense their nitrogen status? *J. Exp. Bot.* **68**, 2531–2540 (2017).

256. B. G. Forde, P. J. Lea, Glutamate in plants: Metabolism, regulation, and signalling. *J. Exp. Bot.* **58**, 2339–2358 (2007).

257. J. Kang, F. J. Turano, The putative glutamate receptor 1.1 (AtGLR1.1) functions as a regulator of carbon and nitrogen metabolism in Arabidopsis thaliana. *Proc. Natl. Acad. Sci.* **100**, 6872–6877 (2003).

258. G. Lu, *et al.*, Application of T-DNA activation tagging to identify glutamate receptor-like genes that enhance drought tolerance in plants. *Plant Cell Rep.* **33**, 617–631 (2014).

259. D. Kong, *et al.*, Arabidopsis glutamate receptor homolog3.5 modulates cytosolic Ca2+ level to counteract effect of abscisic acid in seed germination. *Plant Physiol.* **167**, 1630–1642 (2015).

260. M. Iwano, *et al.*, Calcium signalling mediates self-incompatibility response in the Brassicaceae. *Nat. Plants* **1**, Article number: 15128 (2015).

261. C. Ju, *et al.*, Methionine synthase 1 provides methionine for activation of the GLR3.5 Ca2+ channel and regulation of germination in Arabidopsis. *J. Exp. Bot.* **71**, 178–187 (2020).

262. S. K. Singh, C. Te Chien, I. F. Chang, The Arabidopsis glutamate receptor-like gene GLR3.6 controls root development by repressing the Kip-related protein gene KRP4. *J. Exp. Bot.* **67**, 1853–1869 (2016).

263. K. L. Dennison, E. P. Spalding, Glutamate-Gated Calcium Fluxes in Arabidopsis. *Plant Physiol.* **124**, 1511–1514 (2000).

264. C. Dubos, D. Huggins, G. H. Grant, M. R. Knight, M. M. Campbell, A role for glycine in the gating of plant NMDA-like receptors. *Plant J.* **35**, 800–810 (2003).

265. D. Cho, *et al.*, De-regulated expression of the plant glutamate receptor homolog AtGLR3.1 impairs long-term Ca2+-programmed stomatal closure. *Plant J.* **58**, 437–449 (2009).

266. D. Kong, *et al.*, L-Met Activates Arabidopsis GLR Ca2+ Channels Upstream of ROS Production and Regulates Stomatal Movement. *Cell Rep.* **17**, 2553–2561 (2016).

267. F. Li, *et al.*, Glutamate Receptor-Like Channel3.3 Is Involved in Mediating Glutathione-Triggered Cytosolic Calcium Transients, Transcriptional Changes, and Innate Immunity Responses in Arabidopsis. *Plant Physiol.* **162**, 1497–1509

(2013).

268. V. Salvador-Recatalà, New roles for the GLUTAMATE RECEPTOR-LIKE 3.3, 3.5, and 3.6 genes as on/off switches of wound-induced systemic electrical signals. *Plant Signal. Behav.* **11** (2016).

269. E. E. Farmer, D. Gasperini, I. F. Acosta, The squeeze cell hypothesis for the activation of jasmonate synthesis in response to wounding. *J. Physiol.* **204**, 282–288 (2014).

270. Z. Qi, N. R. Stephens, E. P. Spalding, Calcium entry mediated by GLR3.3, an Arabidopsis glutamate receptor with a broad agonist profile. *Plant Physiol.* **142**, 963–971 (2006).

271. N. R. Stephens, Z. Qi, E. P. Spalding, Glutamate Receptor Subtypes Evidenced by Differences in Desensitization and Dependence on the GLR3.3 and GLR3.4 Genes. *Plant Physiol.* **146**, 529–538 (2008).

272. D. Tapken, *et al.*, A Plant Homolog of Animal Glutamate Receptors Is an Ion Channel Gated by Multiple Hydrophobic Amino Acids. *Sci. Signal.* **6**, ra47–ra47 (2013).

273. S. P. Gangwar, M. N. Green, E. Michard, A. A. Simon, A. I. Sobolevsky, Structure of the Arabidopsis Glutamate Receptor-like Channel GLR3 . 2 Ligand-Binding Domain. *Structure* **28**, 1–9 (2020).

274. A. Alfieri, *et al.*, The structural bases for agonist diversity in an Arabidopsis thaliana glutamate receptor-like channel. *Proc. Natl. Acad. Sci. U. S. A.* **117**, 752–760 (2020).

275. J. Chiu, R. Desalle, H. Lam, L. Meisel, G. Coruzzi, Molecular Evolution of Glutamate Receptors : A Primitive Signaling Mechanism that Existed Before Plants and Animals Diverged. 826–838 (1998).

276. P. Dietrich, U. Anschütz, A. Kugler, D. Becker, Physiology and biophysics of plant ligand-gated ion channels. *Plant Biol.* **12**, 80–93 (2010).

277. D. Tapken, M. Hollmann, Arabidopsis thaliana Glutamate Receptor Ion Channel Function Demonstrated by Ion Pore Transplantation. *J. Mol. Biol.* **383**, 36–48 (2008).

278. E. D. Vincill, a. M. Bieck, E. P. Spalding, Ca2+ Conduction by an Amino Acid-Gated Ion Channel Related to Glutamate Receptors. *Plant Physiol.* **159**, 40–46 (2012).

279. J. Ni, *et al.*, Heterologous Expression and Functional Analysis of Rice

GLUTAMATE RECEPTOR-LIKE Family Indicates its Role in Glutamate Triggered Calcium Flux in Rice Roots. *Rice* **9**, 9 (2016).

280. M. B. Price, S. Okumoto, Inter-subunit interactions between Glutamate-Like Receptors in Arabidopsis. *Plant Signal. Behav.* **8**, 1–7 (2013).

281. F. Miguez-Cabello, *et al.*, AMPAR/TARP stoichiometry differentially modulates channel properties. *Elife* **9**, 1 (2020).

282. P. Kenrick, P. R. Crane, The origin and early evolution of plants on land. *Nature* **389**, 33–39 (1997).

283. N. D. Pires, L. Dolan, Morphological evolution in land plants: New designs with old genes. *Philos. Trans. R. Soc. B Biol. Sci.* **367**, 508–518 (2012).

284. C. Ortiz-Ramírez, *et al.*, A Transcriptome Atlas of Physcomitrella patens Provides Insights into the Evolution and Development of Land Plants. *Mol. Plant* **9**, 205–220 (2016).

285. P. F. Perroud, *et al.*, The Physcomitrella patens gene atlas project: large-scale RNA-seq based expression data. *Plant J.* **95**, 168–182 (2018).

286. G. Jang, L. Dolan, Auxin promotes the transition from chloronema to caulonema in moss protonema by positively regulating PpRSL1and PpRSL2 in Physcomitrella patens. *New Phytol.* **192**, 319–327 (2011).

287. B. Menand, G. Calder, L. Dolan, Both chloronemal and caulonemal cells expand by tip growth in the moss Physcomitrella patens. *J. Exp. Bot.* **58**, 1843–1849 (2007).

288. S. A. Rensing, B. Goffinet, R. Meyberg, S. Z. Wu, M. Bezanilla, The moss physcomitrium (Physcomitrella) patens: A model organism for non-seed plants. *Plant Cell* **32**, 1361–1376 (2020).

289. P. Zimmermann, M. Hirsch-Hoffmann, L. Hennig, W. Gruissem, GENEVESTIGATOR. Arabidopsis microarray database and analysis toolbox. *Plant Physiol.* **136**, 2621–2632 (2004).

290. K. Mukae, Y. Inoue, Y. Moriyasu, ATG5-knockout mutants of physcomitrella provide a platform for analyzing the involvement of autophagy in senescence processes in plant cells. *Plant Signal. Behav.* **10**, 1–11 (2015).

291. V. Sanchez-Vera, *et al.*, Autophagy is required for gamete differentiation in the moss Physcomitrella patens. *Autophagy* **13**, 1939–1951 (2017).

292. K. Yoshimoto, H. Hanaoka, S. Sato, T. Kato, S. Tabata, Processing of ATG8s ,

Ubiquitin-Like Proteins , and Their Deconjugation by ATG4s Are Essential for Plant Autophagy. *Plant Cell* **16**, 2967–2983 (2004).

293. S. De Bortoli, E. Teardo, I. Szabò, T. Morosinotto, A. Alboresi, Evolutionary insight into the ionotropic glutamate receptor superfamily of photosynthetic organisms. *Biophys. Chem.* **218**, 14–26 (2016).

294. A. Inanobe, H. Furukawa, E. Gouaux, Mechanism of partial agonist action at the NR1 subunit of NMDA receptors. *Neuron* **47**, 71–84 (2005).

295. S. Kawamoto, *et al.*, Arginine-481 mutation abolishes ligand-binding of the AMPA-selective glutamate receptor channel α1-subunit. *Mol. Brain Res.* **47**, 339–344 (1997).

296. M. Lampinen, O. Pentikäinen, M. S. Johnson, K. Keinänen, AMPA receptors and bacterial periplasmic amino acid-binding proteins share the ionic mechanism of ligand recognition. *EMBO J.* **17**, 4704–4711 (1998).

297. C. A. Lewis, Ion Concentration Dependence of the Reversal Potential and the Single Channel Conductance of Ion Channels at the Frog Neuromuscular Junction. *J. Physiol* **286**, 417–445 (1979).

298. D. Morgan, V. V Cherny, M. O. Price, M. C. Dinauer, T. E. DeCoursey, Absence of proton channels in COS-7 cells expressing functional NADPH oxidase components. *J. Gen. Physiol.* **119**, 571–80 (2002).

299. M. Stamm, R. Staritzbichler, K. Khafizov, L. R. Forrest, Alignment of Helical Membrane Protein Sequences Using AlignMe. *PLoS One* **8** (2013).

300. R. Davenport, Glutamate receptors in plants. *Ann. Bot.* **90**, 549–557 (2002).

301. J. Zuo, *et al.*, Neurodegeneration in Lurcher mice caused by mutation in d2 glutamate receptor gene. *Nature* **388**, 769–773 (1997).

302. R. M. Klein, J. R. Howe, Effects of the lurcher mutation on GluR1 desensitization and activation kinetics. *J. Neurosci.* **24**, 4941–4951 (2004).

303. P. Naur, *et al.*, Ionotropic glutamate-like receptor δ2 binds D-serine and glycine. *Proc. Natl. Acad. Sci. U. S. A.* **104**, 14116–14121 (2007).

304. F. Taverna, *et al.*, The Lurcher mutation of an α-amino-3-hydroxy-5-methyl-4-isoxazolepropionic acid receptor subunit enhances potency of glutamate and converts an antagonist to an agonist. *J. Biol. Chem.* **275**, 8475–8479 (2000).

305. J. C. Chiu, *et al.*, Phylogenetic and expression analysis of the glutamate-receptor-like gene family in Arabidopsis thaliana. *Mol. Biol. Evol.* **19**, 1066–1082 (2002).

306. M. V. Yelshansky, A. I. Sobolevsky, C. Jatzke, L. P. Wollmuth, Block of AMPA receptor desensitization by a point mutation outside the ligand-binding domain. *J. Neurosci.* **24**, 4728–4736 (2004).

307. I. Talukder, P. Borker, L. P. Wollmuth, Specific sites within the ligand-binding domain and ion channel linkers modulate NMDA receptor gating. *J. Neurosci.* **30**, 11792–11804 (2010).

308. M. J. McDaniel, *et al.*, NMDA receptor channel gating control by the pre-M1 helix. *J. Gen. Physiol.* **152** (2020).

309. R. S. Marshall, R. D. Vierstra, Autophagy: The Master of Bulk and Selective Recycling. *Annu. Rev. Plant Biol.* **69**, 173–208 (2018).

310. S. Wada, *et al.*, Autophagy plays a role in chloroplast degradation during senescence in individually darkened leaves. *Plant Physiol.* **149**, 885–893 (2009).

311. Z. Deng, *et al.*, Autophagy Receptors and Neurodegenerative Diseases. *Trends Cell Biol.* **27**, 491–504 (2017).

312. H. Wang, *et al.*, Atg7 is required for acrosome biogenesis during spermatogenesis in mice. *Cell Res.* **24**, 852–869 (2014).

313. A. Criollo, *et al.*, Regulation of autophagy by the inositol trisphosphate receptor. *Cell Death Differ.* **14**, 1029–1039 (2007).

314. C. Cardenas, *et al.*, Essential regulation of cell bioenergetics by constitutive InsP3 receptor Ca2+ transfer to mitochondria. *Cell* **142**, 270–283 (2010).

315. X. Tian, *et al.*, A Voltage-Gated Calcium Channel Regulates Lysosomal Fusion with Endosomes and Autophagosomes and Is Required for Neuronal Homeostasis. *PLoS Biol.* **13**, 1–25 (2015).

316. A. A. Soyombo, *et al.*, TRP-ML1 regulates lysosomal pH and acidic lysosomal lipid hydrolytic activity. *J. Biol. Chem.* **281**, 7294–7301 (2006).

317. X.-P. Dong, *et al.*, The type IV mucolipidosis-associated protein TRPML1 is an endolysosomal iron release channel. *Nature* **455**, 992–996 (2008).

318. C. Curcio-Morelli, *et al.*, Macroautophagy is defective in mucolipin-1-deficient mouse neurons. *Neurobiol. Dis.* **40**, 370–377 (2010).

319. A. Kondratskyi, K. Kondratska, R. Skryma, D. J. Klionsky, N. Prevarskaya, Ion channels in the regulation of autophagy. *Autophagy* **14**, 3–21 (2018).

320. K. Kohda, Y. Wang, M. Yuzaki, Mutation of a glutamate receptor motif reveals its

role in gating and delta2 receptor channel properties. *Nat. Neurosci.* **3**, 315–322 (2000).

321. A. Copani, *et al.*, Interaction between ß-N-methylamino- l-alanine and excitatory amino acid receptors in brain slices and neuronal cultures. *Brain Res.* **558**, 79–86 (1991).

322. E. D. Brenner, *et al.*, Arabidopsis mutants resistant to S(+)-β-methyl-α, β-diaminopropionic, acid, a cycad-derived glutamate receptor agonist. *Plant Physiol.* **124**, 1615–1624 (2000).

323. P. S. Spencer, *et al.*, Guam amyotrophic lateral sclerosis-parkinsonism dementia linked to a plant excitant neurotoxin. *Science.* **237**, 517–522 (1987).

324. E. D. Brenner, P. Feinberg, S. Runko, G. M. Coruzzi, A mutation in the Proteosomal Regulatory Particle AAA-ATPase-3 in Arabidopsis impairs the light-specific hypocotyl elongation response elicited by a glutamate receptor agonist, BMAA. *Plant Mol. Biol.* **70**, 523–533 (2009).

325. J. Sai, C. H. Johnson, Dark-stimulated calcium ion fluxes in the chloroplast stroma and cytosol. *Plant Cell* **14**, 1279–1291 (2002).

326. S. J. Müller-Schüssele, *et al.*, Chloroplasts require glutathione reductase to balance reactive oxygen species and maintain efficient photosynthesis. *Plant J.* **103**, 1140–1154 (2020).

327. S. S. Oja, R. Janáky, V. Varga, P. Saransaari, Modulation of glutamate receptor functions by glutathione. *Neurochem. Int.* **37**, 299–306 (2000).

328. R. Janáky, *et al.*, Glutathione and signal transduction in the mammalian CNS. *J. Neurochem.* **73**, 889–902 (1999).

329. L. D. Gomez, G. Noctor, M. R. Knight, C. H. Foyer, Regulation of calcium signalling and gene expression by glutathione. *J. Exp. Bot.* **55**, 1851–1859 (2004).

330. Z. Qi, N. R. Stephens, E. P. Spalding, Calcium Entry Mediated by GLR3.3, an Arabidopsis Glutamate Receptor with a Broad Agonist Profile. *Plant Physiol.* **142**, 963–971 (2006).

331. J. M. Sullivan, *et al.*, Identification of two cysteine residues that are required for redox modulation of the NMDA subtype of glutamate receptor. *Neuron* **13**, 929–936 (1994).

332. G. Köhr, S. Eckardt, H. Lüddens, H. Monyer, P. H. Seeburg, NMDA receptor channels: Subunit-specific potentiation by reducing agents. *Neuron* **12**, 1031–1040 (1994).

333. V. Nadler, Y. Kloog, M. Sokolovsky, 1-Aminocyclopropane-1-carboxylic acid (ACC) mimics the effects of glycine on the NMDA receptor ion channel. *Eur. J. Pharmacol.* **157**, 115–116 (1988).

334. R. Nahum-Levy, L. H. Fossom, P. Skolnick, M. Benveniste, Putative partial agonist 1-aminocyclopropanecarboxylic acid acts concurrently as a glycine-site agonist and a glutamate-site antagonist at N- methyl-D-aspartate receptors. *Mol. Pharmacol.* **56**, 1207–1218 (1999).

335. C. Ju, *et al.*, Conservation of ethylene as a plant hormone over 450 million years of evolution. *Nat. Plants* **1**, 1–7 (2015).

336. W. Mou, *et al.*, Ethylene-independent signaling by the ethylene precursor ACC in Arabidopsis ovular pollen tube attraction. *Nat. Commun.* **11**, 1–11 (2020).

337. S. Okuda, *et al.*, Defensin-like polypeptide LUREs are pollen tube attractants secreted from synergid cells. *Nature* **458**, 357–361 (2009).

338. R. Muralla, C. Sweeney, A. Stepansky, T. Leustek, D. Meinke, Genetic dissection of histidine biosynthesis in Arabidopsis. *Plant Physiol.* **144**, 890–903 (2007).

339. L. Vanderstraeten, D. Van Der Straeten, Accumulation and Transport of 1-Aminocyclopropane-1-Carboxylic Acid (ACC) in Plants: Current Status, Considerations for Future Research and Agronomic Applications. *Front. Plant Sci.* **8**, 1–18 (2017).

340. A. V. Glushakov, *et al.*, Specific inhibition of N-methyl-D-aspartate receptor function in rat hippocampal neurons by L-phenylalanine at concentrations observed during phenylketonuria. *Mol. Psychiatry* **7**, 359–367 (2002).

341. E. Hunt, *et al.*, A mutation in amino acid permease AAP6 reduces the amino acid content of the Arabidopsis sieve elements but leaves aphid herbivores unaffected. *J. Exp. Bot.* **61**, 55–64 (2010).

342. Q. Shao, Q. Gao, D. Lhamo, H. Zhang, S. Luan, Two glutamate- and pH-regulated Ca2+ channels are required for systemic wound signaling in Arabidopsis. *Sci. Signal.* **13**, 1–14 (2020).

343. H. T. Kurata, M. Rapedius, M. J. Kleinman, T. Baukrowitz, C. G. Nichols, Voltage-dependent gating in a “voltage sensor-less” ion channel. *PLoS Biol.* **8** (2010).

344. M. Schewe, *et al.*, A Non-canonical Voltage-Sensing Mechanism Controls Gating in K2P K+Channels. *Cell* **164**, 937–949 (2016).

345. B. A. Maki, G. K. Popescu, Extracellular Ca2+ ions reduce NMDA receptor

conductance and gating. *J. Gen. Physiol.* **144**, 379–92 (2014).

346. A. Keramidas, A. J. Moorhouse, C. R. French, P. R. Schofield, P. H. Barry, M2 pore mutations convert the glycine receptor channel from being anion- to cation-selective. *Biophys J* **79**, 247–259 (2000).

347. T. Shimomura, *et al.*, A native prokaryotic voltage-dependent calcium channel with a novel selectivity filter sequence. *Elife* **9**, 1–21 (2020).

348. E. M. Jorgensen, Animal evolution: Looking for the first nervous system. *Curr. Biol.* **24**, 655–658 (2014).

349. F. C. Acher, H. O. Bertrand, Amino acid recognition by venus flytrap domains is encoded in an 8-residue motif. *Biopolym. - Pept. Sci. Sect.* **80**, 357–366 (2005).

350. B. H. Oh, *et al.*, The bacterial periplasmic histidine-binding protein. Structure/function analysis of the ligand-binding site and comparison with related proteins. *J. Biol. Chem.* **269**, 4135–4143 (1994).

351. B. H. Oh, *et al.*, Three-dimensional structures of the periplasmic lysine/arginine/ornithine- binding protein with and without a ligand. *J. Biol. Chem.* **268**, 11348–11355 (1993).

352. B. G. Forde, M. R. Roberts, Glutamate receptor-like channels in plants: a role as amino acid sensors in plant defence? *F1000Prime Rep.* **6**, 1–7 (2014).

353. M. W. Wood, H. M. A. Vandongen, A. M. J. Vandongen, Structural conservation of ion conduction pathways in K channels and glutamate receptors. *Proc. Natl. Acad. Sci. U. S. A.* **92**, 4882–4886 (1995).

354. T. Kuner, P. H. Seeburg, H. R. Guy, A common architecture for K+ channels and ionotropic glutamate receptors? *Trends Neurosci.* **26**, 27–32 (2003).

355. S. Lomash, S. Chittori, P. Brown, M. L. Mayer, Anions mediate ligand binding in adineta vaga glutamate receptor ion channels. *Structure* **21**, 414–425 (2013).

356. M. Schönrock, G. Thiel, B. Laube, Coupling of a viral K+-channel with a glutamate-binding-domain highlights the modular design of ionotropic glutamate-receptors. *Commun. Biol.* **2**, 1–10 (2019).

357. S. Wege, M. Gilliham, S. W. Henderson, Chloride: Not simply a “cheap osmoticum”, but a beneficial plant macronutrient. *J. Exp. Bot.* **68**, 3057–3069 (2017).

358. J. H. Hu, *et al.*, Identification of Glutamate Receptors and Transporters in Mouse and Human Sperm. *J. Androl.* **25**, 140–146 (2004).

359. D. Endo, *et al.*, NMDA-type glutamate receptors mediate the acrosome reaction and motility initiation in newt sperm. *Mol. Reprod. Dev.* **86** (2019).

360. R. Hedrich, V. Salvador-Recatalà, I. Dreyer, Electrical Wiring and Long-Distance Plant Communication. *Trends Plant Sci.* **21**, 376–387 (2016).

361. D. Jaślan, *et al.*, Voltage-dependent gating of SV channel TPC1 confers vacuole excitability. *Nat. Commun.* **10**, 1–9 (2019).

362. B. Schulz-Lessdorf, R. Hedrich, Protons and calcium modulate SV-type channels in the vacuolar-lysosomal compartment - channel interaction with calmodulin inhibitors. *Planta* **197**, 655–671 (1995).

363. T. Čermák, *et al.*, A multipurpose toolkit to enable advanced genome engineering in plants. *Plant Cell* **29**, 1196–1217 (2017).

364. A. Lampropoulos, *et al.*, GreenGate - A novel, versatile, and efficient cloning system for plant transgenesis. *PLoS One* **8** (2013).

365. D. G. Gibson, *et al.*, Enzymatic assembly of DNA molecules up to several hundred kilobases. *Nat. Methods* **6**, 343–345 (2009).

366. R. Reski, W. O. Abel, Induction of budding on chloronemata and caulonemata of the moss, Physcomitrella patens, using isopentenyladenine. *Planta* **165**, 354–358 (1985).

367. J. D. Hiscox, G. F. Israelstam, A method for the extraction of chlorophyll from leaf tissue without maceration. *Can. J. Bot.* **57**, 1332–1334 (1979).

368. A. D. Richardson, S. P. Duigan, G. P. Berlyn, An evaluation of noninvasive methods to estimate foliar chlorophyll content. 185–194 (2002).

369. Arnon, COPPER ENZYMES IN ISOLATED CHLOROPLASTS. POLYPHENOLOXIDASE IN BETA VULGARIS. *Plant Physiol.* **24**, 682 (1949).

370. O. P. Hamill, A. Marty, E. Neher, B. Sakmann, F. J. Sigworth, Improved patch-clamp techniques for high-resolution current recording from cells and cell-free membrane patches. *Pflügers Arch. Eur. J. Physiol.* **391**, 85–100 (1981).

371. E. Neher, B. Sakmann, The Patch Clamp Technique. *Sci. Am.* **266**, 44–51 (1992).

372. B. Barbour, Electronics for electrophysiologists. 1–23 (2011).

373. T. Nagai, S. Yamada, T. Tominaga, M. Ichikawa, A. Miyawaki, Expanded dynamic range of fluorescent indicators for Ca2+ by circularly permuted yellow fluorescent proteins. *Proc. Natl. Acad. Sci. U. S. A.* **101**, 10554–10559 (2004).

374. V. Pérez Koldenkova, T. Nagai, Genetically encoded Ca2+ indicators: Properties and evaluation. *Biochim. Biophys. Acta - Mol. Cell Res.* **1833**, 1787–1797 (2013).